Electron Tunneling Studies in Ta Overlayers on Nb and in Ta and NbN Films

A Dissertation

Presented to the Faculty of the Graduate School

of

Yale University

in Candidacy for the Degree of

Doctor of Philosophy

by

Elie Khalil Track

May 1988

ABSTRACT

Electron Tunneling Studies in Ta Overlayers on Nb and in Ta and NbN Films

Elie Khalil Track

Yale University

1988

Tunneling measurements have been performed on tantalum surface layers on niobium. The thickness of the tantalum layer ranges from 10 to 100 Å. The critical current, bound-state energy, phonon structure, and oxide barrier shape are investigated. The results are compared with an extended version of the Gallagher theory which accounts for both the finite mean free path in the Ta overlayers and suppression of the I_cR product due to strong electron-phonon coupling effects. Excellent fits to the data yield a value of the intrinsic scattering probability for electrons at the Ta/Nb interface of $r^2=0.01$. In addition, a new fabrication technique - dual ion-beam sputtering - is used to deposit thin films of NbN. The properties of these films and of tunnel junctions formed with NbN as base electrode and native-oxide as well as artificial barriers are reported. A universal empirical correlation is found between the average barrier height ϕ and the effective barrier width d for measured junctions. This correlation, which holds both for our data and for available data in the literature for oxide-barrier junctions, is discussed in the general context of oxide growth and compared with results for artificial tunnel barriers. Finally, high quality Ta/PbBi tunnel junction of area $\leq 1\ \mu m^2$ and current density

10^3-10^5 A/cm^2 are produced using a window geometry. The electrical noise properties of these junctions are investigated. Discrete voltage switching events allow the identification of the effect of single localized states in the oxide barrier. The voltage and temperature dependence of the switching rates are consistent with a microscopic model based on the emission and capture of individual electrons at the localized sites within the barrier.

ACKNOWLEDGEMENTS

My journey through graduate school would not have been possible without the support of several people. They generously gave their time, shared their insights, and, with their sustained confidence and encouragement, helped me sail successfully to safe harbor.

My advisor, professor Daniel Prober, followed the education philosophy par excellence: teaching by example. His outstanding scholarship is complemented by a remarkable scientific intuition. His ability to cut through the crust and fat and distill the physics in complex problems has been primordial in keeping my work on track. Dan's high standards and expectations of academic excellence are matched by a genuine concern for the well-being of his students. His friendship constituted an essential ingredient of my success. Professor Steven Ruggiero - now at the University of Notre Dame - introduced me to the wonderful word of "junctionology". His years at Yale benefited all those who interacted with him, especially those - like me - who collaborated closely with him.

Of the senior graduate students, I owe to Dean Face long hours of fruitful discussions, a consistent willingness to lend a helping hand, a meticulous sense of order, and above all, a contagious love of science and a persistent desire to know "how things work". Dean's thesis represented pillars on which some of my work rested, and he contributed considerably to everything in the lab, from electronic instrumentation to debugging the laser printer. Bruce Dalrymple, Padmanabhan Santhanam, and Shalom Wind willingly shared their knowledge and wit and insured the presence of the right amount of humor - promoting general sanity.

Michael Rooks - our computer guru - wrote all the interfacing and plotting programs and many of the analysis programs. Mike was always at hand to discuss processing problems and alternatives. Most of all, his candid friendship is greatly valued. Venkat Chandrasekhar and Tom Kopley quickly moved up the ladder from trainees to experts I could consult and learn from. Venkat always lent a charitable and amused ear to my Friday afternoon wisdom speeches. Chris Tigges helped me interface to the spectrum analyzer, and never missed a chance to challenge me with intriguing scientific paradoxes. Anthony Worsham grew fast to become the carrier of the torch of junction expertise. He generously helped in statistical analyses of data. Paul McEuen and Steve Klepper - each shining in his own endeavour, wholeheartedly offered constructive comments. Guang-Ji Cui helped develop the fabrication processes for the small area junctions and set an example of perseverance and hard work for all to follow.

Mr. Clifford Sneider expertly provided all the machining support I needed. Ms. Sara Batter went far beyond the call of duty in facilitating my initial settling at Yale and continued to expertly guide me through all the administrative requirements of the physics department and the graduate school. Her genuine concern for my - (and all physics graduate students') - well-being is gratefully appreciated. Ms. June Yarosh expertly rendered secretarial support.

Special thanks go to my thesis committee, Professors Daniel Prober, Robert Wheeler, Doug Stone, Ramamutri Shankar, and William Lichten for their valuable time and propitious comments. Outside Yale, I would like to thank Professor Gerald Arnold of the University of Notre Dame who supplied the theoretical support for the proximity effect studies. Professor Jurgen Halbritter of the Karlsruhe Nuclear Center

(KFK) offered perceptive insights into the barrier properties of our junctions and I am grateful to him for agreeing to be my "outside reader".

I am grateful for the financial support of Yale University through a University Fellowship for the first two years. The financial support of NSF grants ECS-8604350, ECS-8305000, DMR-8019739 and of ONR grant N00014-80-C-0855 is also gratefully acknowledged.

The love and support of my family was the springboard for my successful jump into the world of science. Early on, my father instilled in me the love of education. My mother and sister sacrificed generously during very trying times to give me the freedom to pursue my goals. My brother often elucidated for me the most complex mathematical concepts with simple but astute insights. Finally, I would like to dedicate this thesis to my wife Rowena, whose love, support and confidence were a constant source of encouragement and kept my torch of happiness brightly lit.

TABLE OF CONTENTS

	Page
Acknowledgements	ii
List of Symbols and Abbreviations	ix
List of Figures	xii
List of Tables	xvi
I. INTRODUCTION	1
II. THEORETICAL BACKGROUND	5
II.A. Superconductivity	5
II.A.1. BCS Theory: weak-coupling limit	6
II.A.2. Strong Coupling Superconductors	12
II.B. Tunneling Between Metals	15
II.B.1. Quasiparticle Tunneling	15
II.B.2. Cooper-Pair Tunneling: the Josephson Effect	20
III. THIN FILM DEPOSITION AND MATERIAL PROPERTIES	24
III.A. Soft Materials: Thermal Evaporation	24
III.B. Ion-Beam Sputter-Deposition: Nb and Ta	31
III.B.1. Description of an Ion-Source	31
III.B.2. Properties of Nb and Ta produced by ion-beam sputtering	35
III.C. Dual Ion-beam Deposition of NbN	37
III.C.1. Motivation for use of NbN	37
III.C.2. Motivation for using Dual Ion-Beam Deposition	40
III.C.3. Optimization Scheme	41

III.C.4. NbN Films: Results and Discussion 44

III.D. Summary 52

IV. JUNCTION FABRICATION 53

IV.A. Large Area Junctions 53

IV.B. Small Area Junctions 55

IV.B.1. Patterning of the Base Electrode 58

IV.B.2. Patterning of the Junction Area: Defining the Window 58

IV.B.3. Tunnel Barrier Formation and Counterelectrode Deposition and Patterning 62

V. JUNCTION MEASUREMENTS AND DC PROPERTIES 72

V.A. Electronic Instrumentation 72

V.A.1. Low-Noise Current Source 72

V.A.2. Buffer Amplifiers 75

V.A.3. Derivative Measurements: ac modulation technique 75

V.B. Low-Temperature Apparatus 82

V.B.1. Dewars and Cryostats 82

V.B.2. Sample Mounting 83

V.C. DC I-V Characteristics 87

V.C.1. Large Area Junctions 88

V.C.2. Small Area Junctions 94

VI. PROXIMITY EFFECT TUNNELING 100

VI.A. Introduction: The Proximity Effect 100

VI.B. Tunneling into Proximity-Effect Systems 104

VI.C. Ta Overlayers on Nb 105

VI.C.1. Experimental Considerations 105

VI.C.2. I-V curves 106

VI.C.3. The Model 109

VI.C.4. Discussion 112

VI.C.5. Energy Gap and Critical Current 116

VI.C.6. Phonon Structure 122

VI.D. NbN: Effect of Oxidized Metal Overlayers 124

VI.E. Conclusions 128

VII. TUNNEL BARRIER PROPERTIES 130

VII.A. Introduction: The Tunnel Barrier 130

VII.B. Tunnel Barrier Models 133

VII.C. Nb/Ta-based Junctions 138

VII.C.1. Experimental Results 138

VII.C.2. Comparison with other work: General Trends 142

VII.C.3. Correlation with the Theory of Oxidation of Metals 147

VII.D. NbN-based Junctions 151

VII.D.1. NbN Native Oxide Barriers 151

VII.D.2. Artificial Barriers on NbN 152

VII.E. Conclusions 164

VIII. TUNNELING NOISE SPECTROSCOPY 166

VIII.A. Introduction: Low Frequency Fluctuations and 1/f Noise 166

VIII.B. Noise Measurements in Submicron Ta/PbBi Junctions 169

VIII.C. Telegraph Noise Spectroscopy: Results and Discussion 178

VIII.C.1. Analysis of the Telegraph Noise 178

VIII.C.2. Effect of Voltage, Temperature, and Magnetic Field; Microscopic Model 181

VIII.C.3. Correlation with Barrier Spectroscopy 187

VIII.D. Conclusions 190

IX. SUMMARY AND CONCLUSIONS 191

APPENDIX A. Fabrication Sequence for Small-Area Ta/PbBi Junctions 194

APPENDIX B. Microwave Measurements of Ta/PbBi Junctions 197

REFERENCES 202

LIST OF SYMBOLS AND ABBREVIATIONS

$\alpha(\omega)$	Electron-phonon coupling constant
α	Ginzburg-Landau parameter
$\vec{A}$	Magnetic Vector Potential
β	Ginzburg-Landau parameter
BCS	Bardeen-Cooper-Schrieffer
bcc	Body-centered cubic
C_V	Voltage-voltage autocorrelation function
d	Tunnel-Barrier width
D_N	Diffusion Coefficient
DSB	Double-Sideband
Δ	Superconducting Energy gap
Δ_k	BCS Gap function
Δ_{NS}	Voltage of the midpoint of the current-rise
e	Charge of the electron
e^*	= 2e, charge of a Cooper pair
eV	Electron-Volt
E_F	Fermi Energy
ϵ_k	Normal-metal energy for an electronic state of wavevector $\vec{k}$
E_k	Superconductor's excitation energy forquasiparticle state $\vec{k}$
f	frequency
f(E)	Fermi function $=1/(1+\exp(E/k_BT))$
fF	femto-Farad
$F(\omega)$	Phonon Density of States
ϕ	Tunneling Barrier Height

$\Delta\phi$	Tunneling Barrier Asymmetry
fcc	Face-centered cubic
Φ	Magnetic Flux
G	Differential Conductance dI/dV
G_{nn}	Conductance (I/V) of Normal-Insulator-Normal tunnel junction
G(k,E)	Green function
$\hat{g}$	Logarithmic derivative of the conductance = d[ln(I/V)]/dV
h	Planck's constant = 4.1357×10^{-15} eV.sec
$\hbar$	$h/2\pi = 6.582 \times 10^{-16}$ eV.sec
hcp	Hexagonal close-packed
h_k	Pair-state occupation probability
I_c	Josephson critical current
I_cR	I_c multiplied by the junction resistance
IF	Intermediate frequency
I-V	Current (I) vs. Voltage (V)
in situ	Without Breaking Vacuum
J_e	Electronic current
J_i	Ionic current
J_s	Pair supercurrent
$\vec{k}$	wavevector
$\vec{k}\uparrow(\downarrow)$	State with wavevector $\vec{k}$ and spin up (down)
k_B	Boltzman's constant = 8.617×10^{-5} eV/K
K	Degrees Kelvin
LO	Local Oscillator
ℓ	Mean free path
λ	Electron-phonon coupling strength

m^*	Mass of a Cooper-pair (= twice the electronic mass)
n_s	Density of superconducting electrons
$N_n(0)$	Normal-metal density of states at the Fermi energy
$N_S(E)$	Superconductor's density of states
N-I-N	Normal metal - Insulator - Normal metal
NBS	National Bureau of Standards
ψ	Wavefunction
ξ	Coherence length
R_N,R_n	Normal-state tunnel junction resistance
RRR	Residual resistance ratio
R_D	Dynamic (=differential) resistance
r	Reflection Coefficient
RPM	Revolutions per minute
RF	Radio Frequency
ω	Angular frequency in rad/sec
S-I-S	Superconductor-Insulator-Superconductor
S-I-N	Superconductor-Insulator-Normal metal
SSB	Single-Sideband
S_V	Power Spectral Density
T	Temperature
$\|T\|$	Tunneling matrix
T_c	Superconducting transition temperature
US	Ultrasonic agitation
v_F	Fermi velocity (for most metals ~ 10^7 furlongs/fortnight)

LIST OF FIGURES

Figure		Page
1-1	Schematic illustration of a tunnel junction and its I-V curve.	2
2-1	BCS electron-electron interaction potential.	7
2-2	Pair density and excitation spectrum of a superconductor.	10
2-3	Density of states of normal metals and superconductors.	11
2-4	Energy diagram and I-V characteristic of an N-I-S junction.	17
2-5	Energy diagram and I-V characteristic of an S-I-S junction.	18
2-6	Josephson tunneling and its magnetic field dependence.	21
3-1	Schematic of the thermal evaporator.	25
3-2	Cross section of the SiO evaporation "baffled box".	28
3-3	Phase diagram, T_c , and energy gap of Pb_xBi_y.	30
3-4	Schematic of a Kaufman ion source.	32
3-5	Schematic of the ion-beam deposition system.	34
3-6	Equilibrium phase diagram of the Nb-N system.	38
3-7	Crystal structure of the different NbN phases.	39
3-8	Dual Ion-Beam Sputtering Configuration.	42
3-9	Transmission Electron Micrograph of a NbN film.	46
3-10	Transition temperature of NbC_xN_y versus molecular percent of CH_4 in the second ion-source gas mixture.	48
4-1	Large area junction geometry.	54
4-2	Window geometry for the small area junctions.	57
4-3	Sequence of steps in lift-off patterning	59
4-4	Undercut profiles in the photoresist lift-off stencil.	60
4-5	Sequence of steps in RIE patterning.	61
4-6	Micrograph of the photoresist lift-off pattern for SiO.	63

4-7	Different exposures of chlorobenzene-soaked photoresist.	64
4-8	Illustration of the Face step process for Ta/PbBi junctions.	66
4-9	Glow discharge oxidation configuration.	67
4-10	Proposed process for submicron junctions.	70
5-1	Circuit diagram of the low-noise current source.	73
5-2	Circuit diagram of the buffer amplifiers.	76
5-3	Schematic of the derivative harmonic detection technique.	77
5-4	Four terminal bridge configuration.	80
5-5	Schematic of the "solder-on can" cryostat.	84
5-6	Schematic of the "no-solder cryostat".	85
5-7	Cross section of the POGO-pin spring loaded contacts.	86
5-8	I-V characteristics of large area Nb junctions with native oxide.	89
5-9	I-V characteristics of large area Ta-overlayers-on-Nb junctions.	90
5-10	I-V characteristic of a large area NbN junction with native oxide.	91
5-11	I-V characteristic of large area NbN-based junctions.	92
5-12	I-V characteristics of small area NbN-based junctions.	95
5-13	I-V characteristics of small area Ta/PbBi junctions.	96
5-14	Ta/PbBi junction resistance vs. glow discharge oxidation time.	97
6-1	Pair-potential variation at a superconductor-normal metal interface.	101
6-2	I-V characteristic of a Nb/75 Å Ta/PbBi junction.	107
6-3	Proximity density of state of a Nb/75 Å Ta bilayer.	108
6-4	Schematic of the proximity effect tunneling geometry and the corresponding density of states.	110
6-5	Bound-state structure in the I-V of a Pb/insulator/Zn/Pb junction.	111
6-6	Conductance data for Ta overlayer system.	113
6-7	I-V and dI/dV of a Nb/40 Å Ta/Pb junction.	115

6-8	Prediction of Gallagher for Josephson current and bound-state energy in a proximity-effect system.	117
6-9	Josephson current and bound-state energy in the Nb/Ta system.	118
6-10	Oscilloscope traces for two Ta overlayer junction with thin (50 Å) and thick (1000 Å) Ta.	119
6-11	Phonon structure in the d^2V/dI^2 signal of Nb/Ta/oxide/Ag junctions.	123
6-12	I-V characteristics of oxidized metal overlayers (OMO) on NbN.	125
6-13	Conductance data for a NbN/Nb(10Å)+Ta(18Å)/PbBi junction.	127
7-1	Energy diagram for a metal-insulator-metal structure.	131
7-2	Sketch of complex barrier at the surface of Niobium.	132
7-3	Trapezoidal barrier model and corresponding conductance.	134
7-4	Theoretical logarithmic derivative $\hat{g}$ of the conductance.	136
7-5	Illutration of peaks in $\hat{g}$ corresponding to onsets of new tunneling channels.	137
7-6	Variation of barrier height with barrier width for Nb/Ta junctions.	141
7-7	Barrier height vs. barrier width for a variety of junctions.	143
7-8	Illustration of resonant tunneling via a localized state in the barrier.	145
7-9	Conductance data for a Nb/25 Å Ta/Ag junction.	146
7-10	Energy diagram at a metal/air interface.	148
7-11	Conductance data for a NbN/Ag junction.	153
7-12	I-V characteristics of NbN/AlN/PbBi junctions.	155
7-13	Resistance vs. AlN thickness for AlN-barrier junctions.	156
7-14	Resistance vs. junction position for AlN-barrier junctions.	157
7-15	WKB barrier width versus deposited thickness of AlN and Al.	158
7-16	Logarithmic derivative $\hat{g}$ for a NbN/48Å AlN/PbBi junction.	159
7-17	Differential conductance for a NbN/48Å AlN/PbBi junction.	160
7-18	Conductance data for a NbN/13 Å Al/PbBi junction.	161

7-19	Conductance data for a NbN/Nb(4Å)+Ta(10Å)/PbBi junction.	162
8-1	Noise spectrum for a large area junction.	168
8-2	I-V characteristics of submicron Ta/PbBi junctions.	170
8-3	Block diagram of the noise measurement apparatus.	172
8-4	Power Spectral density of a Ta/PbBi submicron junction.	174
8-5	Switching behavior observed in Ta/PbBi submicron junctions.	175
8-6	Increase in switching frequency with increasing bias voltage.	176
8-7	Increase in switching frequency with increasing temperature.	177
8-8	Exponential dependence of the switching probability on time.	179
8-9	Power spectral density dominated by switching of a single trap.	180
8-10	Voltage dependence of the noise power spectral density.	182
8-11	Temperature dependence of the noise power spectral density.	183
8-12	Illustration of the Rogers and Buhrman model.	184
8-13	Magnetic field dependence of the noise power spectral density.	186
8-14	Correlation of the switching noise with barrier spectroscopy.	188
8-15	1/f noise arising from a superposition of Lorentzian contributions.	189
B-1	Filter structure design for the electrodes of SIS broadband mixers.	198

LIST OF TABLES

Table		Page
3-1	Relevant parameters for evaporated materials.	26
3-2	Typical operating conditions of the first ion-source.	36
3-3	Summary of the properties of NbN films produced.	43
3-4	Typical results for selected NbN film depositions.	45
3-5	Parameters for deposition of AlN films.	51
4-1	Ion-milling etch rates with 300 V Xe for various materials.	69
7-1	Parameters of Ta surface-layer tunnel junctions.	140
7-2	Barrier parameters for NbN-based tunnel junctions.	163
B-1	Summary of mixer results for Ta/PbBi junctions.	200

I. INTRODUCTION

The pioneering work of Fisher and Giaever (1961) first demonstrated electron tunneling through an oxide barrier formed by exposing a clean metal strip to oxygen or laboratory air. Their work has opened a new field of research in superconductivity – tunneling spectroscopy. Electron tunneling is used as a probe to measure various properties of superconductors and normal metals, such as the superconducting energy gap and the electron-phonon interaction spectrum. Tunnel junctions also permeate several areas of physics. They are used as model systems for the study of macroscopic quantum tunneling, metal-insulator transitions, and fluctuation phenomena [Likharev (1986)]. They have provided the most accurate measurement of the ratio of the fundamental constants e/h [Parker et al. (1969)] and are now used as voltage standards [Witt et al. (1983)]. Superconducting Quantum Interference Devices (SQUIDs) made of two tunnel junctions in parallel constitute the most sensitive magnetometers, and have recently been used to measure the variation of the electrochemical potential difference in a gravitational field [Jain et al. (1987)]. An array of SQUIDs is used in the search for cosmic-ray magnetic monopoles [Bermon (1987)].

A tunnel junction is illustrated schematically in Fig. 1-1. Two metal electrodes are separated by a thin (~20 Å) insulating barrier. When the electrodes are connected to a current source, electrons tunnel across the barrier. This current provides a probe of the properties of the tunnel barrier and of the density of electronic states in the metal electrodes. The full potential of such a spectroscopy rests upon the ability to reproducibly fabricate high quality tunnel junctions. The experimental challenges include the synthesis of thin superconducting films with

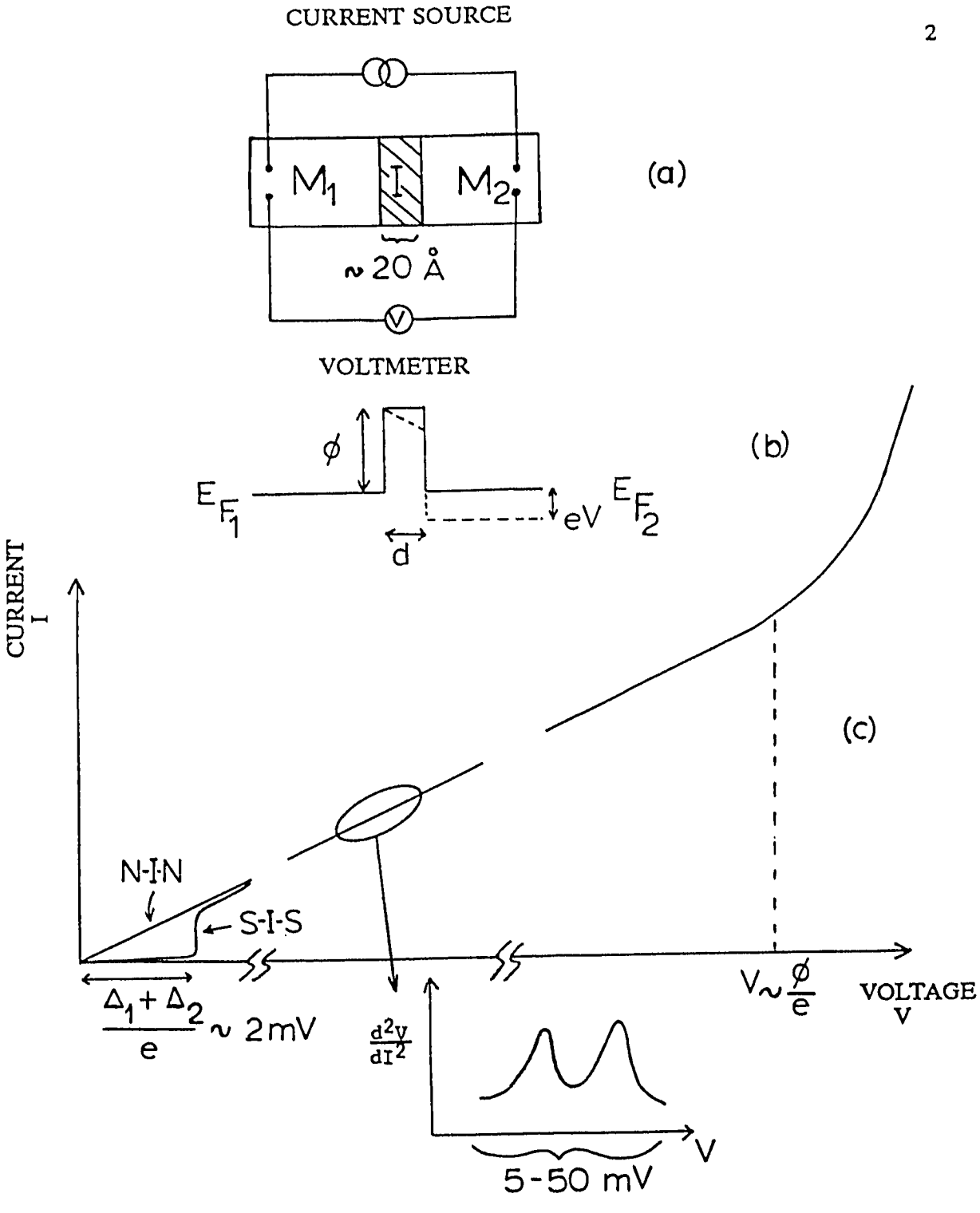

Fig. 1-1 (a) Schematic illustration of a tunnel junction; M_1 and M_2 are the metal electrodes which can be superconductors. (b) Potential barrier model for the insulator, where ϕ is the height and d the width of the barrier; E_{F1} and E_{F2} are the Fermi levels of metals M_1 and M_2, and V the bias voltage. (c) Schematic current-voltage characteristic for a tunnel junction showing some of the structure that reflects the density of states of the electrodes [sum-gap $(\Delta_1+\Delta_2)$ when the electrodes are superconducting, phonon structure] and the properties of the barrier (change of slope of the I-V curve when the bias voltage exceeds the barrier height).

properties approaching those of bulk single crystals, the controlled and reproducible formation of a defect-free ~ 20 Å thick tunnel barrier, and the micron-size patterning of structures needed to produce junctions with given capacitance. The understanding and interpretation of tunneling data pose the problems of testing and extending the existing theories which account for a spectrum of phenomena including but not limited to superconductivity, the proximity effect, resonant tunneling, and fluctuations giving rise to 1/f noise. This thesis proposes to address a number of these issues as they appear in tunnel junctions made with Nb, Ta and NbN base electrodes.

A theoretical overview of superconductivity and tunneling is presented in Chapter 2. This chapter offers only a general background for the theory. The pertinent theories with the relevant details and special topics are introduced along with the appropriate results in chapters 6, 7, and 8 in the hope of keeping theory and experiment integrated and coherent. The experimental techniques for producing and characterizing the tunnel junctions, including a new fabrication technique for NbN thin films are described in chapters 3, 4, and 5. These chapters also report the material properties of thin films produced – resistivity, residual resistivity ratio, superconducting transition temperature, etc., and the dc properties of the various tunnel junctions produced. A step-by-step fabrication sequence for the Ta/PbBi small area tunnel junctions, and their performance as SIS mixers in the 90-110 GHz range are relegated to the two appendices. Chapters 6, 7, and 8 describe and analyze the main results of the measurements. Chapter 6 deals with the properties of Ta overlayers on Nb and models the observations using the theory of the proximity effect. It also describes the effect of artificial barriers on NbN base electrodes. The barrier properties of native-oxide and artificial barriers, their modeling using a

WKB approximation, and interpretations based on the theory of oxidation of metals and localized states in the barrier are discussed in chapter 7. Switching-like fluctuations in small area Ta/PbBi tunnel junctions, their relation to 1/f noise, and the mechanism by which these fluctuations could arise are described and analyzed in chapter 8. Finally, chapter 9 presents a summary and the major conclusions of this work.

II. THEORETICAL BACKGROUND

This chapter provides an overview of the theoretical treatment of superconductivity and of tunneling. This overview is meant to provide a background for the specific issues that are addressed in this thesis. Highlights of the main results of the theory are presented. No attempt is made at a thorough and rigorous treatment which can be found in the references cited and would be beyond the scope and size of this thesis. Further details and discussions will be presented later in the thesis, in parallel with the experimental results.

II.A. Superconductivity

The two basic experimental features of superconductivity are the disappearance of electrical resistance below a critical temperature T_c [Onnes (1911)] and a complete expulsion of magnetic flux below a critical field H_c [Meissner et al. (1933)]. A simple characterization of the superconducting state is as a macroscopic quantum state, described by an order parameter $\psi(r,t)$. This function, which has many of the properties of a ground-state wavefunction, describes the condensate of pairs in a superconductor, known to exhibit phase coherence over macroscopic distances. Ginzburg and Landau (1950) introduced such a complex pseudo-wavefunction ψ as an order parameter for the superconducting electrons such that the local density of superconducting electrons, n_s, is given by:

$$n_s = |\psi(r)|^2 \tag{2.1}$$

Using a variational principle and working from an assumed expansion of the free energy in powers of ψ and $\nabla\psi$, they derived a differential equation for ψ:

$$\frac{1}{2m^*}\left[\frac{\hbar}{i}\vec{\nabla} - \frac{e^*}{c}\vec{A}\right]^2 + \beta|\psi|^2\psi = -\alpha(T)\psi \qquad (2.2)$$

which is similar to the Schrodinger equation for a free particle, but with a nonlinear term. Here $m^* = 2m$ and $e^* = 2e$, where m and e are respectively the mass and charge of the electron. The corresponding equation for the supercurrent:

$$\vec{J}_s = \frac{e^*\hbar}{i2m^*}(\psi^*\vec{\nabla}\psi - \psi\vec{\nabla}\psi^*) - \frac{e^{*2}}{m^*c}|\psi|^2\vec{A} \qquad (2.3)$$

is also the same as the usual quantum-mechanical one for particles of charge e^* and mass m^*. When first proposed, the theory appeared rather phenomenological. However, in 1959 Gor'kov was able to show that the Ginzburg-Landau (GL) theory was in fact a limiting form of the microscopic theory of BCS (Bardeen-Cooper-Schreiffer), valid near T_c. Here ψ is directly proportional to the gap parameter Δ of BCS. ψ can be thought of as the wavefunction of the center-of-mass of the Cooper pairs.

II.A.1. BCS Theory: weak-coupling limit

The microscopic BCS theory describes superconductivity as an attractive electron-electron interaction mediated by phonons. This interaction is characterized by an interaction constant V. If this attraction is larger than the Coulomb repulsion, then electrons of equal and opposite spin and momenta will couple together and form Cooper pairs [Cooper, 1956]. Thermal excitations tend to break those pairs and, above a critical temperature T_c, the metal becomes normal. The physical idea of the attractive electron-electron interaction is simple: lattice polarization by one conduction electron lowers the energy of a second electron appearing at the same position at a later time. In a quantum mechanical picture shown in Fig. 2-1a, the

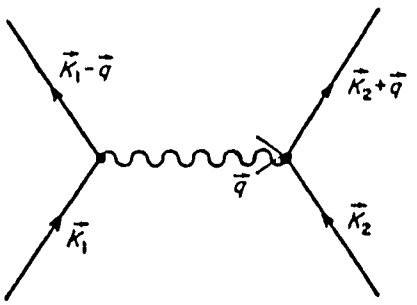

(a)

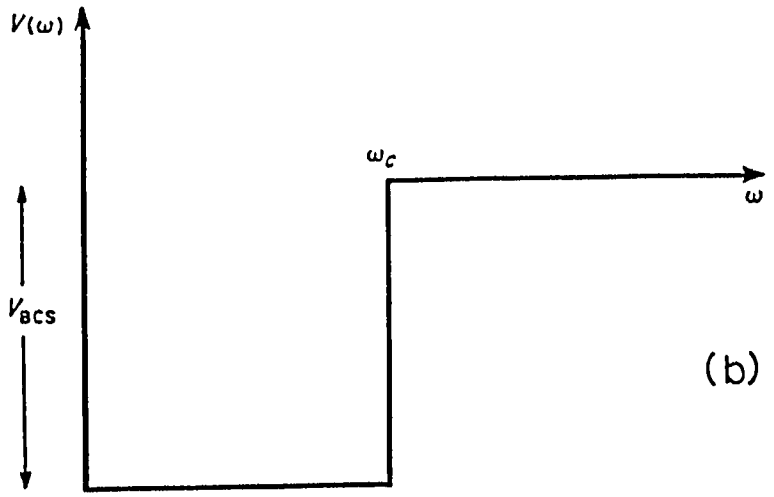

(b)

Fig. 2-1 (a) Electron-electron interaction by exchange of a phonon. (b) BCS model potential which assumes a constant attractive energy for pairs of electrons whose energies are less than the cutoff energy from the Fermi surface. From Wolf (1985).

initial electron $\vec{k}$ scatters to $\vec{k}-\vec{q}$ by emitting a phonon, of wavevector $\vec{q}$ and energy $\hbar\omega_q$, which is absorbed as the second electron scatters from $-\vec{k}$ to $-\vec{k}+\vec{q}$. If the net interaction V is attractive, the N-electron system will be unstable against transition to the superconducting state. In this state, at T = 0, all electrons occupy pair-states ($\vec{k}\uparrow$, $-\vec{k}\downarrow$) so that for all $\vec{k}$ the two single-electron states $\vec{k}\uparrow$ and $-\vec{k}\downarrow$ are both occupied or both empty, but no single electron occupancy is possible. The BCS theory assumes the existence of such a ground state and uses a variational calculation to obtain the occupation probability $h_k \equiv v_k^2$ of the pair states which produces the minimum energy. A major simplifying assumption in the BCS theory is that the difference between the attractive electron-phonon-electron and the repulsive screened Coulomb interactions, $-V_{kk'}$, is taken to be a constant, equal to V, for electron energies less than a cutoff energy $\hbar\omega_c$ on the order of the Debye energy. $V_{kk'}$ is zero otherwise, as shown in Fig. 2-1b. The energy of the superconducting state at T = 0 K relative to the normal state may be written as:

$$W_0 = \sum_{k>k_F} \epsilon_k h_k + \sum_{k<k_F} |\epsilon_k|(1-h_k) - \sum_{k,k'} V_{kk'} [h_{k'}(1-h_{k'})]^{1/2} [h_k(1-h_k)]^{1/2} \qquad (2.4)$$

The desired h_k is obtained by minimizing W_0, i.e. satisfies $\partial W_0/\partial h_k = 0$. Thus

$$\epsilon_k = \frac{\Delta_k(1-2h_k)}{[h_k(1-h_k)]^{1/2}} \qquad (2.5)$$

where the gap function Δ_k is defined as

$$\Delta_k \equiv \sum_{k'} V_{kk'} [h_{k'}(1-h_{k'})]^{1/2} \qquad (2.6)$$

Eq. (2.5) is quadratic in h_k. Its solution gives (see Fig. 2-2a)

$$h_k = \frac{1}{2}\left[1 - \frac{\epsilon_k}{E_k}\right] \equiv v_k^2 \; ; \quad 1 - h_k = \frac{1}{2}\left[1 + \frac{\epsilon_k}{Ek}\right] \equiv u_k^2 \tag{2.7}$$

where

$$E_k \equiv (\epsilon_k^2 + \Delta_k^2)^{1/2} \tag{2.8}$$

Having determined the ground state, the next step is to examine the nature of the elementary excitations – termed quasiparticles. From the definition $E_k = (\epsilon_k^2 + \Delta_k^2)^{1/2}$, the density of superconducting excitations is $N_S(E)$ and is given by dn/dE_k. Writing $dn/dE_k = (dn/d\epsilon_k)(d\epsilon_k/dE_k)$, and $N_n(0) \equiv dn/d\epsilon_k$, the density of normal metal states at the Fermi energy, being approximately constant in the relevant energy range, we get for the density of superconducting excitations:

$$N_S(E) = N_n(0)\frac{|E|}{(E^2 - \Delta^2)^{1/2}} = N_n(0)N_T(E) \qquad |E| \geq \Delta \tag{2.9}$$

$$= 0 \qquad |E| < \Delta$$

$N_s(E)$ is shown in Fig. 2-3d. $N_T(E)$ is the normalized "tunneling density of states" and is directly measured by tunneling experiments. The elementary excitation E_k of the fully paired state is defined as $\vec{k} \uparrow$ occupied, $-\vec{k} \downarrow$ unoccupied. The meaning of a $\vec{k}$-quasiparticle of energy E_k changes smoothly from holelike ($\epsilon_k < 0$, $h_k = v_k^2 \simeq 1$) for $k<k_F$ to electronlike ($\epsilon_k>0$, $1 - h_k=u_k^2 \simeq 1$) for $k>k_F$, as can be seen by referring to Fig. 2-2b. The gap function Δ_k sets the energy range above the T=0 Fermi surface where the pair-state occupation probability h_k remains appreciable.

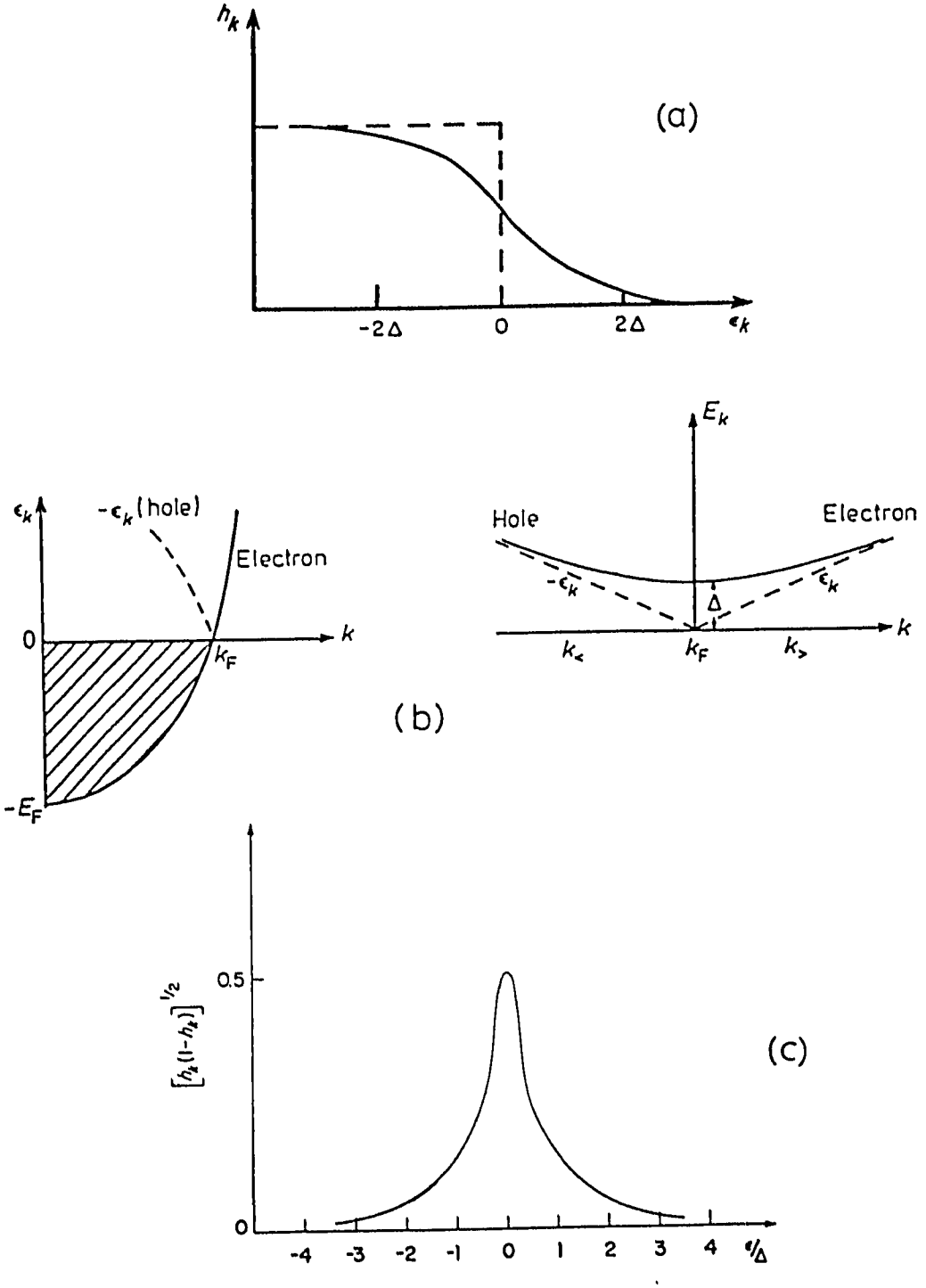

Fig. 2-2 (a) Occupation function $h_k = v_k^2$ of pair-states at T=0 in the BCS theory; the dashed line represents the T=0 Fermi function. (b) Excitation spectrum of a normal metal (left) and a superconductor (right) showing the minimum excitation energy Δ for the superconductor. (c) Pair density function for a BCS superconductor. From Wolf (1985).

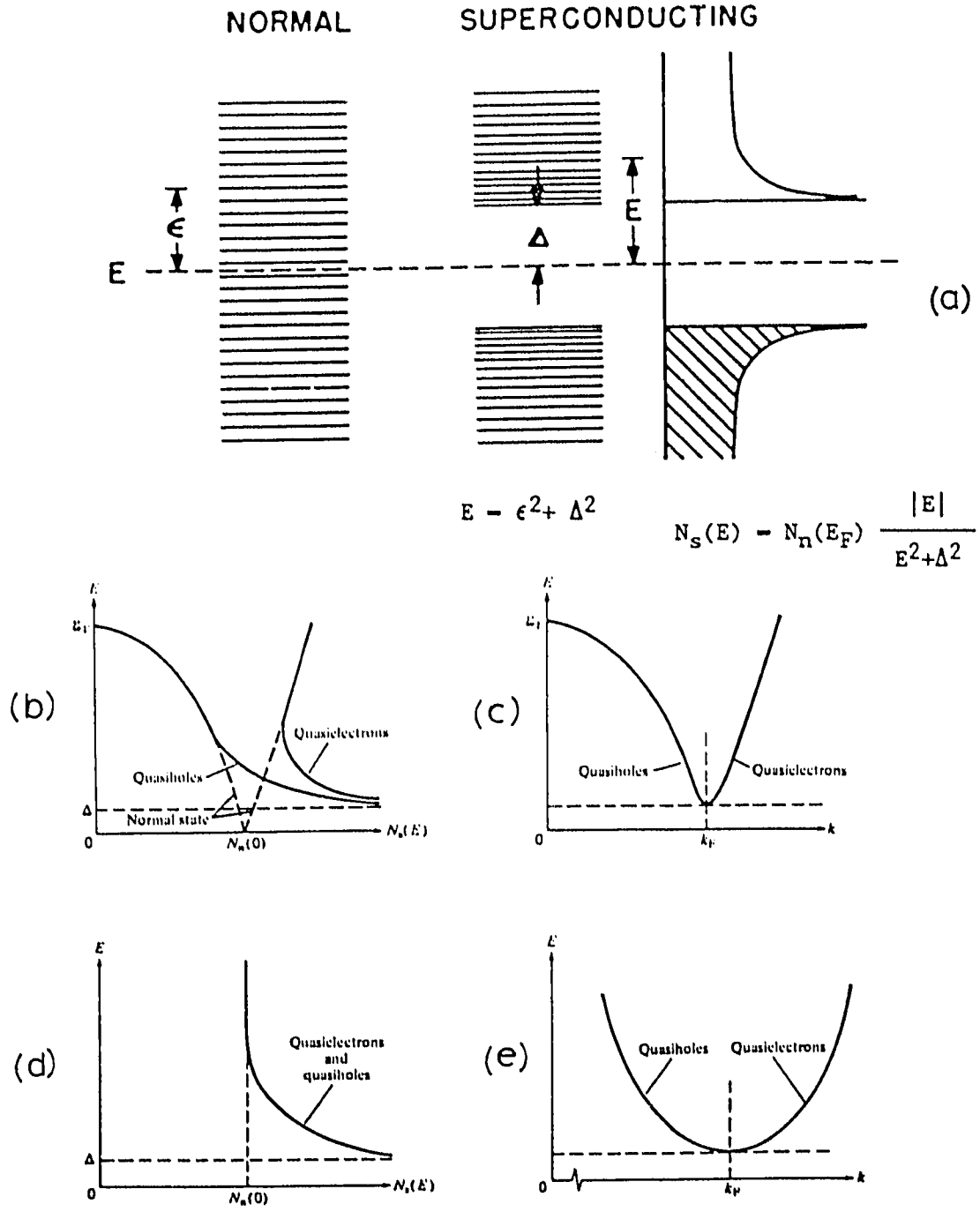

Fig. 2-3 (a) Schematic representation of the electronic states in a normal metal and a superconductor; there is a high density of states (left) in the superconductor near the edge of the gap Δ. If ϵ is the energy of a state in the normal metal, measured from the Fermi energy E_F, the energy of the corresponding state in the superconductor is $E = (\epsilon^2+\Delta^2)^{1/2}$. (b)-(e) Excitation energy and density-of-state diagrams for a superconductor. From Van Duzer and Turner (1981).

Similarly, $1 - h_k$, the probability of finding an empty pair state at $\vec{k}$ is nonzero for an energy range of order Δ_k below the Fermi surface. The pair density function $[h_k(1 - h_k)]^{1/2} = u_k v_k$ is shown in Fig. 2-2c.

By assuming a constant density of states within an energy $\hbar\omega$ of the Fermi energy, the summation in Eq. (2.6) can be replaced by an integral

$$1 = N_n(0)\, V \int_0^{\hbar\omega} \frac{d\epsilon}{E} \tanh\,(E/2k_BT) \tag{2.10}$$

where $E = (\epsilon^2 + \Delta^2)^{1/2}$ and $\Delta_k = \Delta$ for $|\epsilon_k| \leq \hbar\omega$ and $\Delta_k = 0$ otherwise. The transition temperature is defined as the temperature for which Δ vanishes so that E at T_c is just the normal state energy ϵ. Integrating Eq. (2.10), the BCS critical temperature relation is obtained

$$k_BT_c = 1.13\, \hbar\omega \exp\,[-1/N_n(0)V] \tag{2.11}$$

This result, combined with (2.10) gives the estimate, for $N(0)V << 1$

$$2\Delta(0) = 3.52\, k_BT_c \tag{2.12}$$

The above results are valid in the weak electron-phonon coupling limit, where the energy dependence of the electron-phonon coupling can be neglected.

II.A.B. Strong Coupling Superconductors

There are two major shortcomings in the weak coupling BCS theory of superconductivity discussed above. First, the interactions between electrons are assumed to be instantaneous, while we know that the phonons move with a phase velocity which is very small compared to the Fermi velocity, so that a phonon wave packet set up at one point in space by an electron takes a large time to propagate to another point in space where it influences the motion of another electron.

Thus we expect retardation effects to play an important role. In addition, the finite lifetime of excited states is neglected in the weak coupling theory, and these damping effects can become important in determining the properties of the superconducting state. Since Hamiltonian dynamics cannot treat potentials which are retarded in time, the problem has been treated by the Green's function scheme. This problem was first studied by Nambu (1960) and Eliashberg (1960). The main results will be outlined here. The electron-electron coupling interaction used by Eliashberg is:

$$V_{k,k+q} \propto \frac{E_{k+q} + \hbar\omega_q}{(E_{k+q} + \hbar\omega_q)^2 - E_k^2} \tag{2.13}$$

Eliashberg finds that the Green's function is given by

$$G(k,E) = \frac{E + \epsilon(k,E)}{Z(E)\ [\ E^2 - \epsilon^2(k,E) - \Delta^2(E)\ ]} \tag{2.14}$$

where Z(E) plays the role of a renormalization function through the relation

$$\epsilon(k,E) = \epsilon_k/Z(E) \tag{2.15}$$

The quantity $\Delta(E)$ is the analog of the energy gap parameter Δ_k of the weak coupling theory. In general, Z(E) and $\Delta(E)$ are complex quantities, and at zero temperature they satisfy the coupled integral equations (the analog of the energy gap equation of the weak coupling theory),

$$\Delta(E) = \frac{1}{Z(E)} \int_0^{\hbar\omega_c} \mathrm{Re}\left[\frac{\Delta(E')}{[E'^2 - \Delta^2(E)]^{1/2}} \right] [K_+(E,E') - \mu^*] dE' \tag{2.16}$$

$$[Z(E) - 1]\, E = \int_0^{\infty} \mathrm{Re}\left[\frac{E'}{[E'^2 - \Delta^2(E')]^{1/2}} \right] K_-(E,E')\, dE' \qquad (2.17)$$

The interaction kernels are given by

$$K_{\pm}(E,E') = N_n(0)\int \alpha^2(\omega)F(\omega)\left[\frac{1}{E' + E + \omega - i\delta} + \frac{1}{E' - E + \omega - i\delta} \right] d\omega \qquad (2.18)$$

In these equations, ω_c is a cutoff frequency typically taken as five to ten times the maximum phonon frequency. The only material-dependent quantities here are μ^* and $\alpha^2(\omega)F(\omega)$. μ^* is the Coulomb pseudopotential which approximately characterizes the screened Coulomb repulsion between electrons. $\alpha^2(\omega)F(\omega)$ is the product of the square of the electron-phonon matrix element and the phonon density of states averaged over all phonon modes of energy ω. McMillan and Rowell (1969) describe how $\alpha^2(\omega)F(\omega)$ and μ^* can be obtained from tunneling measurements. A useful measure of the electron-phonon coupling strength is given by the McMillan parameter λ:

$$\lambda = 2 \int \alpha^2(\omega)F(\omega)\, \omega^{-1}\, d\omega \qquad (2.19)$$

Superconductors with values of $\lambda < 1$ are generally considered to be weakly-coupled and those with $\lambda > 1$ are strong-coupled.

II.B. Tunneling Between Metals

II.B.1. Quasiparticle Tunneling

Consider two metal electrodes separated by a thin insulating layer. There is a nonzero probability of charge transfer by quantum-mechanical tunneling between the two metals. This probability falls exponentially with the distance of separation and depends on the details of the insulating material, but these aspects can be absorbed in a tunneling matrix element T. If a potential difference V is applied between the two electrodes, the tunneling current from metal 1 to metal 2 can be written as

$$I_{1\to 2} = (2\pi eA/\hbar) \int_{-\infty}^{\infty} |T|^2 N_1(E)f(E)\, N_2(E+eV)\, [1 - f(E+eV)]\, dE \qquad (2.20)$$

where V is the applied voltage, eV is the resulting difference in the chemical potential across the junction and N(E) is the appropriate normal or superconducting density of states. e is the electronic charge, and A the junction area. $f(E) = 1/[1 + \exp(E/k_BT)]$ is the Fermi function. The factors N_1f and $N_2(1-f)$ give the numbers of occupied initial states and of available (empty) final states in the unit energy interval dE. The energy dependence of T will be discussed in chapter 7. This dependence is very slow for $E << \phi$, where ϕ is the barrier height which depends on the insulating material and is on the order of 1 eV. In what follows, T is assumed to be constant. Similarly the reverse current from metal 2 to metal 1 is given by

$$I_{2\to 1} = (2\pi eA/\hbar)\, |T|^2 \int_{-\infty}^{\infty} N_1(E)[1 - f(E)]\, N_2(E+eV)f(E+eV)\, dE \qquad (2.21)$$

so that, subtracting Eq. 2.21 from Eq. 2.20, the net current is

$$I = (2\pi eA/\hbar)\ |T|^2 \int_{-\infty}^{\infty} N_1(E)N_2(E+eV)[f(E) - f(E+eV)]\ dE \qquad (2.22)$$

If both metals are normal, the densities of state can be taken to be constant, equal to their values at the Fermi energy, $N_1(0)$ and $N_2(0)$. This is because the rapid decay of the Fermi function restricts the relevant range of integration to a region where the densities of state are essentially constant:

$$\begin{aligned} I_{N\text{-}I\text{-}N} &= (2\pi eA/\hbar)\ |T|^2\ N_1(0)N_2(0) \int_{-\infty}^{\infty} [f(E) - f(E+eV)]\ dE \qquad (2.23) \\ &\simeq (2\pi eA/\hbar)\ |T|^2\ N_1(0)N_2(0)\ eV \equiv G_{nn}V \end{aligned}$$

The I-V characteristic of a N-I-N junction is linear in the low voltage bias range ($V \lesssim 100$ mV) where $|T|$ is constant. In that bias and temperature range, the junction is ohmic.

If one of the electrodes is superconducting, then Eq. 2.9 must be used for the density of states. The expression for the current is then given by

$$I_{N\text{-}I\text{-}S} = (G_{nn}/e)\int_{-\infty}^{\infty}[|E|/(E^2 - \Delta_2)^{1/2}]\theta(|E| - \Delta_2)[f(E) - f(E+eV)]dE \qquad (2.24)$$

where $\theta(|E| - \Delta) = 1$ for $|E| > \Delta$ and 0 for $|E| < \Delta$. As shown in Fig. 2-4, this current carries the signature of the energy gap of the superconductor. At low temperatures, $T \to 0$, the differential conductance dI_{NIN}/dV is a direct measure of the tunneling density of states of the superconductor:

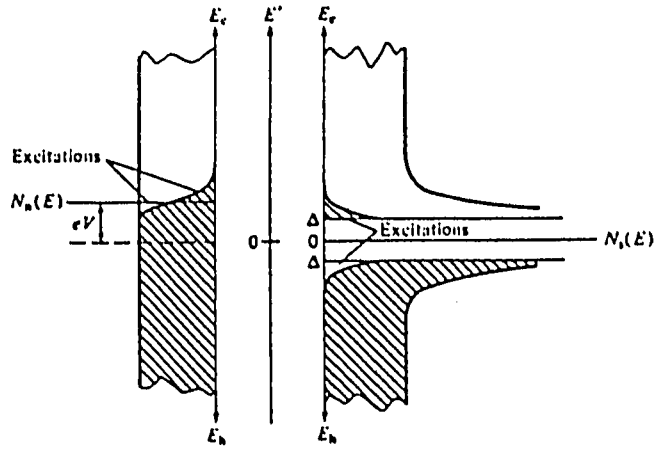

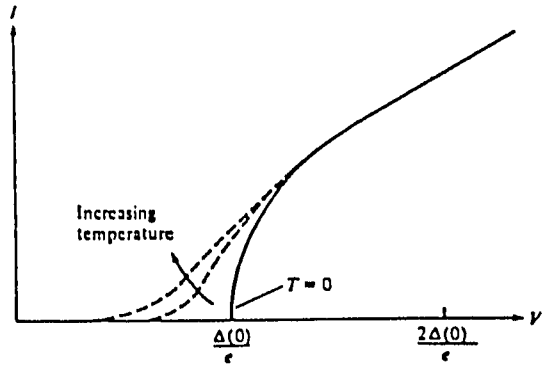

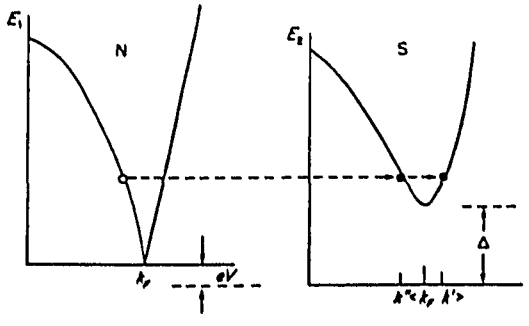

Fig. 2-4 Schematic energy diagrams and I-V characteristic for an N-I-S junction. The excitations shown are thermal excitations at finite temperatures. From Van Duzer and Turner (1981).

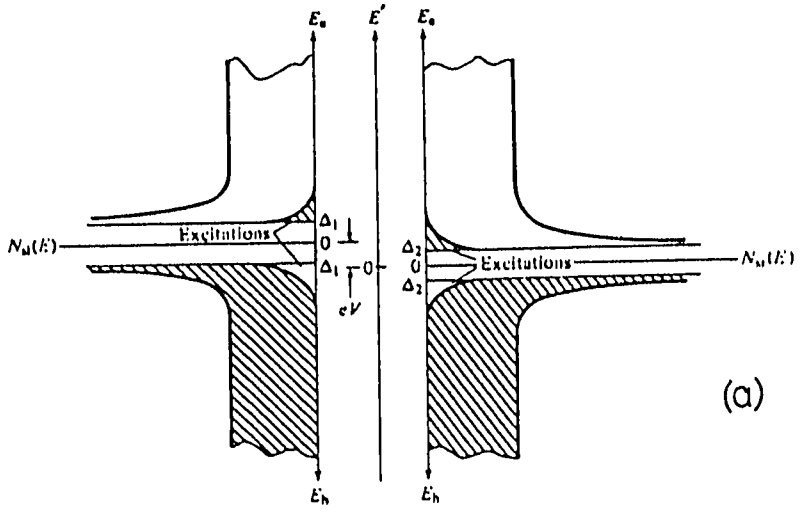

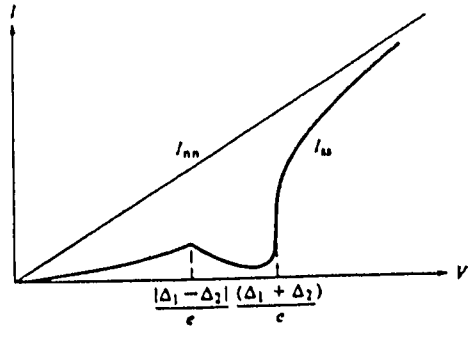

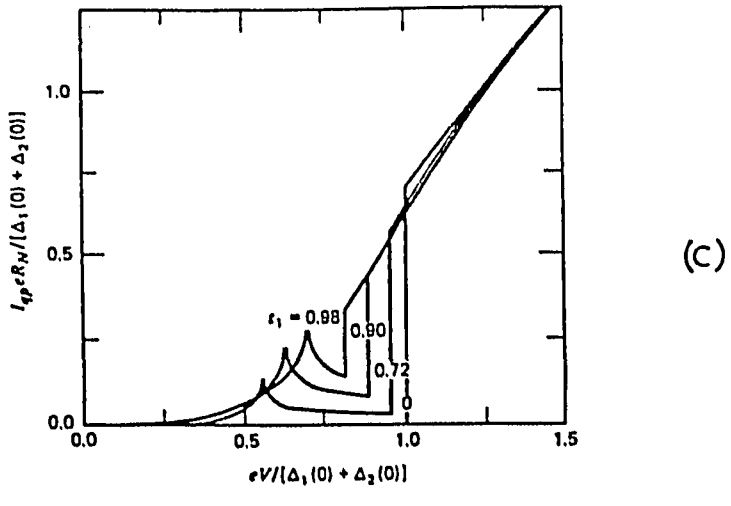

Fig. 2-5 (a) and (b) Schematic energy diagram and I-V characteristic for an S-I-S' junction. From Van Duzer and Turner (1981). (c) Calculated normalized BCS I-V curves for S-I-S' tunneling at different temperatures showing the increase in subgap leakage current and the decrease of the sum-gap voltage with increasing temperature; $t=T/T_c$ is the reduced temperature. From Harris (1974).

$$G_{ns}|_{T=0} = (dI_{NIS}/dV)|_{T=0}$$
$$= G_{nn}\theta(|V| - \Delta)\,[|V|/(V^2 - \Delta_2^2/e^2)^{1/2}] \equiv G_{nn}N_{T2}(eV) \qquad (2.25)$$

If both electrodes are superconducting, then Eq. 2.22 becomes:

$$I_{S\text{-}I\text{-}S} = (G_{nn}/e)\int_{-\infty}^{\infty} [|E|/(E^2 - \Delta_1^2)^{1/2}]\;\theta(|E| - \Delta_1)\;x$$
$$[|E+eV|/\{(E+eV)^2 - \Delta_2^2\}^{1/2}]\;\theta(|E+eV| - \Delta_2^2)\;x$$
$$[f(E) - f(E+eV)]\;dE \qquad (2.26)$$

The density of states diagram and resulting I-V curve for this situation are shown in Fig. 2-5. At all temperatures below T_c, the I-V curve has a discontinuity at the sum-gap voltage $e(\Delta_1+\Delta_2)$. This results from the overlap of the singularities in the density of states of the two superconducting electrodes. Another notable structure is a peak at the difference-gap voltage $e(\Delta_1 - \Delta_2)$, followed by a region of negative resistance. The existence of sharp features at both the sum- and difference-gap voltages allows very accurate determination of Δ_1 and Δ_2 from the tunneling curves.

In addition to the determination of the superconducting energy gap, the conductance of the tunnel junctions is a direct measure of the tunneling density of states of the superconductor in N-I-S junctions, as discussed above. In strong-coupling superconductors - such as Pb and Hg - the energy dependence of the electron-phonon coupling function $\alpha^2(\omega)F(\omega)$ is directly reflected in the voltage bias dependence of the conductance. This allows the determination of $\alpha^2(\omega)F(\omega)$ as described by McMillan and Rowell (1969) and serves as a test of the Eliashberg strong-coupling theory of superconductivity. Such tunneling data give results of

great accuracy for features such as the location of van Hove singularities in the phonon density of states, which appear as peaks in the experimentally obtained trace of the second derivative of the tunneling current. Results on the phonon structure of Ta overlayers on Nb obtained from our data will be presented in chapter 6.

In the above discussion, it is assumed that the tunneling matrix element T is constant. This is a good approximation as long as the bias voltage is small compared to the barrier height of the insulating layer, which holds true generally for $V \lesssim 100$ mV. In that region, the effective height of the barrier is essentially constant. As the bias is increased further, the tunneling current increases faster than linearly, because the effective barrier height is decreasing. The bias-dependence of the conductance of the tunnel junction will then reflect the properties of the tunnel barrier. This dependence and the spectroscopic information that can be obtained from it will be discussed in chapter 7.

II. Cooper-Pair Tunneling: the Josephson Effect

The discussion in the previous section outlined a phenomenological derivation of the tunnel current between two metallic electrodes. This treatment can be shown to be equivalent to a more rigorous derivation using a tunneling Hamiltonian approach [Schrieffer (1969)] if it is restricted to lowest-order perturbation theory. In 1962, Josephson showed how a more complete treatment implies the existence of an additional current in the case where the two electrodes are superconducting. In Josephson's words: "... new effects are predicted, due to the possibility that electron pairs may tunnel through the barrier leaving the quasi-particle distribution unchanged". In 1963, Anderson and Rowell confirmed Josephson's prediction by

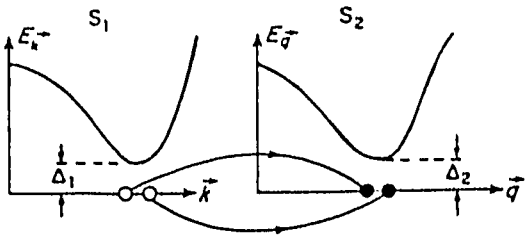

(a)

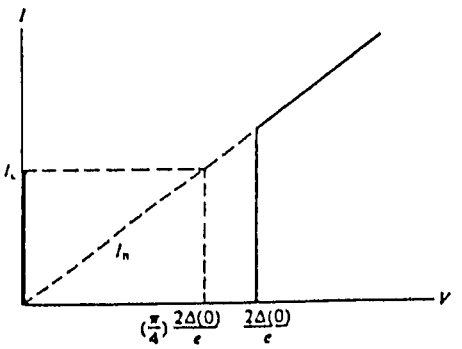

(b)

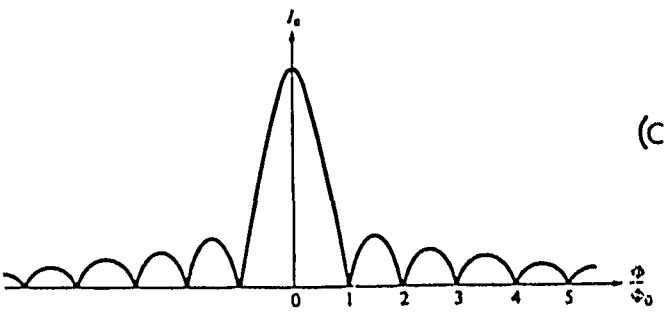

(c)

Fig. 2-6 (a) Josephson tunneling of Cooper pairs between two superconductors. (b) I-V curve showing the zero-bias Josephson current. (c) Magnetic field dependence of the maximum (critical) Josephson current. (a) from Wolf (1985), (b) and (c) from Van Duzer and Turner (1981).

observing "an anomalous dc tunneling current at or near zero voltage in very thin tin oxide barriers between superconducting Sn and Pb ... which behaves in several respects as the Josephson current might be expected to". Unlike quasiparticle tunneling, pair tunneling does not involve excitations and can occur even without bias across the junction. Thus one could connect a current source to an S-I-S junction and, for currents less than a certain critical value, no voltage would be developed if the current were carried across the insulator by Cooper pairs. Fig. 2-6 shows how the dc Josephson current is manifested in an S-I-S junction. The calculations leading to the expression for the dc Josephson current can be found in several texts [for example Wolf (1985)] or in the original papers by Josephson (1962, 1965) and will not be reproduced here. Ambegaokar and Baratoff (1963) derived an expression for the maximum Josephson current (= critical current I_c) in terms of the superconducting energy gap, the temperature, and the normal-state resistance R_n of the junction. For two identical superconductors, the result is

$$I_c(T) = [\pi\Delta(T)/2eR_n] \tanh [\Delta(T)/2k_BT] \qquad (2.27)$$

At T = 0 the critical current I_c equals the tunneling current that would have existed in the absence of pairing at a voltage of $\pi/4$ times the gap voltage $2\Delta/e$. In real junctions, this critical current is often depressed by external noise as will be discussed in chapter 6.

One feature that allows the distinction between Josephson current and micro-shorts in tunnel junction is the dependence of the Josephson critical current on an applied magnetic field B, parallel to the plane of the junction. It can be shown [see, for example, Tinkham (1975)] that with parallel B-field, the Josephson critical current

is modulated by the applied magnetic field according to the relation:

$$I_c(\Phi) = I_c(0) \left| \frac{\sin(\pi\Phi/\Phi_0)}{\pi\Phi/\Phi_0} \right| \qquad (2.28)$$

where $\Phi = B\,A$ is the magnetic flux through the junction as shown in Fig. 2-6c, and $\Phi_0 = hc/2e = 2.07\text{x}10^{-7}$ gauss-cm^2 is the superconducting flux quantum. This feature is used in chapter 6 to help determine accurately the maximum Josephson critical current for the Nb/Ta junctions.

III. THIN FILM DEPOSITION AND MATERIAL PROPERTIES

III.A. Soft Materials: Thermal Evaporation

Soft materials are used as counterelectrodes for all the junctions studied in this work. This is because the deposition of such materials is gentle which prevents damaging the thin insulating barrier formed on the base electrode. Thermal evaporation by resistive heating is used to deposit the following materials : Ge and SiO, used to mask the base electrode and define the area of the junction, Ag, Pb and PbBi used as counterelectrodes, Cr used in the fabrication of optical masks and Al used in the formation of photoresist trilayers for the patterning of small area junctions which will be discussed in chapter 4. Fig. 3-1 illustrates the configuration of the thermal evaporator used. Vacuum is maintained by a diffusion pump. The pressure during evaporation of the above materials ranges between $1x10^{-6}$ Torr and $2x10^{-5}$ Torr. In that pressure range, the mean free path, ℓ, of molecules in the vacuum chamber is much larger than the chamber dimensions ($\ell \geq 5$ meters). This implies that the deposition of materials onto the substrates follows closely a line-of-sight path. Such directional deposition is important for the patterning techniques which will be described in chapter 4.

The techniques for successful evaporation of different materials are well established. [Thermal evaporation is exhaustively reviewed by Glang (1970)]. The material to be evaporated is placed in a boat made of a refractory metal - Tungsten or Tantalum - or wrapped around a rod made of these refractory metals. The boat (rod) is resistively heated by passing current through it. With the exception of SiO, the material melts, then evaporates at a rate set by the heating current. Table 3-1

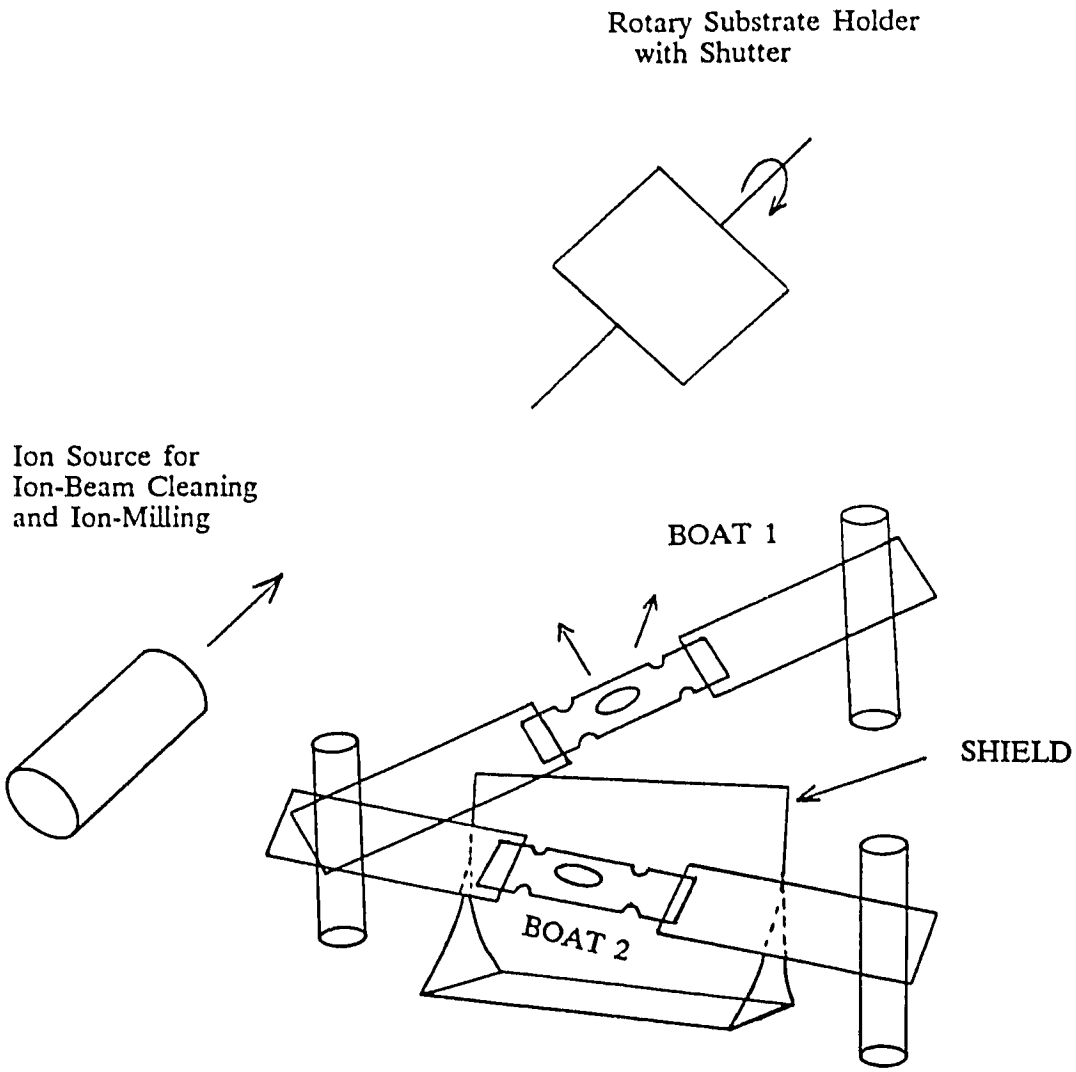

Fig. 3-1 Schematic of the evaporator. Two sources allow the sequential evaporation of different materials in-situ. The shield prevents contamination of one source during the evaporation from the other. The ion source is used for ion-beam cleaning and ion milling discussed in chapter 4.

Table 3-1. Relevant parameters for evaporated materials.

Material	Background Pressure (Torr)	Pressure during Evaporation (Torr)	Deposition Rate (Å/sec)	Remarks and Special Considerations
Ag	$<3\times10^{-6}$	$\sim1.5\times10^{-5}$	20-30	corrodes W boats; use 0.020" Ta boats*.
Pb	$<5\times10^{-6}$	$\sim6\times10^{-6}$	30-50	can use 0.010" W boats.*
$Pb_{0.7}Bi_{0.3}$	$<3\times10^{-6}$	$\sim4\times10^{-6}$	20-40	from alloy source; substrate cooled to 77 K (see text).
$Pb_{0.9}Bi_{0.1}$	$<3\times10^{-6}$	$\sim4\times10^{-6}$	20-40	from alloy source; no substrate cooling.
Al	$<1\times10^{-6}$	$\sim2\times10^{-6}$	15-30	0.020" Ta boat*
Cr	$<8\times10^{-6}$	$\sim5\times10^{-6}$	5-10	from Cr-coated W rods*.
Ge	$<8\times10^{-6}$	$\sim2\times10^{-5}$	20-40	use W rods in 0.020" Ta boats*.
SiO	$<2\times10^{-6}$	$\sim4\times10^{-6}$	25-40	from "baffled box" source* (Fig. 3-2).

*All evaporation sources from R.D. Mathis Co., Box 6187, Long Beach, CA.

lists the relevant parameters for the materials evaporated. In the case of Ge, the use of small tungsten rods in the middle of the Ta boat causes the Ge to wet the tungsten upon melting and prevents "creeping" of the molten Ge to the sides of the boat. SiO is evaporated from a special boat depicted in Fig. 3-2. SiO sublimates and the vapors emerge from the opening in the boat. The absence of a line-of-sight path from the opening to the SiO powder prevents ejection of solid SiO particulates which would otherwise occur. The evaporation rate and film thickness are measured by a standard quartz oscillator [Glang (1970)]

In all the junctions studied in this work, the counterelectrode is made of one of the following soft metals: Ag, Pb, or PbBi. Soft metals (as opposed to refractory metals) have a relatively low melting point which allows them to be deposited by thermal evaporation. A major advantage is that during this deposition, the (thermal) energy of the atoms of the material being deposited is low, on the order of ~ 0.1 eV [$k_BT \simeq 0.1$ eV for $T \simeq 1300$ K $\simeq 1000$ °C]. This helps preserve the thin (~ 20 Å) tunnel barrier which is critical to the quality of the tunnel junction. In addition, the relative inertness of the above counterelectrode materials helps to minimize the interaction with the tunnel barrier. Ag is used when the counterelectrode must be a normal (non-superconducting) metal. This arises, for example when studying the phonon structure of the base electrode material reflected in the conductance characteristics (see chapter 6). In this case, the counterelectrode is chosen to be a normal metal to avoid superposition of its own phonon structure on the signal. Pb is used occasionally because of its ease of deposition requiring very low power levels, and because its superconducting properties are relatively insensitive to impurities and to varied deposition conditions. This makes a Pb counterelectrode helpful in diagnostic runs. Pb films, however, pose two important disadvantages: 1) they

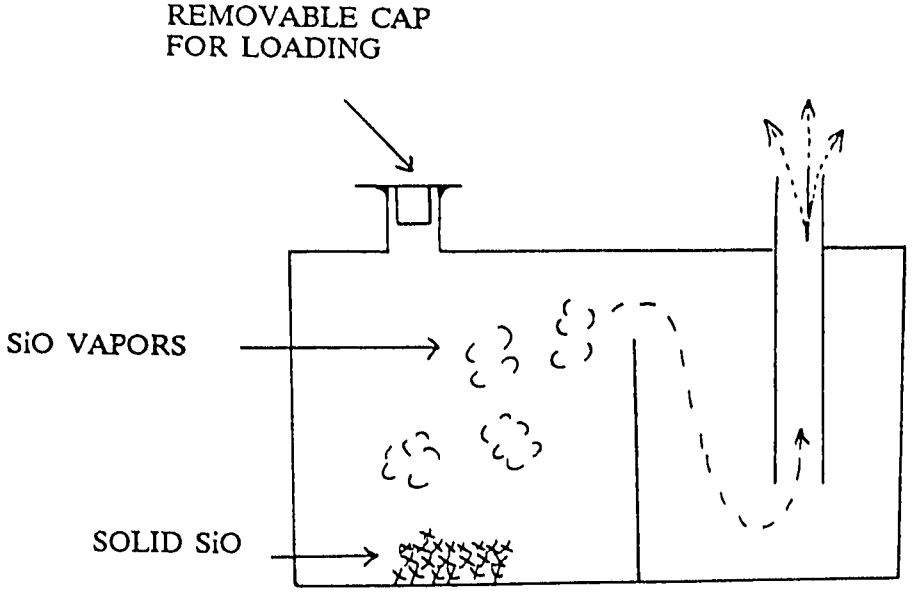

Fig. 3-2 Cross section of the SiO evaporation "baffled box". SiO sublimates and the vapors follow the path indicated by the arrow. The absence of a line-of-sight path from the solid SiO to the substrate eliminates any chance of "spitting and streaming", which causes pinholes in the SiO film.

develop stress-induced micro-cracks upon repeated thermal cycling resulting in the failure of the tunnel junction and 2) the anisotropy of the energy gap in Pb [Rochlin (1967)] causes a distribution of energy gaps in the counterelectrode made up of evaporated polycrystalline Pb films leading to lower quality junctions (see chapter 5). The above problems can be circumvented by the use of the alloy Pb_xBi_y. Fig. 3-3 shows a phase diagram of the PbBi system. Two compositions of PbBi are most adequately suited for tunnel junctions: the α-phase (fcc $Pb_{0.9}Bi_{0.1}$ - weight proportions) and the ϵ-phase (hcp $Pb_{0.71}Bi_{0.29}$). Both phases have good thermal cycling properties and a "sharp", isotropic energy gap. The energy gap in the ϵ-phase is larger (1.74 meV) than the α-phase (1.52 meV). Mukarami et al. (1983) reported that the hcp crystal structure in the ϵ-phase can support more elastic strain without dislocation glide than the α-phase. The disadvantage of the ϵ-phase is that it is realized for only a narrow range of compositions (27.5 % to 31.5% Bi) as opposed to the α-phase (0-17% Bi). As a result, more control is required on the source temperature with the ϵ-phase to stay in the regime of equal vapor pressure for Pb and Bi and therefore preserve the composition of the source. We also find that cooling of the substrates (to 77 K) is necessary to obtain smooth continuous films of the ϵ-phase, whereas the α-phase does not require such cooling. We used the $Pb_{0.71}Bi_{0.29}$ ϵ-phase for the large area junctions and the $Pb_{0.9}Bi_{0.1}$ α-phase for the small area junctions. In the case of the small-area junction, this choice was prompted by a major concern that the cooling of the substrate needed for the ϵ-phase might result in the condensation of background impurities onto the critical junction area.

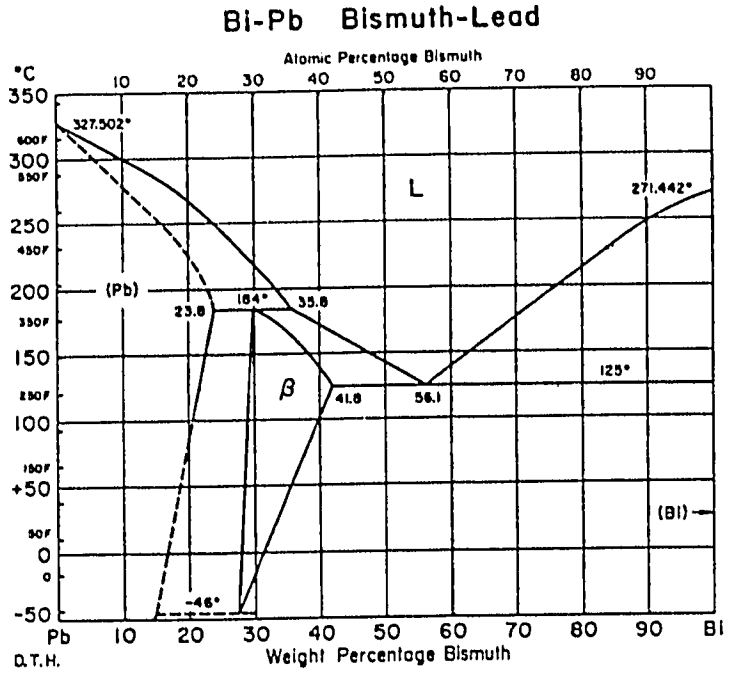

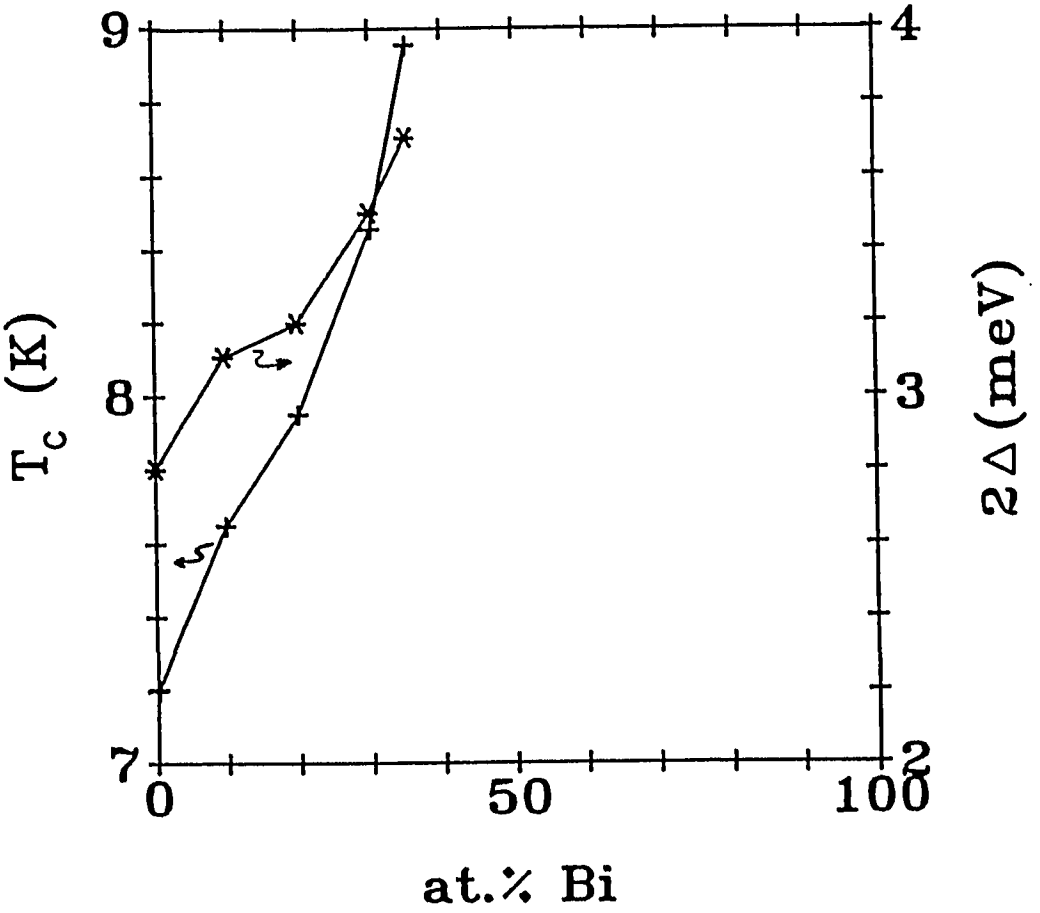

Fig. 3-3 (a) Phase diagram of PbBi [Metals Handbook (1982)]. (b) T_c (+) and suerconducting energy gap Δ (*) for different Pb_xBi_y compositions [data from Dynes and Rowell (1975), Plot from Face (1987)].

III.B. Ion-Beam Sputter-Deposition: Nb and Ta

The use of an ion-beam system for sputter deposition has been explored by a number of workers [See Harper (1983)]. Ion-beam sputtering offers a number of possible advantages for deposition of high melting-point materials such as Nb and Ta. These advantages result from the relative absence of radiant heat and the physical separation of the deposition substrate from the plasma. One such advantage is the ability to maintain the substrate close to room temperature which makes this deposition technique compatible with photoresist processing. Another advantage over more conventional dc or rf sputtering techniques is the ability to independently control the flux and energy of the incident ion beam. The successful deposition of high quality films of Nb and Ta was accomplished at Yale prior to this work and is reported in Face et al. (1982, 1983, 1987). This section will briefly describe the operation of ion sources and describe the ion-beam sputtering system and the properties of Nb and Ta films obtained. This system was used to deposit the base electrode films for the large area junctions to study the properties of Ta overlayers on Nb and the Ta films for the small area junctions.

III.B.1. Description of an Ion-Source

A schematic diagram of a Kaufman-type ion source is shown in Fig. 3-4. The cathode boils off electrons which are accelerated towards the anode by a discharge voltage applied between the cathode filament and the anode. The electrons collide with and ionize the atoms of the inert gas fed into the source. The path of the electron is increased by magnets enhancing the probability of collision with the inert gas atoms. A plasma is obtained, confined within the source. An ion beam is

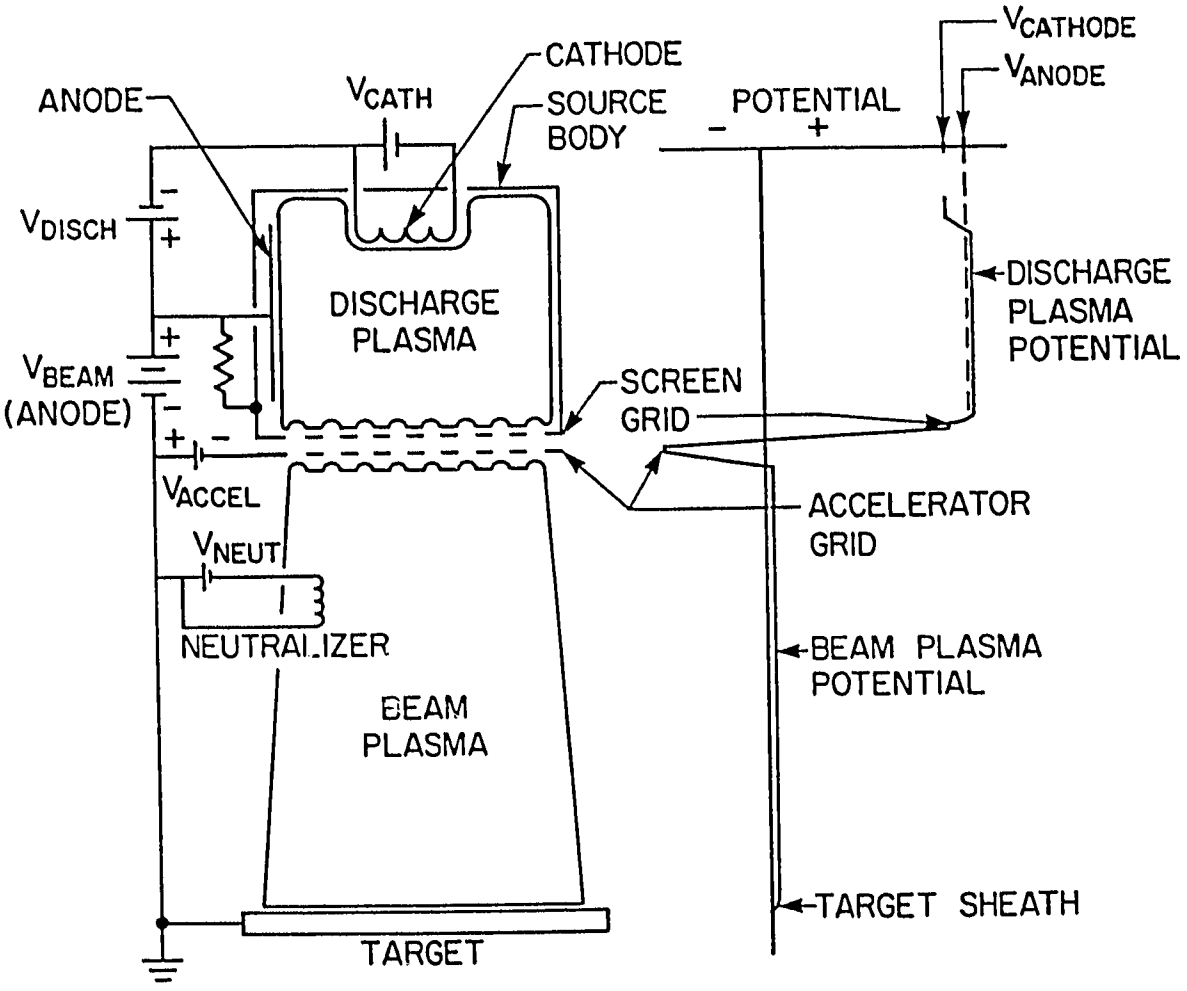

Fig. 3-4 Schematic of a Kaufman ion source showing the bias voltages and the spatial distribution of the potential along the path of the beam [from Kleinsasser et al. (1982)]

extracted from this plasma through a set of grids. A dc bias applied between the outer grid and the source. This causes the positively charged ions to be accelerated towards the outer grid (accelerator grid). The inner grid (screen grid) maintained at the same potential as the plasma and with holes perfectly aligned to those of the accelerator grid prevents the ions from impinging upon the accelerator grid. As a result an ion beam emerges from the grid with the ions continuing their path until they impinge upon the grounded target and cause it to sputter onto the substrate. The energy of the impinging ions is equal approximately to eV where V is the positive bias applied to the discharge chamber. (This assumes the ions are singly charged). The ion-source used in the deposition of Nb and Ta was obtained from Ion Tech, Inc.[1] Two other ion-sources were also used in this work, one from Commonwealth Scientific[2] for the dual ion-beam deposition of NbN discussed in III.C. and one on loan from IBM research[3] for ion-beam cleaning and ion milling discussed in chapter 4.

The sputtering configuration is shown schematically in Fig. 3-5. The ion-source is fixed to the top plate of a diffusion-pumped vacuum chamber. The water-cooled target holder can accommodate up to four different targets. It can be rotated in-situ (i.e., without breaking vacuum) to allow the sequential deposition of layers of different materials. Surrounding each target, properly positioned foils made of the same material allow a sharp interface when sequentially depositing two layers, by minimizing the time when the ion-beam simultaneously impinges on two adjacent targets or the copper target holder as this target holder is rotated.

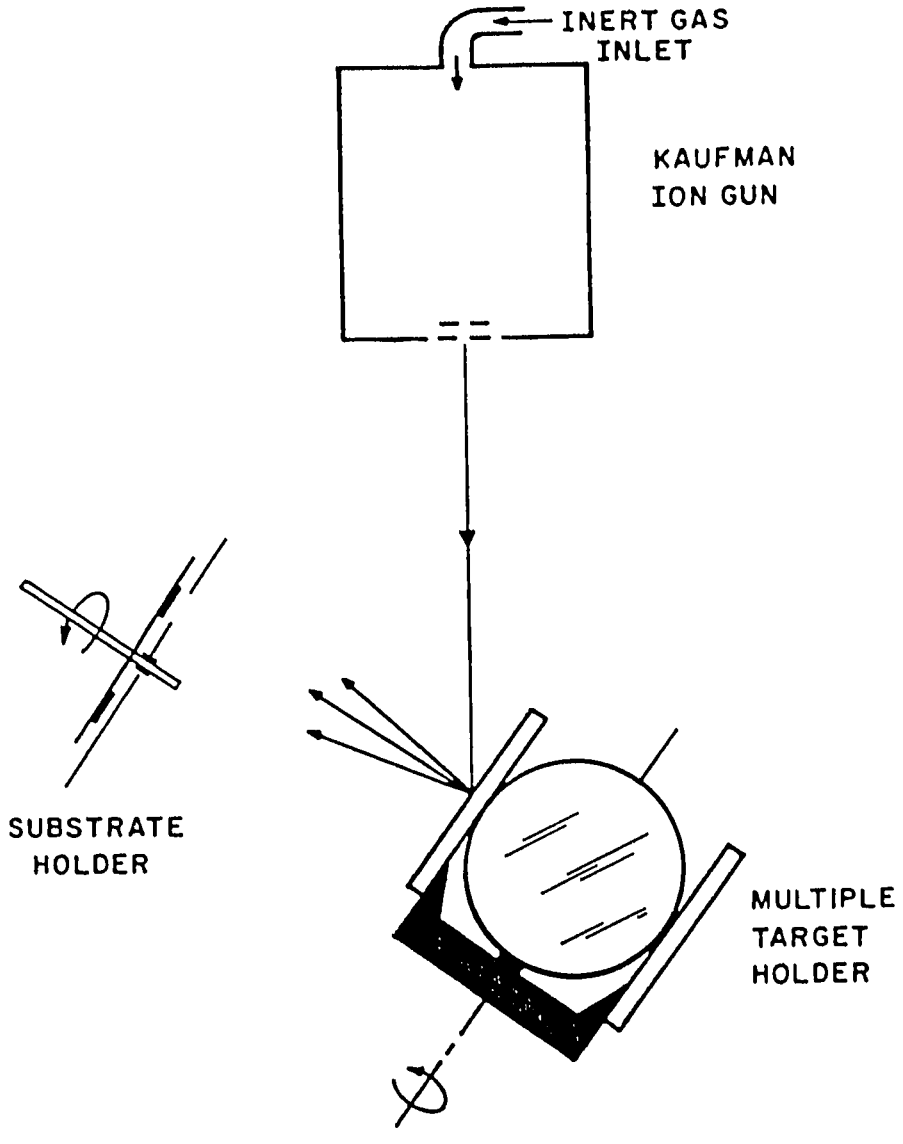

Fig. 3-5 Schematic of the ion-beam deposition system, comprising a 2.5 cm Kaufman ion source, a multiple target holder accomodating four 4-inch targets, and substrate a substrate holder. Not shown is the main sample shutter. [from Ruggiero (1983)].

III.B.2. Properties of Nb and Ta produced by ion-beam sputtering.

Table 3-2 shows the operating parameters of the ion-source that yield the highest quality Nb films [Face et al. (1982, 1983, 1987)]. Ta films were sputtered with these parameters also. Films made with Xe as a sputtering gas have consistently higher superconducting transition temperature T_c than films made with Ar or Kr. The lower T_c of films made with Ar may be due to gas incorporation in the film, or to contamination of the source plasma due to the larger voltage required to sustain an Ar discharge. The Nb films obtained have a superconducting transition temperature of 9.1 K, approaching the bulk value of 9.3 K. Transition width is $\leq$ 0.03 K. The low-temperature film resistivity is ~ 4 $\mu\Omega$cm, and the resistivity ratio ($\rho_{298\ K}/\rho_{10\ K}$) is in the range 3-4. The films are polycrystalline with random in-plane orientation and an average grain size of ~ 150 Å. In all these properties, the Nb films are comparable to those obtained by other workers on room temperature substrates. Fewer data are available on deposited superconducting Ta films by other workers.

When Ta films are deposited directly onto Si substrates using the optimum beam conditions found for Nb, the films grow in the tetragonal phase known as β-phase. β-Ta has a relatively high resistivity (150-200 $\mu\Omega$cm) and a low T_c of 0.5 K [Read et al. (1965)]. To obtain the desired bcc phase of Ta, Face et al. deposited a layer of Nb onto the Si substrates just before depositing the Ta. This was accomplished by depositing a layer of Nb ~ 20 - 50 Å thick and then immediately (within ~ 1 sec) rotating the target holder to the Ta position without turning off the beam or closing the shutter. The almost perfect lattice match between Ta and Nb resulted in the nucleation and growth of high quality bcc Ta films. These Ta films have a T_c of

Table 3-2. Typical operating conditions of the ion-source yielding the optimum Nb and Ta film properties. The sputtering gas is Xe, at a pressure of $1x10^{-4}$ Torr. All parameters remain constant between runs, except the cathode current which slowly decreases as the cathode filament "ages": the resistance of the filament increases requiring less current to produce the same electron emission.

Cathode	Discharge		Accelerator		Beam	
Current	Voltage	Current	Voltage	Current	Voltage	Current
(A)	(V)	(A)	(V)	(mA)	(V)	(mA)
7.0	18.6	1.3	250	1.3	1500	34

4.3 K, approaching the bulk value of 4.4 K, a low temperature resistivity of 5 - 6 $\mu\Omega$cm and a residual resistivity ratio of 3 - 4. Like the Nb films, the Ta films are polycrystalline, with random in-plane orientation and a grain size of ~ 150 Å. In addition to Nb and Ta, the ion-beam sputtering system contains an Al target which is used to deposit Al overlayers on films of NbN. The same beam parameters used for Nb and Ta are used to deposit these Al films. The deposition rate is for Al is 2.6 Å/sec.

III.C. Dual Ion-Beam Deposition of NbN

III.C.1. Motivation for use of NbN

After its discovery in 1941 by Aschermann et al., and a period of activity in the seventies, NbN has seen a resurgence of interest in the eighties [Bacon et al. (1983), Cukauskas et al. (1985), Villegier et al. (1985), Igarashi et al. (1984)]. This is largely due to its potential microelectronics applications. NbN has a T_c of 16-17 K. [This was considered "high T_c" until the advent of the oxide superconductors in early 1987 (cf. March 1987 meeting of the American Physical Society)]. NbN is relatively insensitive to stress and is relatively easy to produce. It has a very high critical field, H_{c2}, up to 50 Tesla [Ashkin et al. (1984)]. Furthermore, there are many unanswered scientific questions, such as the origin of the high resistivity and an understanding of the electron-phonon coupling spectrum.

The equilibrium phase diagram of the Nb-N system has been extensively studied and is summarized by Guard et al. (1967). Fig. 3-6 shows the constitution diagram of the Nb-N system. The desired phase sought after is the δ-phase, with a B-1 crystal

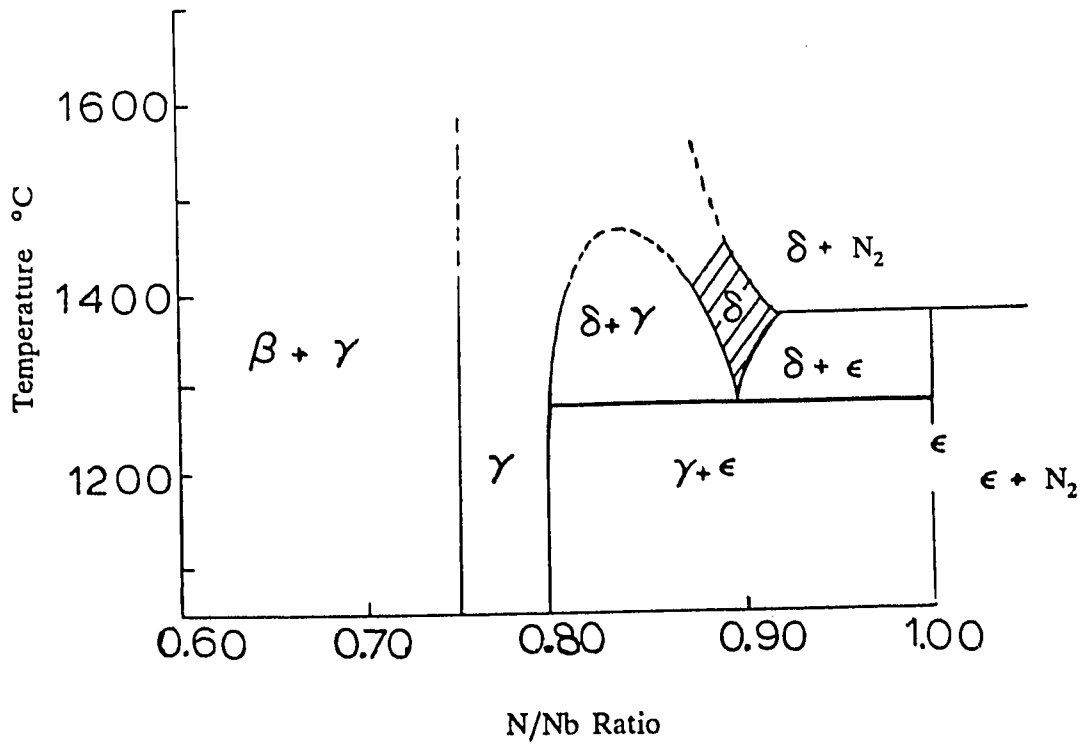

Fig. 3-6 Equilibrium phase diagram of the Nb-N system. δ = fcc NbN; β = hexagonal Nb_2N; γ = tetragonal Nb_4N_3; ϵ = hexagonal NbN [from Guard (1967)].

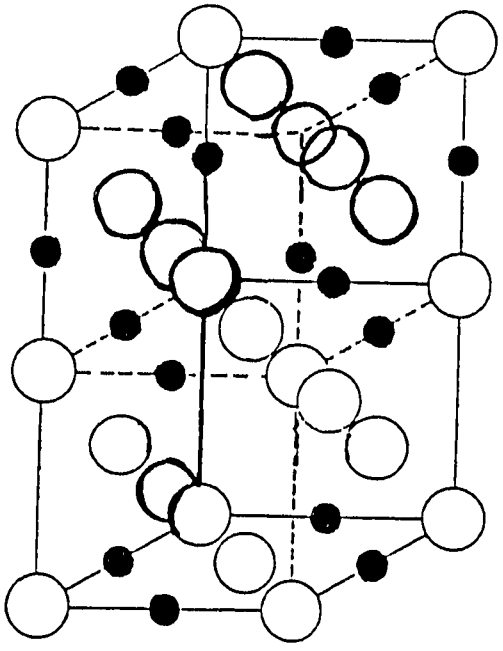

γ-Nb_4N_3

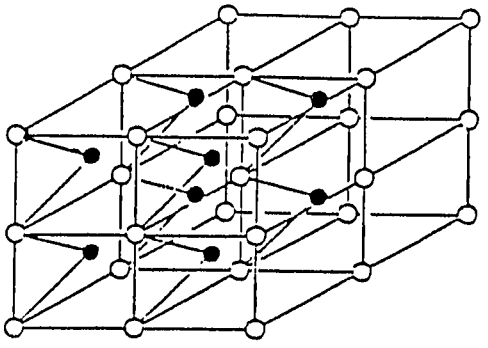

β-Nb_2N

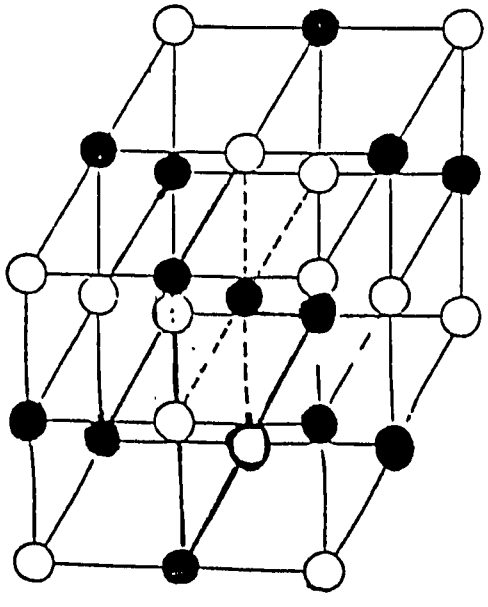

δ-NbN

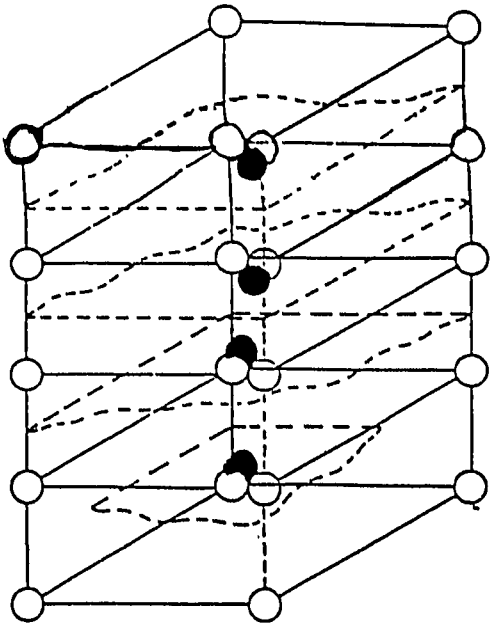

ϵ-NbN

Fig. 3-7 Crystal structure of the different NbN phases. O, Niobium; ●, Nitrogen.

structure (same as NaCl) shown in Fig. 3-7 along with the crystal structure of the other possible phases: β-NbN = Nb_2N, with a hexagonal (W_2C type) structure; γ-NbN = Nb_4N_3, with a tetragonal (distorted NaCl type) structure; ϵ-NbN = NbN, with a hexagonal (TiP type) structure; the α-phase is a solid solution consisting of Niobium (bcc) with nitrogen contained interstitially. Only the δ-phase has the relatively high T_c of 16-17 K. As seen in Fig. 3-6, δ-NbN forms in a relatively small region of the equilibrium phase diagram. One of the challenges of synthesizing pure δ-NbN films is therefore to find the appropriate deposition conditions which will stabilize this desired phase and minimize - if not completely suppress - the admixture of the other phases. It is important to note that thin film fabrication techniques usually cause the formation of the films under non-equilibrium conditions. Therefore, the equilibrium phase diagram, while helpful in indicating the possible phases that may form, does not necessarily guide as to the appropriate conditions for thin-film deposition.

III.C.2. Motivation for using Dual-Ion-Beam Deposition

The technique most commonly used to fabricate NbN thin films is reactive sputtering (dc or rf, diode or magnetron)*. Such techniques employ relatively high pressures (~ 10^{-2} Torr) and substrate heating is usually necessary to attain near-bulk T_c values. One of the few studies using a significantly different method of thin-film synthesis had a growing Nb film, deposited by electron-beam evaporation, bombarded with N_2^+ ions [Cuomo et al. (1982)]. Broad transitions, extending from

*dc magnetron sputtering used by Gavaler et al. (1986), Thakoor et al. (1986), Hikita et al. (1983), Kampwirth et al. (1985), Villegier et al. (1985), Bacon et al. (1983); rf diode sputtering used by Shinoki et al. (1981), Frankavilla et al. (1981); rf magnetron sputtering used by Cukauskas et al. (1985).

9 K to 14.5 K, were reported.

The dual ion-beam technique was pioneered by Weissmantel (1976, 1980) for fabrication of Si_3N_4 films. Later, it was applied to AlN film formation by Harper et al. (1985). The dual-beam method allows independent control of the ion flux and energy during deposition at low pressures (~ $1x10^{-4}$ Torr) such that the mean free path is larger than typical chamber dimensions. As a result, the deposition has a directional character. The basic idea of the dual ion-beam technique for forming NbN films is that a first ion beam (in our case Xe) sputters Nb from a target onto a substrate. Simultaneously, a second ion beam (N_2) bombards the growing film, causing the formation of NbN. For producing NbN films with the dual ion-beam technique, the energy released at the surface of the growing film by the second ion beam may provide a substitute for the thermal energy used previously to attain high T_c values. A deposition method which does not require heated substrates may allow the formation of a NbN counterelectrode (i.e., for an all-NbN junction) while preserving the very thin tunnel barrier.

III.C.3. Optimization Scheme

To implement the dual-beam technique for fabricating NbN films, a second ion source is added to the ion-beam system previously used for Nb and Ta. This system now consists of a diffusion-pumped vacuum chamber with a pyrex glass cylinder. The base pressure is ~ 2 - 3 x 10^{-7} Torr. Fig. 3-8 illustrates the sputtering configuration with the two ion sources fitted in the chamber. The first one is a 2.5 cm diameter source, obtained from Ion Tech[1], and uses Xe as a sputtering gas. It is fixed to the top plate and faces the multiple target holder described above, ~ 15 cm

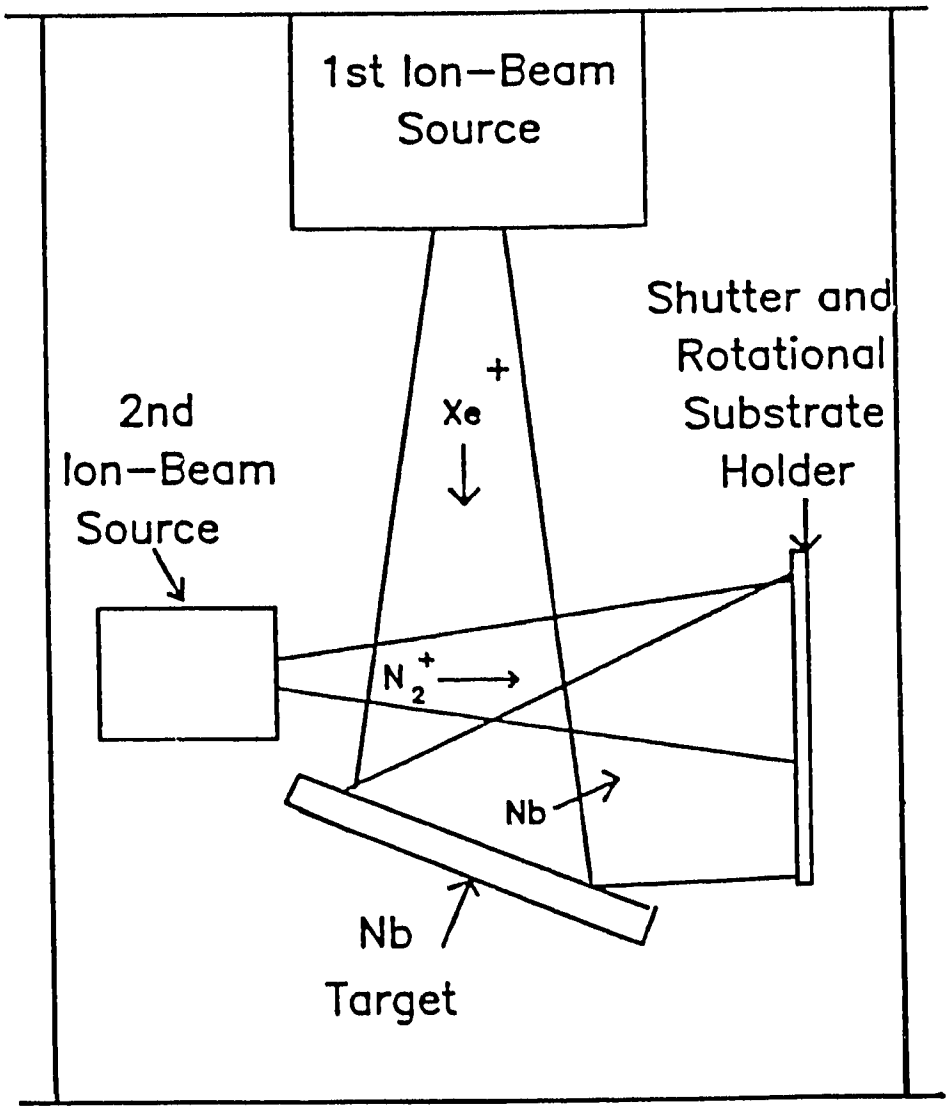

Fig. 3-8 Dual-Ion-Beam Sputtering Configuration.

Table 3-3. Summary table of the properties of the NbN films for the different ranges of parameters examined.

UNHEATED SUBSTRATES

	ONE ion source ("sputtering Nb in a N_2 atmosphere")	TWO ion sources	
		$V_{beam\#2}$ < 500 V	$V_{beam\#2}$ = 1000-1500 V
N2 only in Source #2	Poor Adhesion to the Substrate Multiple Transitions T_c (max) ~ 11 K	Multiple Transitions Some films T_c < 4.2 K	T_c ~ 12 K ΔT_c ~ 0.1 K δ-phase(B1) N/Nb ~ 0.96 RRR ~ 0.9
N_2 + CH_4 in Source #2		T_c ~ 13 K ΔT_c ~ 0.1 K at 50% CH_4 Nb/N/C ~ 1/0.6/0.6 RRR~1.0	T_c ~ 12 K ΔT_c ~ 0.1 K at 10% CH_4 RRR ~ 0.9

away. The second ion-source is a 3-cm source, obtained from Commonwealth Scientific[2], mounted with brackets to the bottom plate and oriented to face the rotary substrate holder, ~ 10 cm away. It uses one of the following gases, or a mixture: N_2, Kr, Ar, and CH_4. Two power supplies are used to drive the ion sources: one is obtained from Ion Tech[1] and the other is model ID-2500, obtained from Advanced Energy[4]. The films are deposited onto 0.6 cm x 0.6 cm Si(100) and Si (111) substrates. The approximate substrate temperature is measured with a thermocouple placed on the substrate holder.

Several parameters can be varied to optimize NbN film formation. These are the energy (beam voltage) and flux (current) of the ion-beams from each of the two ion sources, and the nature and partial pressures of the gases used. Because the system successfully produced high quality Nb films with the single ion beam, the parameters of this first ion source were kept constant at 1500 V, 34 mA and a partial pressure of Xe of ~ $1x10^{-4}$ Torr. An extensive optimization procedure was then followed where the parameters of the second ion-source were spanned and the films obtained were characterized by their T_c, low-temperature resistivity (ρ_{20K}) measured by the standard Van der Pauw (1958) four-point technique, and the residual resistivity ratio (ρ_{298K}/ρ_{20K}). Table 3-3 represents a synopsis of the optimization procedure, and Table 3-4 the beam parameters and properties of representative samples.

III.C.4. NbN Films: Results and Discussion

With just the first ion source operating and N_2 flowing into the chamber, we obtain films which adhere poorly to the Si substrate. Resistance measurements on

Table 3-4. Typical results for selected film depositions. The first ion source is operated at 1500 V, 34 mA, with P_{Xe} ~ $1x10^{-4}$ Torr. RRR = ρ(298 K)/ρ(20K). ΔT_c is the width of the transition (10%-90%).

Sample	Parameters of Second Ion Source				Film Properties			
	V (V)	I (mA)	P_{N_2} ($x10^{-4}$ Torr)	P_{other}	ρ_{20K} ($\mu\Omega$cm)	RRR	T_c (K)	ΔT_c (K)
A	0	0	1.5	-	604	0.97	10.8-11.9	Multiple trans.
B	200	3.6	1.1	-	475	0.90	9-12	Multiple trans. R>0 at 4.2 K
C	500	0.8	1.0	-	870	0.88	10.3-11.7	Multiple trans.
D	1500	3	0.7	-	234	0.90	11.1, 12.3	Two trans.
E	1500	2	1.0	-	206	0.80	11.6	0.08
F	1500	3.5	0.7	Kr: 0.3	214	0.82	11.5	0.09
G	1500	3	0.7	CH_4: 0.1	138	0.86	11.6	0.06
H	200	6.4	0.4	CH_4: 0.7	156	0.99	12.4	0.06
I	100	6.3	0.4	CH_4: 0.7	77	1.02	12.7	0.09

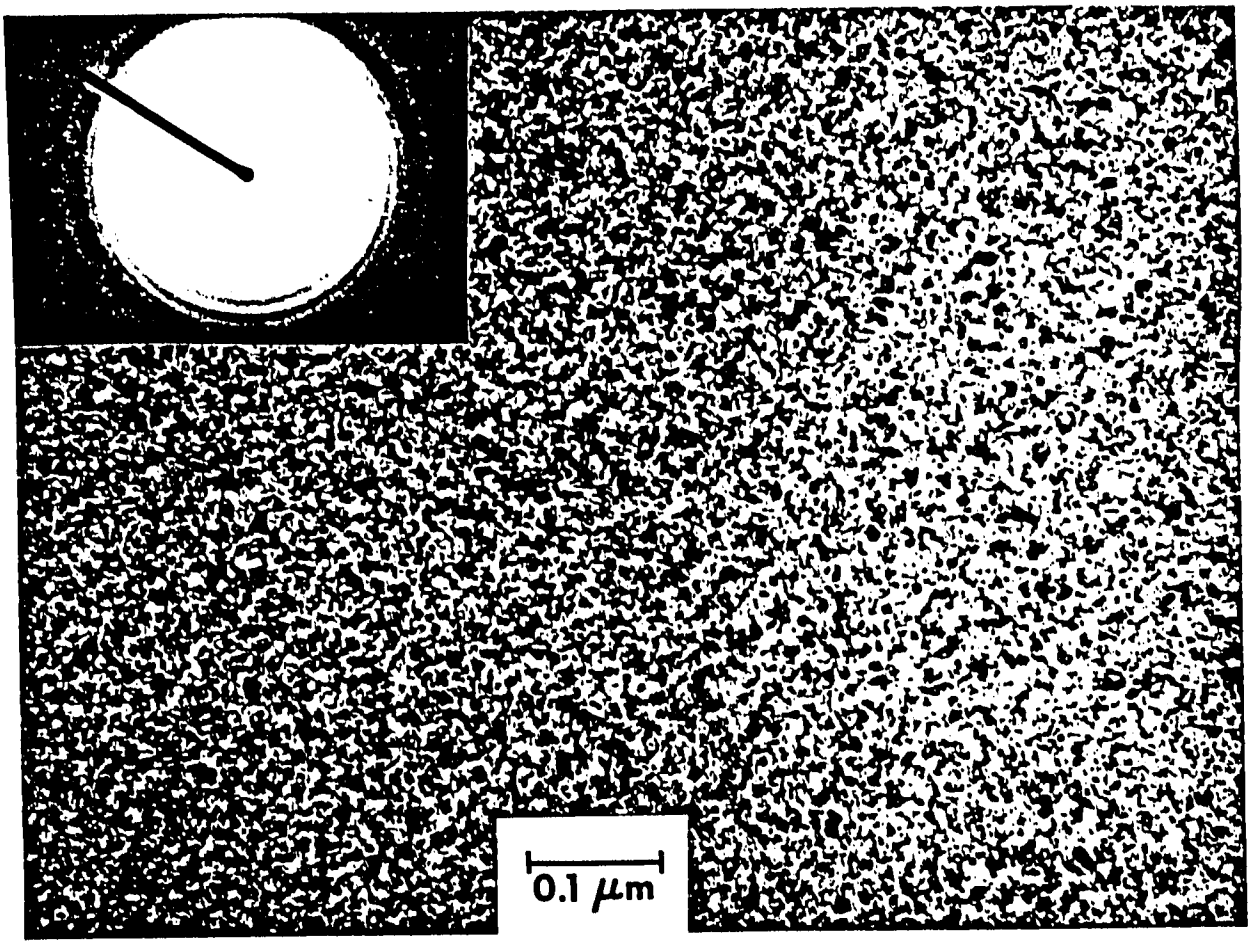

Fig. 3-9 Transmission Electron Microscope (TEM) photograph and electron diffraction pattern of a NbN sample made with the parameters of sample E (see Table 3-4).

these samples show multiple superconducting transitions with a maximum T_c of 11-12 K obtained at higher N_2 partial pressure (~ 1.5 x 10^{-4} Torr). Adhesion to the substrate is improved - but not completely solved - by pre-sputter-cleaning the substrate with 500 eV Krypton ions for a few minutes. Krypton is a rare gas with atomic mass intermediate between Ar and Xe. Krypton was used here because an extra supply of it was available. Alternatively, Ar or Xe are expected to have a similar effect. The poor adhesion of NbN films to the substrate is probably due to stress built into the film during deposition.

When both sources are operating, we find that when the N_2-beam voltage is lower than 500 V, the films display multiple transitions, and in some cases the films are resistive at 4.2 K. When the energy of the N_2^+ ions is increased to > 1000 V, the films display a single superconducting transition, with a T_c between 11 and 12 K. By using only N_2 with the second source, we find an upper limit for the beam current of 2 mA beyond which the films start displaying multiple transitions, presumably from a nitrogen-rich phase of NbN. By mixing Kr or CH_4 with N_2, the total current can be increased, allowing for more stable operation of the source, while not exceeding the critical N_2^+ arrival rate at the substrate. We find that addition of a small amount of CH_4 has the potential of improving T_c, possibly by helping to stabilize the δ-phase of NbN [Cukauskas (1985)]. T_c for the single-transition films deposited with high second-beam voltage is 11-12 K, with a transition width of 60-150 mK (see Table 3-4). The resistivity is typically $\geq$ 150 $\mu\Omega$cm with higher values observed for the inhomogeneous, multiple-transition films. Fig. 3-9 shows an electron diffraction and TEM photograph of a 500-Å film of NbN on a 200-Å carbon film suspended on a standard 200 mesh copper TEM grid. This NbN film was made without the addition of CH_4, with the parameters of sample E. It appears

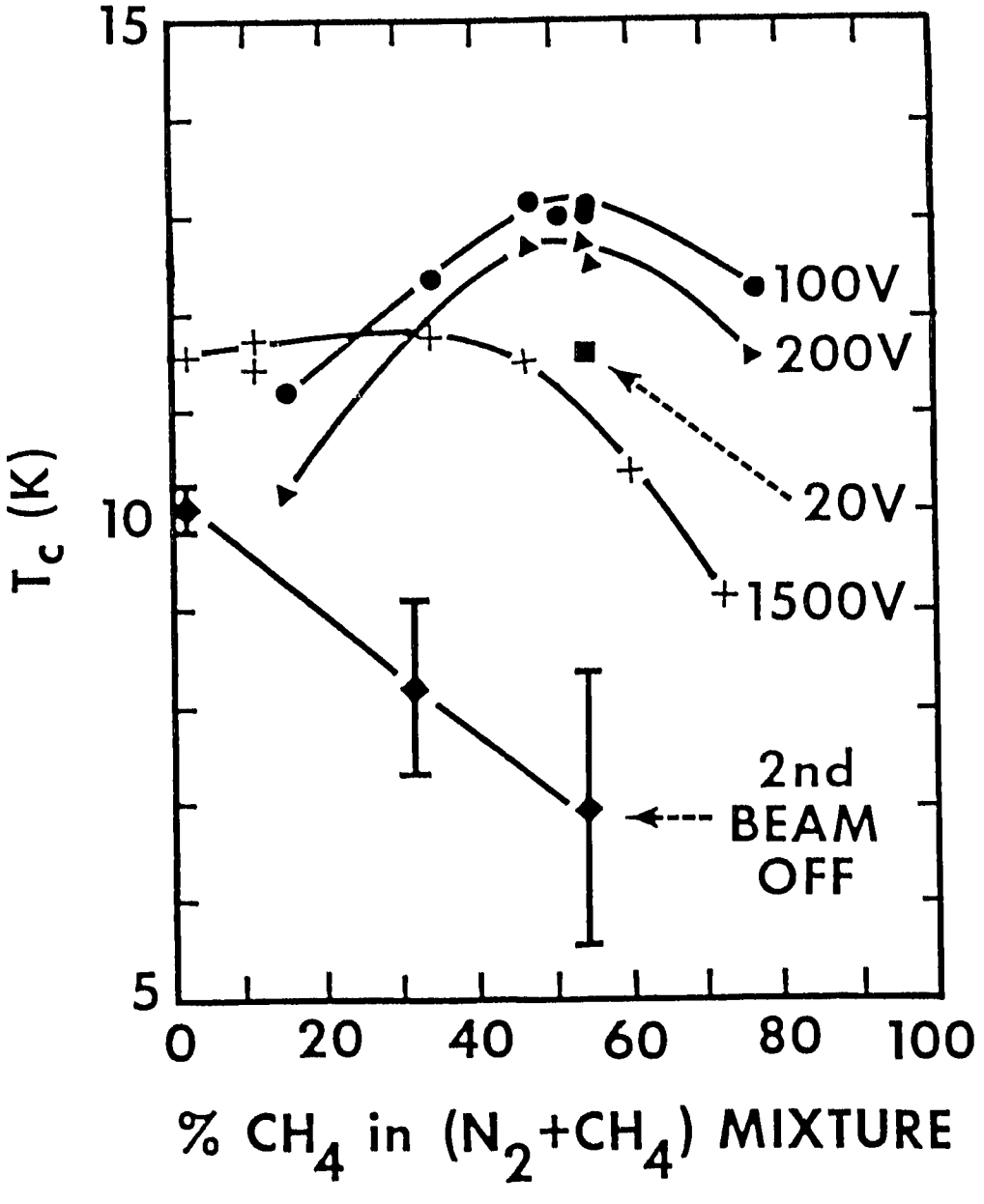

Fig. 3-10 Transition temperature versus molecular percent of CH_4 in (N_2 + CH_4) gas mixture. The voltages indicated refer to the operating voltage of the second ion source. All samples made on unheated substrates. The vertical bars on some points indicates the broad, multiple transitions. [from Lin and Prober (1986)].

to have a grain size ~ 50 Å, with a random in-plane orientation. For a 3000-Å film made on a Si substrate using a mixture of N_2 and Kr in the second ion source (sample F), a Read X-Ray camera (performed by E.J. Cukauskas of the Naval Research Lab) identifies the structure to be single-phase δ-NbN. Auger electron spectroscopy (AES) analyses (performed at the University of Minnesota NSF Regional Instrumentation Facility) on similar samples indicate uniform composition with a N to Nb ratio of 0.96 and traces of a few atomic percent of C and O. This N to Nb ratio of 0.96 is consistent with the phase diagram of the Nb-N system showing a slightly nitrogen-deficient δ-phase. Tunneling studies discussed in chapter 5 yield a superconducting energy gap Δ_{NbN} = 1.93 meV and $2\Delta/k_BT_c$ = 3.9. This is in agreement with previous findings [Gurvitch et al. (1985)] that NbN is a strong coupled superconductor. Given the slight improvement in film quality obtained initially with admixture of small amounts of CH_4 with the N_2 in the second ion source, it appeared useful to investigate the effect of increasing the percentage of CH_4 in the second ion-source [Lin and Prober (1986)]. The results of this investigation are represented in Fig. 3-10. With high voltage (> 1000 V) for the second ion source, addition of larger amounts of CH_4 do not give any further improvements in film quality. Beyond ~ 30 % CH_4, the T_c of the films decreases with increasing CH_4. However by using up to 50 % CH_4 in the second ion source, together with low beam voltages (100-200 V), films with single transitions are obtained, with a T_c of 12 - 13 K. Auger (AES) analysis on these films fabricated with low-energy second beam show a Nb/N/C ratio of 1.0/0.6/0.9. Given the relatively high carbon content of these films, they are more appropriately referred to as NbN_xC_y, with the Carbon probably going in substitutionally to the Nitrogen. Electron diffraction patterns for these films reveal (220) to be the strongest diffraction plane. This may arise from a mixture of the B1 and tetragonal crystal

structures, since the distance between (220) diffraction planes is the same for these two structures [Thakoor et al. (1985)]. In all the above results, the substrates are not intentionally heated. The temperature of the substrate holder is typically 60-80 °C. The deposition rate is ~ 100 Å/min. It is always possible to obtain a higher T_c by heating the substrate during deposition: with a substrate temperature of 200 °C, we obtain a T_c of 14 K.

At this time, one can only speculate as to the mechanism of NbN film formation in the dual ion-beam method. The site of formation of NbN could be either the Nb target, or the substrate, or both. When the Nb target is hit by the 1500 V Xe beam, a purplish glow develops around the area of impact of the beam. When N_2 gas is subsequently introduced in the chamber, this glow changes color to yellow-green. The glow is due to transitions between the atomic or molecular energy levels of the species surrounding the area: Xe, Nb, N_2, NbN. The change in color upon the introduction of N_2 gas may indicate the formation of NbN at the target which is then sputtered onto the substrate. Alternatively, or in addition to that, the N_2^+ ions from the second ion source may react with Nb at the site of the substrate to form NbN. The relatively high energy (1500 eV) required to form NbN without the use of methane may relate to the high activation energy needed to form the N-Nb bond starting from Nb and molecular N_2. If that is the case, then it is my speculation that the use of $\underline{NH_3}$ instead of N_2 in the second ion source will yield improved results and allow the use of lower energy from the second ion source. NH_3 would provide active $\underline{N}^+$ ions instead of N_2^+ ions predominantly obtained with N_2 gas [Harper et al. (1985)]. The N^+ ions would react more readily with Nb to form NbN.

Table 3-5. Optimum parameters for deposition of insulating AlN films. The target holder is rotated to expose the Al target.

Parameters of First Ion Source			Parameters of Second Ion Source			Deposition Rate
V (V)	I (mA)	P_{Xe} ($x10^{-4}$ Torr)	V (V)	I (mA)	P_{N_2} ($x10^{-4}$ Torr)	Å/sec
1500	34	1.0	500	8-12	1.0	2.4

In addition to NbN, we have used the dual ion-beam method to deposit films of AlN, an insulator, by sputtering an Al target onto the substrate while the second ion source directs N_2^+ ions on the growing film. This method for depositing AlN was first demonstrated by Harper et al. (1983) who discussed extensively the constraint and optimization procedure. Unlike NbN, AlN has only one stable crystal structure (hcp). This makes it easier to obtain good quality AlN films. Table 3-5 lists the parameters for our system which yield the optimum AlN films. The sputtering rate is ~ 2.4 Å/sec. The use of AlN as an artificial tunnel barrier on NbN is discussed in chapter 7.

III.D. Summary

This chapter has described the thin film deposition techniques used in the fabrication of the tunnel junction studied. Conventional thermal evaporation is used for the soft materials Pb, PbBi, Ag, Al, Cr and for Ge and SiO. Ion-beam sputtering is used to deposit the refractory metals Nb and Ta. A new fabrication technique is developed for NbN: dual ion-beam deposition. With the constraint of maintaining the substrates at near-room-temperature, we demonstrate the ability of this method to produce good quality NbN films. These films are polycrystalline, with a superconducting transition temperature up to 13 K. The same technique, dual ion-beam deposition can be used to form insulating films of AlN. The ability to sequentially deposit films of NbN and of AlN without breaking vacuum allows the use of AlN as an artificial tunnel barrier on NbN base electrodes.

IV. JUNCTION FABRICATION

The tunnel junctions produced and studied in this work all consist of a base electrode made of a refractory metal (Nb, Ta, or NbN) and a counterelectrode made of a soft metal (Ag, Pb, or PbBi). The fabrication of a tunnel junction involves several steps. The deposition techniques for thin film deposition of the base electrode and counterelectrode were described in the previous chapter. The patterning techniques to define the junction area and the techniques for producing the thin tunnel barrier are discussed in this chapter.

IV.A. Large Area Junctions

"Large" area here refers to junction sizes where the patterning can be made by use of mechanical masks. In our case, the "large area" junction dimensions are ~ 350 μm x 75 μm: the base electrode consisting of ~3000 Å of Nb, Ta, or NbN is deposited onto the substrate through a mechanical mask of width ~2 mm. In this fashion a 2 mm-wide strip of the base-electrode material is obtained. The substrate is in contact with the mask to minimize any shadowing that could result in non-uniform film thickness. After the base electrode film deposition is completed, and before the film is exposed to room air for oxidation, 1-2 Torr of 99.99%-pure oxygen is sometimes introduced into the vacuum chamber for a period of 10-12 minutes. This step helps initiate the growth of a good quality oxide on the base electrode. The vacuum chamber is subsequently vented to atmosphere with dry nitrogen gas. The sample is then transferred to the evaporator for the deposition of a 3000 Å layer of Ge through a 75-μm wire mask parallel to the base electrode strip. This layer of Ge completely covers the base electrode except for 75-μm slot, and serves to define one

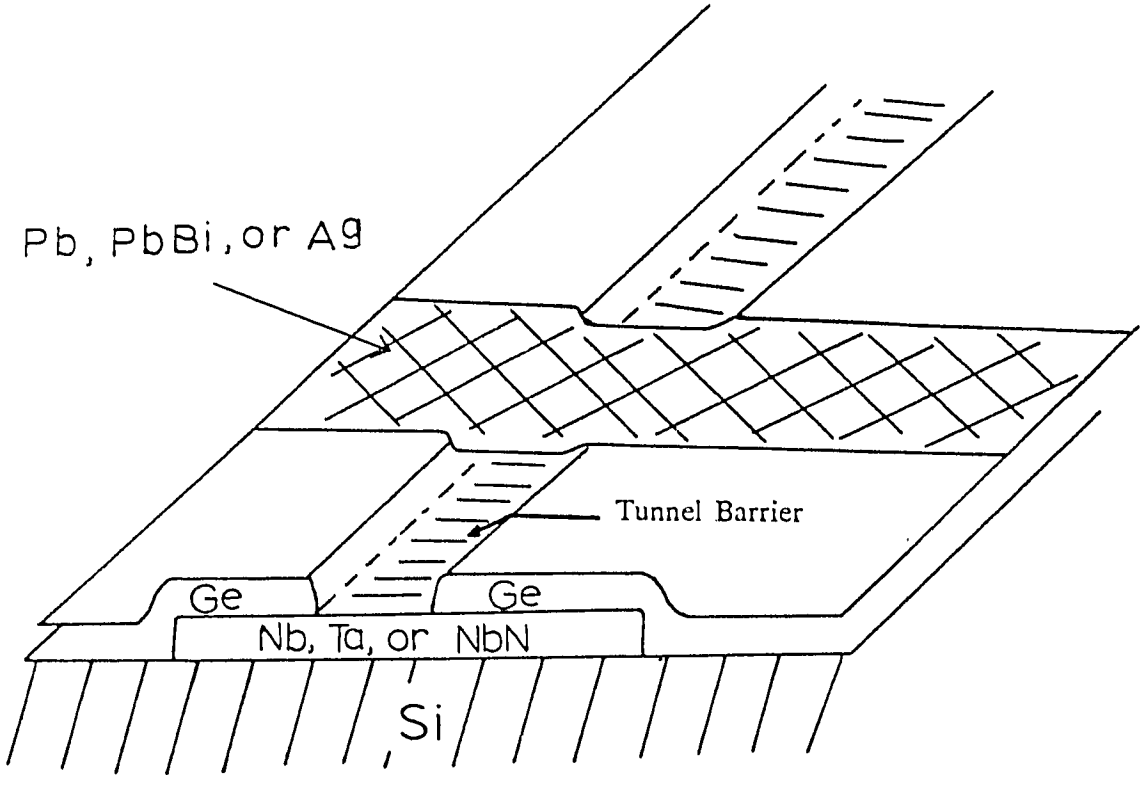

Fig. 4-1 Large area junction geometry. Ge acts as an insulator below 20 K. The junction area is ~ 75 μm x 350 μm. Each substrate accomodates either 3 (Nb/Ta) or 5 (NbN) identical junctions.

of the dimensions of the junction. Ge is an insulator at the low temperatures (< 20 K) where the measurements are made. The next step is to evaporate the counterelectrode through a ~ 350 μm-wide mechanical mask oriented so that the counterelectrode forms a cross-strip with the base electrode. This completes the junction, shown schematically in Fig. 4-1. The oxidation of the base electrode films occurs by exposure to atmospheric air. The minimum oxidation time is the time it takes to accomplish sample mounting and unloading between the different steps, and is approximately 10-15 minutes. In the case of Ta and Ta overlayers on Nb, this time was adequate to yield a junction resistance in the range 1 Ω - 1 kΩ. Nb oxidizes much more slowly, and a longer oxidation time was usually allowed. NbN produced junctions with resistance in the range 0.1 Ω - 10 Ω for air oxidation even up to several hours. All the junctions discussed in chapters 6 and 7 were fabricated in this fashion.

IV.B. Small Area Junctions

The need to have junctions of small area is prompted by a variety of applications. For a tunnel junction to be usable as a phase-sensitive detector of microwaves and mm-waves, its capacitance must not exceed a maximum value determined by the frequency range to be detected, to avoid short-circuiting the signal [Tucker and Feldman (1985)]. The switching speed of a tunnel junction used in digital applications is directly proportional to its current density [Faris et al. (1983)]; the requirement of faster switching speeds along with the constraint of a moderate value of the junction resistance translate in a requirement of small area. Other applications (SQUID magnetometers, IR direct detectors) are also improved with smaller area junctions. Further, as discussed in chapter eight, small area

junctions allow the resolution of the effect of individual defects and traps in the thin tunnel barrier.

Two elements become important patterning small area junctions. On the one hand, the mechanical masking techniques are no longer applicable for the patterning of micron-size features. Rather, photolithographic techniques have to be developed and used. On the other hand, the oxidation by exposure to atmospheric air yields too thick an oxide for the small-area junctions. For the same oxide thickness (and hence current density), the small-area junctions would have a resistance smaller than that for a large-area junction by the ratio of the areas, which can be as high as 10^5. To maintain the same resistance, a thinner oxide must be obtained, which requires the development of techniques to grow such an oxide under controlled conditions.

Several techniques and approaches have been developed for fabricating small area junctions. Our goal has been to develop a process that would be flexible and amenable to modification to accommodate later changes in materials and geometries. With these constraint in mind, we adopted the so-called "window" geometry. The fabrication procedure can be broken down into three steps: 1) deposition and patterning of the base electrode, 2) definition of the window area (= junction area), and 3) formation of the tunnel barrier and deposition and patterning of the base electrode. This sequence is schematically illustrated in Fig. 4-2. Two types of small-area junctions were fabricated in this work: 1) Ta/ Ta oxide/ PbBi junctions and 2) NbN/ NbN oxide/ PbBi junctions.

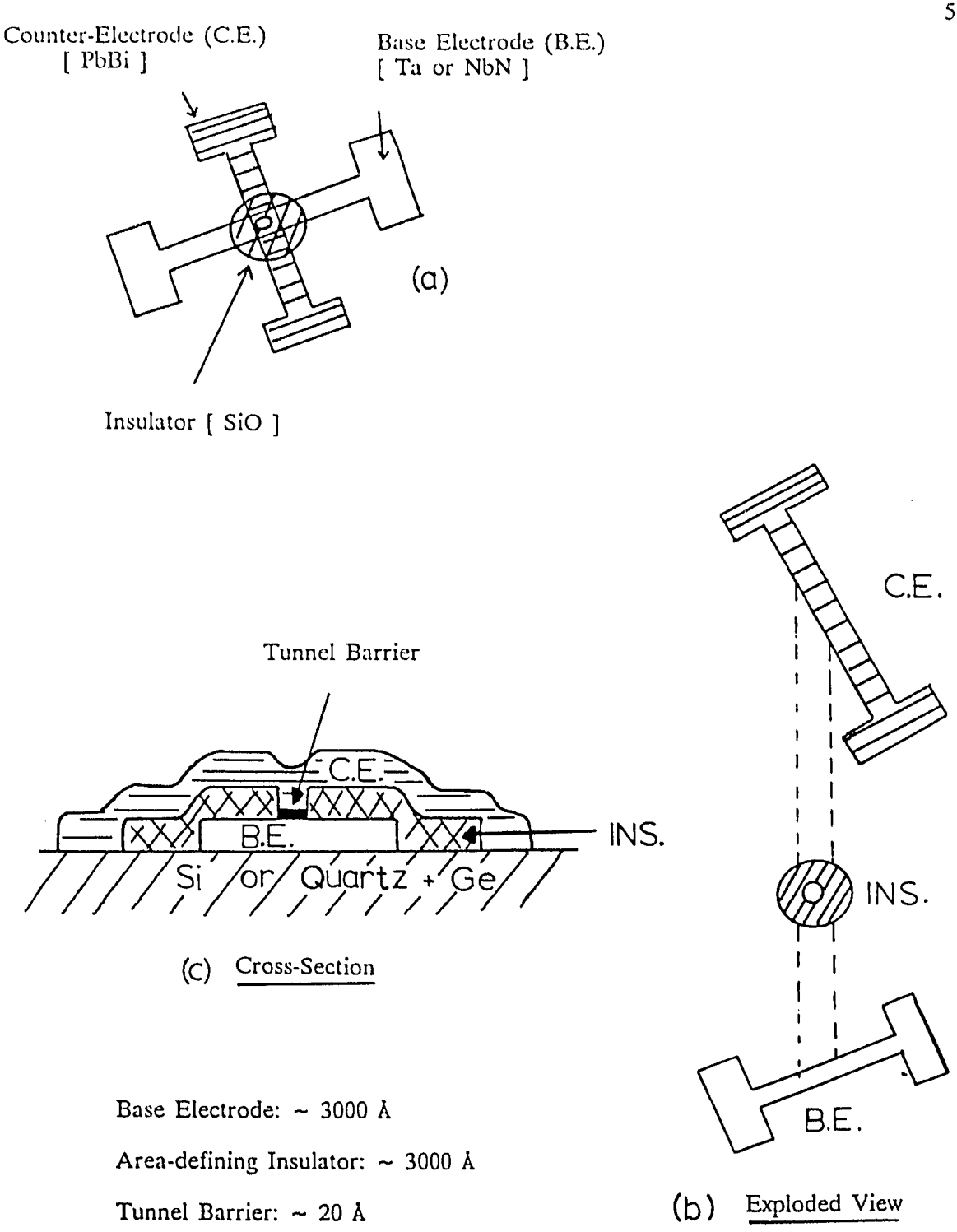

Fig. 4-2 Window geometry used for the small area junctions, shown schematically in top view (a), exploded view (b), and cross-section (c).

IV.B.1. Patterning of the base electrode.

The Ta base electrode is deposited by ion-beam sputtering and patterned by photoresist lift-off. Fig. 4-3 illustrates the principle of the lift-off technique, which is relatively standard in the semiconductor industry [Thompson (1983)]. This technique relies on the discontinuity of the layer deposited on the photoresist. The chances of success of the lift-off are enhanced by 1) use of a directional deposition technique from a quasi-point source and 2) formation of an undercut at the edges of the photoresist. The ion-beam deposition of Ta is directional as discussed in chapter 3. To obtain an undercut, we use a photoresist trilayer [Dunkelberger (1978)] as illustrated in Fig. 4-4. For patterning of the NbN base electrode, we use reactive ion-etching [Coburn (1982)], illustrated in Fig. 4-5. A NbN film is first deposited on the entire substrate and subsequently patterned. In both cases, the exposure of the photoresist is done by contact with a Chrome-on-glass mask.

IV.B.2. Patterning of the Junction Area: Defining the Window.

The second step consists of covering the base electrode with a 3000-Å thick insulating layer of SiO. A window opening in this SiO layer exposes the base electrode and defines the junction area. The patterning of this SiO layer is again done by photoresist lift-off. The undercut is obtained in this case by soaking the photoresist in chlorobenzene prior to development [Hatzakis et al.(1980)]. This has the effect of hardening the top layer of the resist, making its development rate slower. As a result, the bottom layer develops faster, and an undercut is produced. The exposure of the photoresist in this case is done by projection using a Zeiss microscope. The mask is demagnified by the microscope and projected onto the

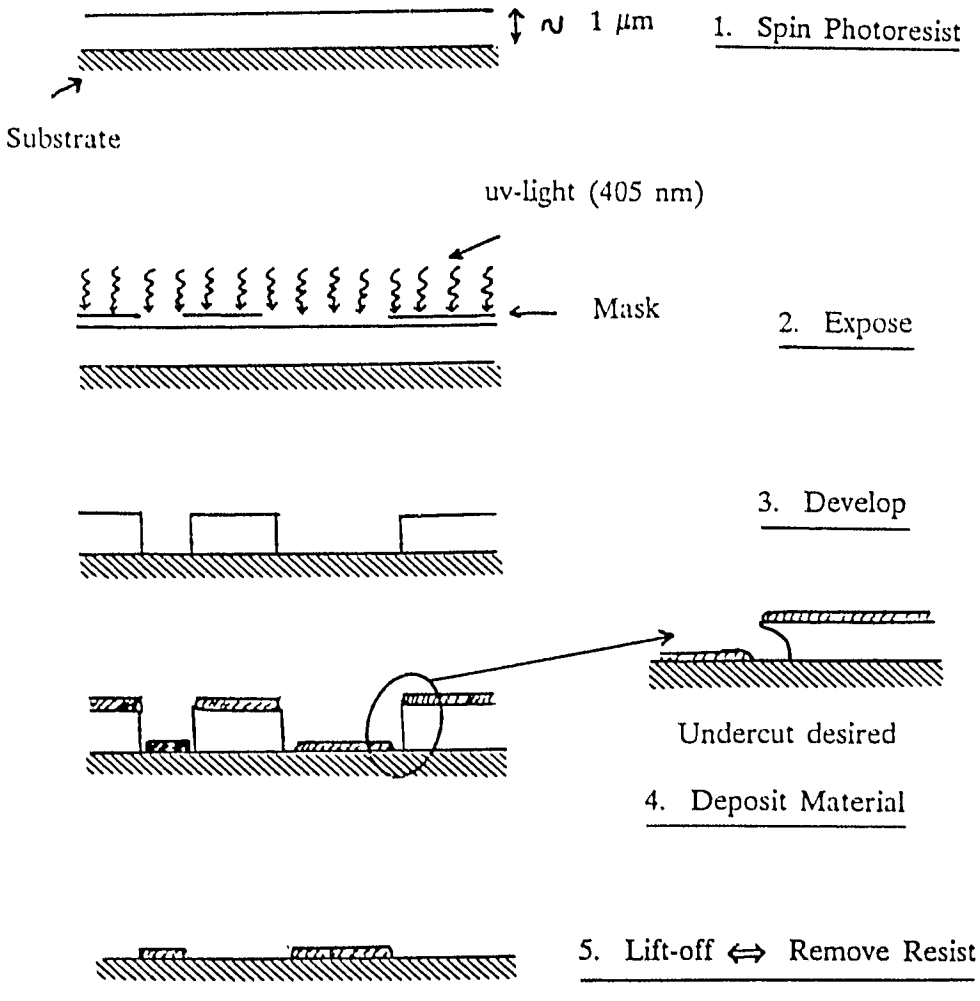

Fig. 4-3 Sequence of steps in lift-off patterning.

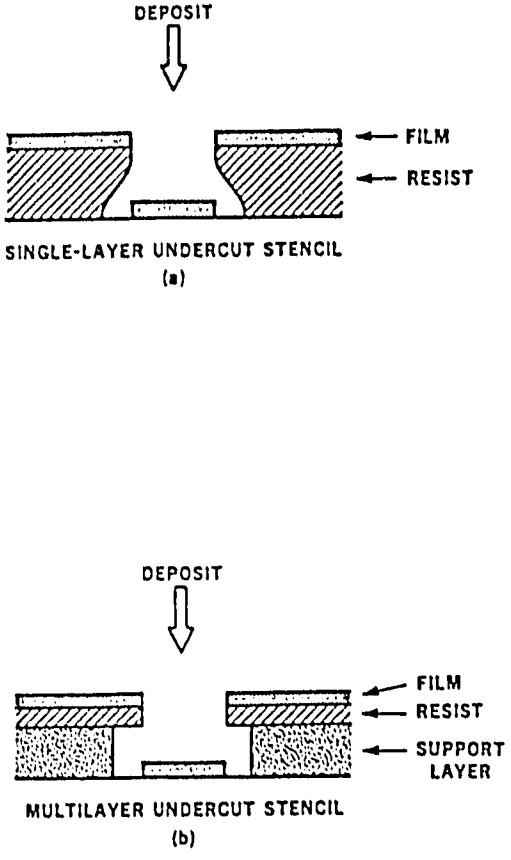

Fig. 4-4 Undercut profiles in the photoresist lift-off stencil. (a) Single-layer resist, the undercut being produced by chlorobenzene soaking which hardens the top of the photoresist. (b) A more reliable, though longer, procedure consists of using two layers of photoresist. The bottom (support) layer is blanket-exposed and the top layer is exposed through the mask. As a result, an undercut is produced during development. A thin, 50-100 Å layer of evaporated Al (not shown) is deposited between the two layers to prevent their intermixing.

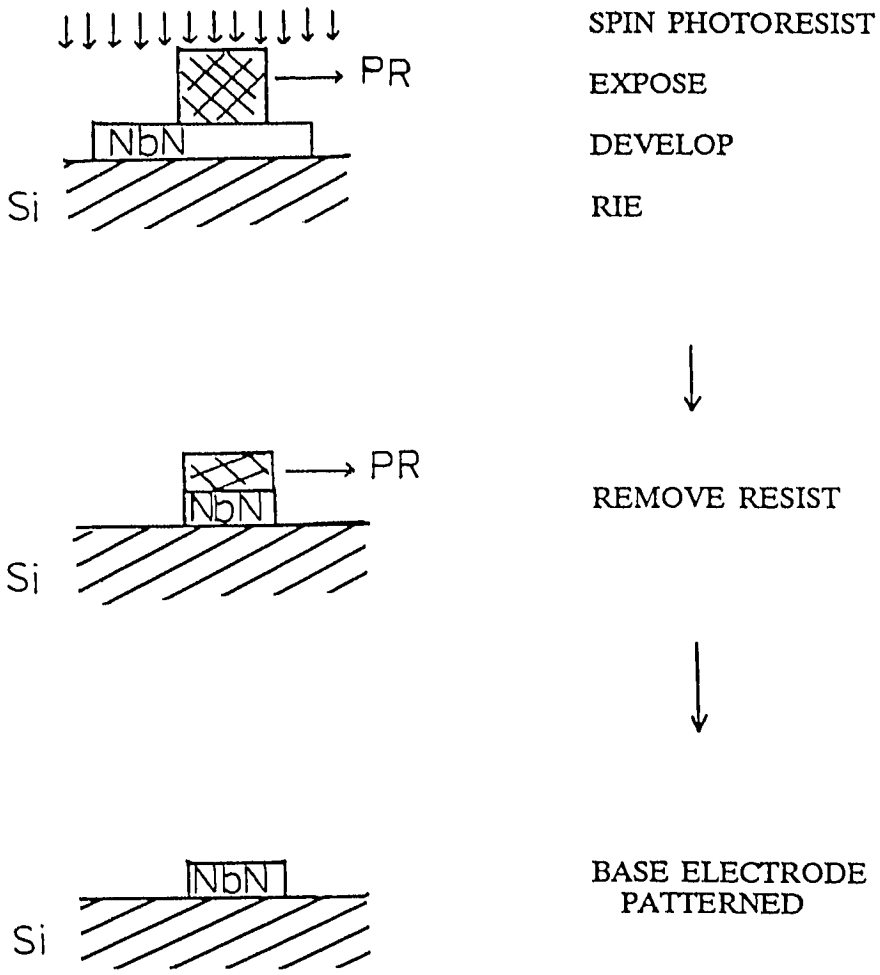

Fig. 4-5 Sequence of steps in the patterning of the NbN base electrode by reactive-ion-etching (RIE). This RIE is carried out using CF_3Br as the reactive gas, at a pressure of ~ 20 mTorr. The total RF power is 30 W and the dc self-bias 365 V. Under these conditions, the etch rate of NbN is 400 Å/min, and that of the photoresist mask 400 Å/min.

substrate. This technique has been described in detail by Feuer (1980). The light-source used, a Hg-vapor lamp with a filter restricting the exposing wavelength to 405 nm, has been installed and described by Wisnieff (1986) who also fitted the system with an accurate and reliable shuttering mechanism which allows control of the exposure time to 0.1 sec. The chlorobenzene-soak technique has been previously used to produce windows in SiO of diameter 5 μm [Greiner et al. (1980)]. In our work, we succeeded in producing windows of diameter ~ 1 μm. An example of the photoresist pattern used in obtaining such SiO windows is shown in Fig. 4-6. The tolerance on the exposing and development parameters becomes stringent for these sizes, since the width of the features becomes comparable to the thickness of the photoresist (~ 1 μm) and to the diffraction limited resolution of the microscope. Fig. 4-7 shows an example of an unsuccessful exposure. To obtain junction areas ~ 0.2 μm^2, we have had to approach the resolution limit of the projection photolithography system: window diameters ~ 0.5 μm can be produced, though such sizes are not routinely nor reliably achieved.

IV.B.3. Tunnel Barrier Formation and Counterelectrode Deposition and Patterning.

The formation of the tunnel barrier is the key step in tunnel junction fabrication. The current through the junction depends exponentially on the product of the tunneling barrier thickness and the square root of the barrier height times the effective mass of tunneling electrons (see Chapter 7). Thus, precise control of the tunnel barrier oxide thickness and composition are required in order to achieve reproducible values of the tunneling current. For Ta-based junctions, a method of achieving a high quality, reproducible oxide barrier has been developed by Dean Face at Yale for junctions of comparable size but different geometry. We found the same

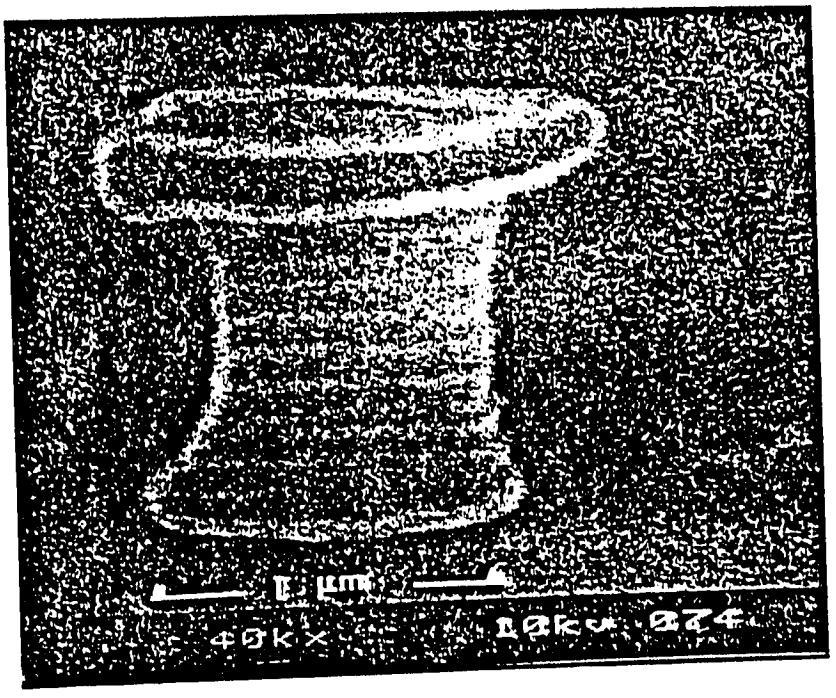

(a)

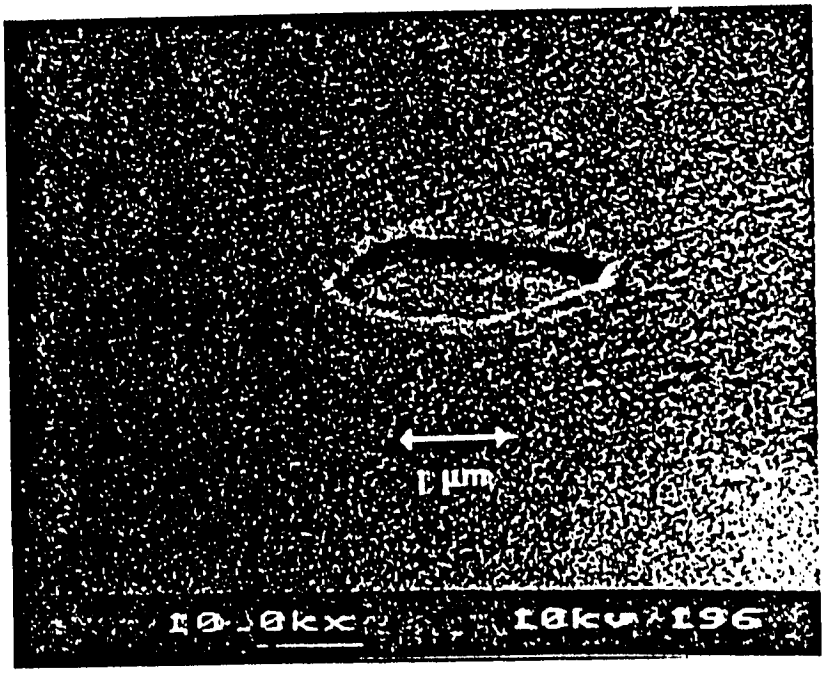

(b)

Fig. 4-6 **(a)** Photoresist lift-off pattern used to define the SiO window. The undercut is produced by chlorobenzene soaking of the photoresist. The steps in the pattern are due to interference between the exposing monochromatic uv light and its reflection from the substrate. These steps could be eliminated by use of a polychromatic light source, but in our case do not have any negative effects. **(b)** Window area in SiO, shown after evaporation of SiO and lift-off of the photoresist stencil.

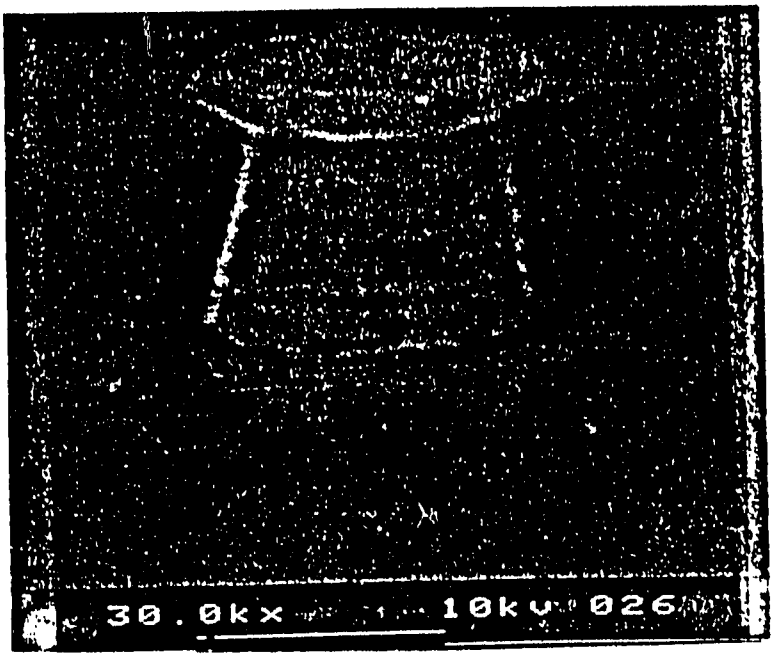

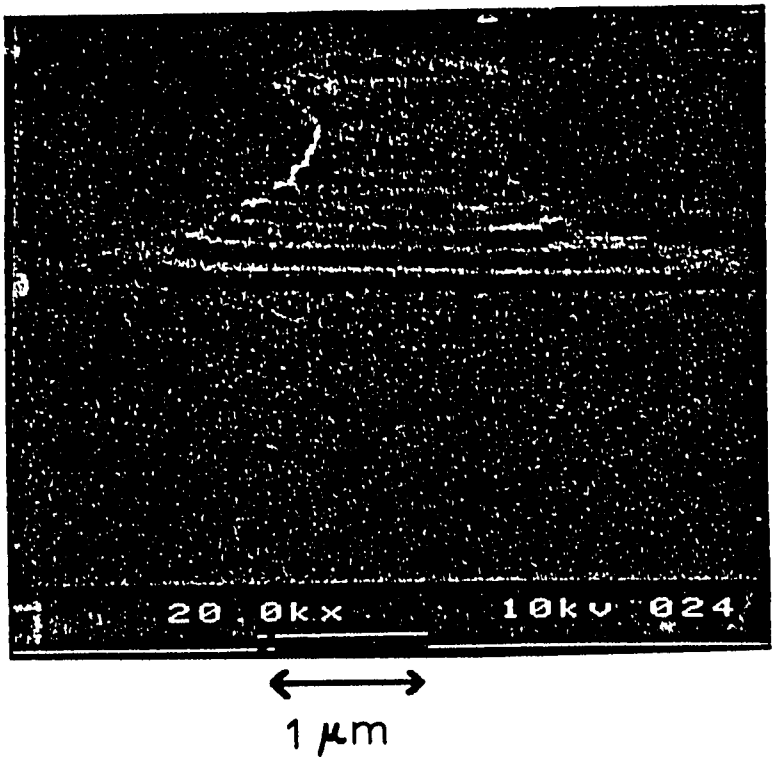

Fig. 4-7 Contrast between a successful (a) and an unsuccessful (b) exposure of the cholorobenzene-soaked photoresist. In (b) the photoresist is underexposed.

method to be successful for the window geometry, with minor modifications. Face used a step-defined geometry on Si substrates shown schematically in Fig. 4-8. In this work, in addition to the different window geometry, fused quartz substrates were used instead of Si. This was done to allow the junctions to be tested as SIS mixers in the 90-110 GHz range [(Cui et al. (1987)]. Fused quartz is preferred over Si for this application because it minimizes the dielectric loading of the waveguide [Goldsmith (1982)]. Fused quartz has the lowest dielectric constant (~ 3.8) of available substrate materials (Si, Sapphire, MgO,...).

After the window area is defined, a photoresist lift-off trilayer is developed, carrying the counterelectrode pattern. The sample is then transferred to the evaporator (see Fig. 3-1). The junction area is ion-beam cleaned, first with a mixed beam (50% Xe, 50 %O_2) at a beam voltage of 200 V, and then with a pure Xe beam at 160 V. The total chamber pressure during cleaning is ~ 1-2 x 10^{-4} Torr. This cleaning sputters away the Ta oxide and contamination due to air exposure. We found it necessary to include oxygen in the ion-beam cleaning step (O_2 was not used by Face). This inclusion of oxygen may help to efficiently remove photoresist residue. After ion beam cleaning, the exposed Ta is oxidized by a pure O_2 dc glow discharge for 5-20 seconds at a pressure of ~ 120 mTorr (see Fig. 4-9). This oxidation method was found by Face to give the best results for junction quality and reproducibility. Other oxidation methods investigated by Face were found to be either too slow (thermal oxidation) or too violent and irreproducible (ion beam oxidation). The use of fused quartz, which is a better insulator than Si, required in our case the evaporation of a 3000-4000Å film of amorphous Ge onto the fused quartz substrate prior to the deposition of Ta. If the quartz substrate is not coated with Ge, we find incomplete cleaning or poor oxidation of the junction area with the ion

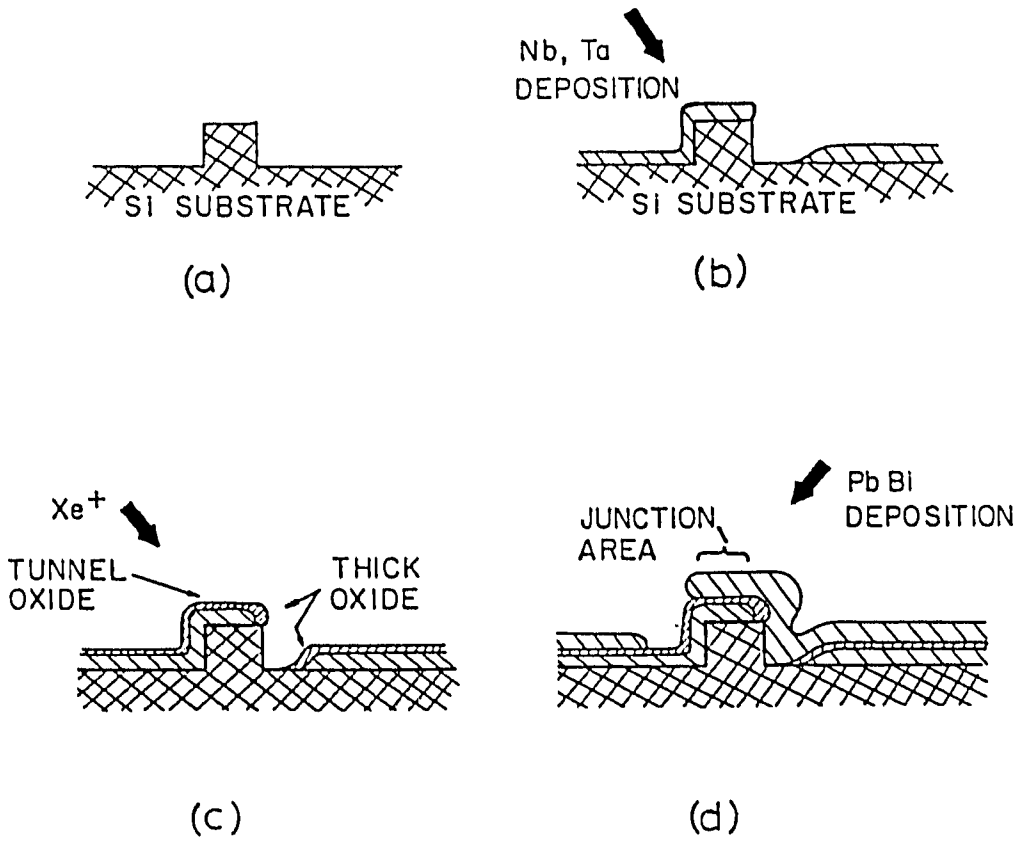

Fig. 4-8 Sequence of steps in the fabrication of Ta/PbBi junctions by the Face technique. (a) formation of a step in the Si substrate; (b) angle deposition of Nb and Ta; (c) Ion-beam cleaning and glow discharge oxidation; (d) angle deposition of the PbBi counterelectrode. From Face (1987).

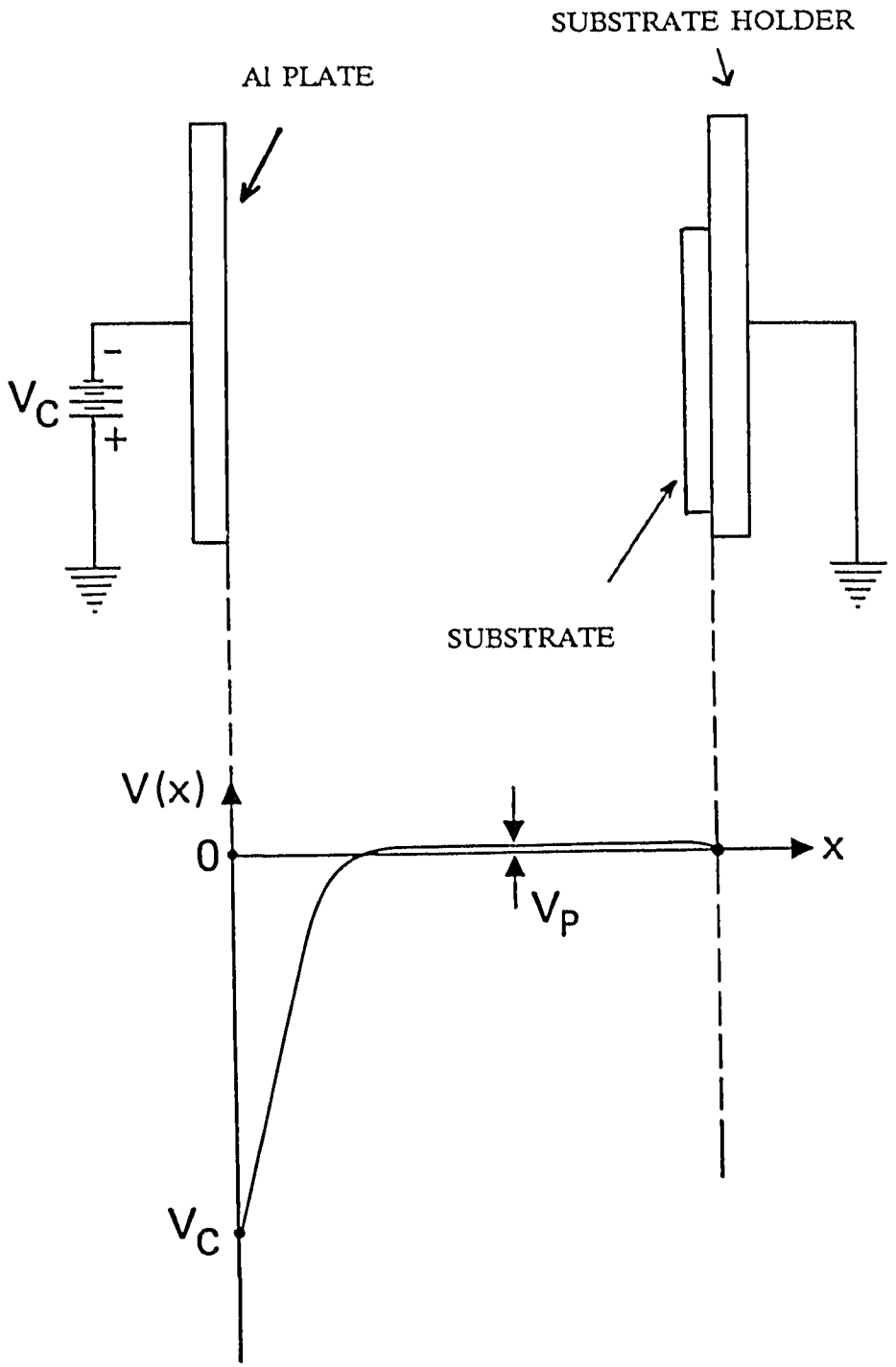

Fig. 4-9 Glow discharge oxidation configuration. The sample is mounted onto a grounded sample holder. Facing the sample is an Al plate which is negatively biased to ~ 400 V. As a result, the oxygen introduced in the vacuum chamber at a pressure of ~ 120 mTorr forms a plasma which is at a plasma potential V_p ~ a few volts. This corresponds to the energy of the oxygen ions impinging upon the sample and oxidizing it.

beam. This is probably due to a charging of the substrate by the ion beam. During ion beam cleaning and oxidation, the Ge is grounded to the sample holder. This provides a drain for the charge from the ion-beam, which in our case is not neutralized. The 3000 Å PbBi counterelectrode is then evaporated from an alloy source. This evaporation is immediately followed in-situ by a second evaporation of 120 Å of Indium. This Indium coating makes the junctions insensitive to air exposure; this will be discussed in chapter 5. The final step is the lift-off of the counterelectrode. The completed junctions are then tested at 1.3 K and stored in liquid nitrogen. The dc characteristics of these Ta/PbBi junctions are discussed in chapter 5 and their noise properties in chapter 8. The step-by-step fabrication sequence of the Ta/PbBi window junctions on fused quartz substrate is given in Appendix A. Their performance as SIS mixers in the 90-110 GHz range is discussed in Appendix B.

In the case of NbN/PbBi junctions, Si substrates are used. The same procedure is followed for ion-beam cleaning. However, in spite of lengthy efforts, glow discharge oxidation did not yield reproducible junctions. Instead, when oxidation was performed by exposing the cleaned NbN to 100 Torr of pure oxygen for 10-20 minutes, fairly good junctions started to be obtained with a current density of $\sim 10^3$-10^4 A/cm^2. The patterning of the PbBi was also done differently in this case. Instead of lift-off, the PbBi was patterned by ion-milling [Gloersen (1975)]. After ion-beam cleaning and oxidation, PbBi was evaporated on the whole substrate. The sample was then taken out of the evaporator, and a single-layer photoresist pattern defining the counterelectrode was developed. This photoresist pattern was then used as an etch mask through which a 500 V Xe ion beam sputtered away the PbBi. Cooling of the substrate (to 77 K) during the ion milling was found to help prevent

Table 4-1. Ion-milling etch rates with Xe at a beam voltage of 300 V, and a beam current density at the substrate of ~ 2 mA/cm^2.

Material	PbBi	Ag	NbN	SiO	Si	Photoresist (Shipley* 1470)
Etch Rate (Å/min)	1200	500	< 100	< 100	< 100	< 200

*Shipley Company, Inc., Newton, MA.

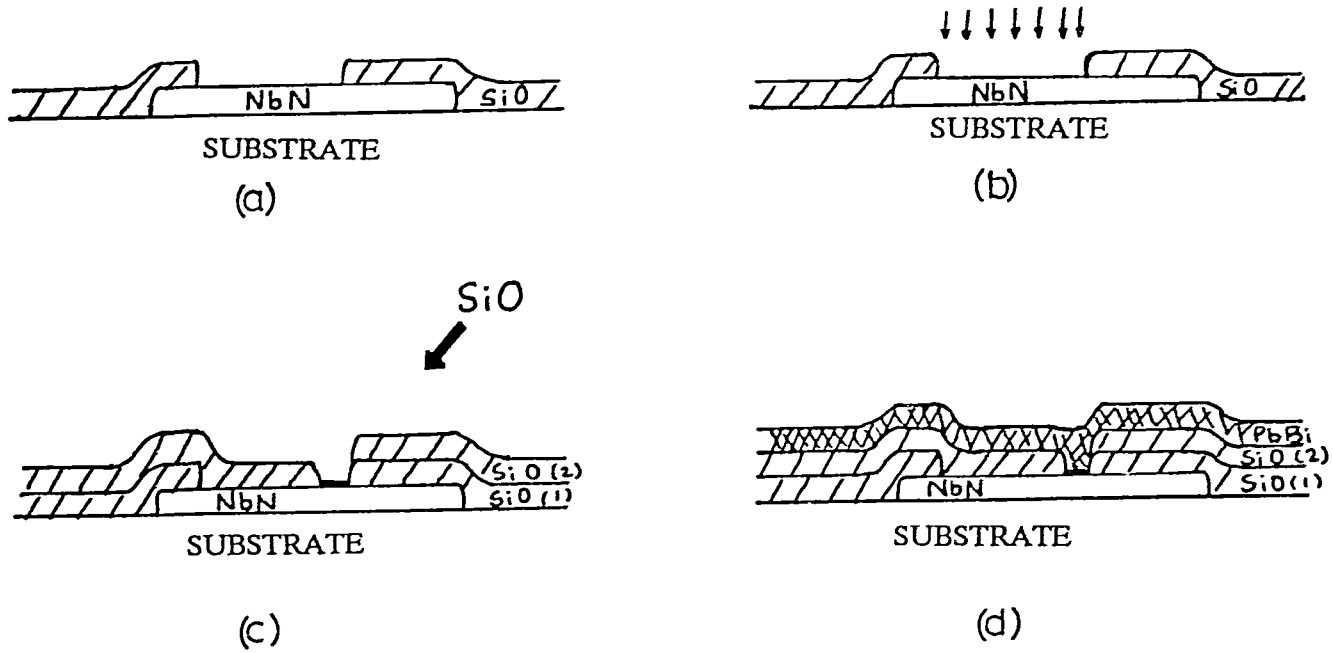

Fig. 4-10 Sequence of steps proposed in the window geometry configuration with one modification of the procedure shown in Fig. 4-2 [step (c) added]. This modified sequence should allow the reduction of the junction area without any further processing. The added angle evaporation of SiO in (c) reduces one of the window dimensions to ~ 1/4 μm; this is followed by oxidation of the NbN. All the other steps remain the same as described in the text. This procedure was not actually employed in our research.

the photoresist mask from hardening. The etch rate of PbBi is about ten times larger than any of the other materials on the substrate, including the photoresist (see Table 4-1). This allows wide tolerance in the milling time. Ion-milling was chosen in this case to avoid the presence of the photoresist mask during ion-beam cleaning. Although this mask did not pose a problem with Ta-based junctions, the initial failure of the NbN/PbBi junctions fabricated with glow discharge oxidation led to the consideration of this possibility for NbN. The final step is the removal of the photoresist mask, by use of a photoresist remover, such as Shipley 1165 Microposit Remover. Finally, as a suggestion for future work, Fig. 4-10 shows how an additional angle-evaporation of SiO would allow the reduction of the junction area to submicron dimensions without the use of any additional lithographic steps. This procedure was not tried in our studies.

V. JUNCTION MEASUREMENTS AND DC PROPERTIES

This chapter describes some of the specialized instrumentation used in the measurements of the properties of the tunnel junctions studied in this work. The dc I-V characteristics of the various tunnel junctions produced are then discussed.

V.A. Electronic Instrumentation

V.A.1. Low-Noise Current Source

The current source required in accurate measurements of the electrical characteristics of tunnel junction must satisfy a number of requirements. The voltages of interest typically range from 1 to 20 mV, for structures occurring around the superconducting energy gap and structures involving phonon densities of states. Thus, extrinsic noise must be kept to a minimum. Also, phenomena of interest can occur at zero voltage, therefore it is important that zero current output not be a special point to the power supply. Further, since probing of the tunnel barrier properties requires biasing the junction to ~ 0.5 - 1 V, the same current source should be able to supply a large enough current to apply this bias. The ability to modulate the dc current with a small ac bias is also necessary for measurement of the derivative curves dV/dI and d^2V/dI^2. These requirement are not usually available commercially. For this reason, a special current source was built in this work.

The schematic for this current source is shown in Fig. 5-1. It consists of two independent, active current sources which drive current through the load at all times. One current source, in the bottom of the figure, provides a fixed current I_f,

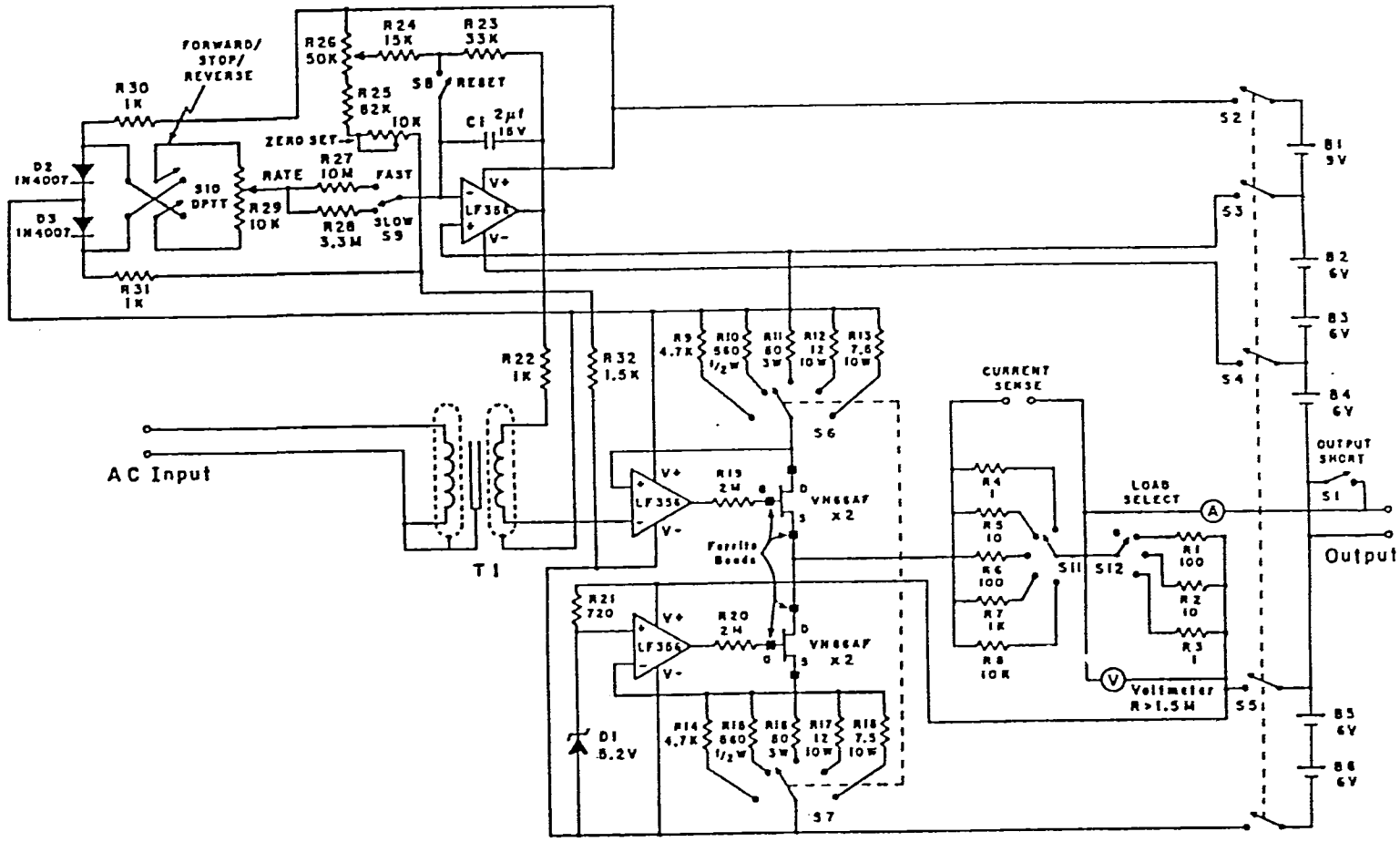

Fig. 5-1 Circuit diagram for the low-noise current source with continuous zero crossing. Each section of the source contains two VN66AF transistors connected in parallel. All resistors are 1/4 W unless otherwise indicated. Ferrite beads are placed on each transistor lead to prevent rf oscillations.

while the second source, above it, provides a variable current I_v. This variable current source can sweep from currents $0<I_v<I_f$. This arrangement provides the ability to ramp the junction current from negative to positive values smoothly through zero. The zero current output point ($I_f=I_v$) is not special to the current source and does not involve any turn-on transients. The current I_f is determined by the selection of one of five feedback resistors R14-R18. The voltage across these resistors is held fixed at 5 V by comparison to a Zener diode D1. Two V-MOS transistors in parallel are used to drive the current. The complementary current source shown in the upper part of the schematic incorporates an identical gang of feedback resistors. There, the current is compared with both the output of a variable voltage source, shown in the upper-left-hand corner of the schematic, summed with the ac input of a shielded transformer. This allows the modulation of the dc current by an external ac source. The internal voltage source can be used to manually sweep the current output or else a time-sweep may be engaged to do so automatically at a selectable rate. The current may be modulated by inputting a small ac voltage to the transformer T1 which isolates this input. Power is provided by rechargeable 6-V sealed gel batteries*. These batteries have been in operation for 5 years without any degradation in their performance. Battery B1 is a 9-V battery on which there are small current demands and for which a small dry cell is adequate. This current source is used in all our tunnel junction measurements.

---

*Obtained from Power Sonic Corp., Redwood City, CA.

V.A.2. Buffer Amplifiers

In measuring the voltage across a tunnel junction, the chopper input of most digital voltmeters and chart recorders was found to introduce extra noise into the sample and cause rounding of sharp structures in the I-V characteristics [Face (1987)]. To avoid this problem, voltage measurements in most cases were made by first amplifying the voltage with a precision instrumentation amplifier [Analog Devices AD-524C*] shown in Fig. 5-2. These amplifiers have accurate gain calibration (± 0.1%), low noise (7 nV/$\sqrt{\text{Hz}}$) and a high input impedance of 1 GΩ. The amplifiers were battery powered to avoid 60 Hz pick-up. The output of the amplifiers were then directed to the chart recorder (HP 7047A) and/or digital voltmeters (HP 3556A or HP 3478A). These voltmeters were interfaced to a computer (HP 9816 or HP 9817) where the digitized data was stored. For the noise measurements described in chapter 8, the AD-524C amplifier was replaced with an AD-624C which has lower noise (4 nV/$\sqrt{\text{Hz}}$).

V.A.3. Derivative measurements: ac modulation technique

Important to the study of the density of states of superconductors and to the study of phonon effects in superconducting tunnel junctions, is an accurate determination of the differential conductance dI/dV and d^2I/dV^2. Although in principle it is possible to determine these quantities by evaluating the slope of the dc current-voltage characteristic of the tunnel junction, the accuracy required (1 part in 10^4 for phonon effects) and the limitation of the digitizing equipment

*From Analog Devices, Norwood, MA.

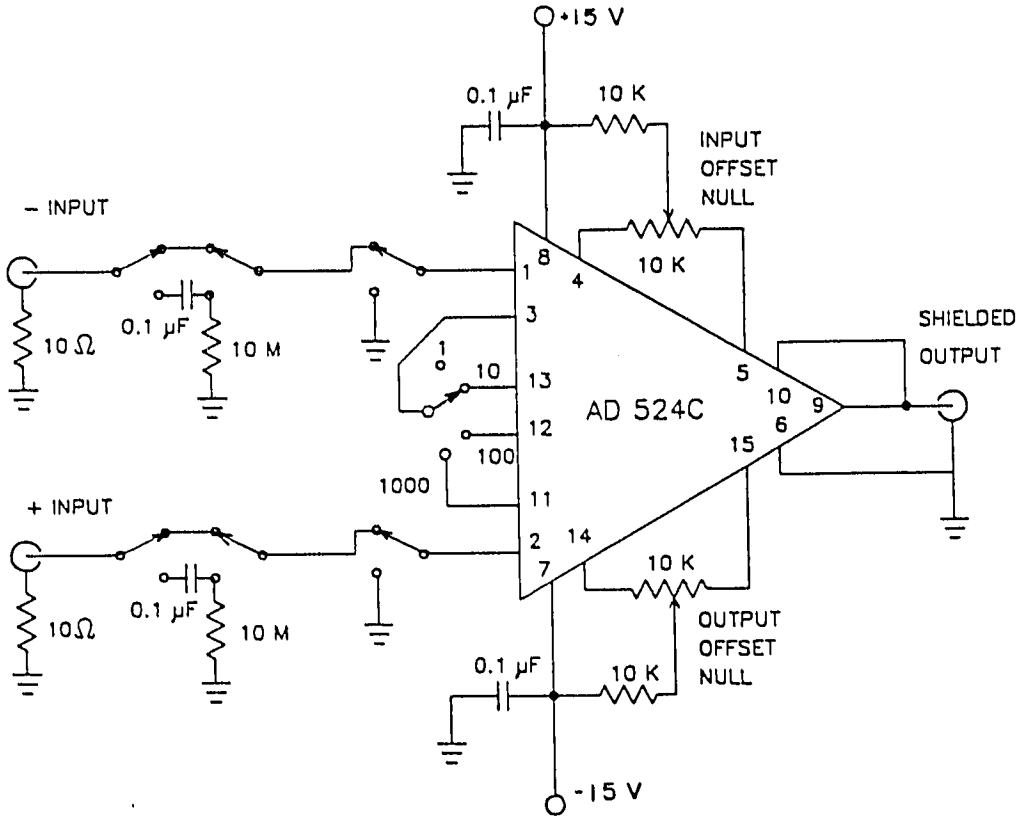

Fig. 5-2 Circuit diagram for the buffer amplifiers. For lower background noise, the AD524C may be replaced by the AD624C.

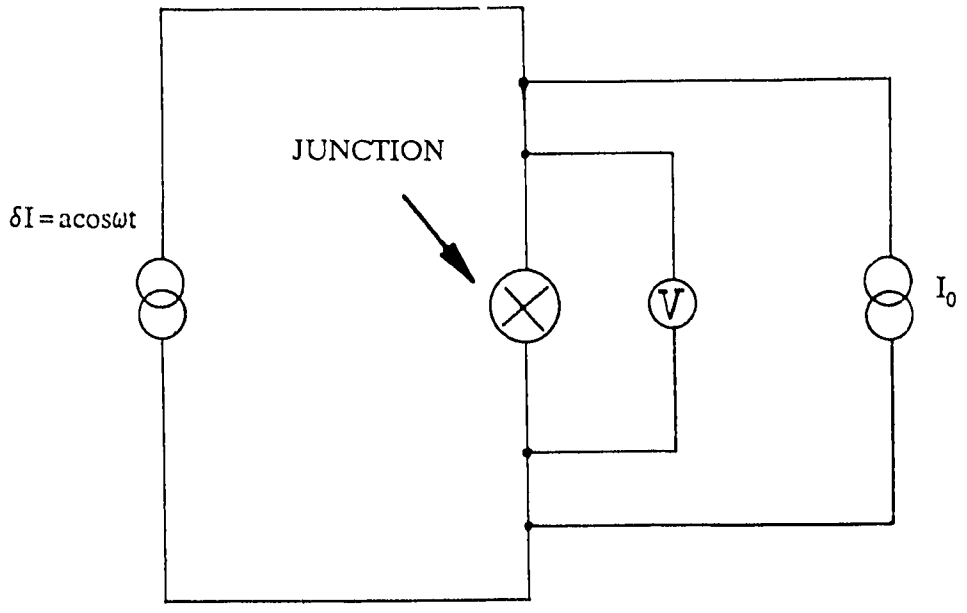

Fig. 5-3 Simplified schematic for the analog dV/dI measurement by harmonic detection.

available make it more advantageous to use established ac-modulation techniques [Adler and Jackson (1966)] to directly measure these derivatives. The principle of the method is illustrated in Fig. 5-3. If the junction is biased with a current $I = I_0 + \delta I$ consisting of a dc part I_0 and an ac modulation $\delta I = a\cos\omega t$, then the voltage across the junction can be written in terms of a Taylor series:

$$V(I) = V(I_0) + (dV/dI)_{I_0} a\cos\omega t + (1/2)(d^2V/dI^2)_{I_0} a^2\cos^2\omega t + \ldots \quad (5.1)$$

or, by writing $\cos^2\omega t$ in terms of $\cos 2\omega t$,

$$V(I) = V(I_0) + (dV/dI)_{I_0} a\cos\omega t + (1/4)(d^2V/dI^2)_{I_0} a^2(1 + \cos 2\omega t) + \ldots \quad (5.2)$$

where $V(I_0)$ is the dc bias of the tunnel junction and ω is 2π times the modulating frequency. It follows from Eq. (5.2) that if δ is constant then the component of voltage across the junction at angular frequency ω is proportional to $(dV/dI)_{I_0}$ and the component at 2ω is proportional to $(d^2V/dI^2)_{I_0}$. This technique was used to generate the first derivative data shown in chapters 6 and 7 [see for example Fig. 6-7]. The current was generated by the current source described above and the voltage across the junction, after going through the amplifiers described above, was sent to a lock-in amplifier [PAR 124]* which detected the signal at the first harmonic, proportional to the differential resistance dV/dI. The differential conductance dI/dV is simply obtained by $dI/dV = 1/(dV/dI)$. In situations where the I-V displayed a region of negative resistance, as in Fig. 6-6, the junction is voltage-biased by using a 1 Ω shunt resistance in parallel with the junction. As long as the

*From Princeton Applied Research, Princeton, NJ.

junction resistance is much larger than the shunt resistance, the constant current flows almost entirely in through the shunt, forcing a constant voltage across the junction. In this situation, I and V are interchanged in equation (5.2), and by detecting the first harmonic signal of the current, we get a signal proportional to the differential conductance dI/dV.

The structure in the I-V curves reflecting the phonon density of states represents only a small part of the total signal across the junction. In this situation, most of the lock-in amplifier output signal must be bucked out in order to display these small variations. The most effective way to accomplish this is by use of an ac Wheatstone bridge as shown in Fig. 5-4. One arm of the bridge contains the tunnel junction R_T, which is treated as a nonlinear passive element, while the other arm has R_{bal} set so that $R_{bal} \simeq R_T$. The dc bias for the junction is provided by the current source described above. The inductance L = 6 H, along with the very high output impedance of the current source described above minimize and allow the neglect of the ac shunting of the tunnel junction by the dc bias supply. $R_A = R_B = R_C = R_D = 50\ k\Omega$ are precision resistors matched to have very close values of the temperature coefficient. Their resistance is much larger than typical junction resistances. As a result, the ac voltage modulation applied to the bridge is seen by the junction and by the balance resistance R_{bal} as an ac current source with the ac current in the two arms of the bridge very closely the same. If $a\cos\omega t$ is the ac current in each arm, then

$$V_1 = R_{bal} a\cos\omega t \tag{5.3}$$

$$V_2 \simeq I_0 R_{bal} + \left(dV/dI\right)_{I_0} a\cos\omega t + (1/4)\left(d^2V/dI^2\right)_{I_0}(1+\cos 2\omega t) + \ldots \tag{5.4}$$

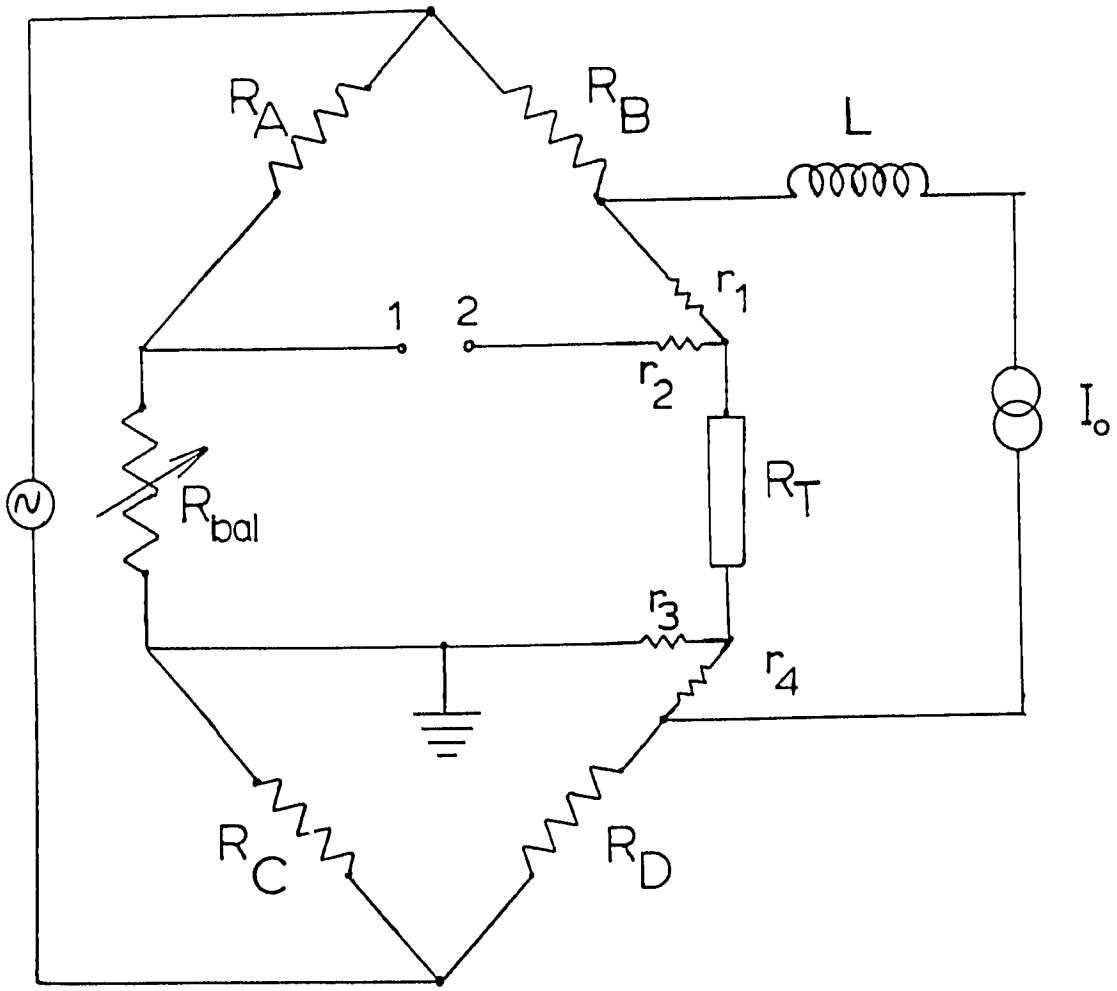

Fig. 5-4 Four terminal bridge configuration for measuring small variations in dV/dI riding on a large signal and for measuring d^2V/dI^2.

where I_0 is the dc bias current flowing through the junction, and the bridge is balanced so that $R_{bal} \simeq R_T$. The potential difference between 1 and 2, detected by a lock-in amplifier has then components at ω and 2ω given by:

$$V_{12}(\omega) = a[R_{bal} - (dV/dI)_{I_0}]\cos\omega t \tag{5.5}$$

$$V_{12}(2\omega) = (1/4)a^2(d^2V/dI^2)_{I_0}\cos 2\omega t \tag{5.6}$$

The advantage of the bridge here is that a large portion of the first harmonic signal is cancelled by R_{bal} which allows for amplification of the fine structure in dV/dI without being limited by the dynamic range of the lock-in amplifier. Another advantage is related to the resistance of the junction electrodes represented by r_1 - r_4. When a normal metal is used for one of the electrode (for example Ag as in chapter 6), or when the superconducting electrode is above its T_c, these lead resistances may be appreciable and therefore prevent measurement of the true characteristics of the junction itself. However, by using the four-point bridge configuration shown in Fig. 5-4, this problem is eliminated since the contribution of the lead resistances cancel each other to first order as long as the electrodes are symmetrical [A detailed treatment is given by J.S. Rogers et al. (1964)]. This bridge configuration is used to obtain the phonon structure data presented in chapter 6.

V.B. Low-temperature Apparatus

V.B.1. Dewars and Cryostats

The principles and techniques of generating and measuring cryogenic temperatures are well established and are discussed extensively by White (1979). Two dipstick cryostat probes are used in this work. One of the dipsticks is very similar in design to that used by B.J. Dalrymple and described in detail in his thesis [Dalrymple (1983)]. The other is based on a design by Umbach (1982b). Both dipsticks comprise a sample block made of Oxygen-Free-High-Conductivity (OFHC) copper. The tunnel junction is placed in good thermal contact with this sample block. To insure this good thermal contact, a Silicone heat sink compound* is occasionally used. The sample block also contains a calibrated resistance thermometer** and an electrical heater consisting of a 1 kΩ metal film resistor. A copper can surrounds the sample block and is placed in a bath of liquid Helium. A weak thermal link (a brass screw in one case and a thin copper wire in another) connects the sample block to the copper can and the space between them is evacuated. When the heater is turned off, the temperature of the sample block (and therefore the sample) eventually (within 1 hour) approaches the bath temperature. The small temperature difference is due to the heat flow from the room-temperature part of the dipstick. When the heater is turned on, the temperature of the sample is raised above the bath temperature by an amount proportional to the Joule power generated by the heater. The bath temperature is ~ 4.2 K when He is at atmospheric

*Type Z9, from GC ELECTRONICS, Rockford, IL.

**From Cryocal Inc., St. Paul, MN.

pressure, and can be reduced to ~ 1.3 K by pumping on the bath with two large mechanical pumps.

One of the important requirements in a cryostat is to provide good thermal contact to the bath. In one of the dipsticks used, this is easily achieved by having the copper can soldered using, low-temperature solder, to the portion of the dipstick just above the sample block. In the second dipstick, a different configuration is used to avoid use of solder, with the goal of facilitating loading and unloading of samples. The vacuum seal in this second dipstick is an O-ring seal at the room temperature end of the cryostat. Thermal contact is achieved by a "tight friction-fit" between the outside can and a portion of the inner dipstick made of copper, just above the sample block. A small amount of Silicone heat sink compound* is used to improve this thermal contact. Figs. 5-5 and 5-6 illustrate the configuration of the cryostats used.

V.B.2. Sample Mounting

The substrates carrying the junctions are placed in good thermal contact with the copper sample block as described above. Initially, electrical contact to the electrodes was made by use of Silver Paint to connect a thin copper wire extending from a fixed post on the sample block to the electrode. Sample mounting was later improved by use of spring contact pins called POGO* pins (model ASR) as shown in Fig. 5-7. This allowed the rapid testing of NbN films for T_c and resistivity measurements and expedited the measurements of junctions as well. The "no-solder"

*POGO is a registered trademark of the Pylon Co. Inc., 51 Newcomb St., Attleboro, MA.

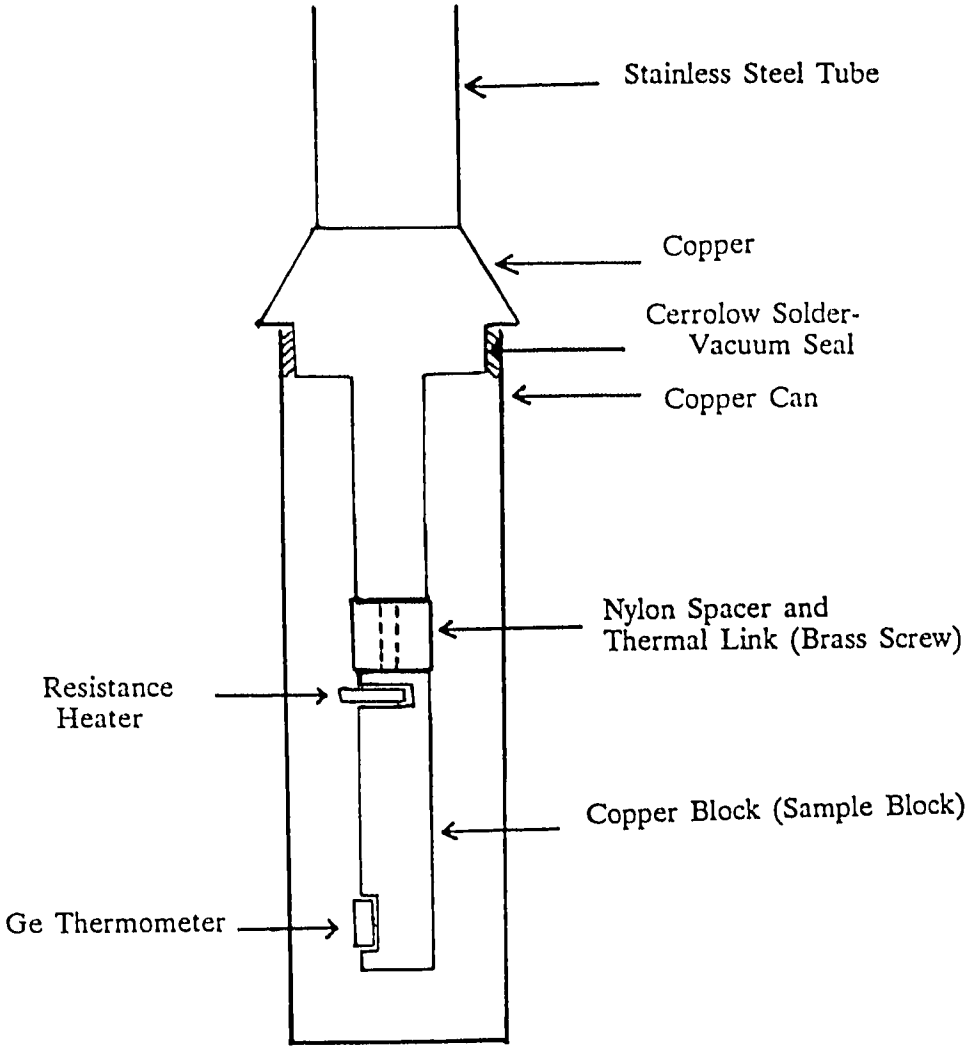

Fig. 5-5 Schematic of the low-temperature end of the "solder-on can" cryostat.

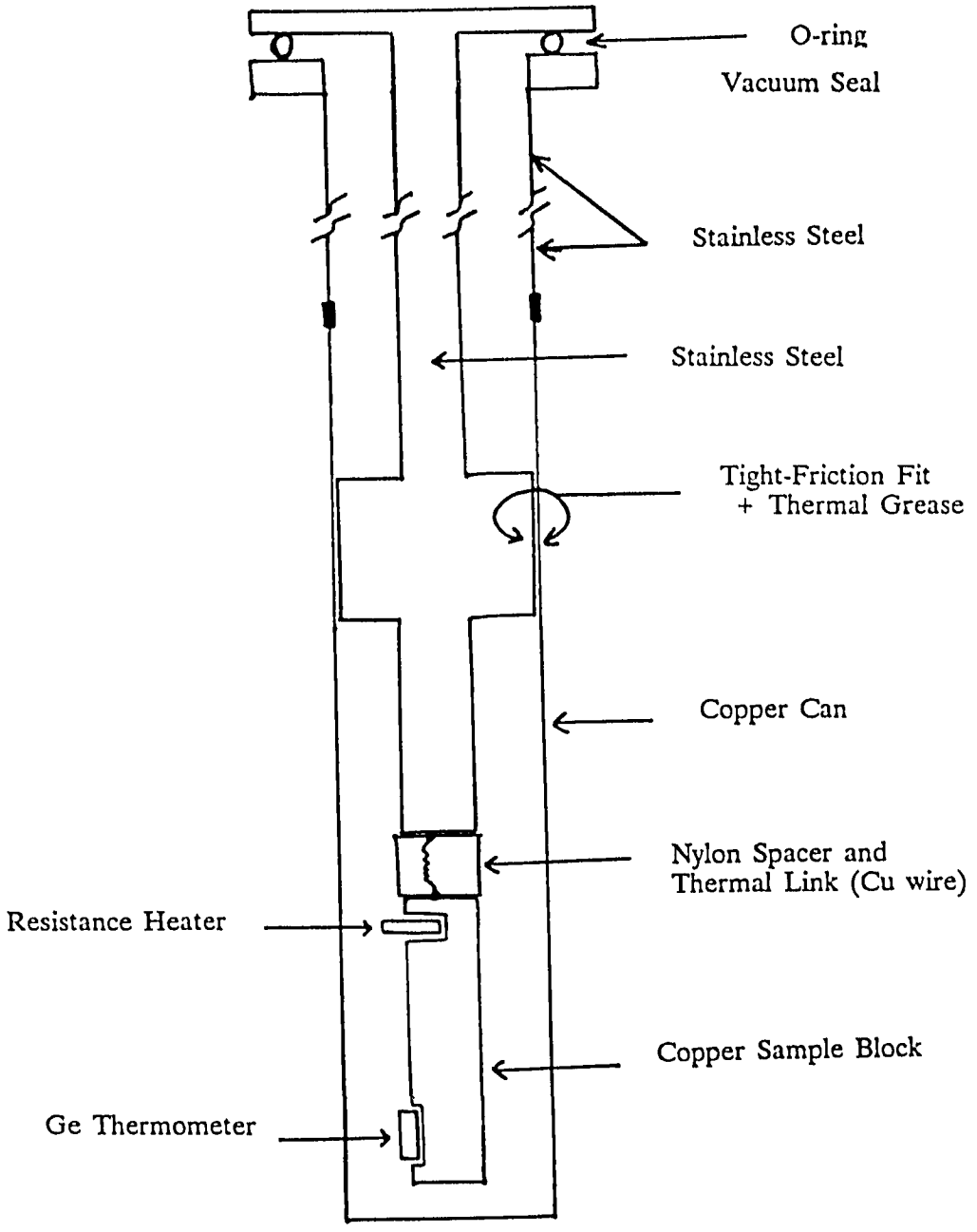

Fig. 5-6 Schematic of the "no-solder" cryostat. The vacuum seal is achieved by an O-ring connection at the room-temperature end of the dipstick.

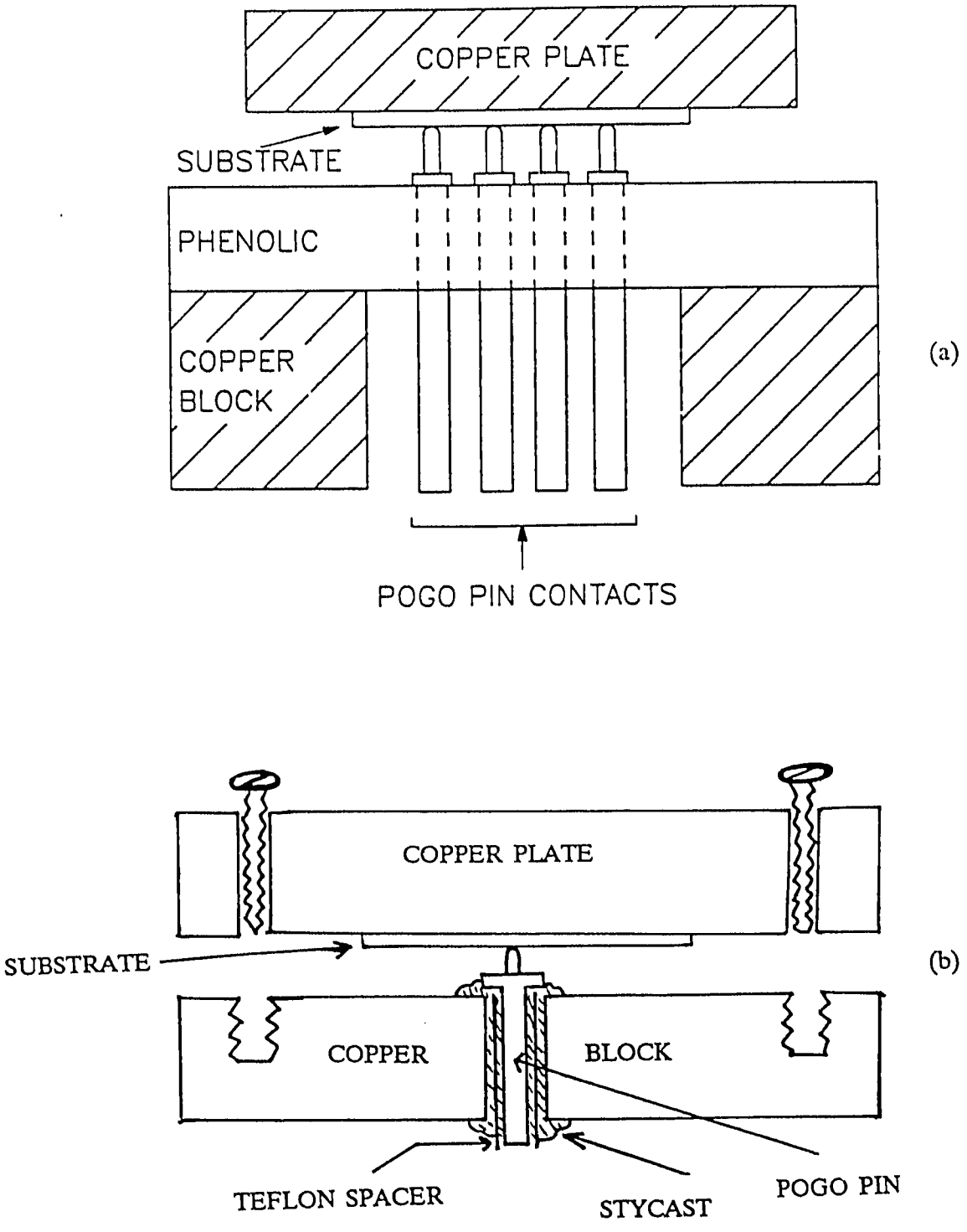

Fig. 5-7 Cross section of the POGO-pin spring loaded electrical contacts to the junction electrodes. Two alternative mounting techniques are used for the POGO pins in the two cryostats. In (b), the Stycast (2850 FT) is chosen to match the expansion coefficient of the copper block while the teflon sleeve insures electrical insulation of the POGO-pin.

cryostat had 32 pins allowing the simultaneous measurement of 4 film samples or 10 tunnel junctions. The other cryostat, used for measuring the small area Ta/PbBi tunnel junctions had sixteen pins allowing the simultaneous measurement of 4 junctions.

V.C. DC I-V Characteristics

This section presents an overview of the dc I-V characteristics of the various S-I-S junctions produced in this work. The voltage range considered is 0-5 mV. In this range the major structure in the I-V is the current increase at the sum-gap voltage. Chapter 2 discussed the "ideal" BCS I-V characteristic for different temperatures. As shown in Fig. 2-5, below the sum-gap voltage and at temperatures $0<T<T_c$, some current flows due to the thermally excited electrons. However, at low enough temperatures, $t < 0.3$ as is the case in the following data presented, this intrinsic subgap current is very small: it constitutes less than 1% of the current just above the sum-gap voltage. The excess "leakage" current observed in real junctions is then due to imperfections in the oxide or in the electrodes. The "quality" of the tunnel junction is determined in part by how low this leakage current is. Another quality factor is the width of the current rise at the sum-gap voltage. The smaller the width, the higher the junction quality. Again as shown in Fig. 2-5, ideally this width is negligible, even at $0<T<T_c$, due to the sharp singularity in the density of states in the superconductors. In real junctions however, several factors contribute to a finite width of this current rise. These factors include the anisotropy of the energy gap [Weber (1977)] coupled with the polycrystalline structure of the electrodes. In addition, the grain boundaries in the polycrystalline films can contain impurities which may locally reduce the energy gap through the proximity effect

discussed in chapter 6. This results in a distribution of energy gaps and therefore leads to an increased width of the current rise.

An important parameter for tunnel junctions is the current density. A tunnel junction has a capacitance determined by its area and the thickness and dielectric constant of the tunnel barrier. In some applications, such as SIS mixers, the capacitance must be kept to a minimum, which requires the use of very small area junctions. The dc resistance of the junction must still be however in a range adequate for impedance matching of the signal. As a result, higher current densities are required for the smaller area junctions (I_cR = constant; $J_c = I_c/A$). This introduces additional effects where the excess current causes local heating or drives the superconducting electrodes far from equilibrium by breaking Cooper pairs, making it harder to approach the ideal BCS I-V characteristics.

V.C.1. Large Area Junctions

The fabrication of these junctions has been described in chapter 4. Nb, Ta overlayers on Nb, and NbN are used as base electrodes. Junctions with an air-oxidized Nb base electrode typically gave poor quality I-V's. This is illustrated in Fig. 5-8a which shows a typical Nb/ Nb oxide/ PbBi junction. The excess subgap leakage current is probably related to the complex structure of the Nb oxide which has been studied extensively by Halbritter (1987). Occasionally, an improved I-V is obtained as shown in Fig. 5-8b, but the process is not reproducible. A dramatic improvement in the I-V quality is obtained by use of a thin Ta overlayer on Nb. In this case, the barrier is formed by air-oxidizing the Ta overlayer. Fig. 5-9 shows typical I-V curves for Nb/Ta junctions with different Ta thicknesses. The extremely

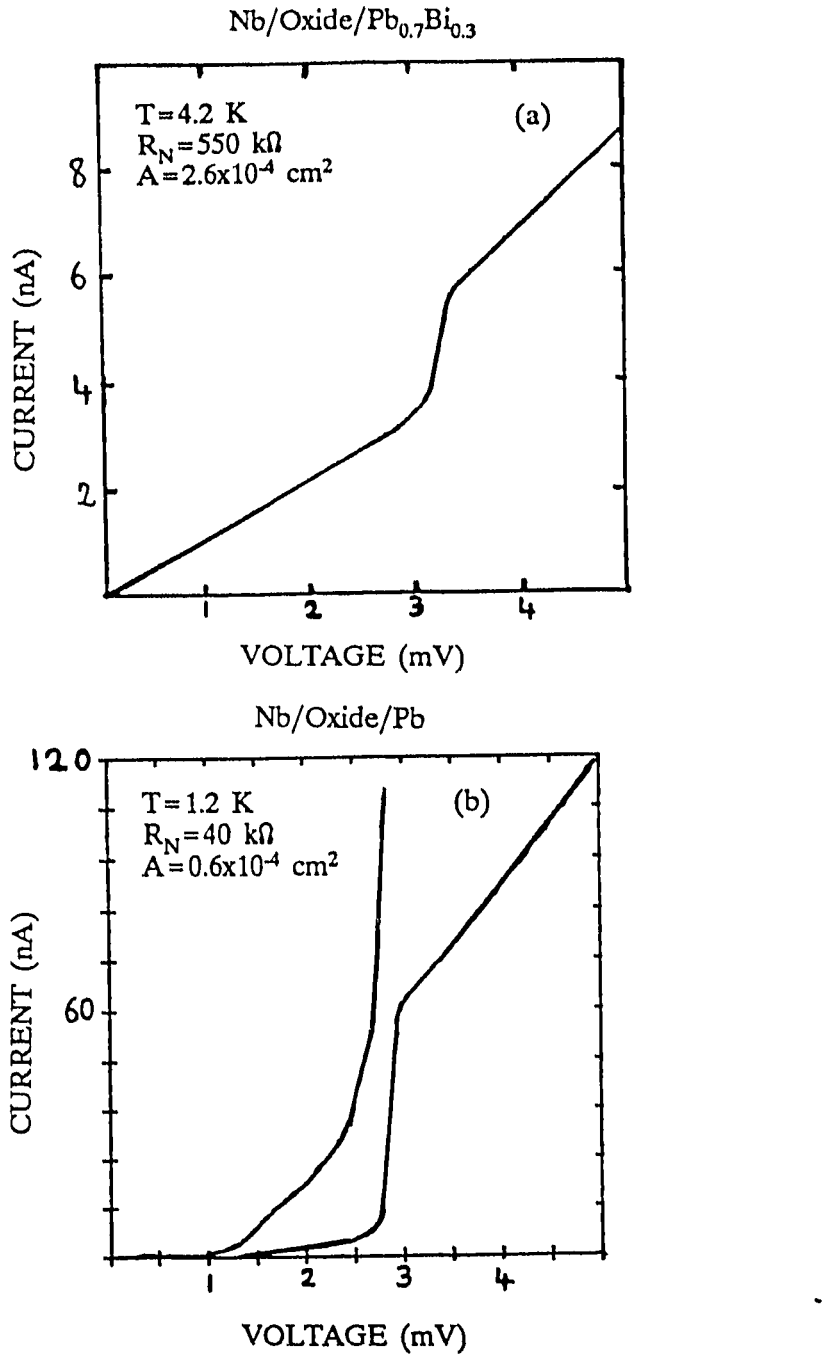

Fig. 5-8 I-V characteristics of large area Nb-based junctions. (a) Typical result with large subgap leakage current. (b) Best I-V achieved in this work with a Nb base electrode.

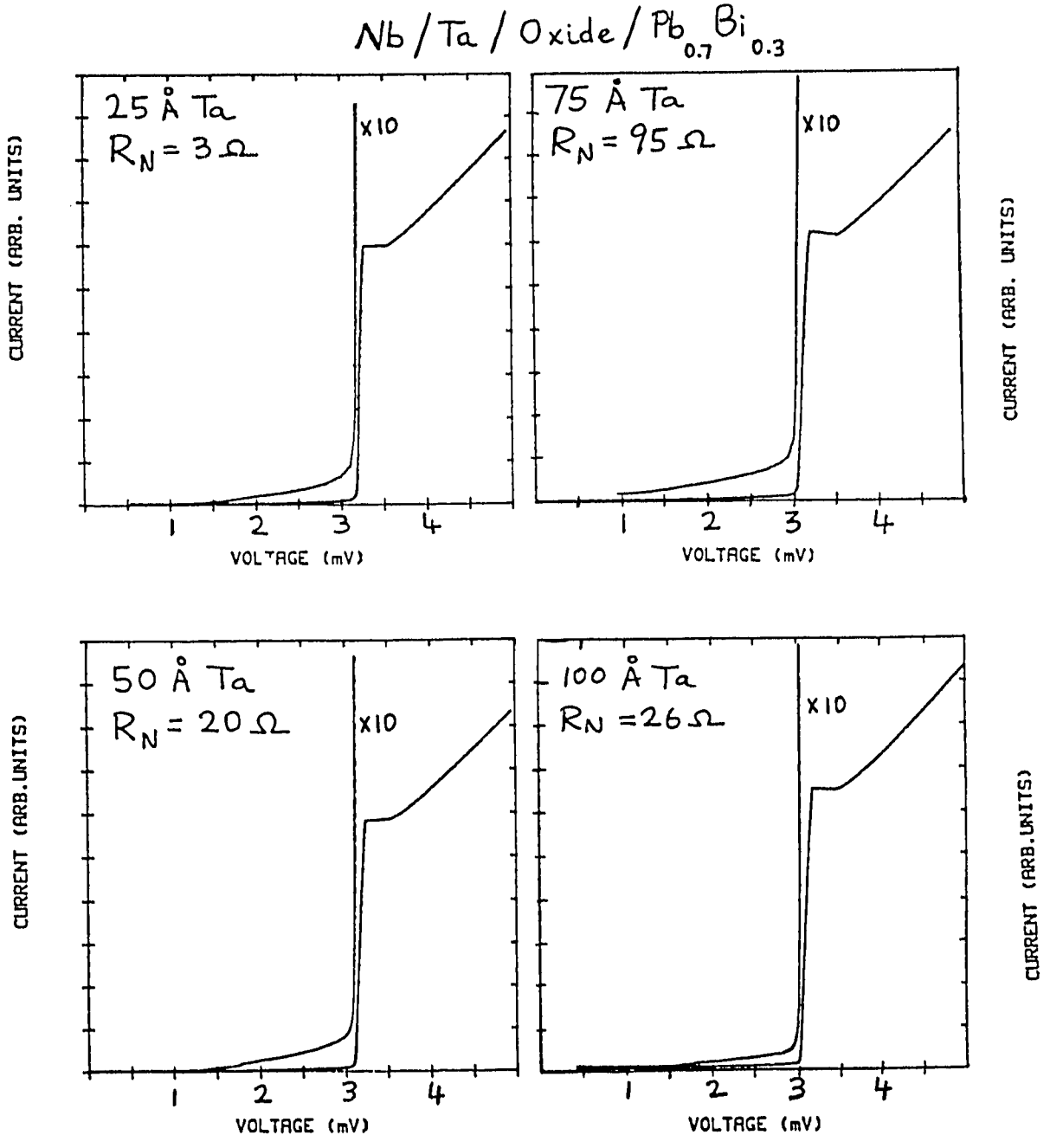

Fig. 5-9 I-V characteristics of Ta-overlayer-on-Nb junctions. Dramatic improvement in the I-V quality over Nb-based juntions is seen even for a 25-Å Ta layer. The structure above the current rise is not resolved here because a current-biasing scheme is used in these measurements. This structure is due to the proximity effect and will be resolved and discussed in detail in Chapter 6.

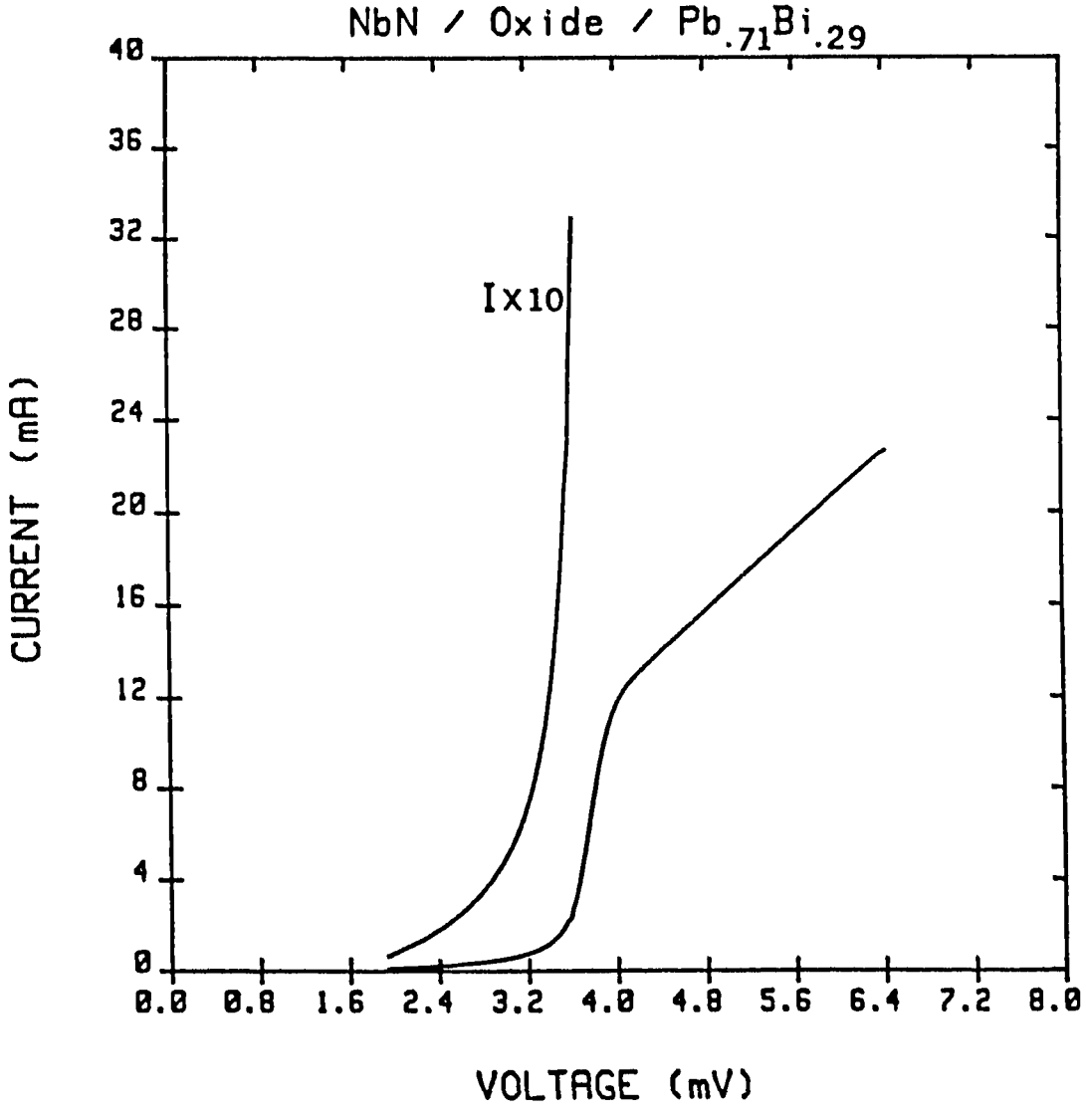

Fig. 5-10 Typical I-V characteristic for a large area NbN-based junction with a native NbN oxide barrier.

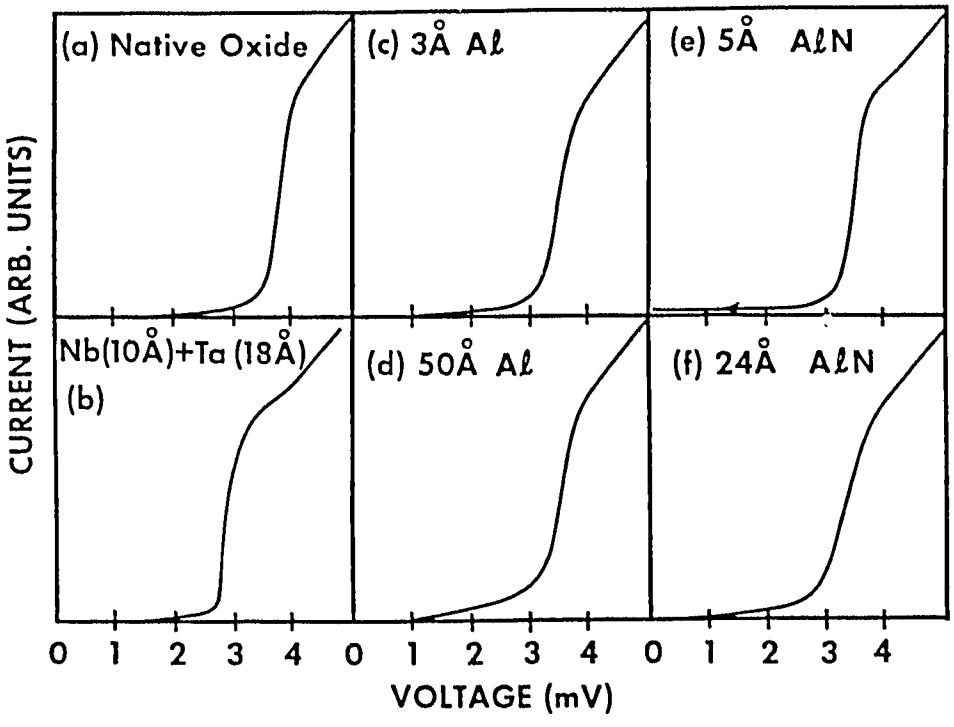

Fig. 5-11 I-V characteristics for large area NbN-based junctions with (a) native oxide barrier; (b),(c),(d) oxidized metal overlayers discussed in chapter 6; (e), (f) artificial barrier (AlN) directly deposited and discussed in chapter 7. (a) and (b) are at T = 1.4 K, (c)-(f) at T = 4.2 K. Counterelectrode is $Pb_{.7}Bi_{.3}$ in all cases.

low subgap leakage current and the sharp current rise at the sum-gap are due to the high quality tunnel barrier obtained with Ta oxide. Another notable difference between Nb and Ta is the rate of oxidation in air. Whereas a 15-20 minute oxidation of Ta gave a junction resistance in the 10-100 Ω range, the same oxidation time for Nb produced short-circuited junctions. It was therefore necessary to oxidize the Nb-based junctions for a much longer time - typically two days - to obtain a measurable junction resistance. Given the size of these large area junctions, 75 μm x 350 μm, such a resistance range corresponds to a (low) current density (at a bias of ~ 3mV) of 1 - 10 A/cm^2. The structure of the tunnel barriers will be discussed in chapter 7. The "knee" in the Ta overlayer junctions is due to the proximity effect which is treated in detail in chapter 6.

Junctions with NbN air-oxidized base electrodes are reproducible and of fair quality. Air oxidation for up to 4 hours consistently yielded junctions with a current density of 10-100 A/cm^2 and with I-V's similar to the typical NbN/NbN oxide/PbBi junction I-V shown in Fig. 5-10. The subgap conductance at 2 mV is 1.5% of the conductance above the sum-gap voltage. This low subgap leakage indicates a good quality oxide. It is likely that in NbN the presence of nitrogen helps minimize the number of defects that are found in Nb oxide [Halbritter (1985)]. The current rise at the sum-gap voltage extends over about 0.4 mV. Similar widths of the current-rise have been reported by other workers [references listed in Track et al. (1986)]. This width appears to be intrinsic to the NbN films, and not due to anisotropy effects, since it is also observed in tunneling data of single-crystal NbN films [Gavaler et al. (1985)]. In addition, unlike Nb, NbN-based junctions are not improved by use of oxidized metallic overlayers of Ta or Al [see Fig. 5-11]. The properties of such overlayer junctions are discussed in chapter 6. The same width of the

current-rise is observed in these overlayer junctions, furthering the contention that such width is related to the energy dependence of the gap-parameter in NbN.

V.C.2. Small Area Junctions

Small area junctions with NbN base electrodes and Pb or PbBi counterelectrodes were fabricated as described in chapter 4. We find that glow discharge oxidation, which works well for Ta-based junctions, does not yield reproducible results with NbN. This is possibly due to surface damage that the glow discharge may induce in NbN [Hikita et al. (1983)]. Given the short coherence length of NbN ($\xi \simeq 50$ Å), such damage is detrimental to the tunneling characteristics which directly reflect the density of states within a coherence length from the tunnel barrier. In-situ thermal oxidation by exposing the ion-beam cleaned NbN film to high purity oxygen works best. Typical results are shown in Fig 5-12. At higher current densities, $j \geq 10^4$ A/cm^2 we observe a depression of the gap and a negative resistance region (Fig. 5-12d) which are due to a combination of heating effects and quasiparticle injection, as discussed above.

Small area junctions with Ta base electrodes displayed outstanding I-V characteristics as shown in Fig. 5-13. Glow discharge oxidation was found to produce a high quality tunnel barrier in our window geometry as it did in the step geometry developed by Face (1987). The current densities obtained range from 10^2 to 10^5 A/cm^2 [see Fig. 5-14]. Single junctions as well as six-junction series arrays were produced. In SIS mixer applications, the arrays should provide improved dynamic range due to their increased saturation power limit [Tucker and Feldman (1985)]. The I-V characteristics of the junction arrays reflect the uniformity of the

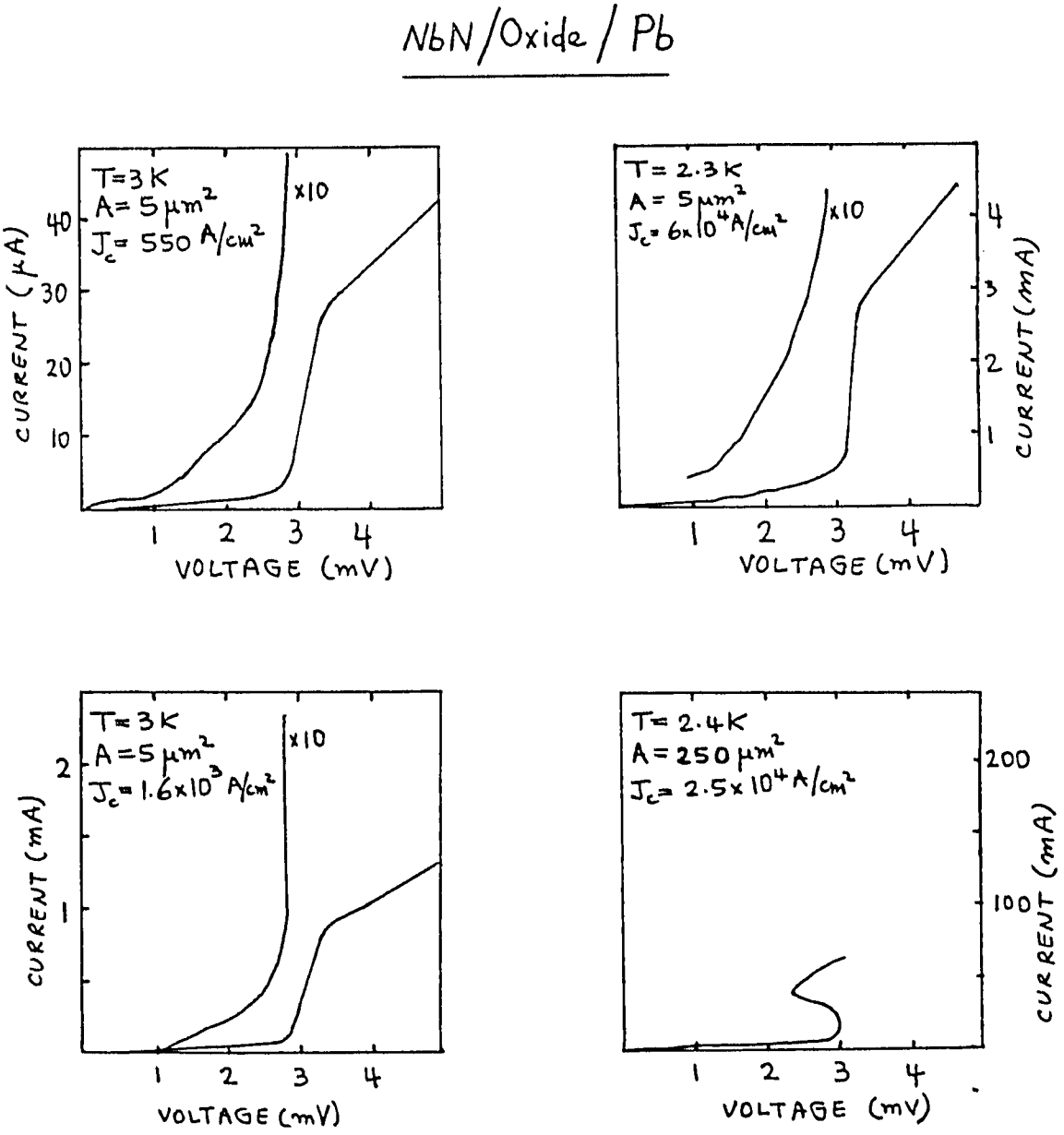

Fig. 5-12 Small area, high current-density NbN-based junctions. In (d) the excess current causes heating which depresses the energy gap and results in a negative resistance region.

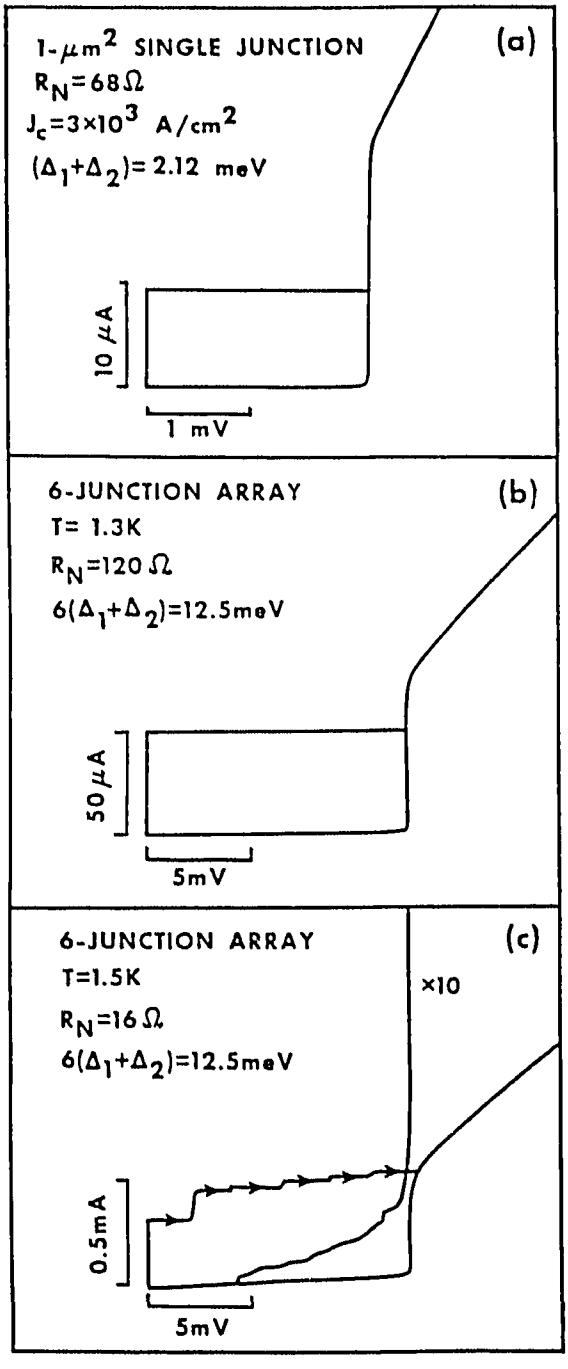

Fig. 5-13 Small area, high current-density Ta-based junction with (a) nearly ideal I-V characteristics. (b) I-V characteristic of a six-junction series array with current density 2×10^3 A/cm^2. (c) Non-ideal I-V for a six-junction array with current density ~ 1×10^4 A/cm^2 showing non-uniformity of the critical current and increased leakage current. The area of each junction in the arrays is 6 μm^2.

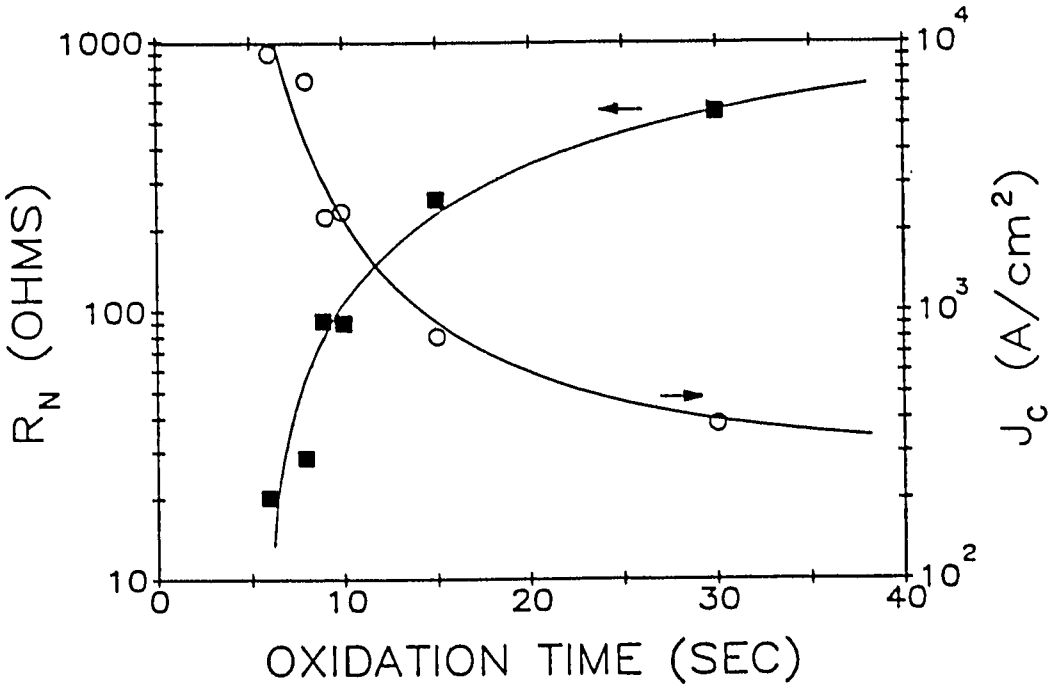

Fig. 5-14 Normal state resistance R_N current density (at 13 mV) as a function of glow discharge oxidation times for the six-junction Ta/Ta Oxide/PbBi arrays.

tunnel barrier as shown in Fig. 5-13. When the current density approached about 10^4 A/cm^2, heating effects due to large amounts of quasiparticle injection are observed in the I-V curve. The larger current density junctions also had increased sub-gap leakage currents. The appearance of increased leakage current at high current densities approaching 10^4 A/cm^2 is consistent with the general trends observed by Raider (1985) for many different junction technologies. By reducing the junction area to 0.2 μm^2, we find it possible to produce single junctions with current densities ~ 10^5 A/cm^2 which do not display heating effects. The I-V for such a junction is shown in chapter 8, Fig. 8-5b. This and similar observations in NbN-based junctions indicate that Joule heating (proportional to the square of the total current through the junction) is an important factor in gap-depression in the small area junctions and can be minimized by reducing the junction area.

Another important quality factor for tunnel junctions is their stability against exposure to air and cycling to cryogenic temperatures. All the NbN- and Ta-based junctions with PbBi counterelectrodes survived repeated thermal cycling from room temperature to below 4.2 K without failure or degradation of their I-V characteristics. Upon exposure to air, however, the resistance of the junctions with PbBi counterelectrodes increases. This increase in resistance ("aging") is typically 10 % for every hour of exposure to air and is cumulative. It could be due to oxygen diffusing through the PbBi counterelectrode, reaching the junction area, and further oxidizing the base electrode [Raider (1986)]. A passivation layer (such as SiO) could be used to prevent such "aging" effects. Alternatively, and following a suggestion by Raider (1986), we have succeeded in avoiding this aging problem by coating the PbBi counterelectrode with a thin (~ 150 Å) layer of indium. We find that the resistance and I-V quality of such In-coated junctions are unaffected by air exposure. With the

In coating, the change in resistance of the junctions is less than 5% after several days of exposure to air. This improvement is probably due to a passivating In_2O_3 layer forming on the surface of the counterelectrode and preventing oxygen diffusion. Similar improvement can be obtained by use of a PbAuIn alloy counterelectrode as was done by workers at IBM. In that case, however, the inclusion of the low T_c phase $AuPb_3$ at the junction interface can broaden the width of the current rise at the sum-gap and increase the subgap leakage current [Lahiri et al. (1980)]. Our method of coating the PbBi counterelectrode with In preserves the high quality of the junction while solving the "aging" problem.

VI. PROXIMITY EFFECT TUNNELING

VI.A. Introduction: The Proximity Effect

If a normal metal, N, is placed in intimate contact with a superconductor, S, Cooper pairs can leak from S into N, and quasiparticles can leak from N into S. This results in a reduction of the pair density in the superconductor and the appearance in the normal metal of a pair density. This phenomenon is known as the "proximity effect". Thermal excitations tend to break the pairs and result in a lifetime, τ, of the Cooper pairs in the N-metal given by the uncertainty relation

$$\tau = \hbar/2\pi k_B T \tag{6.1}$$

τ is of the order of 10^{-12} seconds at $T \simeq 1$ K. The spatial extent of the induced pair potential variations on the S-side and N-side is illustrated in Fig. 6-1 and can be as large as 1000 Å in N. The decay length for these variations depends on the superconducting coherence length, ξ_S, on the S-side. On the N-side, the decay length, ξ_N, of the induced pair potential is equal to

$$\xi_N = \hbar v_{FN}/2\pi k_B T \tag{6.2}$$

in the clean limit when the mean free path, ℓ_N, of the N-metal is larger than ξ_N. Here v_{FN} is the Fermi velocity in N. In the dirty limit, the decay length is governed by diffusion processes and is given by

$$\xi_N = (\hbar D_N/2\pi k_B T)^{1/2} \tag{6.3}$$

with the diffusivity D_N given as

$$D_N = (v_{FN}\ell_N)/3 \tag{6.4}$$

The N-metal could be a superconductor itself, with a smaller transition temperature, T_{cN}, than the S-metal. In this case, the difference $(T - T_{cN})$ enters the denominator of (6.2) and (6.3).

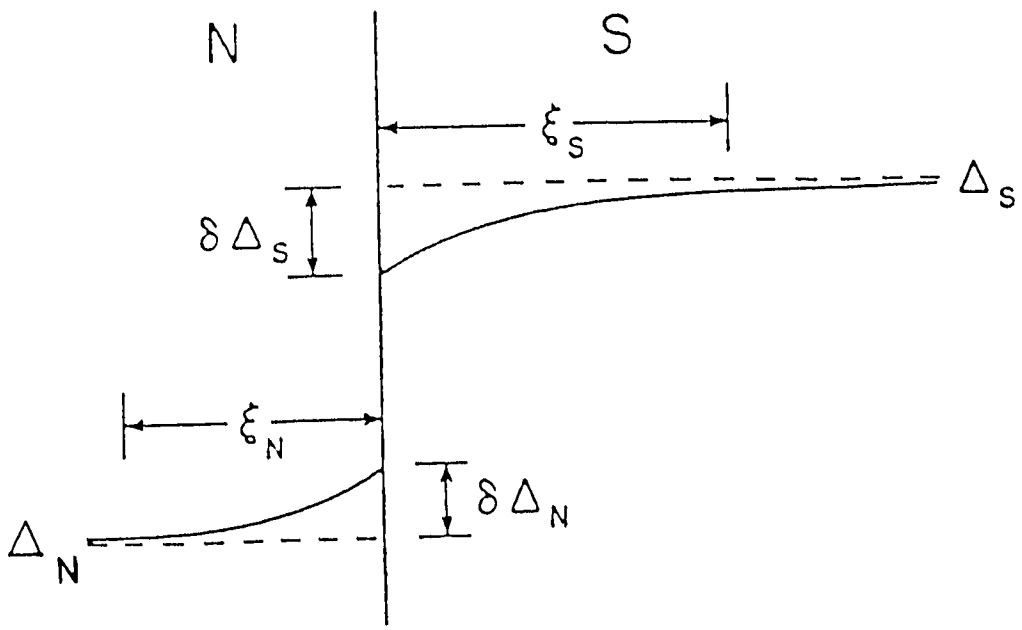

Fig. 6-1 Induced pair-potential (Δ) variations in an NS proximity bilayer. N is either a normal metal or a weaker superconductor than S. There is depression of Δ_S at the NS interface and enhancement of Δ_N (or the appearance of an induced Δ_N - if N is a normal metal).

Historically, studies of the proximity effect had a relatively slow start and were purely experimental. The first experiments indicating the existence of a proximity effect were reported by Holm and W. Meissner (1932), who observed zero resistance between pressed contacts in an SNS sequence of metals. In the mid-1930's, Misener et al. (1935) observed the disappearance of superconductivity in lead and tin films deposited on top of normal-metal wires when the films were thinner than certain "critical" thicknesses ($\sim 10^4$ Å). This effect was thought to be characteristic of the thin film superconductors and not to be related to the substrate metal. Later experiments by Shal'nikov (1938), done with thin films deposited on insulating substrates, showed that tin remained superconducting down to a thickness of about 50 Å. The earlier experiments of Misener et al. were then thought to be in error [Feigin (1957), Shoenberg (1952)]. Only in the late 1950's was the proximity effect finally observed and identified as such. In a series of experiments, H. Meissner et al. (1958, 1959, 1960) showed that two superconducting wires when coated with thin ($\leq 10^4$ Å) normal metal coatings would carry a supercurrent between them when they were placed in contact. Moreover he demonstrated that when a superconducting coating is deposited on a normal metal, the coating would not be superconducting unless it were above a certain thickness, corroborating the earlier experiments of Misener et al. (1935). A few years later, a definitive fingerprint of the superconductivity induced in a normal metal via the proximity effect was given by tunneling experiments [Smith et al. (1961)] which demonstrated the existence of an energy gap in the normal side of a SN metal sandwich structure.

The progress in the study and understanding of the proximity effect is summarized in a series of reviews: Deutscher and de Gennes (1969) summarize the developments up to 1969, Gilabert (1977) extends the review to 1977, and Wolf (1985)

to 1985. Quantitative probing of the proximity effect relies on measurements of transport and thermodynamic properties of NS structures. Studies of the transition temperature, T_{cNS} , of an NS layer as a function of the thickness of the N layer [e.g. Hauser et al. (1964)] yield information on the spatial extent of the effect. Information on the excitation spectrum in NS layers may be obtained from the measurements of various dissipative properties : tunneling measurements probe the excitations perpendicular to the interface, thermal conductivity is sensitive to excitations parallel to the interface, and specific heat is affected by excitations in all directions. The behavior in a magnetic field of NS layers is important to the understanding of depairing processes and of flux pinning in superconductors by providing model systems where the distribution of pinning centers and the pair density can be controlled. Finally, a complete understanding of the Josephson effect in SNS structures requires an accounting of the proximity effect at the two NS interfaces.

The theoretical techniques which have been developed to analyze the proximity effect differ according to which of the above features is under study. A review of the different approaches is presented by Gilabert (1977). The basic physics is governed by the Schrodinger equation and the requirement that the wave function be continuous at the interface even though the effective electron-electron interaction induced by phonons is discontinuous (on the scale of a few Å). A continuous macroscopic wave function means that the superconductivity must extend through the interface. Furthermore, the distances over which significant spatial variations of the order parameter can occur is on the order of the coherence length. The proximity effect is thus the natural result of the quantum mechanics of a macroscopic wave function which can only show spatial variations on the scale of the superconducting

coherence length.

VI.B. Tunneling into Proximity-Effect Systems

Tunneling into a proximity structure NS provides information about the excitation spectrum, or density of states in the NS bilayer. Because of the induced superconductivity in the N layer, this technique allows probing of the phonon spectrum in the N-metal: Chaikin et al. (1975,1976) have determined in this fashion the phonon density of states in Ag, Al, Cu... when backed by a thick lead film. Their results are in good agreement with phonon spectra obtained by neutron scattering. At present, the theory of tunneling into proximity systems can be described in quantitative detail by microscopic theory and is reviewed by Wolf (1985). Gallagher (1981) further developed the theory to allow the calculation of the Josephson current in tunnel junctions where one or both electrodes are proximity-effect bilayers. He showed that the Josephson current can then be calculated with the same theory that is used to interpret quasiparticle tunneling characteristics in quantitative detail. A major conclusion of his work is that "the Josephson current is much more rapidly attenuated by thin normal layers adjacent to the tunnel barrier than is the gap in the quasiparticle current" [Gallagher (1981)]. An experimental verification for this conclusion and a clear demonstration of quantitative agreement between theory and experiment was warranted. We set out to accomplish that task and successfully did so using as proximity system Ta overlayers on Nb. The next section of this chapter will describe the set of experiments and their analysis corroborating the Gallagher predictions.

VI.C. Ta Overlayers on Nb

VI.C.1. Experimental Considerations

One of the major requirements for a good proximity effect system is to have as close to an ideal interface as possible. The electrical contact between N and S must be very good, implying a rapid sequence of deposition of the two layers to avoid the formation of thin layers of insulating impurities. The atoms of N must not migrate to S and vice versa, implying the choice of N and S metals which are not miscible and do not form intermetallic compounds. Ion-beam sputter-deposited Nb and Ta appear to satisfy all the above requirements. In addition to having an almost perfect lattice match, our ability to sequentially deposit layers of Nb and Ta with virtually no time delay and in vacuum ensures a very clean and sharp interface. Thin layers of Ta in the range 10-100 Å were deposited on thick (3000 Å) layers of Nb, in situ, and oxidized. This was accomplished by first placing the Nb target beneath the ion beam to deposit Nb on all substrates simultaneously. Next, the Ta target was placed in the beam within 1 second. During this short time, and given the 10^{-7} Torr background gas pressure, less than ~ $1/30^{th}$ of a monolayer of vacuum background gases impinge upon the Nb surface insuring a clean Nb/Ta interface. Ta was then deposited on all substrates for a desired interval. A series of Ta surface thicknesses was obtained by sequentially shuttering substrates from the Ta source. In this way a series of samples, each with an identical Nb/Ta interface, was produced. The junctions (of area 75 μm x 350 μm) were completed with Ag, Pb, and Pb-Bi counterelectrodes. Details of junction fabrication have been given in chapter 4. The characteristics of these junctions were studied as a function the Ta-layer thickness. These include the critical current, bound-state energy, phonon structure

which will be discussed below, and oxide barrier shape which will be discussed in chapter 7.

VI.C.2. I-V curves

Initial measurements of the composite-base-electrode junctions typically showed them either to be of high quality (low leakage, sharp gap structure) or to have obvious defects (low-resistance shorts, etc.). Although the detailed mechanisms influencing the junction "mortality" rate are not fully understood, a contributing factor may likely be the characteristics of the air to which the films are exposed (temperature, humidity, etc.) and improved results appeared to be achievable by an initial exposure of the films to pure oxygen. A complete understanding of this behavior may await studies where fabrication takes place entirely in situ (i.e. without breaking vacuum).

Shown in Fig. 6-2 is an I-V curve which typifies the results for good junctions with Pb-Bi counterelectrodes. As discussed in chapter 5, the application of thin overlayers of Ta, as with Al, can dramatically improve the I-V characteristics of Nb-based junctions. Unless the Ta surface layer is thinner than ~ 10 - 20 Å, junctions show sharp gap structure and very low relative conductance at zero bias, typically from 10^{-4} to 10^{-3} of the normal-state conductance. The curves tend to show a small onset of conduction at $eV = \Delta_{PbBi}$ (1.74 meV at 1.4 K), usually attributed to tunneling from the PB-Bi electrode into normal material in the base electrode. Also shown in Fig. 6-2 is the calculated I-V characteristic for this junction. This I-V was obtained in the standard way by integration over the normalized zero-temperature densities of state for the base and counterelectrode via the formula

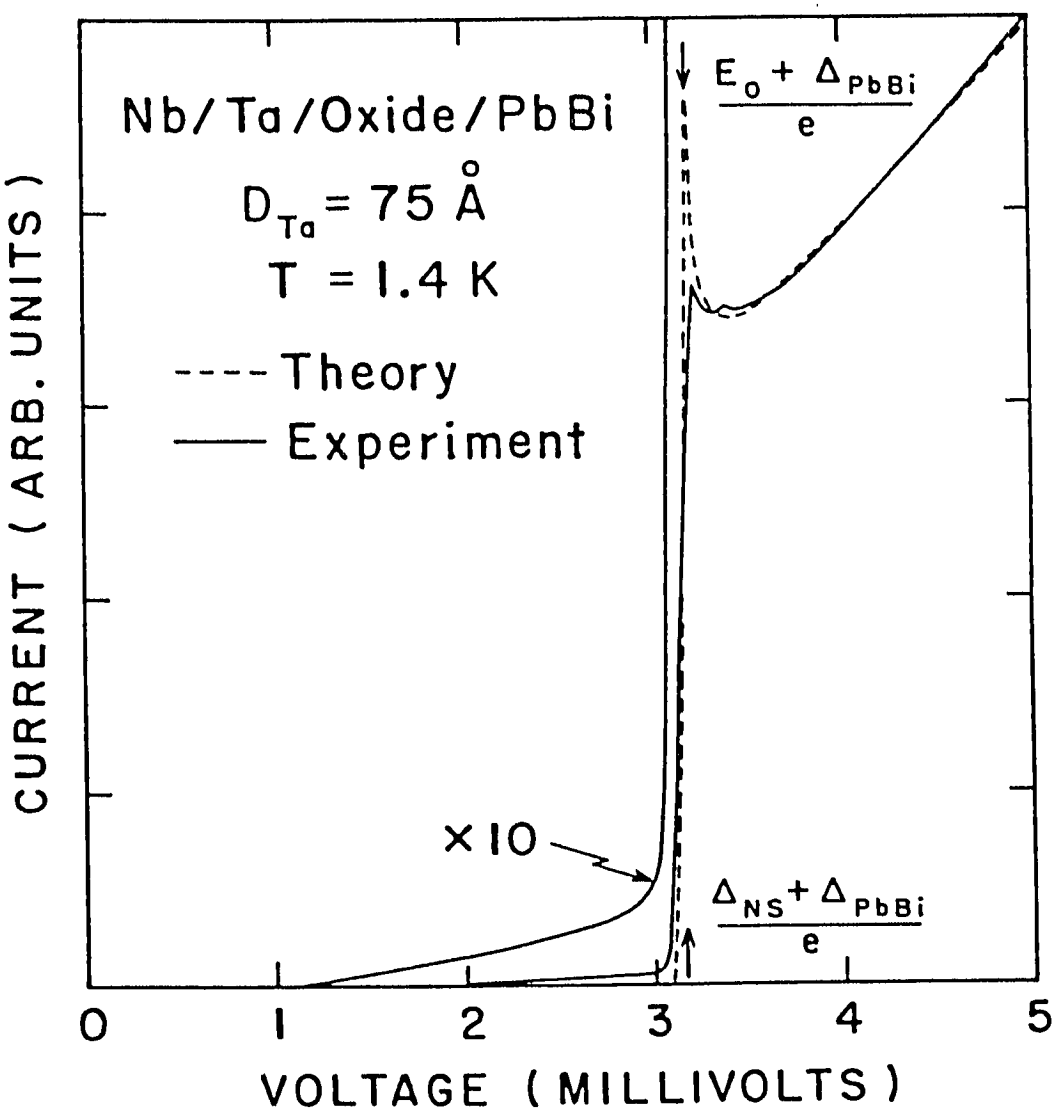

Fig. 6-2 Current-voltage (I-V) characteristic of a tunnel junction with a base electrode comprising of a 75-Å Ta overlayer on 3000 Å of Nb. Both the theoretical (dashed line) and experimental (solid line) curves show a sharp peak due to the presence of a quasiparticle bound state in the Ta overlayer. The peak occurs at a voltage $(E_0+\Delta_{PbBi})/e$.

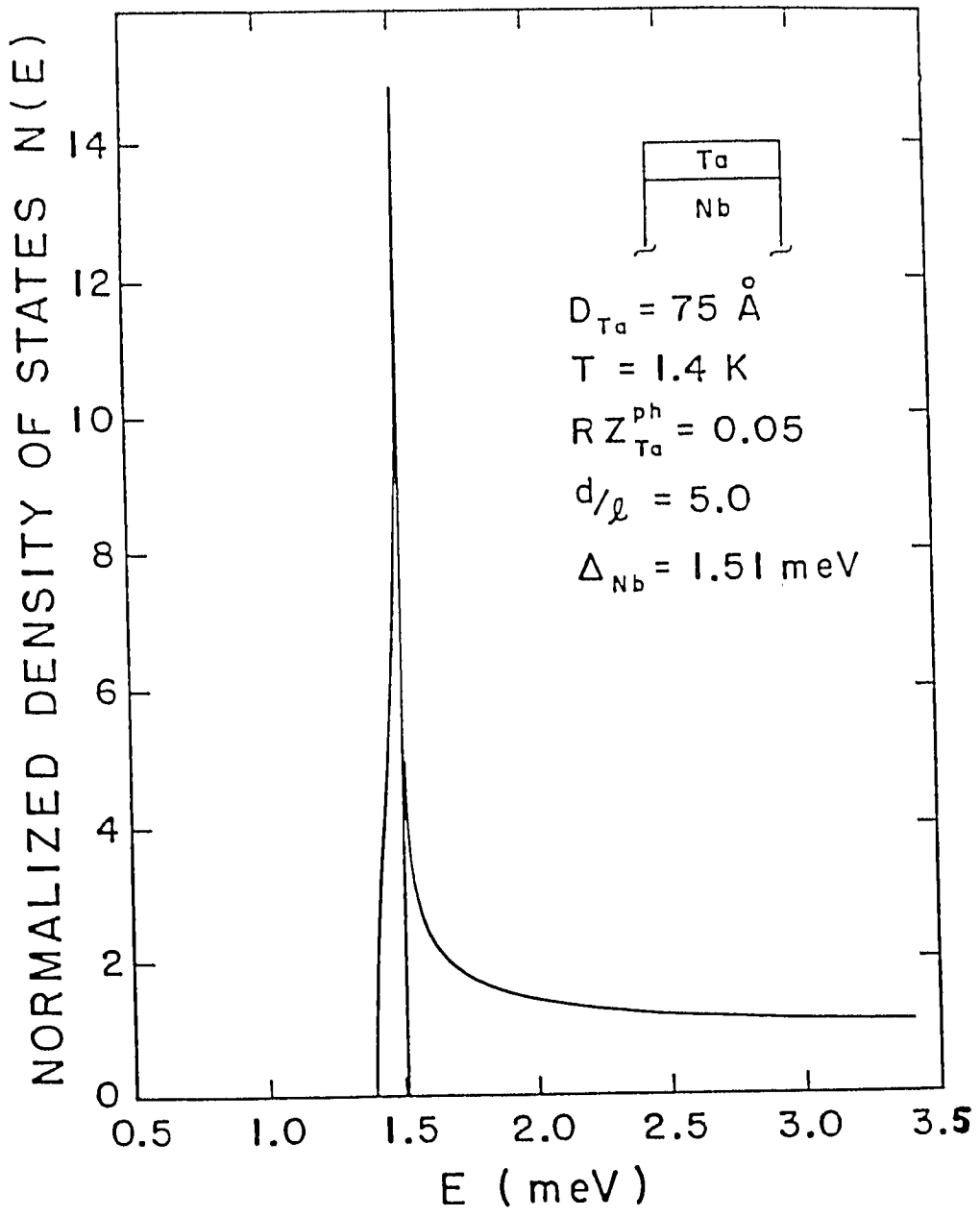

Fig. 6-3 Proximity density of states of the Ta surface-layer system which was employed to generate the theoretical curve shown in Fig. 6-2. The first sharp peak represents the quasiparticle bound state in the Ta overlayer occuring at an energy E_0. The dip and rise of N(E) in the vicinity of 1.5 mV is due to a very narrow gap in the density of states between this bound state and the residual BCS peak of the Nb underlayer.

$$I(V) = \int_{-\infty}^{\infty} dE\ N_{Nb/Ta}(E)N_{Pb\text{-}Bi}(E)[f(E) - f(E+eV)] \qquad (6.5)$$

where $f(E) = [1 + \exp(E/k_BT)]^{-1}$ is the Fermi function evaluated at the temperature of the experiment. $N_{Pb\text{-}Bi}(E)$ is taken to be a BCS density of states with $\Delta_{Pb\text{-}Bi}$=1.74 meV. $N_{Nb/Ta}(E)$, shown in Fig. 6-3, is calculated from the proximity-effect theory of Wolf and Arnold, as discussed below.

VI.C.3. The Model

The basic physical concepts underlying the Arnold and Wolf theory is illustrated in Fig. 6-4a and 6-4b. The pair potential variation can be approximated as the step-variation shown in 6-4b. Consider an electron in the N region propagating toward d_N at an energy $E<\Delta_S$. At the NS interface, $x=d_N$, this particle must be reflected, for it lacks the energy Δ_S needed to create a propagating quasiparticle excitation in S. The actual process, first described by Andreev (1964), is one in which the electron joins a second electron at -E in N to form a pair in S, leaving a hole in N which propagates back toward the N-insulator interface. The result of this process for the electron in N, as first shown by de Gennes and Saint-James (1963), is to form one or more coupled electron-hole bound states, whose energies must lie below Δ_S. The origin of bound state(s) in the double layer spectrum is a consequence of quantization in an "energy well" of depth Δ_S-Δ_N. A straightforward calculation (solving for the wavefunction in the potential well with Δ_N = 0) by de Gennes and Saint-James (1963) finds the bound state energy E_0 to be given by

$$E_0 = \Delta_S[1 - (d_N\Delta_S/2\hbar v_F)^2] \qquad (6.6)$$

A more complete analysis by Arnold (1978,1981) including strong coupling effects and scattering in the N layer shows that E_0 is given approximately by

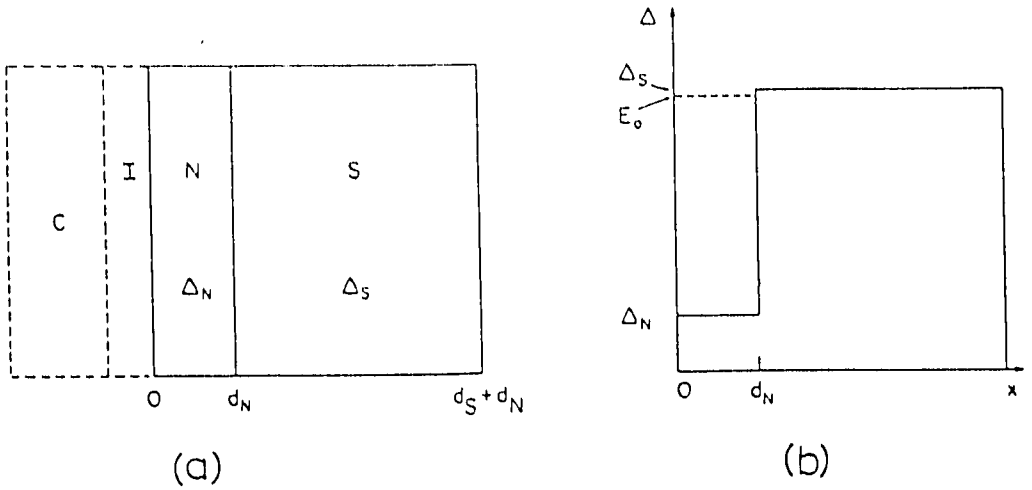

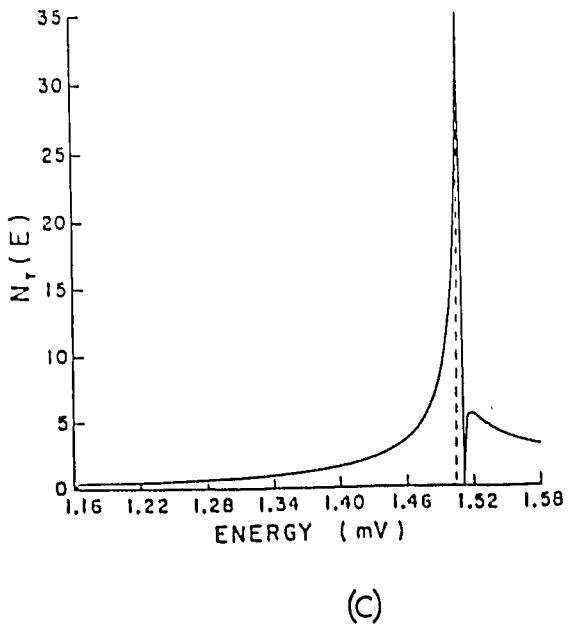

Fig. 6-4 (a) Schematic of the proximity effect tunneling geometry (C = Counterlectrode, I = Insulator = Tunneling Barrier).
(b) Pair potential, approximated by a step-variation representing a potential well with one bound-state, E_0, energy level.
(c) Corresponding tunneling density of states $N_T(E)$ showing a singularity at E_0, a peak at Δ_S, and a gap in-between. From Wolf (1985).

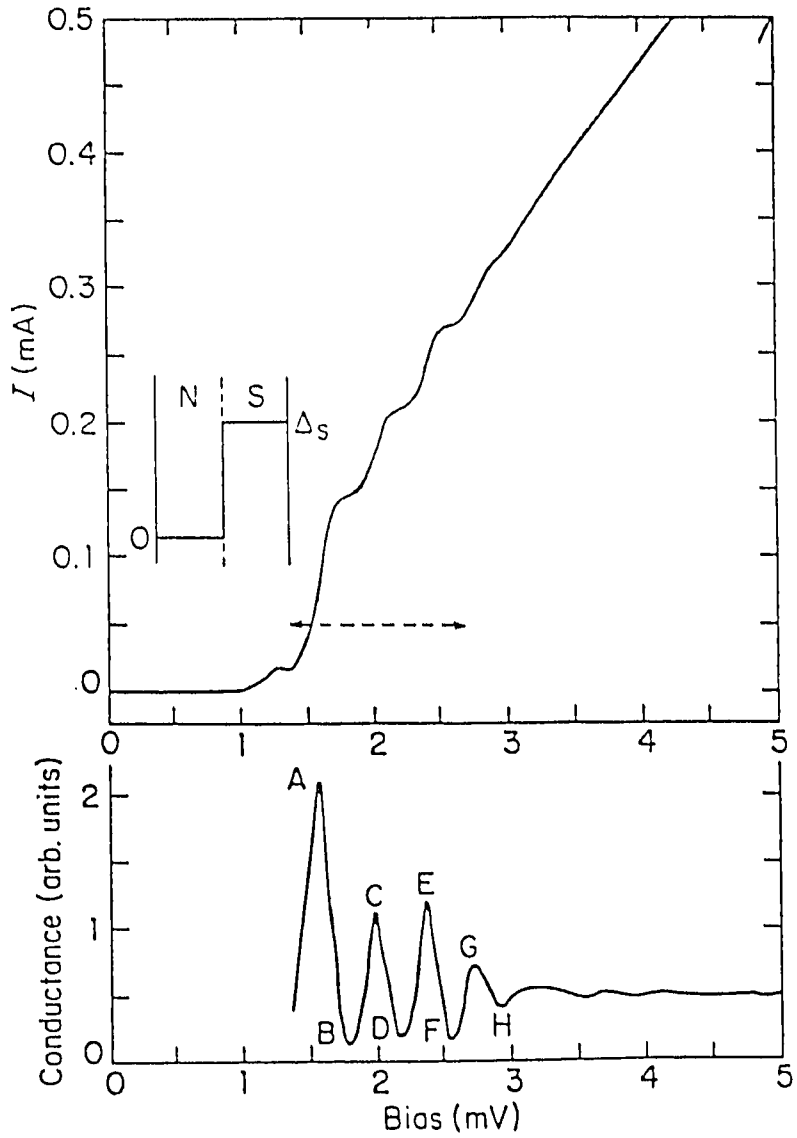

Fig. 6-5 Observation of bound-state structure in I-V (upper trace) and conductance (lower trace) of a Pb-insulator_ZnPb junction with Zn thickness of 3.5 μm, measured at 0.4 K. The dashed arrow in the upper figure indicate the range in which the energy E of the quasiparticle injected into the zinc lies in the range $0 \leq E \leq \Delta_{Pb}$. From Rowell (1973). The limit of thin overlayer has been more difficult to achieve and test experimentally and is successfully observed and modelled in the present thesis.

$$E_0 = \Delta_S[1 - {}^1/_2(RZ\Delta_S)^2] \tag{6.7}$$

where

$$R = \frac{2Zd_N(1+r)}{\hbar v_F(1-r)} \tag{6.8}$$

and

$$r = \left| \frac{v_F(S) - v_F(N)}{v_F(S) + v_F(N)} \right| \tag{6.9}$$

Z is approximately equal to $1 + \lambda$ where λ is the electron phonon coupling constant discussed in chapter 2 and is in the range $0 < \lambda < 1$. r is a measure of the reflection off the small potential step due to the difference in Fermi velocities between N and S. The number of bound states is given by [Wolf and Arnold (1982)] $1 + d/\pi\xi_{prox}$ where $\xi_{prox} = \hbar v_{FN}/2Zd_N$. The first observation of these bound states was by Rowell (1973) in thick Zn films (d_N = 3.5 μm) backed by Pb and observed with a Pb counterelectrode (Fig. 6-5). For $d_N < \xi_{prox}$, there is only one bound state. Arnold also calculates the tunneling density of states for this system (Fig. 6-4c) with strong coupling effects and including scattering in the N layer. It is this density of states that is shown in Fig. 6-3 and used to provide the fit to the I-V curve of Fig. 6-2.

VI.C.4. Discussion

In general, theory and experiment are in excellent accord. In the vicinity of the current rise we see the sharp peak and negative-resistance region associated with the bound state in the Ta surface layer. The experimentally observed attenuation of this peak appears to be due to noise smearing, perhaps in conjunction with dissipative effects due to scattering at the Nb/Ta interface. Also absent from the theory is the second peak seen in the experimental I-V characteristic just following

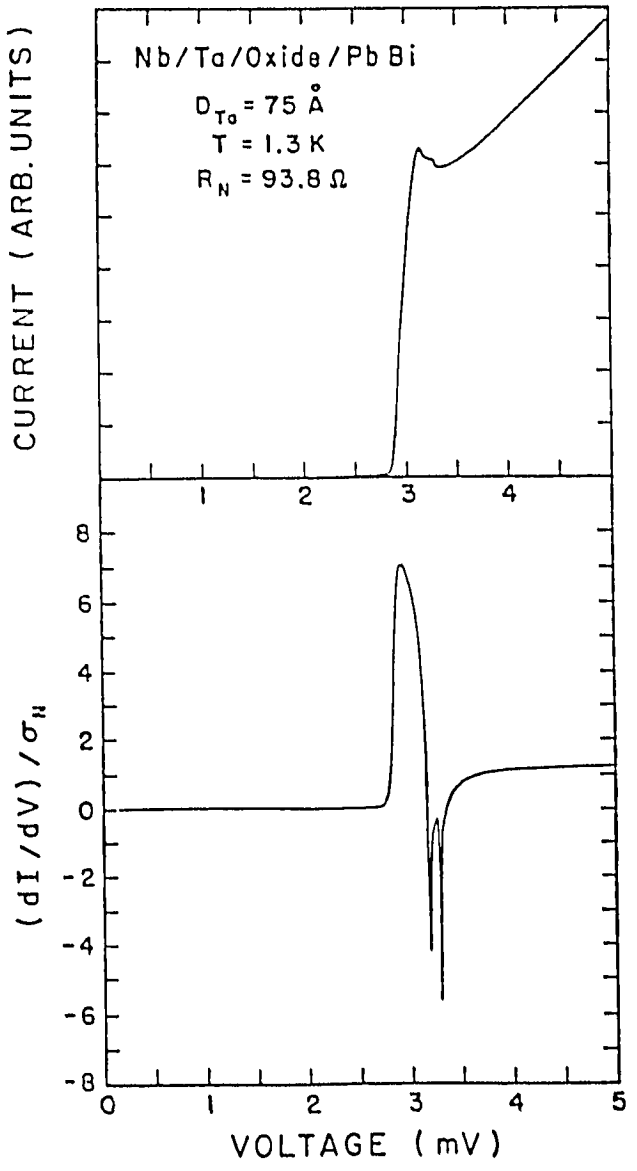

Fig. 6-6 Conductance data of Ta overlayer system revealing both the bound state in the Ta layer and density of states from the Nb underlayer.

the bound-state peak. Shown in Fig. 6-6 are the conductance characteristics of another junction with a 75 Å Ta surface layer. Similar features are seen as in Fig.6-2 with a sharp current rise due to the bound state in the Ta layer. This is followed by a region of negative resistance and by a second peak in the conductance. In both cases, and others measured, the second peak occurs exactly at the voltage V = $(\Delta_{Nb} + \Delta_{PbBi})/e$ = 3.3 mV. Physically, the peak appears to be a consequence of the singularity in the density of states of Nb at the energy gap. However, according to theory, and as shown in Fig. 6-3, the energy difference between the bound-state density of states and the peak of the residual Nb BCS density of states is exceedingly small on the energy scales in question and could not, here, give rise to the observed second peak. In Fig. 6-3, the value for Δ_{Nb} used is 1.51 mV instead of the bulk value of 1.56 mV. This difference is due to the fact that in the theory, the pair potential in S (Nb) is slightly depressed at the interface with N (Ta), over a distance into S of order ξ_S, the coherence length. Writing the surface value of Δ_S as Δ_s^0, Arnold (1978) finds

$$\Delta_S^0 \simeq \Delta_S(1 - \pi R\Delta_S) \tag{6.10}$$

with R from Eq. (6.8). It is Δ_S^0 which should be (and is) used in Eq. (6.7). This correction is a small one, ~ 3%, accounting for the difference between 1.51 mV and 1.56 mV. The experimental observation of the second peak is quite unambiguous and occurs at Δ_{PbBi} + 1.56 mV. It could be due to a very thin proximity layer in the PbBi counterelectrode which would produce such a peak at $\Delta_{PbBi} + \Delta_{Nb}$. Another possibility is that microscopic inhomogeneities cause the presence of Nb with full value of the gap close enough to the insulating barrier and constituting parallel paths for the current without going through the Ta overlayer.

Similar subgap results were observed with Pb counterelectrodes, although

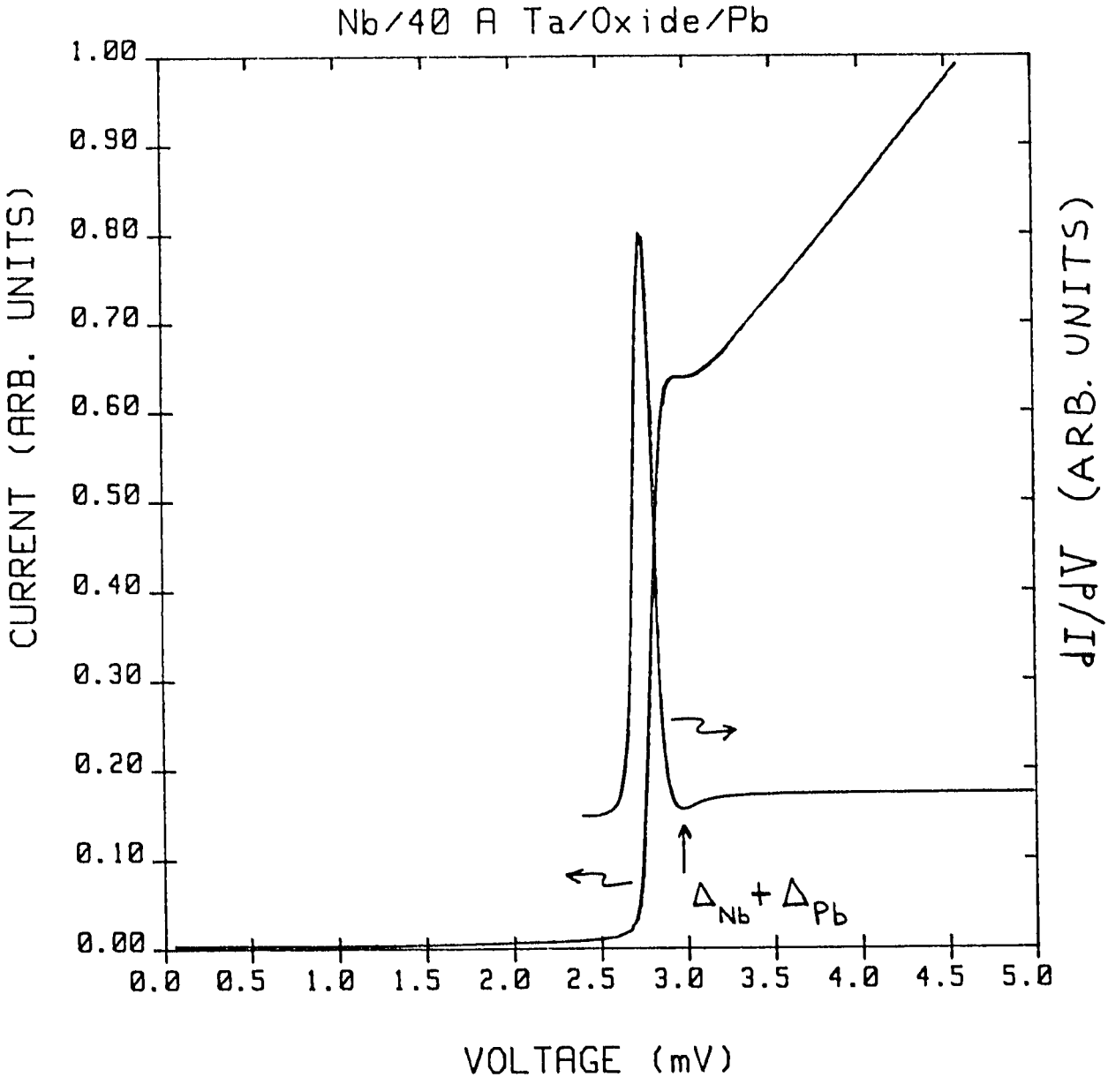

Fig. 6-7 I-V and dI/dV for a Nb/40 Å Ta/ Ta Oxide/Pb junction at 1.2 K. The wider rise in the current at the bound state energy is due to the width of the Pb gap. The second peak at $\Delta_{Nb}+\Delta_{Pb}$ is not seen here, but the negative resistance region after the current rise is clearly evident.

without the sharp behavior in the gap region. Also absent with Pb is the especially sharp peak and associated negative-resistance region observed with the PbBi junctions. this behavior appears to be due to an intrinsic gap broadening typical of relatively thick polycrystalline lead films, where the energy gap is a function of crystallographic direction. A typical result with a Pb counterelectrode is shown in Fig. 6-7.

VI.C.5. Energy Gap and Critical Current

As first discussed by Gallagher (1981), and illustrated in Fig. 6-8, the value of E_0 and the product I_cR of the critical current and the normal resistance do not vary in the same way with D_{Ta}, the thickness of the Ta film, in a proximity-effect system. This is intuitively plausible since E_0 is related to the quasiparticle density of states whereas the critical current relates the maximum Cooper pair current that can flow through the junction. In fact, what is expected - for relatively thin layers - is a slow decrease in E_0 contrasted by an initially very rapid decrease of I_cR.

Plotted in Fig. 6-9 are the results for E_0 and I_cR as a function of Ta overlayer thickness D_{Ta}. It should be noted that D_{Ta} here is taken to be the thickness of the deposited Ta layer. Given that the surface of this layer is oxidized to form the tunnel barrier, the actual thickness of metallic Ta left over which constitutes the proximity layer is slightly smaller than D_{Ta}. However, given that the oxide thickness for all the junctions is approximately 20 Å, using D_{Ta} as the thickness of the proximity layer introduces a small systematic error which is within the uncertainty in determining D_{Ta} from the sputtering rates. The effective energy gap Δ_{NS}, defined in the usual empirical manner as the point of maximum slope on the

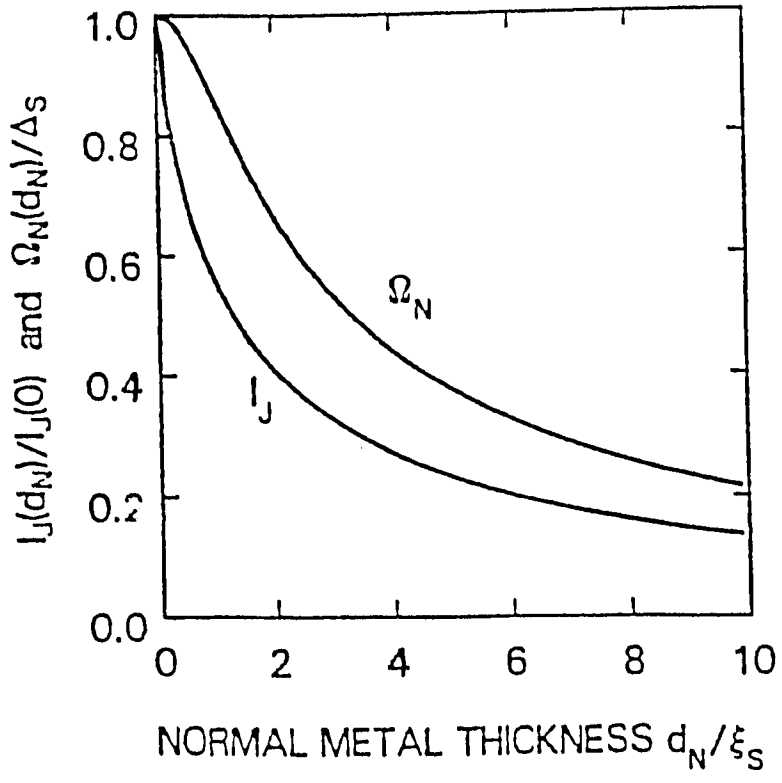

Fig. 6-8 Prediction from Gallagher (1981) for the Josephson current and proximity-sandwich energy gap (= first bound state E_0) of a clean superconductor-insulator-normal metal-superconductor (SINS) junction at T=0 as a function of N-layer thickness normalized to the coherence length ξ_S. In the thin N-layer limit (d_N/ξ_S of order 1), I_J falls off much faster than Ω_N. In the present thesis, this prediction is confirmed and fit quantitatively.

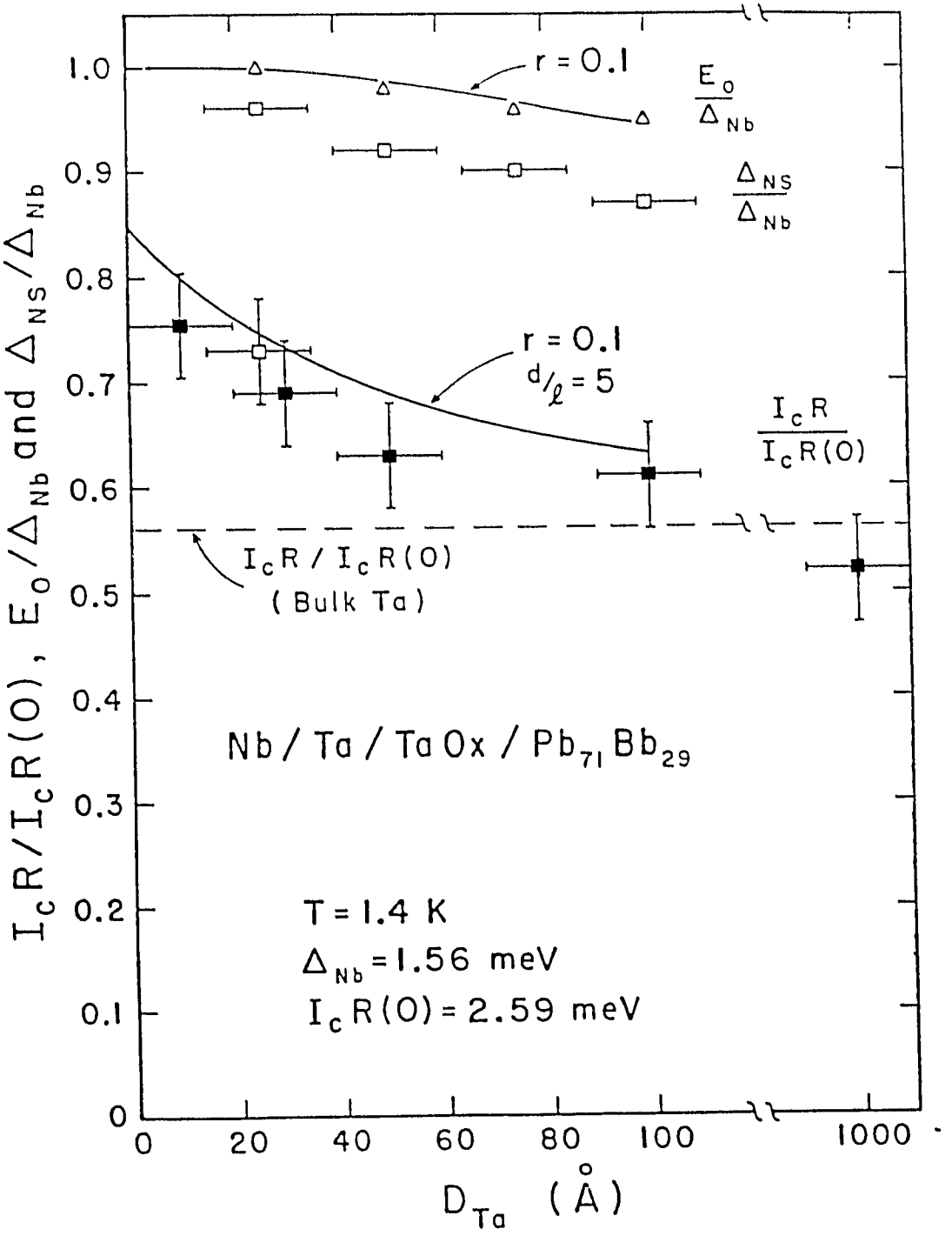

Fig. 6-9 Normalized critical current, bound-state energy, and measured energy gap are plotted for a series of junctions with increasing Ta overlayer thickness on Nb. Critical currents have been normalized to the value for bulk Nb excluding strong-coupling corrections. Calculations of the critical current include strong-coupling effects from both base-elctrode and counterelectrode materials. Solid lines are the self-consistent fits for E_0 and I_cR using a modified version of the Gallagher theory.

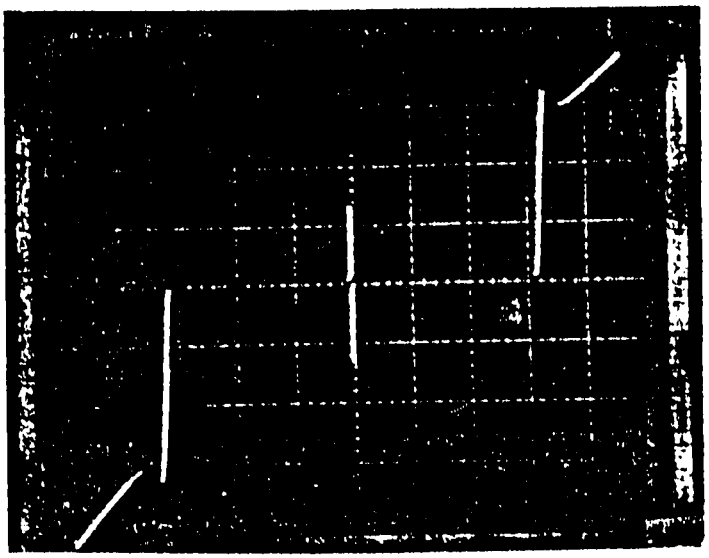

50 Å Ta on Nb
base electrode

V: 1 mV/div.
I: arb. units.

(a)

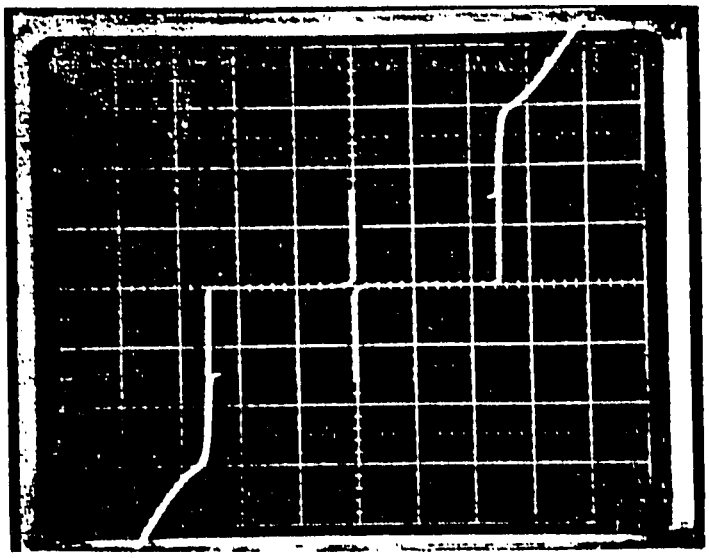

thick Ta (1000 Å)
base electrode

V: 1 mV/div.
I: arb. units.

(b)

Fig. 6-10 Oscilloscope traces of two junctions with (a) thin (50 Å) and (b) very thick (1000 Å) Ta overlayer thickness. In (b) the sharp current rise occurs at 2.5 mV = $\Delta_{Ta}+\Delta_{PbBi}$. A small magnetic field (order of 1 Gauss) is used to "tune" the Josephson current for measuring its maximum value.

rising I-V curve, just below the peak at $E_0 + \Delta_{PbBi}$, is also plotted in Fig. 6-9 for reference.

Results for I_cR are also shown in Fig.6-9. Although direct chart-recorder traces typically gave a reliable indication of the magnitude of the critical current, I_c, a more accurate means of obtaining this information was to display the I-V curves on an oscilloscope (see Fig. 6-10) and "tune" for a maximum I_c value by applying a small (<±1 G) magnetic-field parallel to the junction surface. All measurements were performed in a Dewar which was doubly shielded with μ-metal. It was observed in our studies that the value of the product I_cR (for fixed-area junctions) decreased monotonically with decreasing critical-current density. This result was unexpected as the I_cR product should be a constant of the system [Ambegaokar and Baratoff (1963)]. We note, however, that a similar effect has been observed by Smith et al. (1982) in junctions employing silicon barriers, by Danchi et al. (1984) in Sn-SnO-Pb junctions, and by Face et al. (1987) in $Ta/Ta_2O_5/PbBi$ junctions. Halbritter (1983) has proposed an explanation for this effect based on resonant tunneling. Danchi et al. modeled their observed falloff by assuming an effective noise temperature (presumably extrinsic) of 8±1 K. Therefore, although the participation of extrinsic noise is kept to a minimum by careful shielding and filtering techniques, the effects of noise, in general, perhaps exacerbated by the electronic structure of the barriers themselves, may play a substantial role in the depression of I_cR with junction resistance.

With this in mind we have attempted to remove this effect from our I_cR data. Since one measurement was available on a low-resistance junction ($RA = 7.5\times10^{-4}$ Ωcm^2, D_{Ta}=25 Å, I_cR = 1.9 meV), this data point was plotted as measured (open

symbol), while values of I_cR for other values of D_{Ta} were extrapolated to this resistance using available data for I_cR versus R at a particular Ta thickness.

In Fig.6-9 the fits to the data (solid lines) are based on an extended version of the Gallagher theory [Arnold (1985)]and include the influence of both the finite mean free path in the Ta layers, ℓ, and strong-coupling effects. To compute the latter, the actual phonon densities of state for Nb, Ta, and the Pb-Bi alloy used were employed. The immediate effect of the strong coupling is obvious in the depression of the I_cR product in the case where $D_{Ta} = 0$ (i.e. for pure Nb) to 84% of its full value in the absence of such effects.

Experimentally, E_0 is very clearly defined and its dependence on D_{Ta} is sensitive to the value of the reflection coefficient, r. Therefore, the data for E_0 were used to establish the magnitude of r as 0.1. With this information (including values of $\Delta_{PbBi}=1.74$ meV, $\Delta_{Nb}=1.56$ meV, $\Delta_{Ta}=0.72$ meV, and $\xi_{Ta}=130$ Å) and the phonon spectra for bulk Ta, Nb, and Pb-bi, values of I_cR were generated as a function of D_{Ta}. A fixed value of $d/\ell=5$ was employed to fit the data as shown, where d is Ta film thickness and ℓ the electronic mean free path, although we note that all values $d/\ell>1$ produced very similar curves. We see that the theory gives an excellent account of the data, except for a small overall offset which may be due to our extrapolation procedure or may indicate an intrinsic, systematic suppression of I_cR.

We note finally that the value of r required to self-consistently fit both the E_0 and I_cR data is close to the value expected on the basis of electron scattering off the small potential step associated by the difference in Fermi energies between Nb and Ta given by 6.9. Average band values of the Fermi velocity $\langle v_F^2\rangle^{1/2}$ of

0.61×10^8 cm/sec for Ta and 0.67×10^8 cm/sec for Nb [Chakraborty et al. (1976)], yield a value of r = 0.047. The somewhat higher value as derived from fits to our data (r = 0.1) may imply some additional scattering due to the presence of interfacial disorder or impurities.

VI.C.6. Phonon Structure

To investigate the nature of the phonon structure of Ta surface layers on Nb, we have also made a qualitative study of second-harmonic data for junctions having Ag counterelectrodes. Shown in Fig. 6-11 is the second-harmonic signal (d^2V/dI^2) versus V for a series of junctions with D_{Ta} ranging from 25 to 100 Å. The data here were normalized by the relative excitation amplitude compared with the normal resistance. The experimental technique for this measurement is discussed in chapter 5. The position of the bulk transverse acoustic and longitudinal acoustic Ta (11.4 meV, 17.9 meV) and Nb (16.1 meV, 23.3 meV) phonon peaks are indicated in Fig. 6-11 relative to the Nb gap edge.

It is clear that for $D_{Ta} \sim 75$ - 100 Å the structure is dominated by and has all the appearance of bulk Ta phonon structure with Nb peaks present but weak in amplitude. The crossover thickness seems to be roughly $D_{Ta} \sim 50$ Å. It is interesting to note that both the general trend of these data and the value of D_{Ta} where the Ta phonon structure becomes strongly attenuated is similar to the results by Hertel et al. (1982). In that case the Ta surface layers were first covered (in situ) with a thin Al layer to form the tunnel barrier. In addition, and significantly those Ta surface layers were prepared at elevated temperatures and have much larger (lateral) microcrystalline size. Thus, although Hertel's Ta films were prepared under

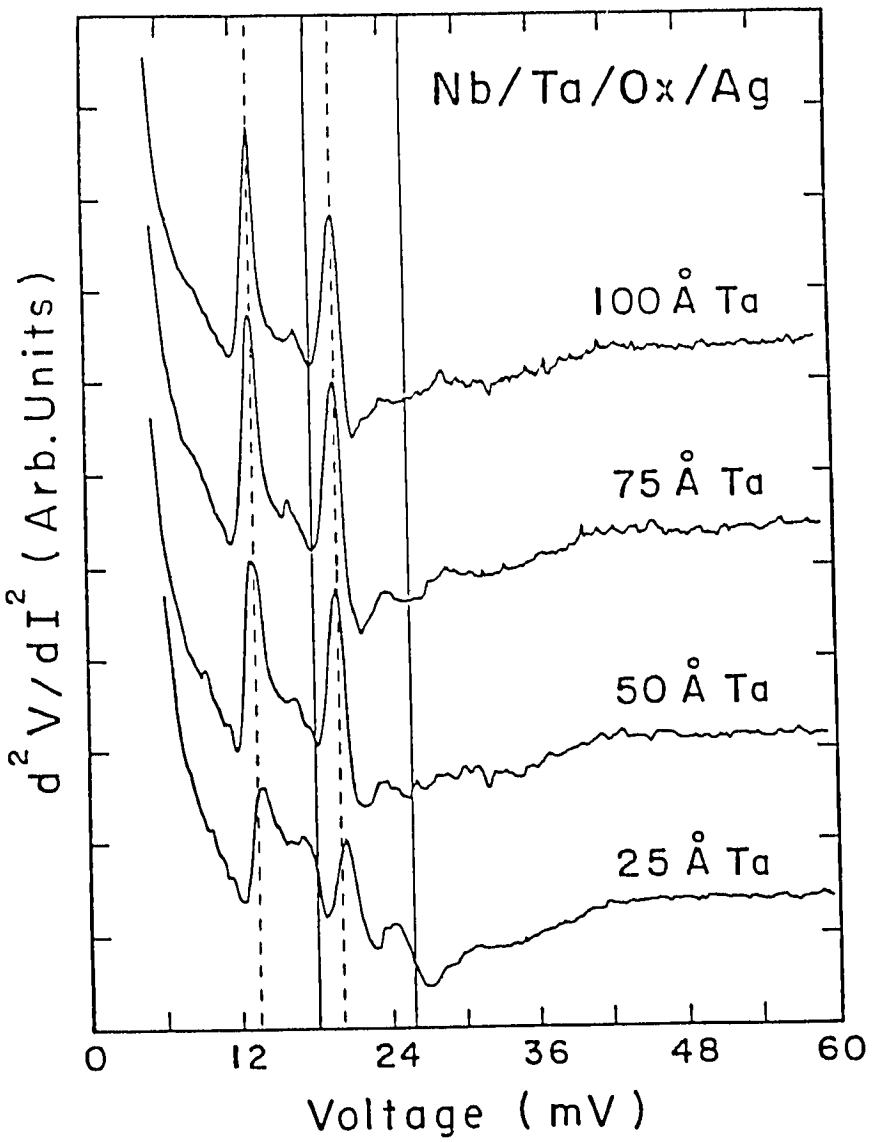

Fig. 6-11 Second-harmonic signal (d^2V/dI^2) versus voltage for a series of Ta surface-layer junctions. Indicated are the relative positions of the Ta (dashed lines) and Nb (solid lines) transverse- and longitudinal-acoustic-phonon energies.

substantially different conditions than those in this work, the phonon characteristics, at least on the basis discussed, appear similar. For the 25 Å Ta overlayer, the apparent shift of the Ta phonon frequencies to higher values may be due to stress in the thin Ta layer induced by the slight lattice mismatch with the underlying Nb.

It should be noted that the very fact of observing clearly the Ta phonon structure for layers as thin as 25 Å is a good diagnostic indicator of the sharpness of the Nb/Ta interface. This further strengthens the claim that the Nb-Ta overlayer system constitutes a good proximity-effect system.

VI.D. NbN: Effect of Oxidized Metal Overlayers

Use of Ta overlayers on Nb as described above has been instrumental in obtaining a clean proximity-effect system to probe and test the behavior predicted by the theory. In addition, oxidized metallic overlayers do have an end in themselves: to provide a high quality tunnel barrier on materials for which a good native oxide barrier is not easily obtained. A most prominent example is Nb. The desire to produce good Nb-based tunnel junctions has been motivated by the desire to study the fundamental properties of Nb and because of its technological importance. Thin layers of Al [Gurvitch et al. (1983), Wolf et al. (1980)], Lu [Umbach et al. (1982)], and Mg, Y, and Er [J. Kwo et al. (1983)] have been employed because of their favorable oxidation properties. It has also been shown that refractory metals, Zr [Celashi et al. (1983)] and Ta [Ruggiero et al. (1983)] can be employed with equal success for this purpose. In all these cases the understanding of the proximity effect becomes a tool to interpret the modification of the I-V characteristic brought about by the thin metallic overlayer. In-situ deposition of the metallic overlayer is

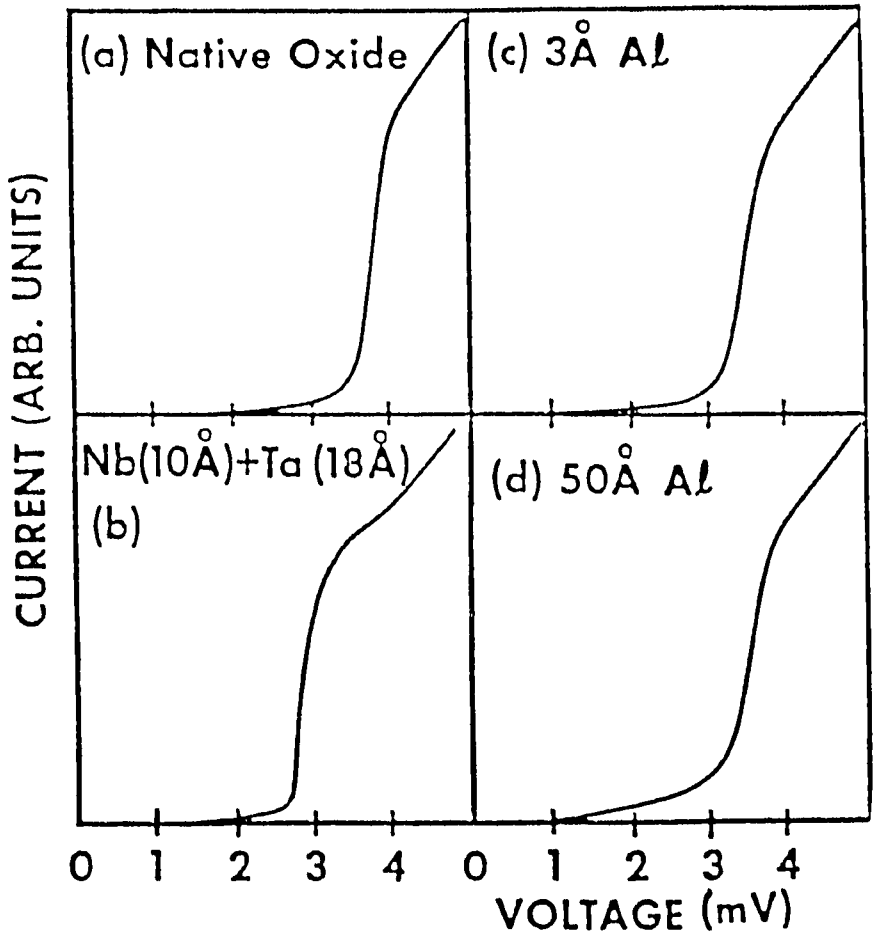

Fig. 6-12 I-V characteristics of junctions with base electrode comprising of (a) NbN (b) NbN with a composite overlayer of 10 Å Nb + 18 Å Ta (c) NbN with a 3 Å Al overlayer (d) NbN with a 50 Å Al overlayer.

essential to minimize contamination of the interface. We set out to explore the effect of artificial barriers on NbN-based junction to determine whether, like in Nb, improvements in the I-V quality could be brought about.

We have used overlayers of Al, Ta, or sequentially deposited Nb+Al or Nb+Ta on the NbN base electrode to form artificial oxide barriers [Track et al. (1985)]. After deposition of the NbN as by the dual ion-beam technique as described in chapter 3, the N_2 gas flow is stopped, 10-15 minutes are allowed for the N_2 to be pumped out, the appropriate target is rotated into place and the overlayer is ion-beam sputter-deposited. The thickness of the overlayer is inferred from the deposition time and the known rates of deposition. The quality of the I-V curves of these overlayer junctions, as determined by subgap leakage, is comparable to, but not better than, the native oxide junctions (see Fig.6-12), but the overlayer junctions have a higher normal tunneling resistance R_n. The fact that there is no improvement of the I-V quality with overlayers may indicate that the leakage current and the width of the current rise are caused by intrinsic properties of the NbN film itself (tailing of the density of states in the gap [Gurvitch et al. (1984)], gap inhomogeneity, etc.) and are not due to defects in the barrier. Alternatively, the 10-15 minute exposure to the background pressure in the vacuum system may have produced imperfections at the interface, causing part of the subgap leakage observed.

Fig. 6-13 shows the I-V curve of a NbN/Nb(10Å)+Ta(18Å)/oxide/PbBi junction. Here the current rise occurs at a reduced bias voltage of 2.78 mV, due to the proximity effect. The proximity effect also causes the structure above the current rise. This structure displays a decrease in the conductance dI/dV, followed by an increase, with the minimum dI/dV occurring at a voltage of 3.68 mV. This voltage

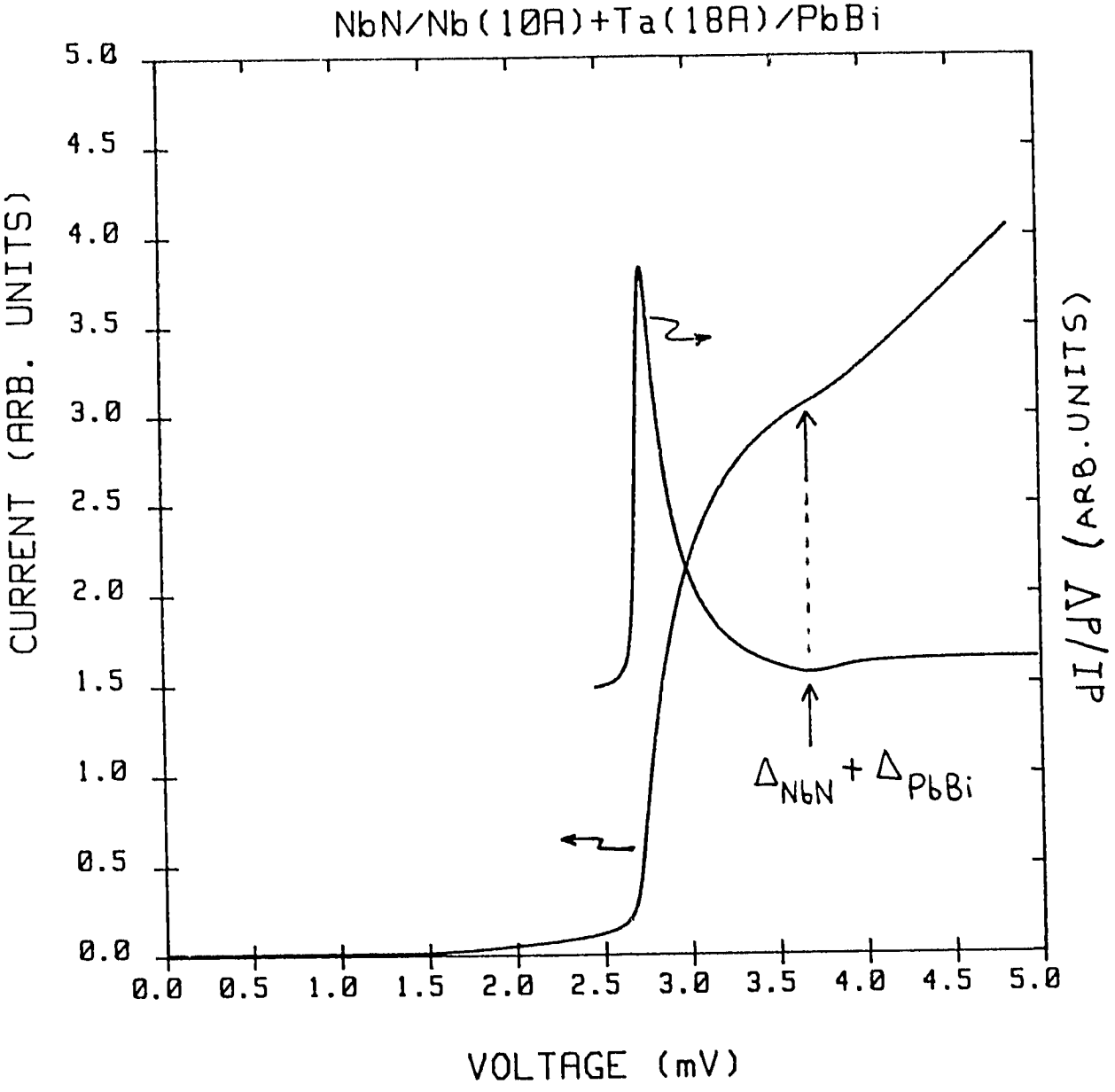

Fig. 6-13 Conductance (I-V and dI/dV) characteristics of a NbN/Nb(10Å)+Ta(18Å)/PbBi tunnel junction reflecting consequences of the proximity effect.

corresponds to the sum-gap of our native-oxide junctions, consistent with the proximity effect model. Use of thinner Nb+Ta overlayers or Al or Nb+Al overlayers produces a smaller depression of the current rise and no resolved structure above the current rise.

All the Al-overlayer junctions had a similar voltage for the current rise (~3.4 mV at 4.2 K). There was a slight increase in subgap leakage with increasing Al thickness. This may be due to Al diffusion along the grain boundaries and subsequent formation of regions of depressed T_c.

VI.E. Conclusions

This chapter has described how thin Ta surface layers on Nb can be used to produce tunnel junctions with nearly ideal characteristics. The detailed shape of the I-V curve of a Nb/Ta junction, including a sharp bound-state peak, has, for the first time, been accurately reproduced by the proximity-effect tunneling theory. Both the critical current and bound-state energy position of the junctions have been studied as a function of Ta surface-layer thickness. Calculations of the critical current were performed including strong-coupling corrections for both base-electrode and counterelectrode metals. Self-consistent fits to the bound-state energy E_0 and product I_cR versus D_{Ta} are in accord and verify the predictions of the proximity-effect theory. A value for the electron reflection probability at the Nb/Ta interface is obtained, $r^2 = 0.01$. This value is consistent with the simple model which assumes that a major fraction of this interfacial scattering is due to the potential step created by the Fermi-level difference between Nb and Ta. The behavior of the phonon structure of Ta surface layers on Nb has been measured as a function of Ta

thickness. It is seen that the Ta phonon structure dominates the observed spectra until $D_{Ta} \leq 50$ Å and that, by all indications, there is no mixing but a simple superposition of these spectra. Finally, artificial barriers have been successfully produced on NbN using oxidized Al or Ta overlayers. The quality of the resulting I-V curves is comparable to that of junctions with native NbN oxide barriers.

VII. TUNNEL BARRIER PROPERTIES

VI.A. Introduction: The Tunnel Barrier

Although paradoxical from a classical point of view, the use of the phrase "Tunnel Barrier" is yet another corollary of quantum mechanics which makes for the finite (non-zero) probability of tunneling through an otherwise perfect potential barrier. In the previous chapter, good contact between the two metals in the proximity layer required a modification of the properties of both metals at the interface. In a tunnel junction however, the presence of a thin insulating layer - constituting under ideal circumstances a perfect potential barrier - allows each electrode to preserve its full properties without any constraints. The tunnel current will then reflect a convolution of the density of states on both sides and allow the probing and interpretation of the intrinsic properties of the electrode materials. This is true as long as the potential barrier can be treated as infinite in height so that the tunneling probability is independent of the bias-voltage. The validity of this assumption ceases in several instances: 1) Even under the assumption of perfectly uniform interfaces and a defect-free insulating layer, what in reality constitutes the potential barrier is a band-gap in this insulating layer, of the order of 1-3 eV. Hence the height of the potential barrier is not infinite, the tunneling probability <u>is</u> bias-voltage-dependent. The tunneling probability becomes the dominant factor in the tunnel current when the bias voltage is on the order of the barrier height, causing an effective "distortion" of the barrier shape (see Fig. 7-1). 2) Real tunnel barriers are not defect-free and the interfaces are far from perfectly uniform. This is reasonable given that the insulating barrier is typically ~ 20 Å thick so that inhomogeneities of even a monolayer constitute a significant fraction of the total thickness (see Fig. 7-2).

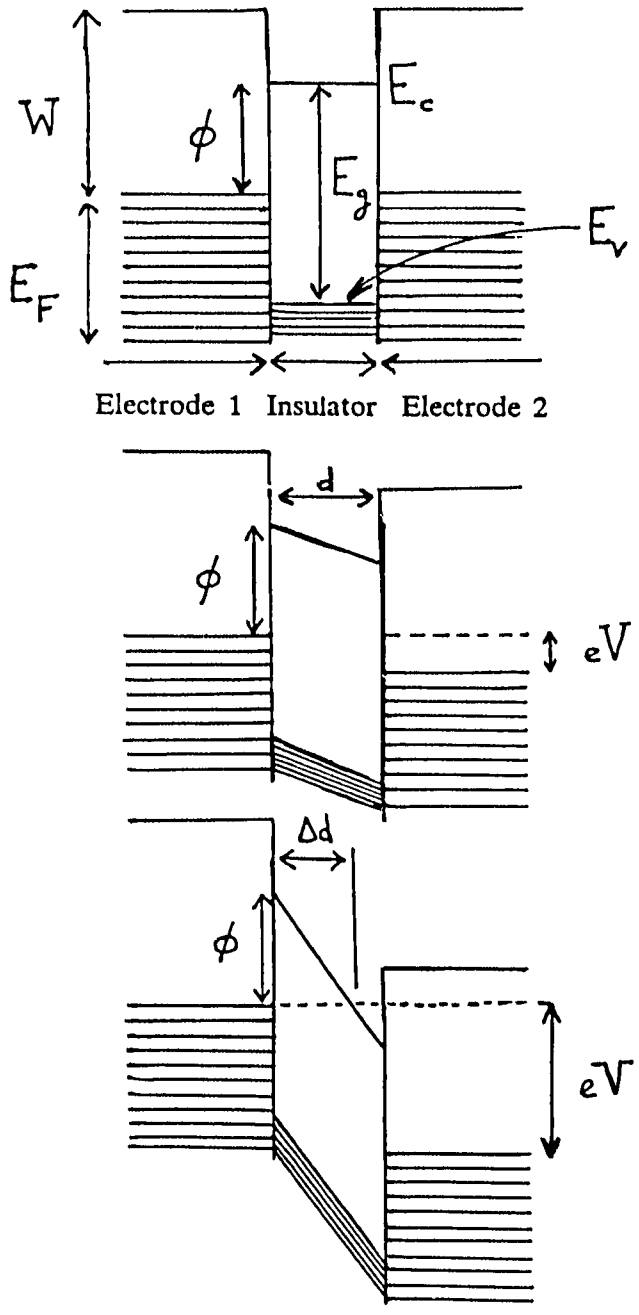

Fig. 7-1 (a) Energy diagram for a metal-insulator-metal tunneling structure with no applied bias showing the edge of the conduction band E_c, and of the valence band E_v, and the band-gap E_g of the insulator. E_F and W are respectively the Fermi energy and the work function of the metal electrodes which, for simplicity are taken to be identical. ϕ, the barrier height, is the energy difference between the bottom of the conduction band in the insulator and the Fermi level in the metal. (b) Energy diagram with a small bias $eV < \phi$ applied. The tunnel current will reflect the density of states of the metal electrodes. (c) When a large bias $eV > \phi$ is applied the barrier is "distorted". For example, the effective barrier width becomes Δd as shown. The conductance will then depend predominantly on the barrier shape.

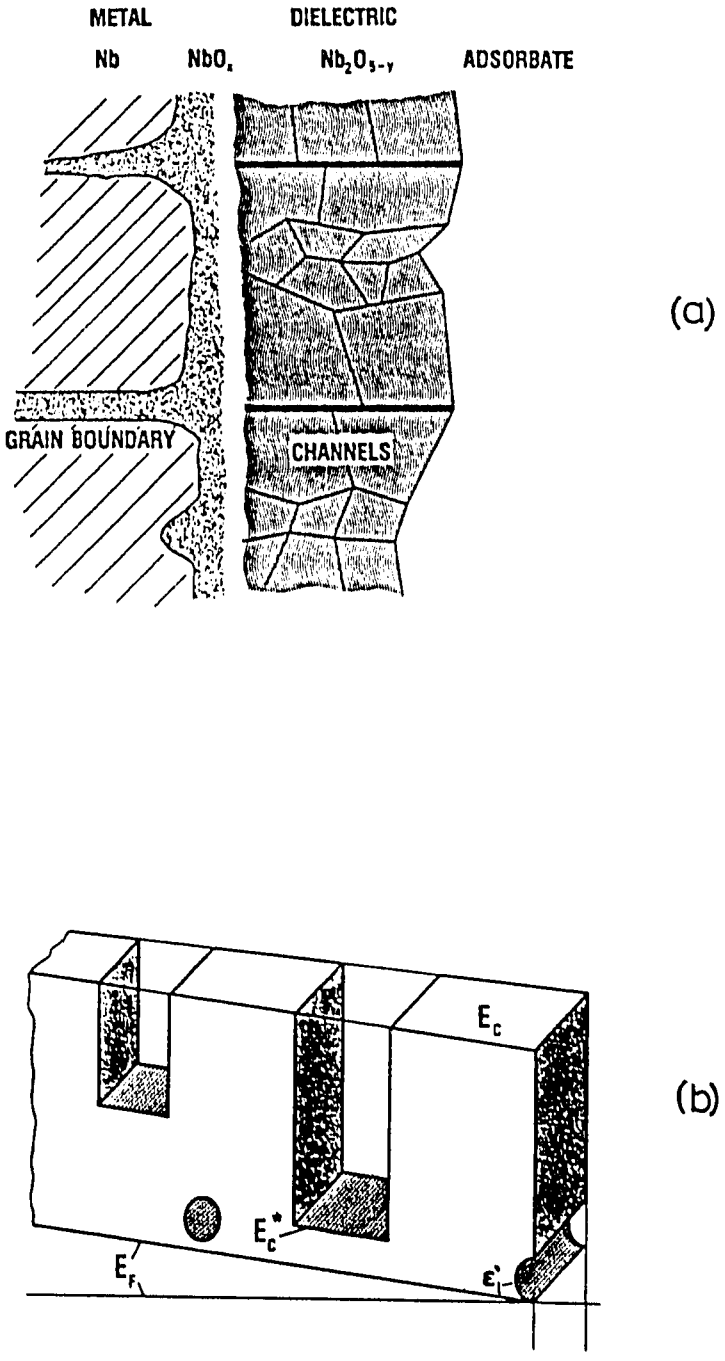

Fig. 7-2 (a) Sketch for complex barrier at the surface of Niobium depicting the many conductance channels that can exist. (b) Model for the composite barrier above showing channels of varying barrier heights (E_c, E_c^*) and channels of resonant tunneling symbolized by holes in the barrier. This model is referred to informally as the "Swiss cheese and Swiss Alps". [From Halbritter (1985)].

VII.B. Tunnel Barrier Models

Important to the electrical characteristics of tunnel junctions is the detailed nature of their tunnel barriers. The simplest means of describing a barrier is to assume that tunneling occurs through a trapezoidal potential barrier of a given width, height, and asymmetry (Fig. 7-3). A simplified expression for the current-voltage relation in this case was originally presented by Simmons (1963) using a WKB approximation for the tunneling probability, and later extended by Chow (1965). Rowell (1969) and Brinkman et al. (1970) have described a simple means of extracting barrier parameters from the Simmons model. The parameters referred to here are 1) d, the barrier width, 2) ϕ, the average barrier height, and 3) $\Delta\phi$, the barrier asymmetry. These parameters are extracted from the data representing the differential conductance G(V) = dI/dV as a function of voltage V. By expanding Simmon's expression for the tunnel current in powers of the voltage and approximating expressions for the coefficients of the linear and quadratic terms, an expression for the conductance, accurate to roughly 10% is obtained:

$$\frac{G(V)}{G(0)} = 1 - \left[\frac{A_0\,\Delta\phi}{16\,\phi^{3/2}}\right]eV + \left[\frac{9\,A_0^2}{128\,\phi}\right](eV)^2 \qquad (7.1)$$

where $A_0 = 4(2m)^{1/2}d/3\hbar$ with m the mass of the electron,

and the conductance at zero bias, G(0), equal to 1/RA where A is the area of the junction and R its zero-bias resistance, is equal to

$$G(0) = (3.16\times10^{10}\,\phi^{1/2}/d)\exp(-1.025\,d\phi^{1/2}) \qquad (7.2)$$

From 7.1, the minimum conductance occurs at a voltage V_{min} given by

$$eV_{min} = 0.649(\Delta\phi/d\phi^{1/2}) \qquad (7.3)$$

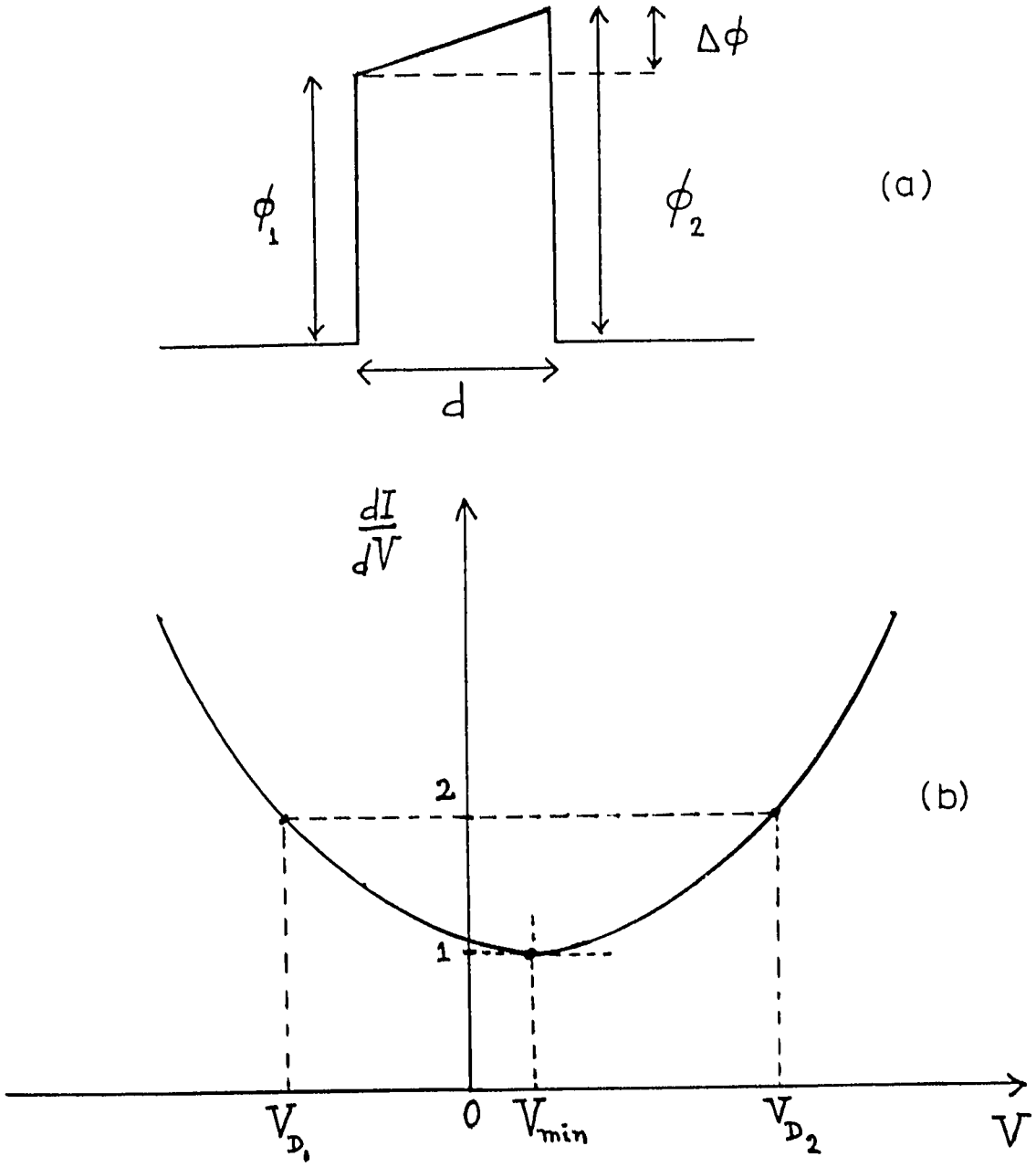

Fig. 7-3 (a) Trapezoidal barrier model used to represent and characterize real tunnel barriers. (b) Differential conductance calculated for above barrier using a WKB approximation for the tunneling probability. The offset of the minimum conductance from zero bias is due to the asymmetry of the barrier.

and the sum, V_D, of the voltages V_{D1} and V_{D2} where the conductance doubles its minimum value is

$$eV_D = eV_{D1}+eV_{D2} = 11\ \phi^{1/2}/d \tag{7.4}$$

The area, A, of the junction, its zero-bias resistance, R, V_{min}, V_{D1}, and V_{D2} are measured, and from the above equations ϕ, $\Delta\phi$, and d are inferred. For reference, the following equations express this solution in practical units:

$$d = \left[\frac{\ell n\ (0.575x10^{10}\ V_D/RA)}{0.186\ V_D}\right] \tag{7.5a}$$

$$\phi = 0.0331\ (V_D)^2 \tag{7.5b}$$

$$\Delta\phi = V_{min} d\ \phi^{-1/2}/0.649 \tag{7.5c}$$

In equations 7.5, d is in Å, all voltages in Volts, R in Ω, A in cm^2, ϕ and $\Delta\phi$ in eV.

This model represents an idealized picture of what in reality may be a rather complicated tunneling process. It has become increasingly clear that secondary tunnel channels may exist in nonuniform oxide layers. It has been pointed out by Gundlach et al. (1973) that under these circumstances a measure of the effective barrier height can be obtained from a plot of the logarithmic derivative of the conductance $\hat{g} = d[\ell n(I/V)]/dV$ versus voltage, which displays a peak at a voltage slightly higher than the barrier height (Fig. 7-4). This should provide a measure of the barrier height, independent of the other barrier parameters. In fact the logarithmic derivative $\hat{g}$ has the general property of displaying a peak at the onset of any new conductance channel. This is illustrated in Fig. 7-5.

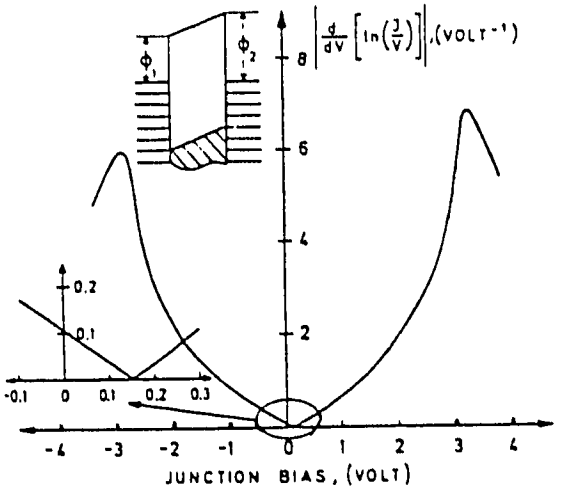

Fig. 7-4 Theoretical curve of $\hat{g}$, the logarithmic derivative of the dc conductance, for the barrier shown in the inset: ϕ_1 = 2.5 eV, ϕ_2 = 3 eV, d = 22 Å. $\hat{g}$ displays a peak at a bias voltage slightly above the barrier height for each polarity. The asymmetry with respect to zero bias is due to the different values of ϕ_1 and ϕ_2. [From Gundlach et al. (1973)].

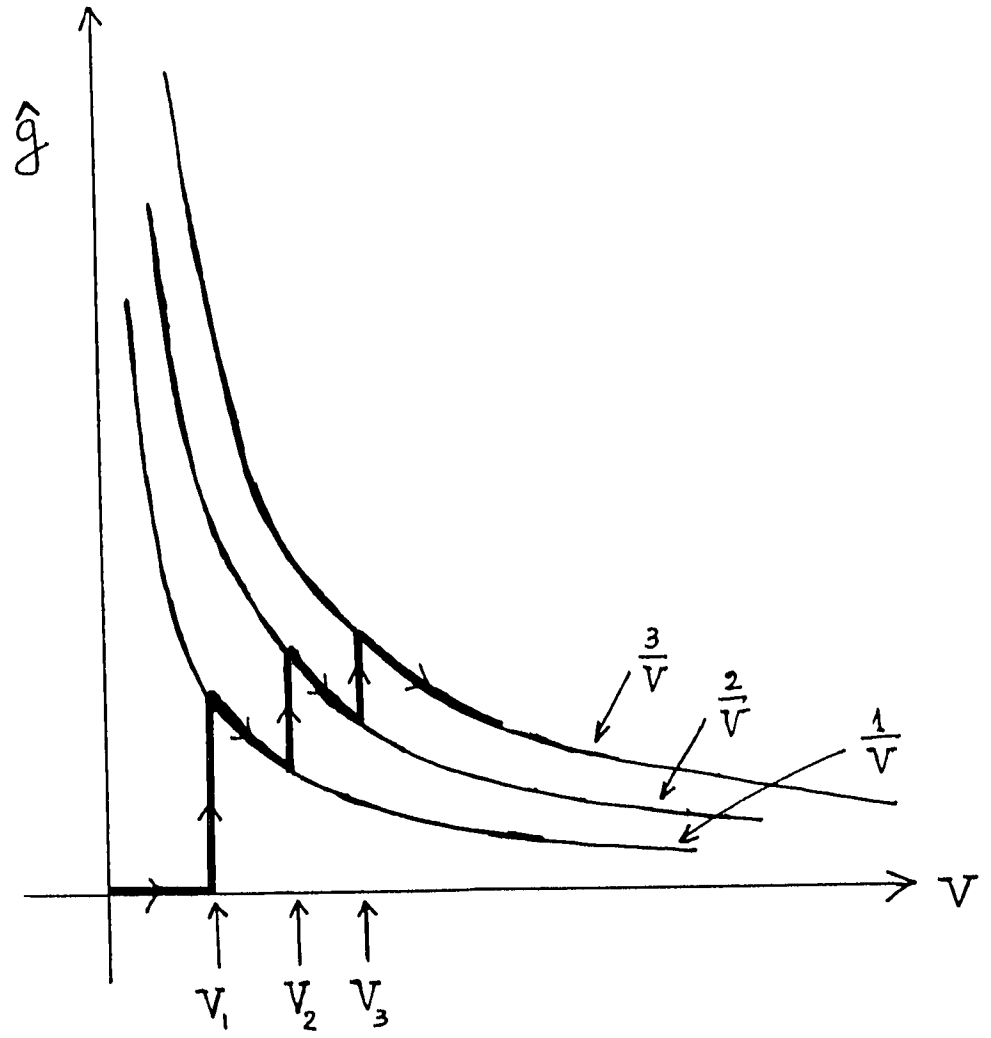

$$I \propto V^n \Rightarrow \hat{g} = (n-1)/V$$

$$0<V<V_1 \Rightarrow I \propto V \Rightarrow \hat{g}=0$$

$$V_1<V<V_2 \Rightarrow I \propto V^2 \Rightarrow \hat{g}=1/V$$

$$V_2<V<V_3 \Rightarrow I \propto V^3 \Rightarrow \hat{g}=2/V$$

$$V>V_3 \Rightarrow I \propto V^4 \Rightarrow \hat{g}=3/V$$

Fig. 7-5 $\hat{g} = d[\ell n(I/V)]/dV$ is a useful tool for identifying onsets of new tunnel channels since it displays a peak whenever there is a change is the functional dependence of I on V as happens when new conductance channels open (at V_1, V_2, V_3).

With these issues in mind, the Simmons model is employed in this chapter as a basic, parametric tool for studying trends in the effective WKB barrier shape in the Nb/Ta junctions and for characterizing native oxide and artificial barriers in NbN-based junctions. A clear correlation is established between the average barrier height and effective barrier width and possible interpretations are presented.

VII.C. Nb/Ta-based Junctions

VII.C.1. Experimental Results

In the context of the trapezoidal barrier model, we find - in agreement with other workers - that typical air-oxidized Nb junctions have rectangular, low (~ 0.3 eV), and broad (~ 25 Å) barriers. Such junctions also show less than ideal tunneling characteristics. Although there is no intrinsic reason why such a barrier should necessarily produce poorer I-V curves, and the actual barrier is in reality perhaps not so simply represented, such a barrier – at least in the case of niobium – is associated with poorer I-V's. Indeed, the presence of multiple tunnel channels may well be the cause for both the lowering of the effective barrier height of these junctions and other associated anomalies.

In this work, it has been found that when sufficiently thick surface layers of tantalum are applied to the surface of niobium (and, as will be discussed, oxidation is not excessive) our junctions display both the high and narrow (and asymmetric) barrier shape and sharp I-V characteristics associated with high-quality junctions formed on pure Ta [Spencer and Rowell (1981); Face (1987a)]. It is particularly interesting to note, in this regard, that recent studies of specially prepared junctions

on pure single crystal Nb films by Celashi et al. (1983) have resulted in the formation of high (0.7 eV), narrow (20 Å) barriers which show high-quality I-V characteristics. It is clear, therefore, that when the effective barrier of a Nb-based junction is made higher, either by the application of a thin surface layer or by the special preparation of pure Nb, highly improved tunneling characteristics result.

Shown in Fig. 7-6 are the results for the average barrier height ϕ and effective width d of the Nb/Ta junctions studied in this work and of pure Ta [Face (1987)] and Nb [Walmsley et al. (1979), Rowell et al. (1981), Celashi et al. (1983)]. These parameters were obtained from the Simmons model as discussed above. It is seen that barrier shape can vary considerably - from the high (> 1 eV), narrow (< 20 Å) barriers associated with pure Ta to the low (~ 0.3 eV), broad (~ 30 Å) shape more common to pure Nb. What we have found is that for sufficiently thick Ta surface layers, D_{Ta} > 20 Å, the initial barrier shape is generally high (ϕ ~ 0.8 eV), narrow (< 20 Å), and independent of D_{Ta}. Also, as depicted in the inset of this figure (7-6) for a series of junctions with D_{Ta} = 100Å and also observed with Al overlayers [Rowell et al. (1981)], and junctions of pure Ta [Hahn et al. (1983)], higher barrier asymmetry was associated with greater average barrier height. Also note that, again as with Al, below some surface-layer thickness, in the case of Ta 10 - 20 Å, symmetric, low, and wide barriers - and impaired junction characteristics - typically associated with pure Nb were observed. In Table 7-1 are listed the available parameters for Nb/Ta junctions studied.

These data for D_{Ta} = 100 Å, and those for Ta surface-layer junctions having a wide range of Ta layer thicknesses, tend to behave according to the general rule that as oxidation proceeds barrier height decreases and barrier width increases.

Table 7-1 Parameters of Ta surface-layer tunnel junctions.

Sample	Counter-electrode	Ta Thickness (Å)	Area (μmxμm)	Resistance (Ω)	Δ_{NS} (meV)	I_c (μA)	I_cR (mV)	Barrier width d (Å)	Average Barrier Height ϕ (eV)	Barrier Asymmetry+ $\Delta\phi$ (eV)
83012-1,1	PbBi	100	75x350	18	3.04	60	1.08	15.36	1.05	2.00
-1,2	PbBi	100	"	26	3.1	30	0.78	15.6	1.07	2.14
-1,3	PbBi	100	"	86	3.1	0.39	0.034	17.81	0.92	(1.87)
-2,4	PbBi	75	"	96.6	3.14			20.6	0.678	0.611
-2,5	PbBi	75	"	94.7	3.14	0.6	0.057	20.7	0.666	0.545
-2,6	PbBi	75	"	100	3.14	0.5	0.05	20.5	0.678	0.521
-3,4	PbBi	50	"	21.7	3.1	46	1.0	20.1	0.587	0.296
-3,6	PbBi	50	"	19.5	3.18	6.3	1.23			
-4,4	PbBi	25	"	91.3	3.24	0.18	.016	21.77	.59	0.411
-4,5	PbBi	25	"	11.68	3.24	127	1.48	16.13	.89	1.09
-4,6	PbBi	25	"	2.87	3.24	660	1.89	14.27	.963	1.12
-5,2	PbBi	0	"	310,000	3.25					
-5,3	PbBi	0	"	550,000	3.25					
-1,4	Ag	100	"	55				16.8	.998	(2.07)
-1,5	Ag	100	"	8.7				13.2	1.35	(2.99)
-1,6	Ag	100	"	9.3				13.24	1.351	3.13
-2,1	Ag	75	"	3.73						
-2,2	Ag	75	"	17				14.9	1.12	2.06
-2,3	Ag	75	"	15				15.1	1.069	1.96
-3,1	Ag	50	"	11.76						
-3,2	Ag	50	"	8.7				14.84	1.033	1.40
-3,3	Ag	50	"	9.5				15.8	0.903	1.29
-4,1	Ag	25	"	10.75				14.58	1.106	2.04
-4,2	Ag	25	"	8.33				14.32	1.113	1.99
-4,3	Ag	25	"	9.46				14.84	1.04	1.67
83015-1,4	Pb	40	"	121.8	2.68			18.36	.897	1.48
-1,5	Pb	40	"	45.4	2.81			15.96	1.086	2.26
-1,6	Pb	40	"	30.6				14.49	1.288	3.23
-3,4	Pb	20	"	151.9	2.7					
-3,5	Pb	20	"	202.4	2.83			18.21	0.969	0.716
-3,6	Pb	20	"	310						
-4,4	Pb	10	"	110.2	2.78					
-4,5	Pb	10	"	83.3	2.87			25.13	0.395	0.304
-4,6	Pb	10	"	49.8						
-5	Pb	0	75x75	34,500	2.88					
-1,1	Ag	40	75x350	16.53				15.33	1.05	1.84
-1,2	Ag	40	"	19.31				15.6	1.03	1.90
-1,3	Ag	40	"	27.1				16.3	0.975	1.79
-2,5	Ag	30	"	8.56				14.27	1.125	1.89
-2,6	Ag	30	"	11.24				14.63	1.105	2.01
-3,2	Ag	20	"	21.7				17.74	0.779	0.903
-3,3	Ag	20	"	18.35				16.98	0.842	0.902
-4.2	Ag	10	"	14				17.3	0.773	(1.72)
-5	Ag	0	75x75							

+Barrier Asymmetries in excess of 2ϕ (indicating a breakdown of the trapezoidal barrier model) have been listed in paranthesis.

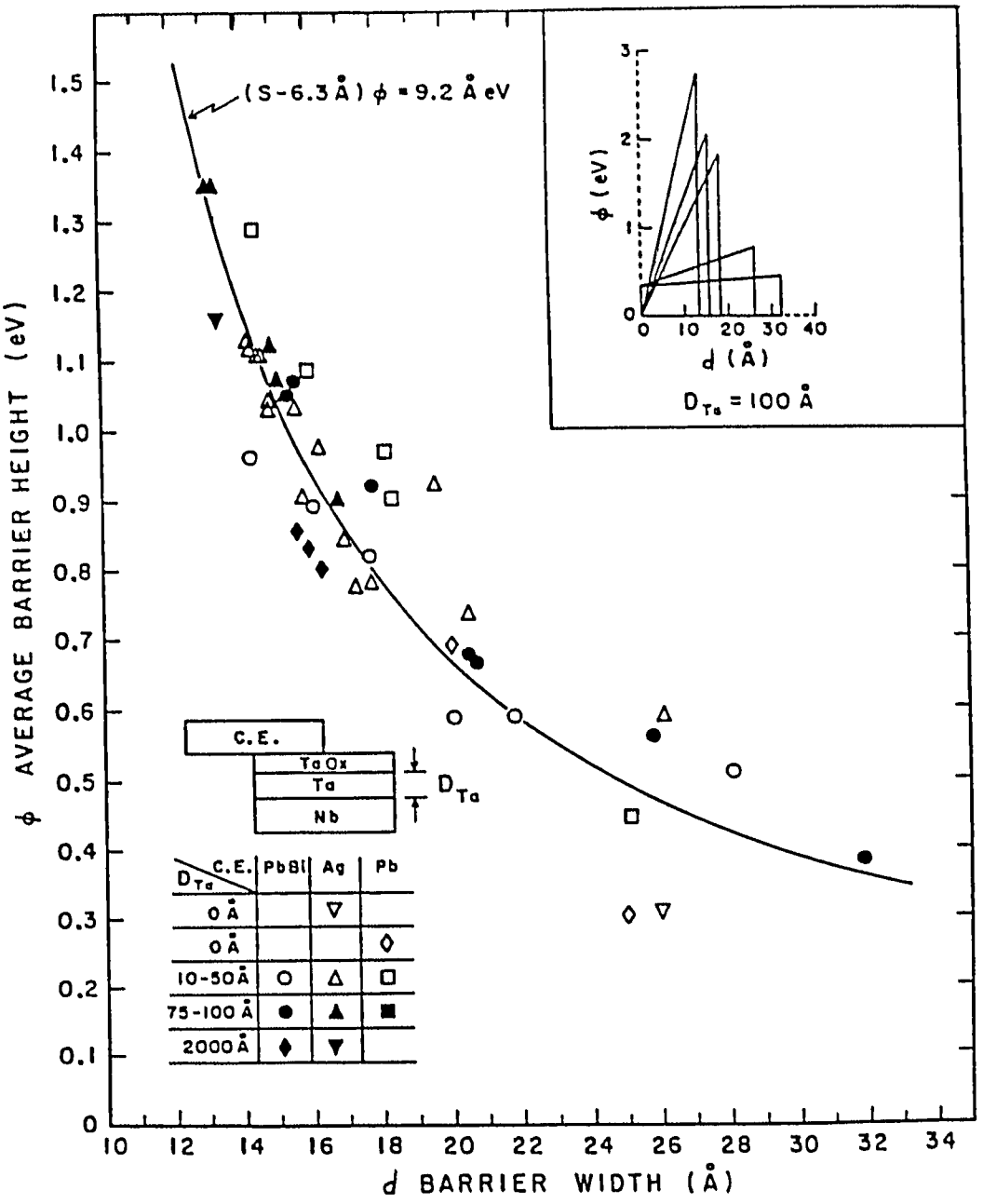

Fig. 7-6 The main portion of this figure shows the average WKB barrier height versus barrier width for tunnel junctions with base electrodes of pure Ta (3000 Å Ta), pure Nb, and various Ta overlayer thicknesses on Nb. The data include results for various counterelectrodes including PbBi, Ag, and Pb. The solid line shows an empirical fit to the data. Shown in the inset are the barrier shapes of a series of our junctions all with base electrodes comprising 100 Å Ta on 3000 Å Nb. This series of data illustrates the trend that as oxidation proceeds, the barriers go from being high, narrow, and asymmetric to low , broad, and symmetric.

Thus, for a given surface-layer thickness one starts at some point on the ϕ - versus - d curve (Fig. 7-6) and proceeds down the curve or parallel to it as d increases. Note that as long as D_{Ta} is greater that ~ 20 Å the overlayer thickness does not appear to strongly influence initial ϕ and d values, which may depend more critically on initial oxidation conditions. In contrast, junctions with thinner Ta layers (< 10 to 20 Å) tend always to have lower broad barriers.

VII.C.2. Comparison with other work: General Trends.

To obtain a broader perspective on this behavior, data for a variety of systems available in the literature, which span a large range of ϕ, have been plotted in Fig. 7-7. Included here are results for pure Al [Rowell et al. (1981), Ocampo et al. (1982)], Ta [Face (1987)], and Nb [Walmsley et al. (1979), Rowell et al. (1981), Celashi et al. (1983)], and data for overlayers of Al [Rowell et al. (1981)] and Ta [this work] on Nb where a variety of counterelectrodes was employed. As seen in Fig. 7-7, both within a given system and for the data in general there is a monotonic decrease in the average barrier height ϕ with barrier width d. In this case, this broader range of data implies a best empirical fit of $\phi(d - 10.4 \text{ Å}) \sim 6$ eV Å.

The observed decrease in the barrier height with width of natural oxide barriers may involve a variety of participating phenomena. For niobium-like oxide barriers, Halbritter (1985) has suggested an explanation based on the existence of a multicomponent oxide layer. In this model depicted in Fig. 7-2, the effective barrier height decreases due to the opening of parallel channels of low effective barrier heights as oxidation proceeds. Besides those channels of depressed barrier height,

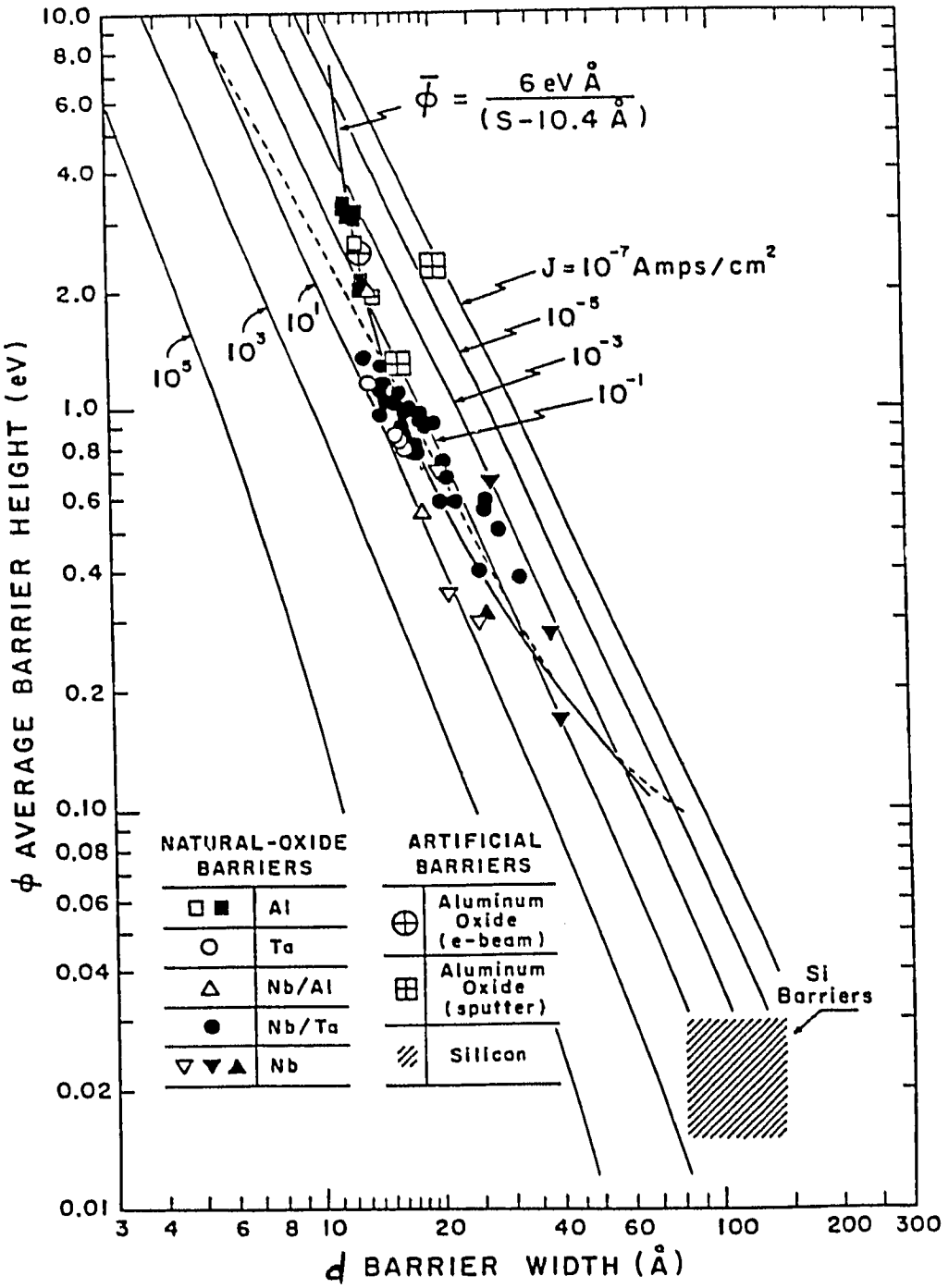

Fig. 7-7 Average barier height versus width for junctions composed of a wide variety of base-electrode and counterelectrode materials. The solid line is an empirical fit to the data. Also shown (dashed line) is the theoretical prediction of the Fromhold-Mott-Cabrera theory which describes self-limiting oxide growth on free metal surfaces. Curves of constant current density for a fixed voltage of 10 mV are shown as solid lines. Data for artificial barriers composed of electron-beam and sputter-deposited aluminum oxide and for Si are also shown for comparison.

resonant tunneling through impurity states in the oxide can increase the total conductance and , if not explicitly accounted for, yield an effective low barrier in the simplified model above. One way to determine the existence of such impurity states is again to look for sudden changes in the conductance-versus-voltage curves. As first calculated by Gadzuk (1970), and extended by Halbritter (1982), the contribution to the total current of the resonant tunneling current through one impurity state will have an onset at a bias voltage $V = 2\Delta U^*/e$ where the energy level of the impurity state is ΔU^* below the Fermi level (Fig. 7-8). This will result in a sharp peak in $\hat{g}$, broadened by thermal effects and by a possible distribution of such impurity states. In order to test the existence of such resonant tunneling in our junction, a plot of $\hat{g}$ was made for every conductance-versus-voltage plot. Fig.7-9 shows a typical result for a junction with a 25 Å Ta overlayer. We observe a peak at a bias voltage of 30-50 mV. This may be due to the onset of resonant tunneling via states in the oxide lying within this voltage range below the Fermi level of the base electrode. We do not, however, observe any additional peaks up to the maximum voltage to which the data were taken (~ 0.6 V). In the context of the resonant-tunneling model, this would tend to indicate the absence of a low-barrier channel of the type attributed to niobium-oxide barriers. It was not possible to extend the measurements to voltages larger than the average barrier height (~ 0.8 V) to check the existence of a broad peak in $\hat{g}$ above which would – as discussed above – give an independent measurement of this barrier height. This is because in these relatively low-resistance junctions, such a bias causes excessive self-heating and other deleterious, non reversible effects. We do observe, however, an increase in $\hat{g}$ showing the tendency to attain such a maximum (Fig. 7-9). Further, once the WKB parameters (d, ϕ, $\Delta\phi$) are extracted, a plot of the theoretical WKB conductance on top of the experimental data (Fig. 7-9) shows good agreement at the higher bias

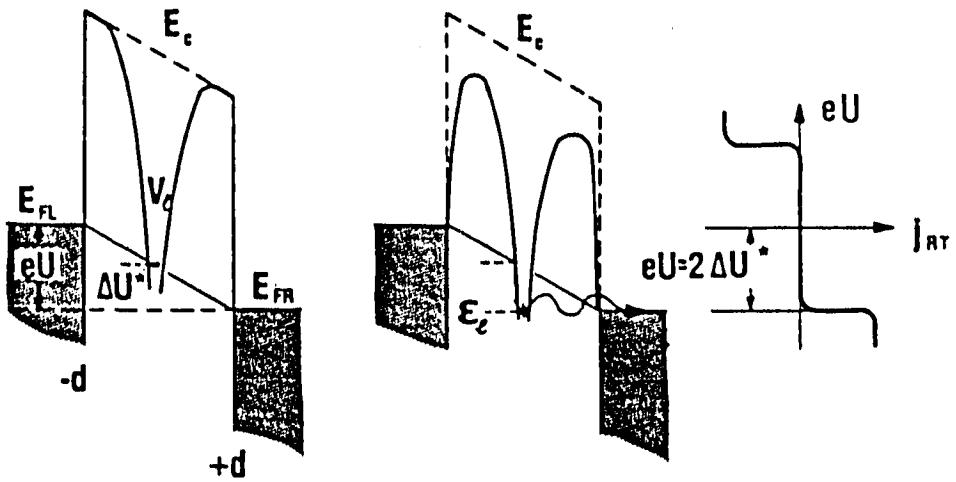

Fig. 7-8 Sketch of resonant tunneling via a state $E_\ell = \Delta U^*$ below E_F. The state is assumed in the middle of the barrrier. The resonant tunneling current has a sharp onset at a bias voltage $eV = 2\,\Delta U^*$ and thereafter saturates to a constant value. [From Halbritter (1982)].

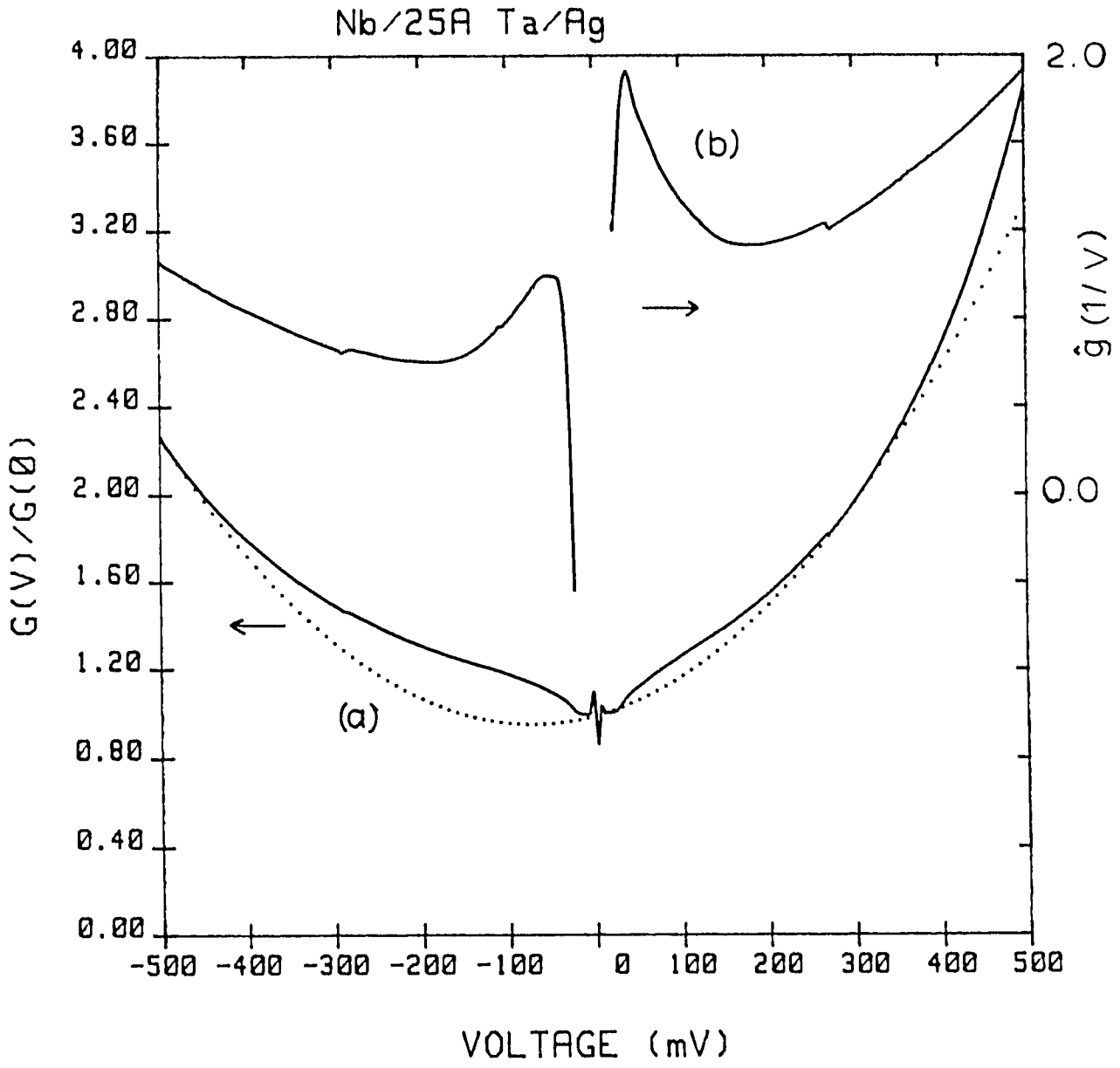

Fig. 7-9 Differential conductance (a) and logarithmic derivative (b) for a Nb/ 25 Å Ta/ Oxide /Ag tunnel junction. g displays relatively sharp peaks symmetric around zero bias which reflect the excess conductance due to resonant tunneling channels. In (a) the solid line is the experimental data and the dotted line the conductance corresponding to a trapezoidal barrier with ϕ = 1 eV, $\Delta\phi$ = 1.7 eV, and d = 14.8 Å.

voltages well within the accuracy of the approximations made to obtain the fit. The excess conductance in the bias voltage range of 30-50 mV is interpreted here as due to resonant tunneling through a distribution of localized states as discussed above. This implies that the WKB parameters extracted - at least for the Nb/Ta junctions - do reflect the intrinsic properties of the oxide barrier and are not distorted by the existence of secondary tunneling channels.

VII.C.3. Correlation with the Theory of Oxidation of Metals

One approach to model the above trend of decreasing barrier height with increasing barrier thickness is to consider oxide growth to be a self-terminating process. Consider a metal surface exposed to an oxygen-bearing atmosphere. Beyond the initial monolayer of oxide that can appear at the surface, there must be both electronic and ionic transport in order to ionize metal and oxygen atoms at the interface and provide material transport across the film [Atkinson (1985); see Fig. 7-10]. As first formulated by Cabrera and Mott (1949) and later extended by Fromhold (1976), the growth of an oxide on a metal surface will essentially terminate when the effective barrier thickness becomes too large to permit sufficient electron tunnel current to balance the ionic transport across the oxide during the growth process. This simply implies that if a growing oxide in question has an intrinsically larger barrier height, it will terminate its free growth (or experience a sharp reduction in growth rate) at a smaller thickness than an oxide with lower barrier height.

The point at which the growth "terminates" can be expressed as the point at which the electron current density just equals the ionic current density through the

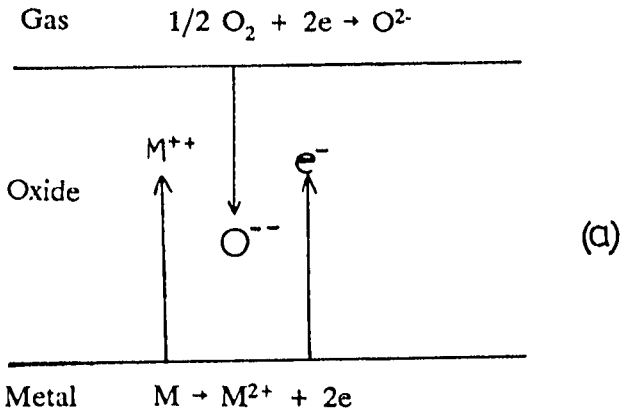

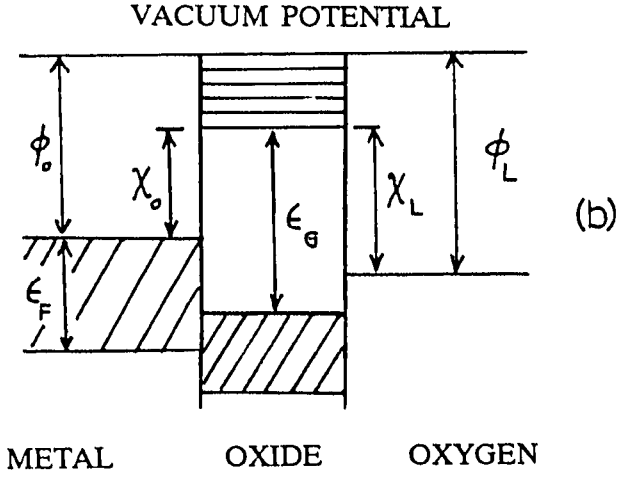

Fig. 7-10 **(a)** Transport or ions and electrons across a growing oxide film. Electron transport is by tunneling, ion transport by diffusion [From Atkinson (1985)]. **(b)** Energy-level diagramm for metal-oxide-oxygen system. The Mott potential $V_m = (\chi_0 - \chi_L)/e$ is the difference between the χ_0 – the energy difference between the conduction band in the oxide and the Fermi level in the metal – and χ_L – the electronic level in the adsorbed oxygen.

oxide. Therefore if

$$J_e = \frac{6.2 \times 10^{10}}{L^2}\left[\phi_1 e^{-1.025L(2\phi_1)^{1/2}} - (\phi_1 - V_m)e^{-1.025\,(2\phi_1 - V_m)^{1/2}}\right] \qquad (7.6a)$$

where

$$\phi_1 = \bar{\phi} + {}^1/_2 V_m \qquad (7.6b)$$

and

$$J_i = (9.63 \times 10^{-4})\,(\bar{A}\,Z/\nu)\,\sinh(\bar{L}\,/L) \qquad (7.6c)$$

then the self-limiting oxide thickness L is defined through the relation $J_e(L) = J_i(L)$ [Cabrera and Mott (1949), Fromhold and Cook (1967), Fromhold (1976), Dingham et al. (1982)]. Here, $\bar{A}$ is the oxide growth rate, $\bar{L}$ a normalized oxide thickness, Z the charge of the diffusing metal ion, and ν the molar volume of the growing oxide. V_m is the Mott potential, given by the initial difference in the metal Fermi level and the electronic level of the valence electron in O^- (Fig. 7-10).

Using measured values for these parameters for carefully controlled oxide growth on metals, within the stated experimental uncertainties [Grundner and Halbritter (1984)], the Celashi (1983) niobium datum exhibiting a barrier height of 0.7 eV is reproduced. Here the Mott potential is taken as $V_m = 0.2\,\bar{\phi} = -0.14$ eV. Keeping parameters fixed (including V_m), and varying the effective barrier height, the rest the barrier–height–versus–width curve has been generated and appears in Fig. 7-7 as the dotted line. This reflects the expected result that a higher oxidation potential (and thus a higher Mott potential) is typically associated with oxides exhibiting larger barrier heights, such as Al_2O_3. In any case, the theory tends to reproduce the general trend of the oxide-barrier data.

This approach cannot, however, answer the question of why for a given material, such as aluminum or niobium, oxides should grow which exhibit effective barrier heights of differing magnitude. The theory simply tells us that if an oxide grows with a lower barrier height, its thickness will terminate at a larger value. The explanation for this may well lie in the detailed microscopic structure of the oxide itself, the effective barrier height it ultimately manifests being determined by a perhaps highly complex physical and electronic structure dependent, in turn, on oxide-growth conditions.

An even more encompassing perspective of the behavior of tunnel barriers has been obtained by including on the plot in Fig. 7-7 the results for so-called "artificial barriers", plotted with larger symbols. These barriers are not natural oxide layers grown on the base-electrode layer of a junction, but rather prepared by the separate deposition of a tunnel barrier on the base-electrode surface. Included here a results for electron-beam- [Moodera et al. (1982)] and sputter-deposited [Barner and Ruggiero (1987)] aluminum oxide and silicon [Meservey et al. (1982)]. these data tend to both lie in the general vicinity of the natural oxide data and tend, to some extent, to follow a similar trend of average barrier height vs. width. This is especially evident for the silicon barriers which have notably low effective barrier heights. In light of these data we have also plotted on this figure (as solid lines) curves of constant current density. Thus for junctions with constant areas, these curves would translate to those for constant junction resistance. In this context, it is clear that the data overall are denser in the vicinity of $0.1 < J < 10$ A/cm^2 . This suggests that there may be a statistical predisposition for data to be found in this region. That is, if one moves sufficiently off this curve, junctions would exhibit current densities beginning to become prohibitively high or low enough to completely

preclude measurement or prohibit measurements to sufficiently high voltages to gather information on barrier shape. However, although both sets of data (natural and "artificial") may therefore naturally lie in the same general region of current density, their individual trends of barrier height with width may be different. A series of oxide barriers, produced under similar conditions, will show a decrease in barrier height for barriers of somewhat greater thickness. This may not be true for artificial barriers. Results for aluminum-oxide barriers [Barner and Ruggiero (1987)] show a greater effective barrier height for thicker barriers, even though - again - these data lie in the general vicinity of the oxide-barrier results.

Therefore, because of the restrictions imposed by actual measurements of junctions and the strong dependence of critical current density with effective barrier parameters, data for effective barrier height versus width will necessarily show a general trend of decreasing barrier height with width.

VII.D. NbN-based Junctions

This section discusses the properties of tunnel barriers on NbN base electrodes in light of the models and results discussed above.

VII.D.1. NbN Native Oxide Barriers

As discussed in chapter IV, the native NbN oxide barrier is formed by exposing the NbN base electrode up to 4 hours in room air. By applying the Brinkman method discussed above, the barrier parameters deduced correspond to low and wide barriers (ϕ = 0.2 - 0.3 eV, d = 23 - 30 Å). A plot of the logarithmic derivative $\hat{g}$ in these

cases (as in Fig. 7-11) however displays relatively broad symmetric peaks around a bias of ~ 70 mV. This indicates excess conductance in that region which may arise from tunneling through an ensemble of resonance levels lying near the Fermi level in the NbN oxide barrier. At the higher bias voltages, the resonance tunneling current saturates, and the direct barrier tunneling becomes dominant. The turning point around 280 mV indicates the cross-over from a resonance tunneling dominated region to the region of direct barrier tunneling.

We use Simmon's (1963) rectangular barrier approximation to fit the experimental conductance curve in the high bias region. The temperature dependence of the tunneling current gives a correction term of the order of 10^{-3} of the tunneling current at 77 K, and is therefore ignored [Stratton (1962)]. The fit is very sensitive to small variations of the fitting parameters ϕ and d. An optimal fit is obtained for ϕ = 0.52 eV and d = 19.3 Å for the positive bias region shown in Fig. 7-11. The same procedure for the negative bias side of the conductance curve yields ϕ = 0.58 eV and d = 18.75 Å. These values reflect better the intrinsic properties of native NbN oxide than the barrier parameters obtained by the Brinkman method. Further confidence in the values of ϕ is obtained by observing the increase in $\hat{g}$ at bias voltages approaching the above values for ϕ.

VII.D.2. Artificial Barriers on NbN

Chapter VI discussed the I-V properties of junctions formed with oxidized overlayers of Ta and Al on NbN. In addition to such oxidized metallic overlayers, AlN – an insulator– is directly deposited onto NbN to form an artificial tunnel barrier. This is done because AlN is a single-phase, wide band-gap (6.3 eV),

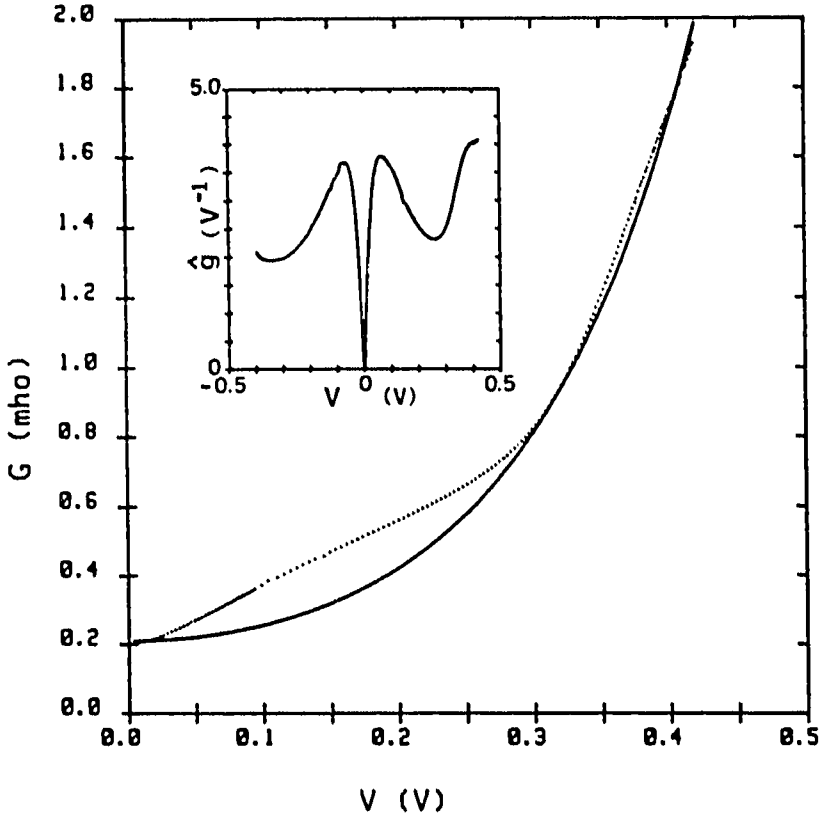

Fig. 7-11 Differential conductance dI/dV for a NbN/oxide/Ag junction at 77 K. The dotted line is the data and the solid line is a fit using a rectangular barrier model with barrier height ϕ = 0.52 eV and d = 19.3 Å. Brinkman's method (see text) of extracting barrier parameter fails in this case due to considerable excess conductance through localized states in the barriers evidenced by the peaks in the logarithmic derivative $\hat{g}$ shown in the inset.

chemically stable insulator [Harper et al. (1985)]. It thus may have good potential for use an artificial tunneling barrier. Furthermore, it can be deposited by the dual ion-beam technique, making it of particular relevance to NbN junctions. To deposit various thicknesses of AlN over the NbN base electrode in-situ, the target holder is rotated from the Nb target to the Al target. Then the parameters of the second ion source (see chapter 3) are changed to those which produce insulating AlN films. The sample is then transferred to a separate system for counterelectrode deposition. Fig. 7-12 shows the I-V curves for AlN thicknesses of 5 Å and 24 Å. As with oxidized metallic overlayers on NbN the quality of the I-V characteristic is comparable to the native oxide junctions. The voltage of the current rise decreases with increasing AlN thickness. This dependence is shown in Fig. 7-13, where is also plotted R_n, the junction resistance as a function of d_{AlN}, the AlN thickness. At low voltages, ~ 10 mV, R_n should be proportional to de^{kd} where d is the barrier thickness, k and the prefactor are functions of the barrier height and the effective mass of electrons in the barrier [see Eq. 7.2 and note that $R_n = 1/G(0)$ A]. Assuming that the barrier properties do not change when the AlN thickness is increased, the values of R_n should fit the functional form Cde^{kd} with constant C and k. Although oxidation of the surface of the AlN layer is a possibility, the fit shown in Fig. 7-13 indicates that for d_{AlN} greater than ~ 10 Å there is good correlation between the barrier width and d_{AlN}. For d_{AlN} = 5 Å, the lower R_n obtained could be due to incomplete coverage of the NbN base electrode yielding a mixed barrier of AlN and NbN oxide. Positions 1 and 2 correspond to the position of the junction on the substrate. The higher R_n values for position 2 are likely due to a gradient in the deposition rate of AlN on the substrate (see Fig.7-14).

When we apply the WKB analysis to the AlN barriers, the inferred effective

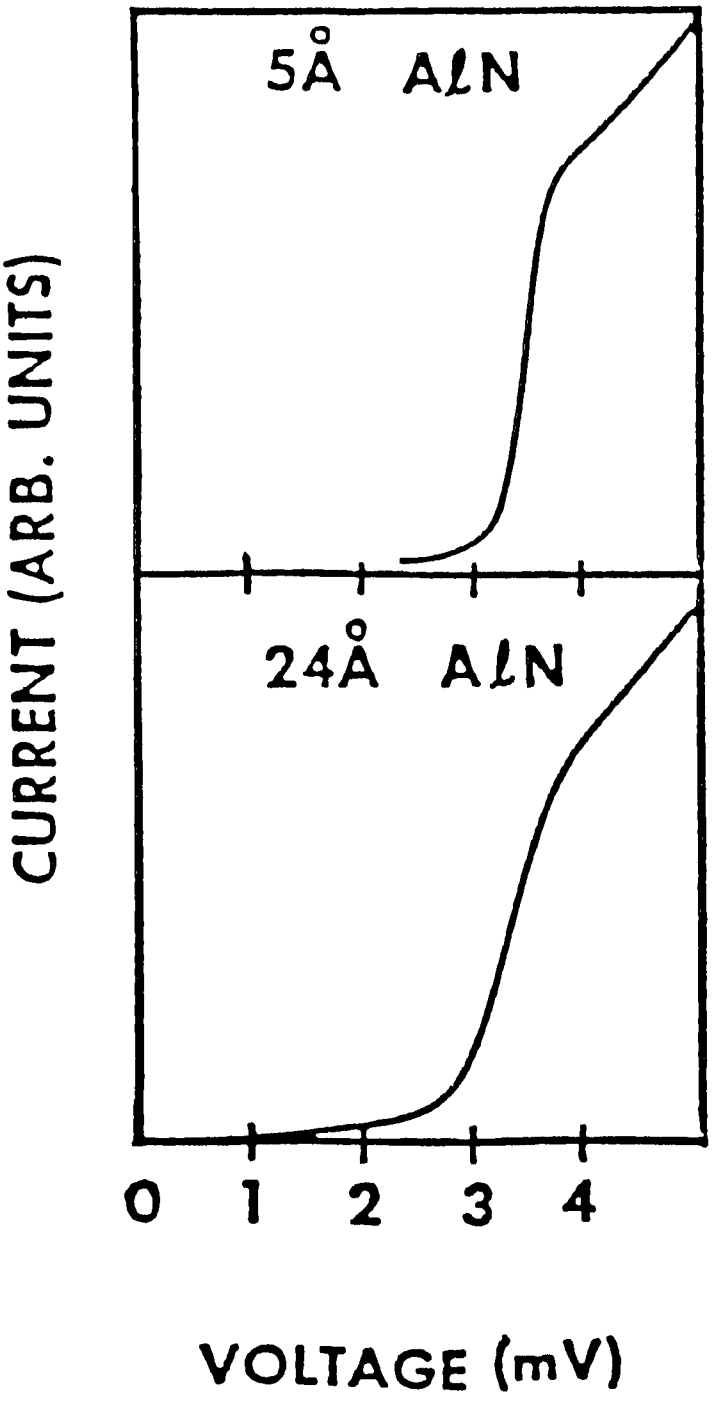

Fig. 7-12 Current voltage characteristics for NbN/AlN/PbBi junctions at 4.2 K.

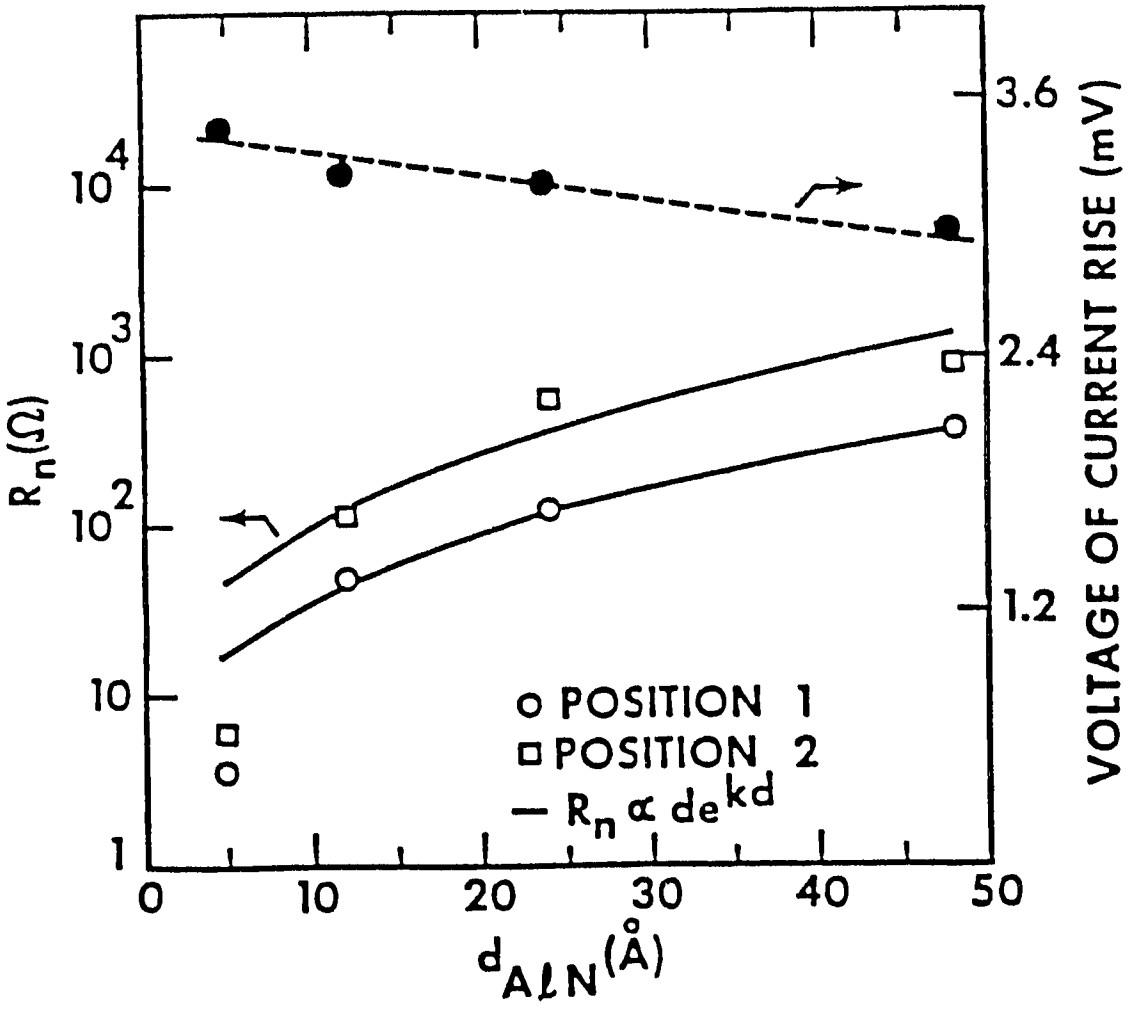

Fig. 7-13 R_n and voltage of midpoint of current rise for AlN barrier junctions. The dashed line is a guide to the eye.

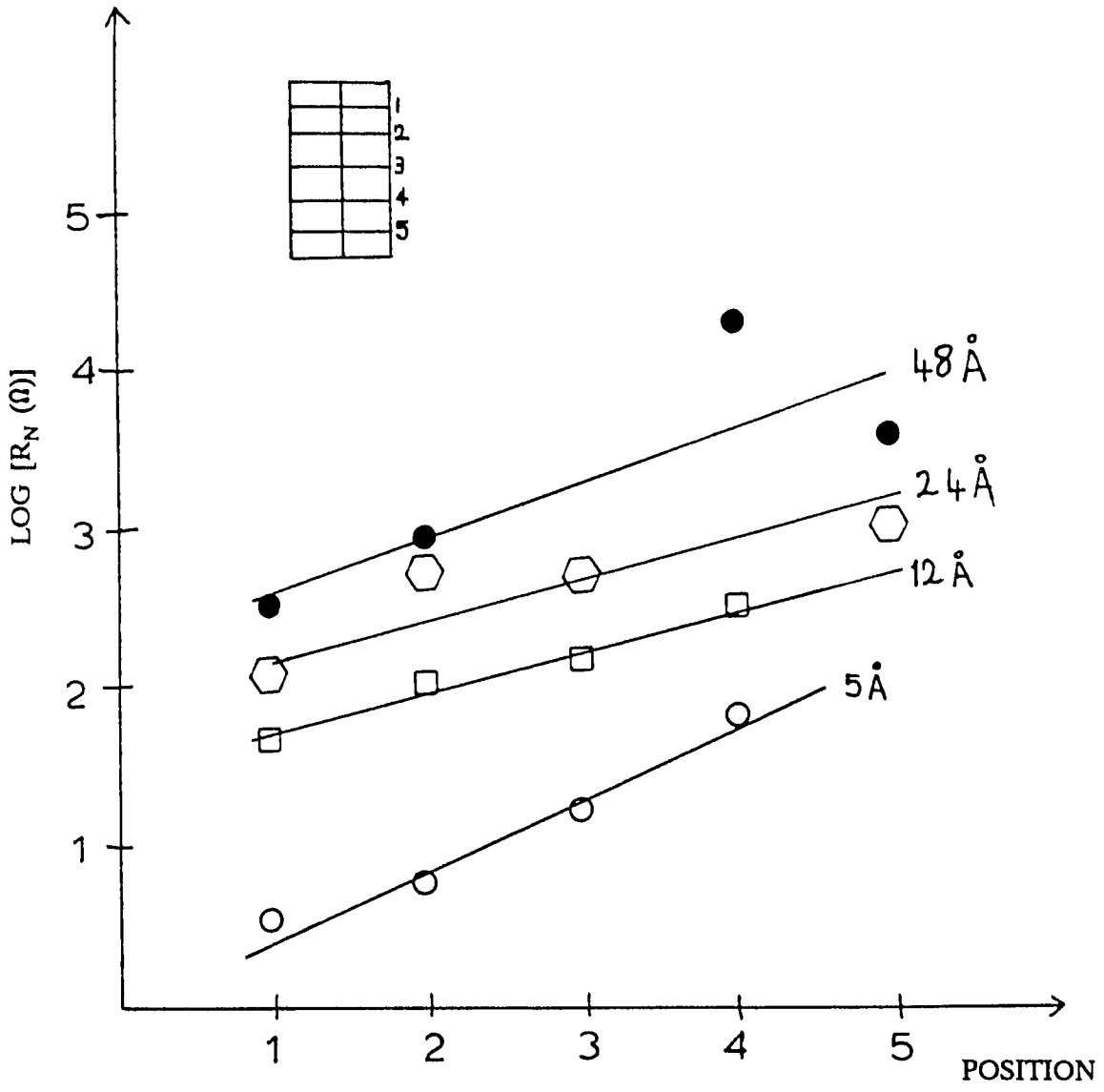

Fig. 7-14 Junction resistance R_n versus position of junction on the substrate for different AlN thicknesses. The variation of junction resistance on the same substrate for the same nominal AlN thickness is likely due to a gradient of the deposition rate of AlN.

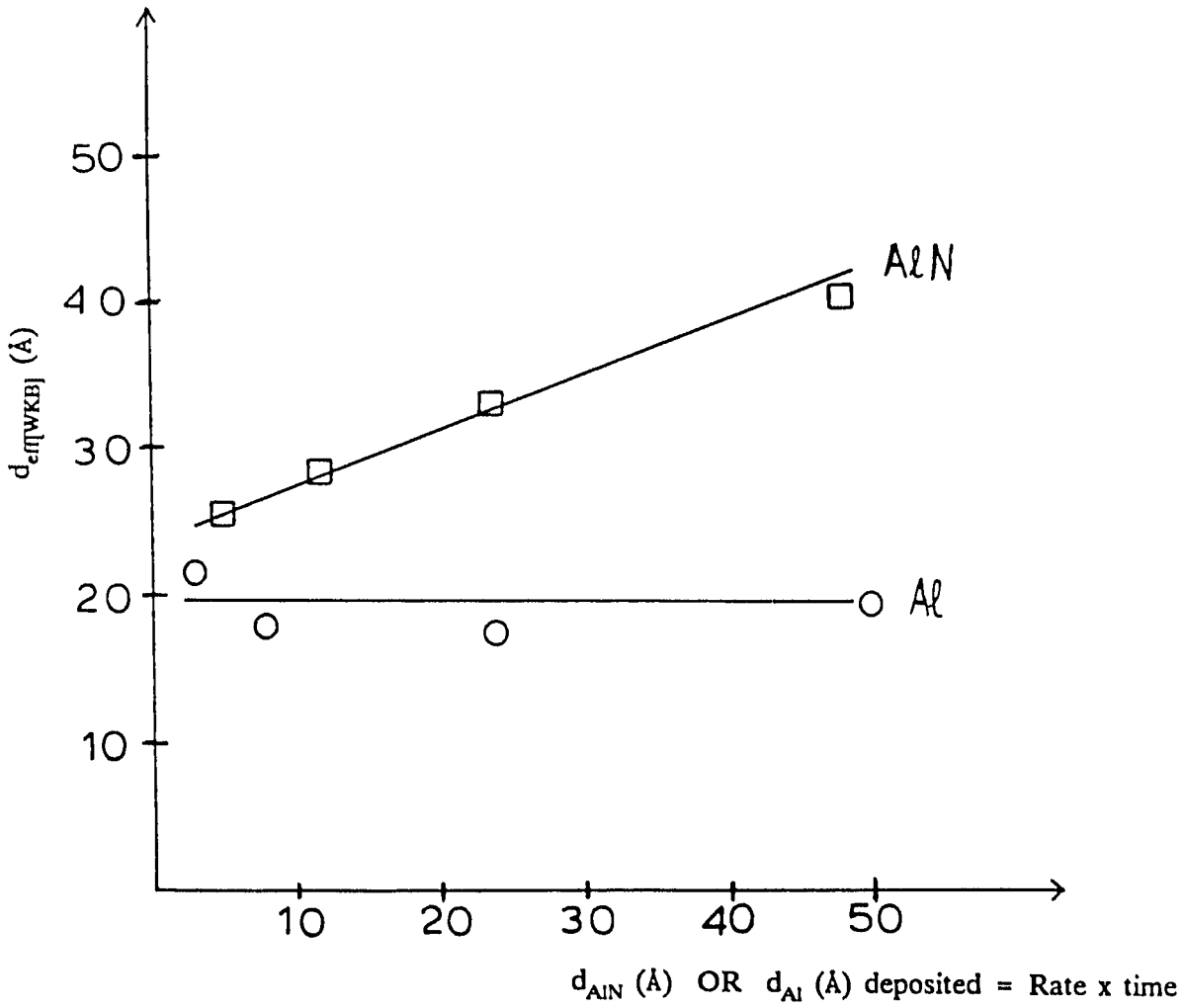

Fig. 7-15 Effective WKB barrier thickness versus deposited thickness of AlN showing good correlation. The effective WKB thickness for NbN/Al/PbBi junctions is constant as a function of Al overlayer thickness since the barrier thickness is determined by the Al oxide thickness, which is expected to be constant for similar oxidation conditions.

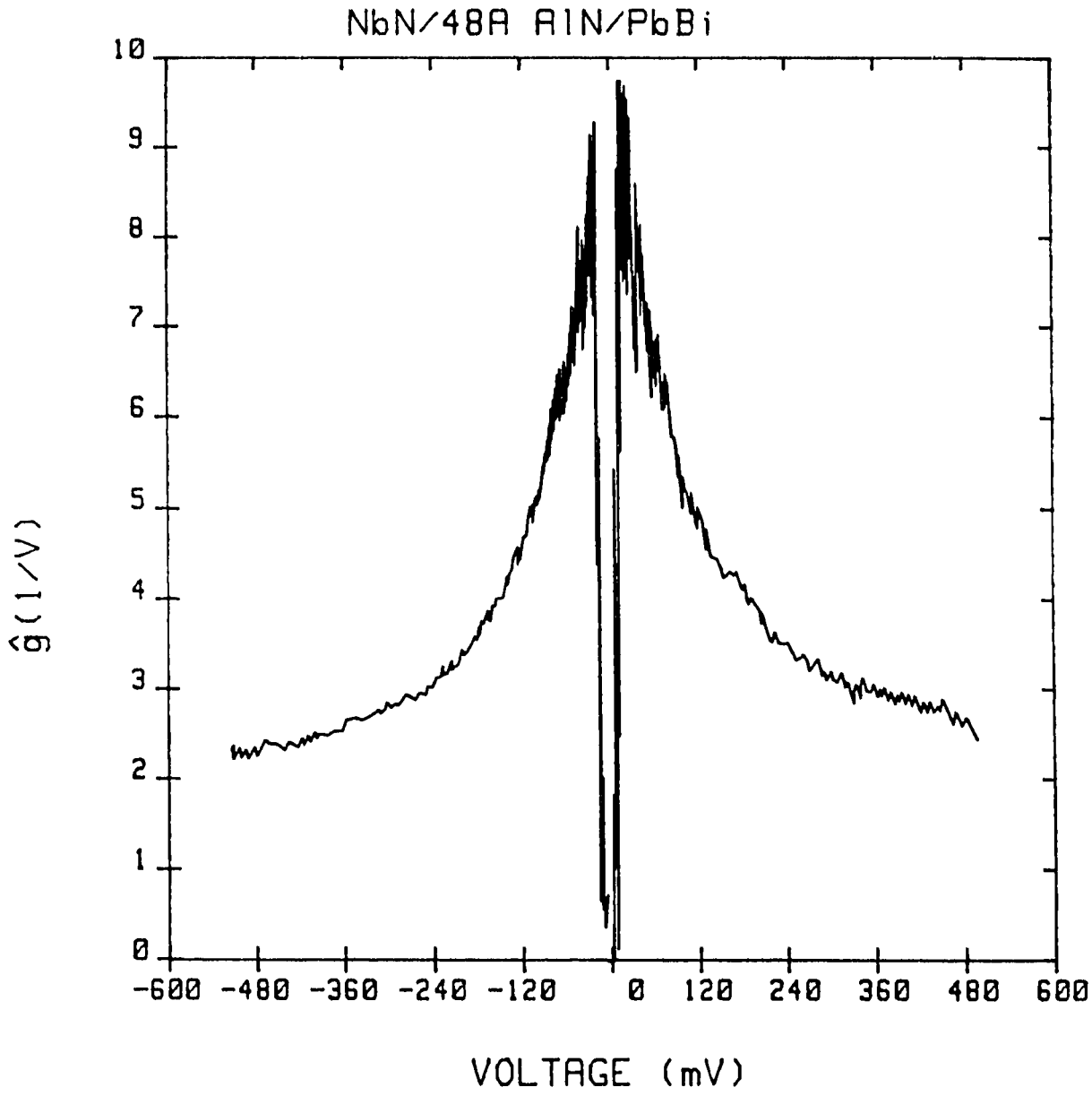

Fig. 7-16 Logarithmic derivative $\hat{g}$ for a NbN/48 Å AlN/PbBi junction at 4.2 K. Excess conductance attributable to resonant tunneling is evidenced by the peaks in $\hat{g}$ symmetric with respect to zero bias.

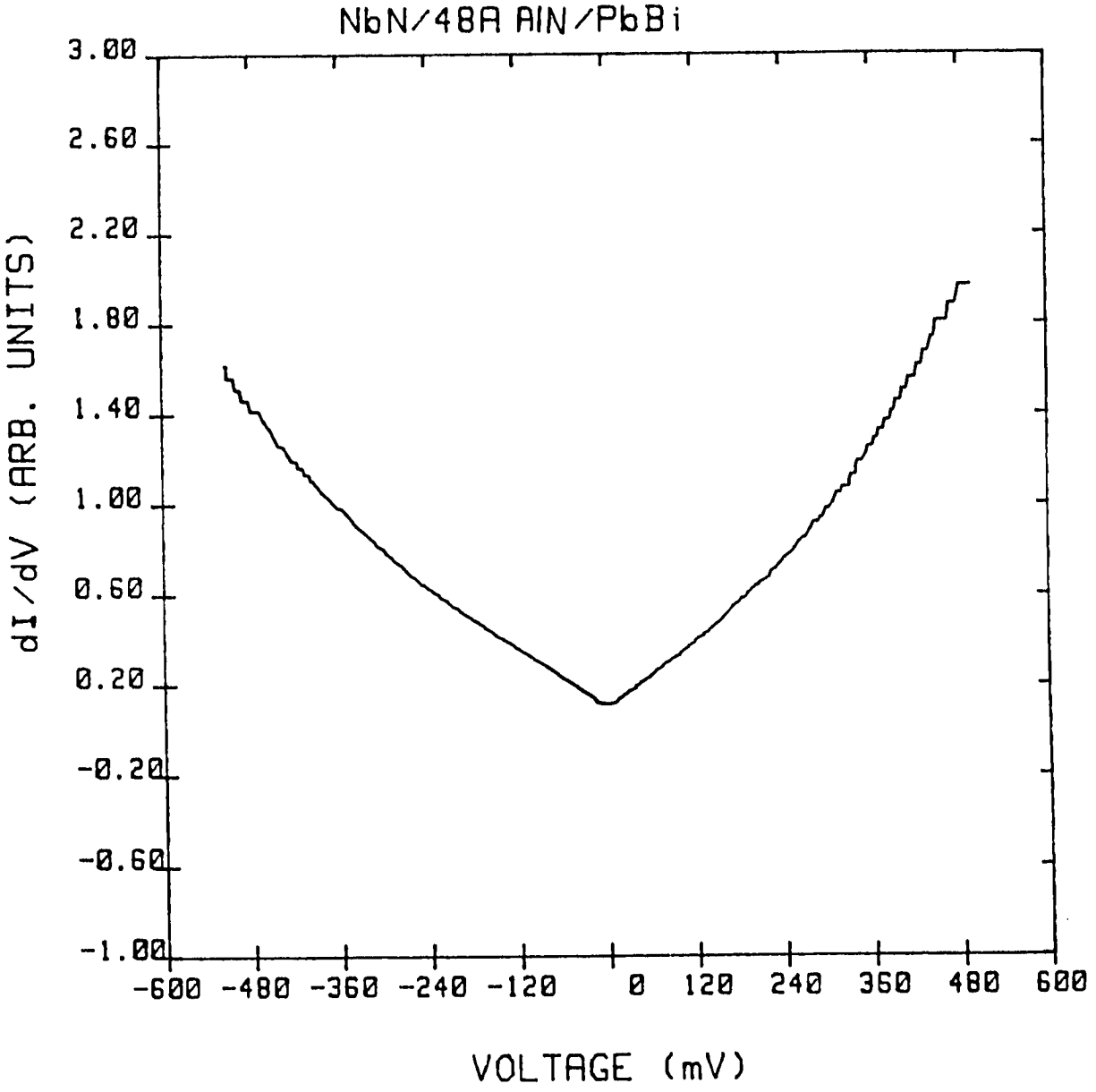

Fig. 7-17 Differential conductance for junction in Fig. 7-16.

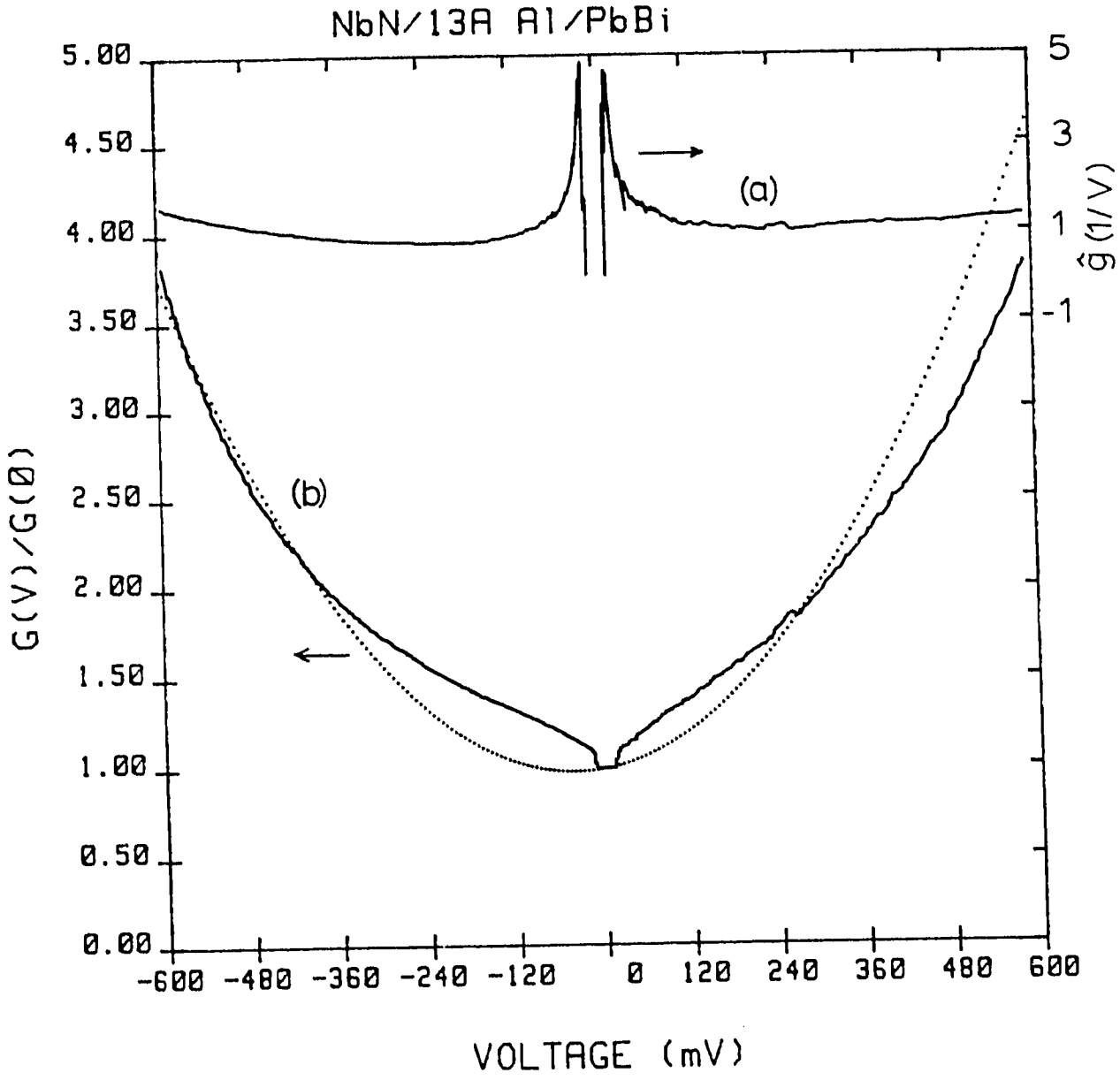

Fig. 7-18 Logarithmic derivative (a) and differential conductance (b) for a NbN/13 Å Al/Oxide/PbBi junction at 4.2 K. In (b) the solid line is the data and the dotted line the fit using ϕ = 1.2 eV, $\Delta\phi$ = 1.4 eV, and d = 18.2 Å extracted from the conductance data by the Brinkman method. The fit is good in this case because the contribution from the resonant tunneling channels are small – although nonzero – as evidenced by the narrow peaks in $\hat{g}$.

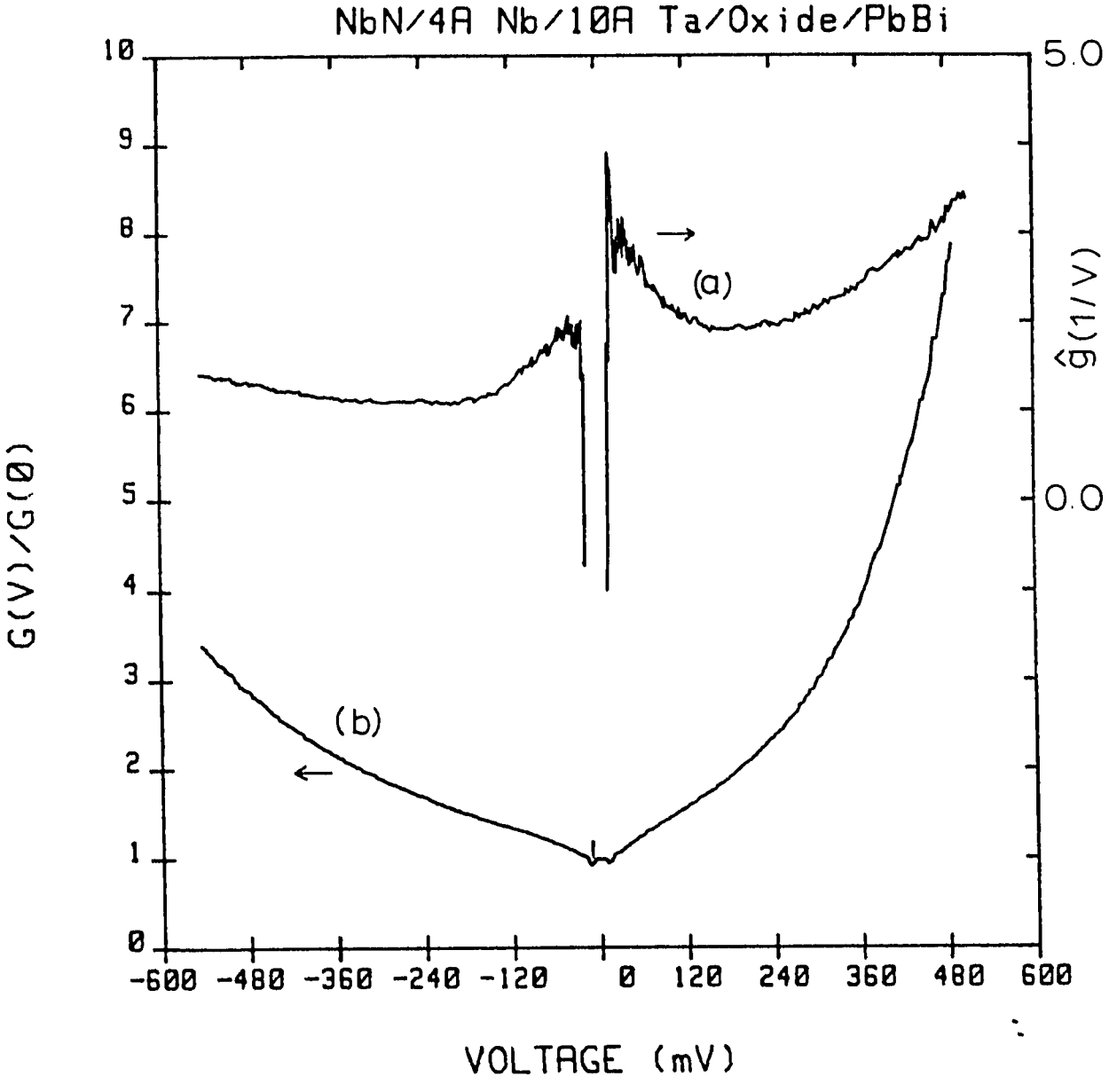

Fig. 7-19 Logarithmic derivative (a) and differential conductance (b) for a NbN/ 4 Å Nb/ 10 Å Ta/Oxide/PbBi. Note the similarity with the conductance properties of the 25-Å-Ta-ovelayer-on-Nb junction shown in Fig. 7-9, due to the fact that both reflect the characteristics of the Ta-oxide barrier.

Table 7-2 Barrier parameters for NbN-based tunnel junctions.

Sample	Counter-electrode	Overlayer or Barrier	Resistance (Ω)	d (Å)	ϕ (eV)	$\Delta\phi$ (eV)
021485F3J3	PbBi	Native Oxide	12	36	0.15	0.031
041185F4J3	PbBi	Native Oxide	5.6	31	0.18	0.092
031185F1J4	Ag	Native Oxide	3	23	0.33	0.12
041885F2J4	Ag	Native Oxide	24	23	0.35	0.19
030685F1J4	PbBi	10Å Nb+18Å Ta	12	18.6	0.66	0.7
041085F5J1	PbBi	4Å Nb+ 9Å Ta	121	20	0.74	1.7
051385F1J5	PbBi	4Å Nb+ 9Å Ta	25.6	17.5	0.84	1.9
041885F1J2	Ag	9Å Ta	72	23	0.52	0.18
-J3	Ag	9Å Ta	67	24.3	0.46	0.13
041085F3J4	PbBi	4Å Nb+14Å Al	3400	21.7	0.91	0.72
062085F2J1	PbBi	3Å Al	92	20.6	0.69	0.66
-F1J2	PbBi	3Å Al	36	22	0.52	0.42
-J3	PbBi	3Å Al	49	22.6	0.51	0.23
-J4	PbBi	3Å Al	35	21.6	0.54	0.31
062085F2J1	PbBi	8Å Al	35	18.2	0.8	0.38
-J2	PbBi	8Å Al	33	16.9	0.94	0.38
-J4	PbBi	8Å Al	42	17.9	0.86	0
-J5	PbBi	8Å Al	39	17.6	0.88	0.44
041985F8J5	Ag	8Å Al	32	22.6	0.5	0.36
051385F4J1	Ag	8Å Al	163	21.7	0.65	0.8
-J2	Ag	8Å Al	48	16.8	0.99	1.2
-J3	Ag	8Å Al	216	18.7	0.94	0.7
-J4	Ag	8Å Al	290	17.2	1.2	1.0
041085F4J3	PbBi	13Å Al	1300	18.2	1.2	1.2
051385F3J4	PbBi	13Å Al	364	24.4	0.55	0.49
062085F3J1	PbBi	24Å Al	28	18	0.81	0.45
-J2	PbBi	24Å Al	25	17.2	0.88	0
-J4	PbBi	24Å Al	13	18	0.76	0.50
-J5	PbBi	24Å Al	33	17.6	0.86	0.12
062085F4J4	PbBi	50Å Al	199	18.4	0.98	1.8
041885F7J2	Ag	3Å AlN	10.6	19.9	0.56	0.17
-J4	Ag	3Å AlN	8.8	16.6	0.82	0.51
061785F1J1	PbBi	5Å AlN	3.6	28	0.21	0.12
-J2	PbBi	5Å AlN	6	26	0.28	0.13
-J3	PbBi	5Å AlN	17	25	0.35	0.19
-J4	PbBi	5Å AlN	67	22	0.57	0.31
061785F2J1	PbBi	13Å AlN	48	33.7	0.21	0.10
-J3	PbBi	13Å AlN	113	26.4	0.40	0.32
-J4	PbBi	13Å AlN	151	25	0.47	0.29
061785F3J4	PbBi	25Å AlN	444	32.7	0.29	0.16
061785F4J1	PbBi	48Å AlN	368	39.8	0.18	0.04
-J2	PbBi	48Å AlN	896	40.8	0.19	0.04

barrier width does correlate roughly with the thickness of AlN deposited as shown in Fig. 7-15 : from d = 25 Å for d_{AlN} = 5 Å, to d = 41 Å for d_{AlN} = 48 Å. The average barrier heights obtained for AlN are ϕ = 0.2 - 0.5 eV. The plots of $\hat{g}$ versus voltage (Fig. 7-16) all show a sharp peak around a bias ~ 40 meV indicating the possible existence of localized states in the barrier. The associated conductance curve (Fig.7-17) however shows only little excess conductance and is well fitted by the WKB conductance inferred from the above parameters.

A similar treatment of the Al overlayer junctions yields the highest and narrowest barriers on NbN (ϕ = 0.8 - 1.2 eV, d = 17 - 22 eV). As expected, the inferred barrier thickness remains constant when the thickness of metallic Al is increased (Fig.7-15), since Al is expected to form a self-limiting oxide of constant thickness for similar oxidation conditions. The logarithmic derivative $\hat{g}$ in this case (Fig. 7-18) also shows a very sharp peak at low bias voltages (20 meV). $\hat{g}$ increases towards the end of the measurement range. This increase is consistent with a possible broad peak at a bias voltage ~ the barrier height. Finally, the barrier properties of the Ta overlayers on NbN are similar to those of the Ta overlayers on Nb (Fig 7-19). Table 7-2 summarizes the properties of the different barriers on NbN.

VII.E. Conclusions

The tunnel barrier properties for Nb/Ta junctions and NbN junctions have been probed by the study of the differential conductance dI/dV and the logarithmic derivative of the conductance $\hat{g}$ = d[ℓn(I/V)]/dV as a function of voltage. A simple trapezoidal barrier calculation making use of a WKB approximation allows one to model the barriers using an average barrier height ϕ and an effective barrier

width d. A general trend in barrier shape and width is observed. It is shown how the processes governing oxide growth on free metal surfaces can account for the systematic decrease in barrier height with increasing width. This, however, cannot account for the similar trend in barriers made of the same material or in "artificial barriers" formed by directly depositing an insulator to form the barrier. Analysis of the logarithmic derivative $\hat{g}$ permits the identification of excess conductance channels, which are possibly due to resonant tunneling through impurity states in the tunnel barriers. When the contribution from these channels are not explicitly accounted for, the simple trapezoidal barrier model yields parameters reflecting a broad and low barrier. However, by fitting the high-bias region of the conductance, more accurate barrier parameters are obtained since in that region the resonant tunneling current saturates andthe direct barrier tunneling becomes dominant. In some cases (e.g. native NbN oxide) this correction is significant; in many others (native Al oxide, native Ta oxide) it is negligible. In any case, even with such corrections included, the general trend of decreasing barrier height with increasing barrier width appears universal and may be due to a combination of intrinsic properties of oxide growth and the detailed electronic structure of the barrier themselves, and may be amplified by basic limitations imposed by data acquisition allowing the study of only a restricted range of current densities.

VIII. TUNNELING NOISE SPECTROSCOPY

VIII.A. Introduction: Low frequency fluctuations and 1/f noise

The previous chapter has probed the structure of the tunnel barrier through the analysis of the conductance as a function of the bias voltage. Because of the measurement techniques used (ac modulation technique for dI/dV described in chapter 5, finite response time (RC) of the instrumentation), these conductance curves represent a "time-averaged" conductance and do not reveal time-domain fluctuations which may shed further light on the microscopic structure of - and dynamics of electron transport in - the tunnel barrier. This chapter explores this other dimension, by investigating the time-fluctuations in the electron transport current when the other system constraints (voltage bias, temperature) are held constant.

Low frequency fluctuations showing a power spectral density inversely proportional to the frequency are observed in various physical, technical, biological, and economic systems. This peculiar phenomenon, which is called 1/f-noise or flicker-noise, has stimulated the research efforts of numerous scientists since the early work of Johnson (1925) and Schottky (1926). Though many results have been found and ingenious theoretical models have been developed [Voss and Clarke (1975b)] the basic problem of the origin of 1/f noise in general remains unsolved up to now. Nor is it trivial to envisage an approach that would apply simultaneously to the fluctuations in the electrical resistance of metal films [Hooge (1976); Clarke and Voss (1974)], the frequency of rotation of the earth [Munk (1960)], the potential of nerve membranes [Verveen and Derksen (1968)], the flow of highway traffic [Musha and Higuchi (1976)], and Bach concertos! [Voss and Clarke (1975a)]. Even within a

given system, present-day understanding of the origins of fluctuations is limited. Little is known, for example, about the microscopic origins of voltage fluctuations in a simple resistor. This situation has led to an attitude towards fluctuations accurately represented by the following quotation from MacDonald (1962):

" It is probably fair comment to say that to many physicists the subject of fluctuations (or 'noise' to put it bluntly) appears rather esoteric and perhaps even pointless; spontaneous fluctuations seem nothing but an unwanted evil which only an unwise experimenter would encounter!"

What about noise in tunnel junctions ? Measurements of the low frequency noise in Metal-Insulator-Metal tunnel junctions have been made by a few groups since the late 1960's [Clarke and Hawkins (1976), Zijlstra (1962), Liu et al. (1967), Lecoy et al. (1968), Kumar et al. (1977), Carruthers (1971)]. Until 1984, all of the work involved large area junctions, with $A > 100\ \mu m^2$. In all cases, the low frequency noise was well described by a classic 1/f spectrum. A typical result is shown in Fig. 8-1. The situation, however, becomes quite different for junctions of small area $\leq 1\ \mu m^2$. Rogers and Buhrman (1984) first showed that the noise-power spectrum of their submicron junctions is not well described by a simple power law. More importantly, Rogers and Buhrman (1985) also reported the observation of a telegraph-like pattern of fluctuations in these small-area junctions which they interpreted as arising from a single electron-trap in the insulating barrier. By studying the temperature and bias-voltage dependence of these phenomena, Rogers and Buhrman set the framework for the study of the trap kinetics involved, termed "Telegraph Noise Spectroscopy". Similar observations were recently reported in other small-area systems: DC SQUIDs [Wakai and Van Harlingen (1986)] and MOSFETs

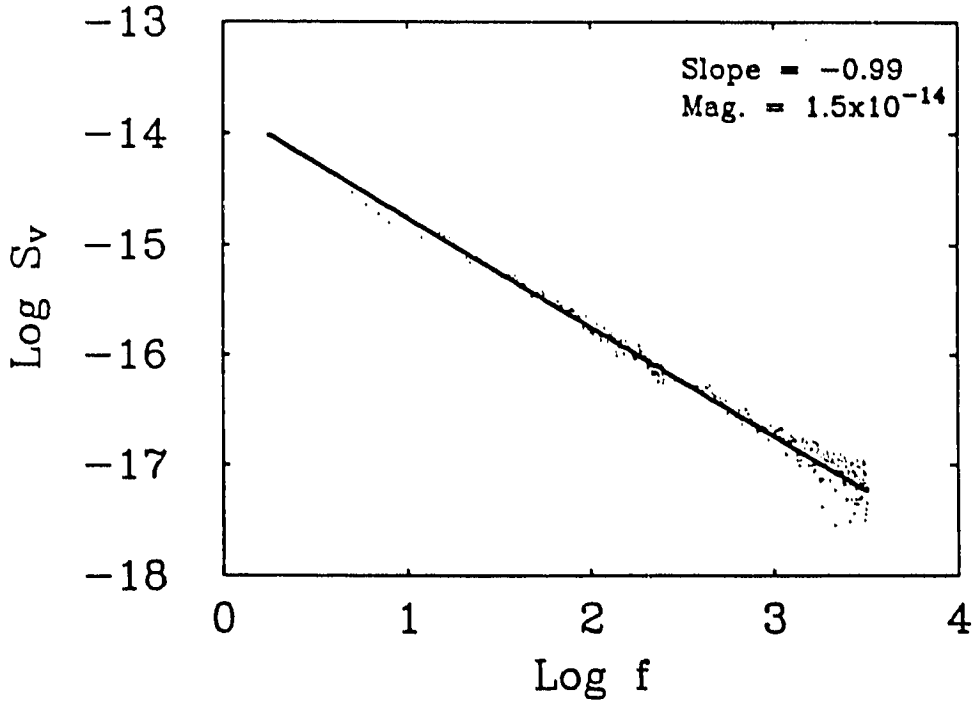

Fig. 8-1 Noise spectrum in a "large-area" Nb/ a-Si/ Nb tunnel junctions showing a classic 1/f dependence; A = 115 μm^2, R = 18 Ω, V_{dc} = 10 mV, T = 38 K. From Rogers (1987).

[Howard et al. (1985), Kirton et al. (1986)].

The importance of such observations lies in the potential they present to resolve the individual components of fluctuations which add up to a given noise-power spectrum in larger area devices. These individual components represent the signature of the true microscopic phenomena giving rise to the observed fluctuations. A key requirement for such observation is the small area of the device. It is necessary to minimize the number of "fluctuators" to increase the possibility of resolving their individual contribution. The remainder of this chapter will describe the measurement, results and analysis of the noise properties of small area ($A \leq 1$ μm^2) Ta / Ta Oxide/ PbBi tunnel junctions.

VIII.B. Noise Measurements in Submicron Ta/PbBi Junctions

The junctions measured have an area of ~ 0.2 μm^2. The fabrication has been described in chapter 4. Fig. 8-2 shows typical I-V characteristics for these junctions as compared to similar junctions of somewhat larger area (~ 1μm^2). The latter display outstanding I-V quality with very low subgap leakage and a very sharp current onset at the sum-gap. These features are essential when these junctions are used as phase-sensitive detectors (SIS mixers) [Tucker and Feldman (1985)]. Some of these junctions were in fact tested as SIS mixers at U.C. Berkeley and the results are reported in Cui et al. (1987). Given the small area of the Ta/PbBi junctions, the current density is in the range $10^4 - 10^5$ A/cm^2 to provide a junction resistance R_N within a convenient range ($10 - 10^3$ Ω) for noise measurements.

To measure the noise power spectral density, the junction is current biased

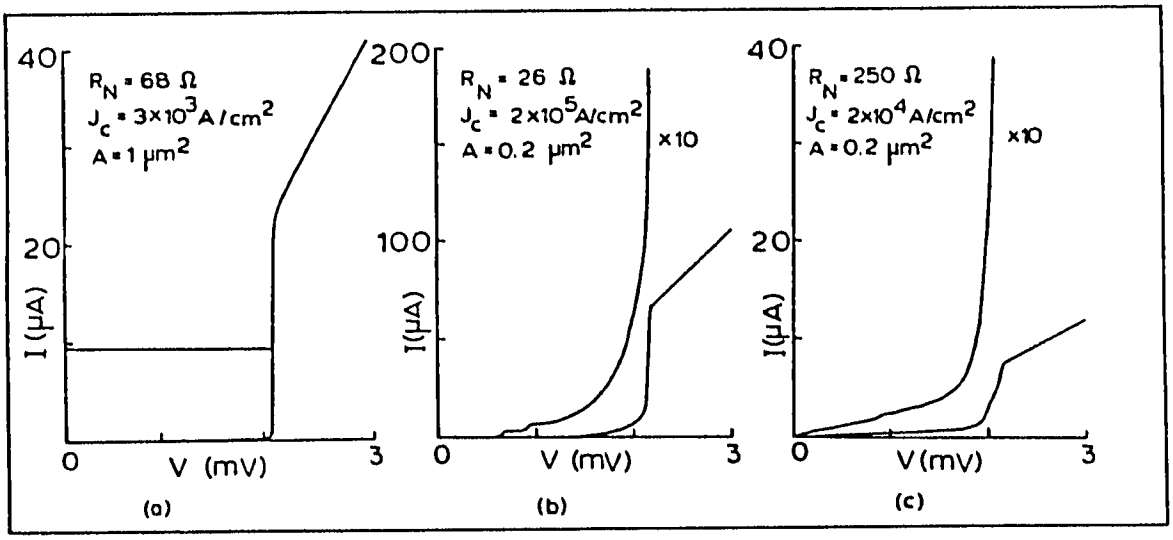

Fig. 8-2 I-V characteristics of Ta/ Ta Oxide/ PbBi junctions at 1.4 K. Above 10^4 A/cm^2, some degradation (c) in the otherwise excellent I-V quality (a) is observed although quite good quality is attainable (b) up to ~ 10^5 A/cm^2.

using the low-noise current source described in chapter 5. The voltage across the junction is amplified by a low-noise pre-amplifier. For this purpose, the amplifier used normally for I-V measurements (Analog Devices AD-524C) is substituted by a similar amplifier (Analog Devices AD-624C) which provides lower noise background. The noise voltage for the AD-624C is 4 $nV/\sqrt{Hz}$ above 10 Hz and 1/f-like below 10 Hz. The output of the amplifier is then sent to an HP3561A signal analyzer which measures the power spectral density in the range 1 - 10^5 Hz and also acts as a digitizing oscilloscope. The background power noise spectrum obtained by replacing the junction with a short-circuit is then subtracted from the total spectrum to obtain the voltage-noise power spectral density of the junction at the given bias and temperature. A schematic of the measurement apparatus is illustrated in Fig. 8-3.

Before describing the results, it seems appropriate at this point to accurately define what is meant by power spectral density and comment on its physical significance. Let V(t) equal the instantaneous voltage drop across the junction. In the steady state (I_{DC} = constant) the sample voltage is observed to fluctuate about its average value $\langle V \rangle \equiv V_{DC}$. The spectral density (or power spectrum) of V(t) is defined [Van Kampen (1964)] as the cosine transform of the voltage-voltage autocorrelation function $C_V(t)$:

$$S_V(f) \equiv 4\int_0^\infty C_V(\tau)\cos(2\pi f\tau)\,d\tau \tag{8.1}$$

where

$$C_V(\tau) = \langle V(\tau)V(0)\rangle - \langle V\rangle^2 \equiv \int S_V(f)\cos(2\pi f\tau)\,df \tag{8.2}$$

If we consider a plot of $S_V(f)$ as a function of frequency, then the area under the curve between two frequencies f_1 and f_2 represents the total power that can be

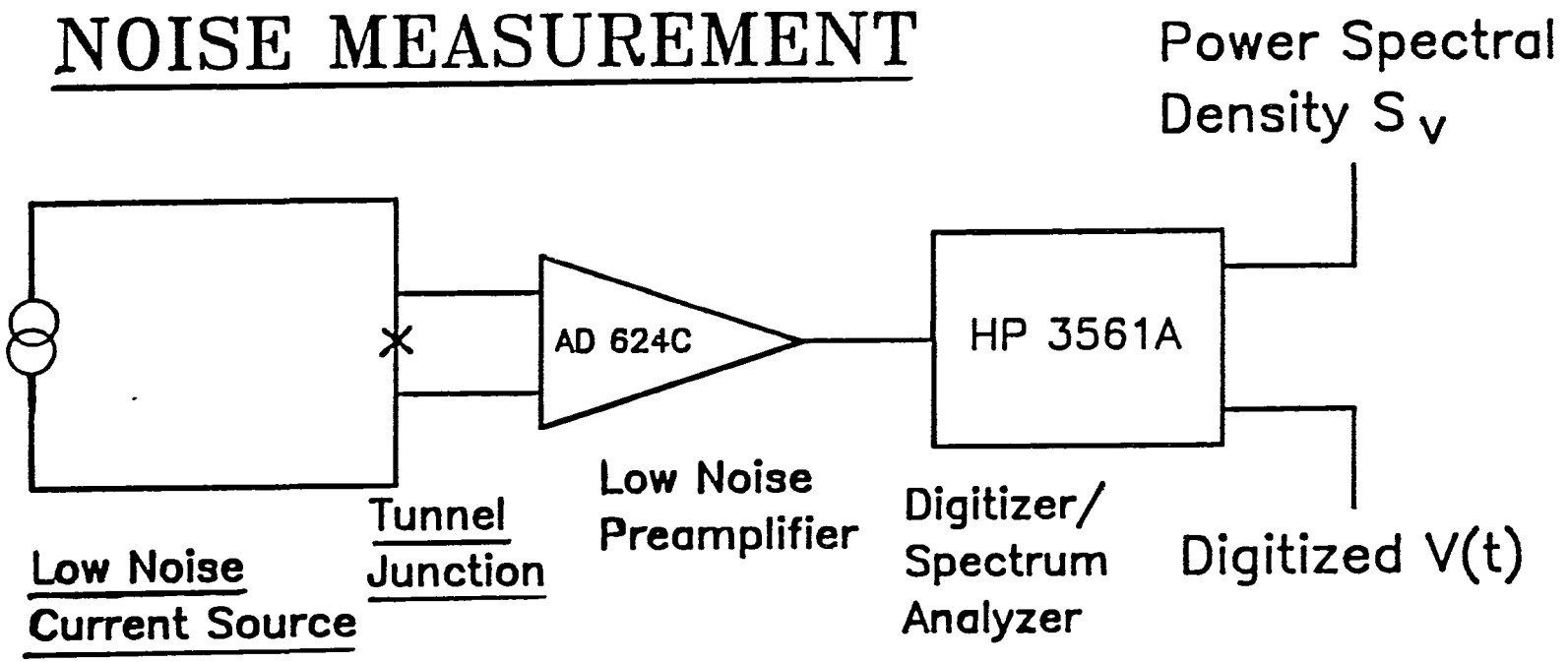

Fig. 8-3 Block diagram of the noise measurement apparatus.

generated from the time signal after filtering it with a bandpass filter between f_1 and f_2. In the actual experimental situation, the voltage is first digitized as a function of time for a period of time T, then a Fast Fourier Transform algorithm generates a power spectrum. This process is repeated, usually 1000 times, and an average spectrum is obtained by adding and normalizing the power spectra.

At certain bias levels, in the current range 0.1 - 3.0 mA and the voltage range 10 - 250 mV, the noise power spectrum displays one or several Lorentzian peaks as shown in Fig. 8-4. At the same time, the voltage displays telegraph-like pattern of fluctuation reflecting the switching of the junction resistance between two or more discrete levels. The switching corresponds to a relative change in resistance $\delta R/R \sim 10^{-3} - 10^{-4}$. For a given junction, the switching is observed only for certain values of the bias voltage. A range of the switching behavior observed is illustrated in Fig. 8-5, displaying clearly one or more two-level switching of differing magnitudes and an occasional three-level switching sequence. The observed rise-time and decay-time of the switching in most cases are limited by the time constant of the instrumentation, but in a few cases a finite extent to the rise or decay is observed (Fig. 8-5d). The frequency of the switching appears to increase when the bias on the junction is increased and when the temperature is increased as shown in Figs. 8-6 and 8-7. Many junctions with varying degree of I-V quality display this behavior.

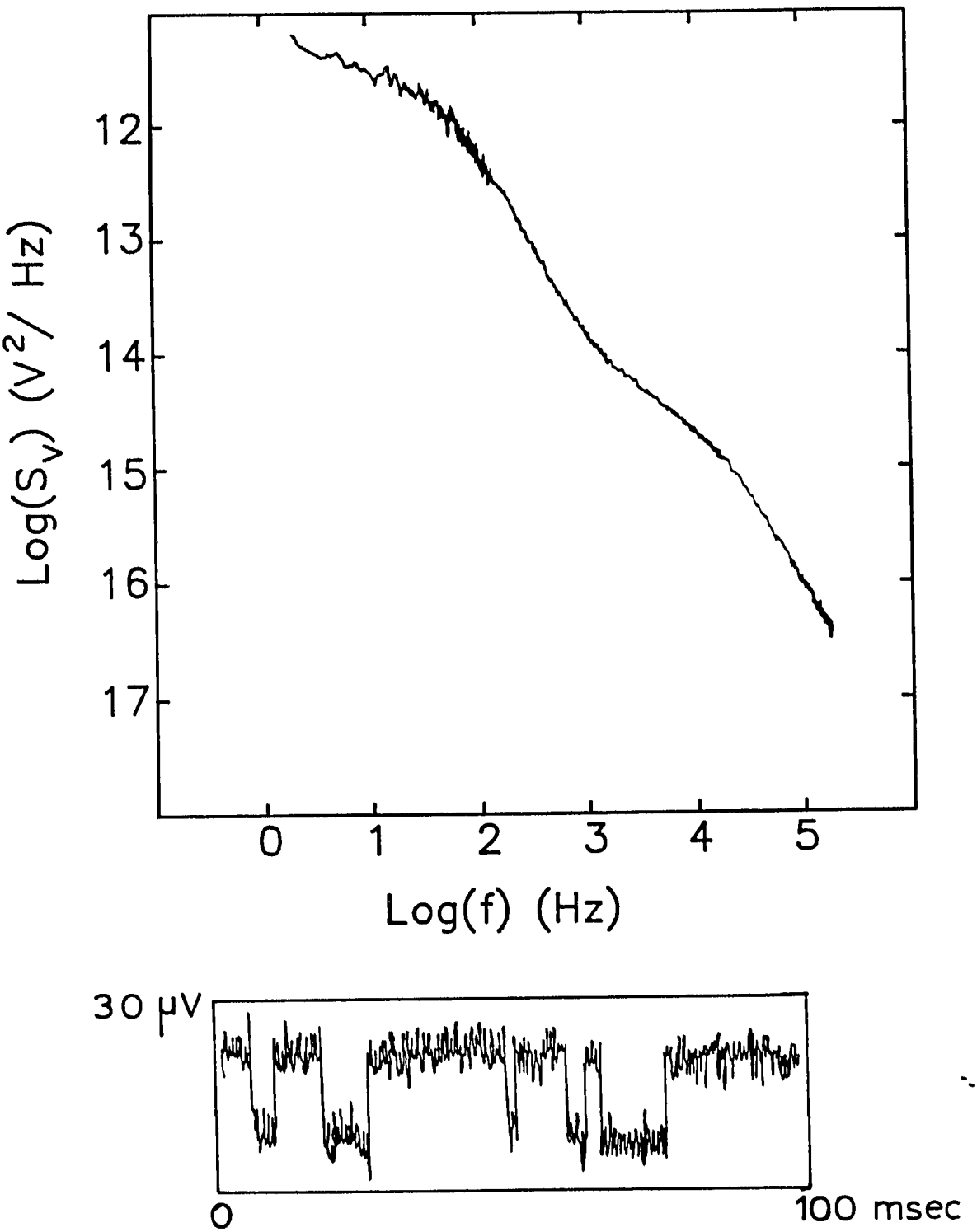

Fig. 8-4 (a) Power spectral density for a Ta/ Ta Oxide/ PbBi junctions showing two Lorentzian peaks arising from the bi-level switching events seen in (b). Notice that in (b) two sets of two-level fluctuations are displayed, each with different frequency. R = 250 Ω, T = 4.2 K, V_{dc} = 50 mV.

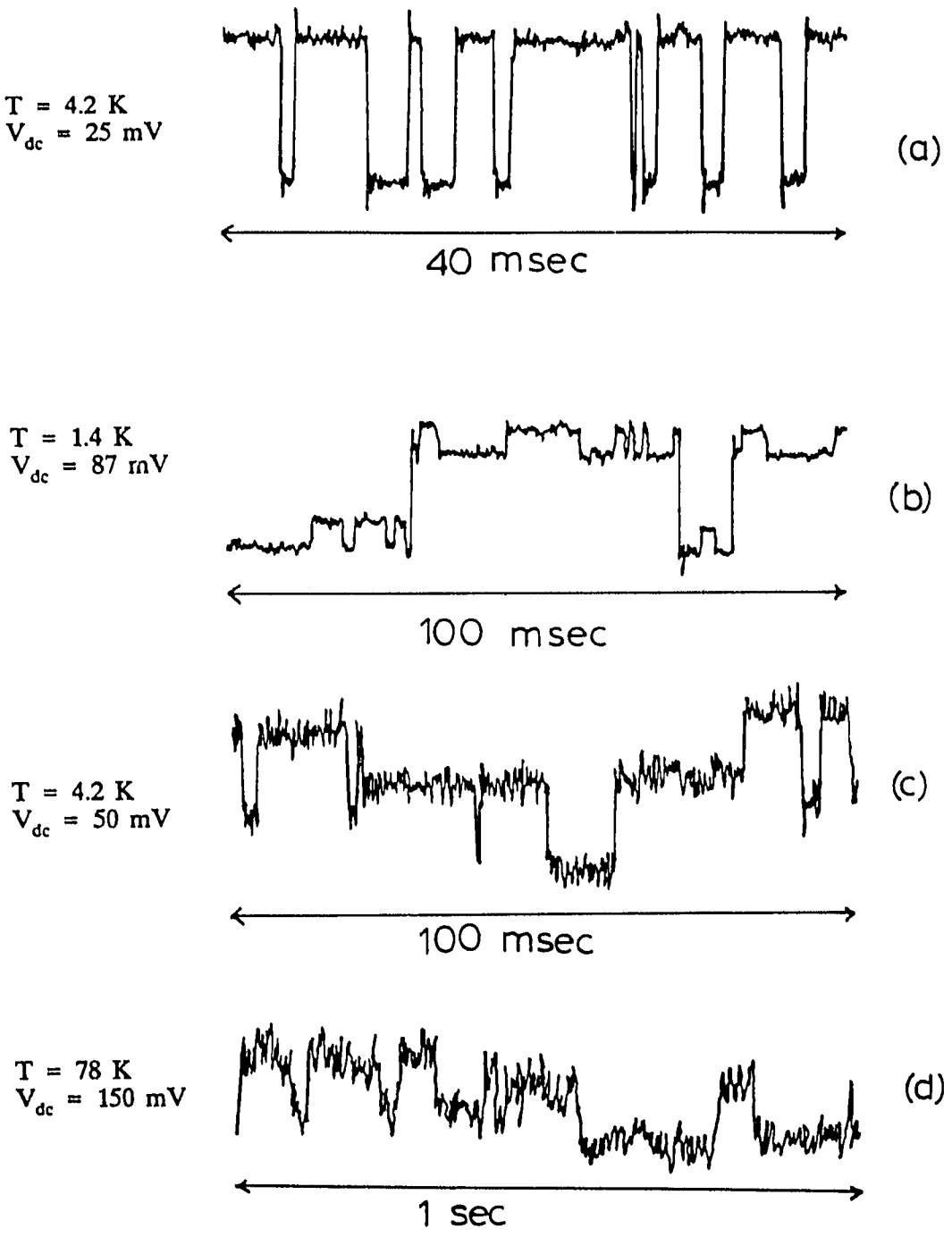

Fig. 8-5 Switching behavior observed for various junctions under different conditions: **(a)** Two-level switching; **(b)** Two sets of two-level switching; **(c)** Three-level swiching; **(d)** Finite rise-time and decay time in the switching.

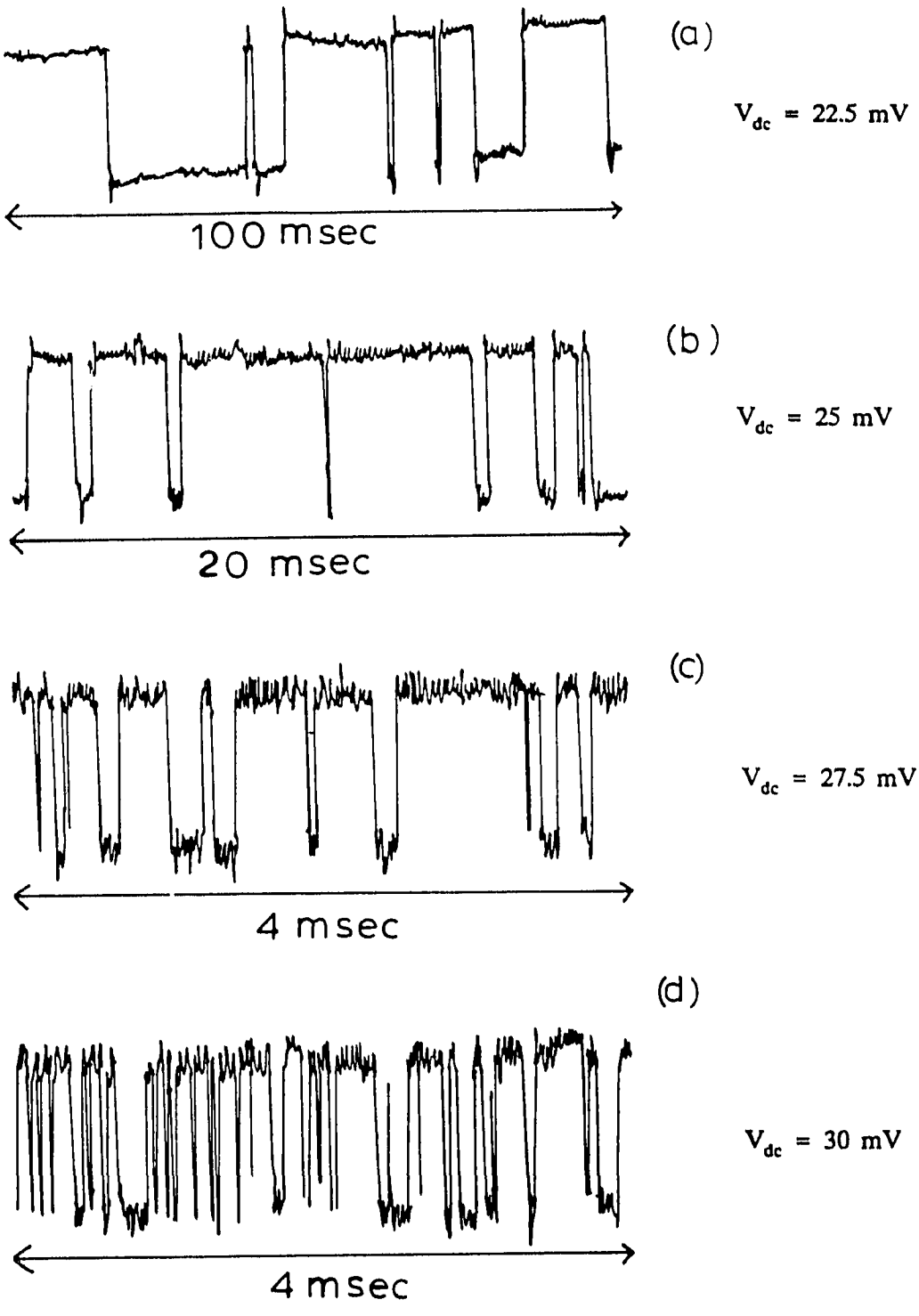

Fig. 8-6 Increase in the frequency of the switching events as the bias voltage is increased at constant temperature, T = 4.2 K.

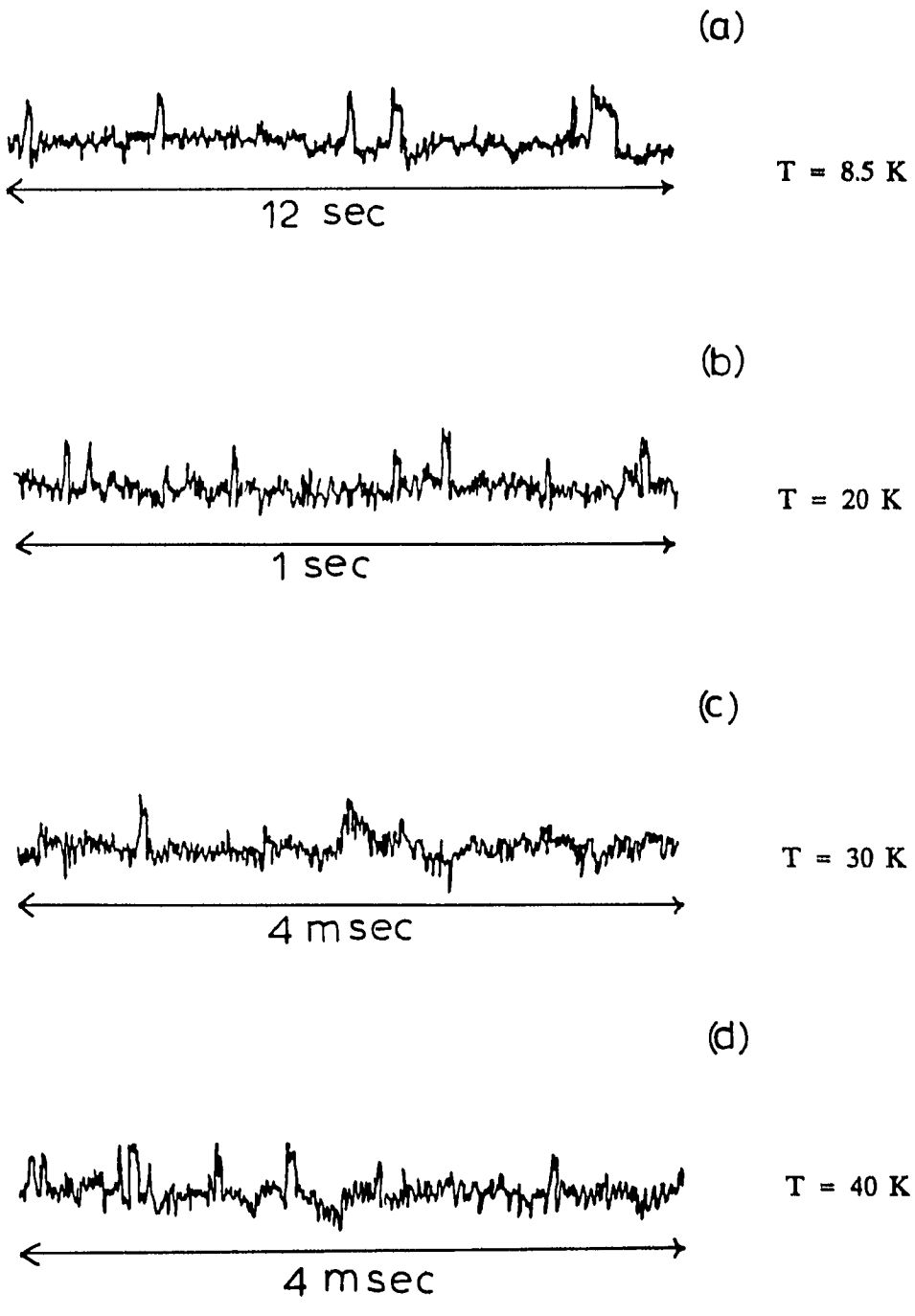

Fig. 8-7 Increase in the frequency of the switching events as the temperature is increased at constant bias, V_{dc} = 188 mV.

VIII.C. Telegraph Noise Spectroscopy: Results and Discussion

VIII.C.1. Analysis of the Telegraph Noise

By collecting a sequence of time traces displaying two-level switching and measuring the distribution of times in the high-resistance state, t_{up}, and low resistance state, t_{down}, we find that each of these times is exponentially distributed: this is evidenced by the fact that the average, $<t_{up}> = \tau_{up}$ ($<t_{down}> = \tau_{down}$), is equal to the standard deviation, σ_{up} (σ_{down}), of the distribution and by the fact that a histogram (Fig. 8-8) shows an exponential distribution with a slope equal to both τ_{up} and σ_{up} (τ_{down} and σ_{down}), within a few percent. By determining τ_{up} and τ_{down} as described and measuring the voltage jump δV, we can calculate the power spectral density due to this random switching sequence using the following equations of Machlup (1954) for a random telegraph signal:

$$1/\tau = 1/\tau_{up} + 1/\tau_{down} \tag{8.3a}$$

$$P = 4(\delta V)^2 [\tau/(\tau_{up} + \tau_{down})] \tag{8.3b}$$

$$S_V = P [\tau/(1 + \omega^2\tau^2)] \tag{8.3c}$$

Here S_V is the voltage noise power spectral density, expressed in V^2/Hz when δV is in Volts, τ in seconds, and $\omega = 2\pi f$ in rad/sec. Fig. 8-9 shows the power spectral density in a situation where the excess low frequency noise is dominated by the telegraph-like voltage fluctuation shown in the inset: the fit to Eq. 8.3 appears as the open circles and demonstrates clearly that the excess low frequency noise in this situation arises from the random switching observed in the time trace. Similar fits can be obtained when the power spectrum displays two Lorentzian peaks.

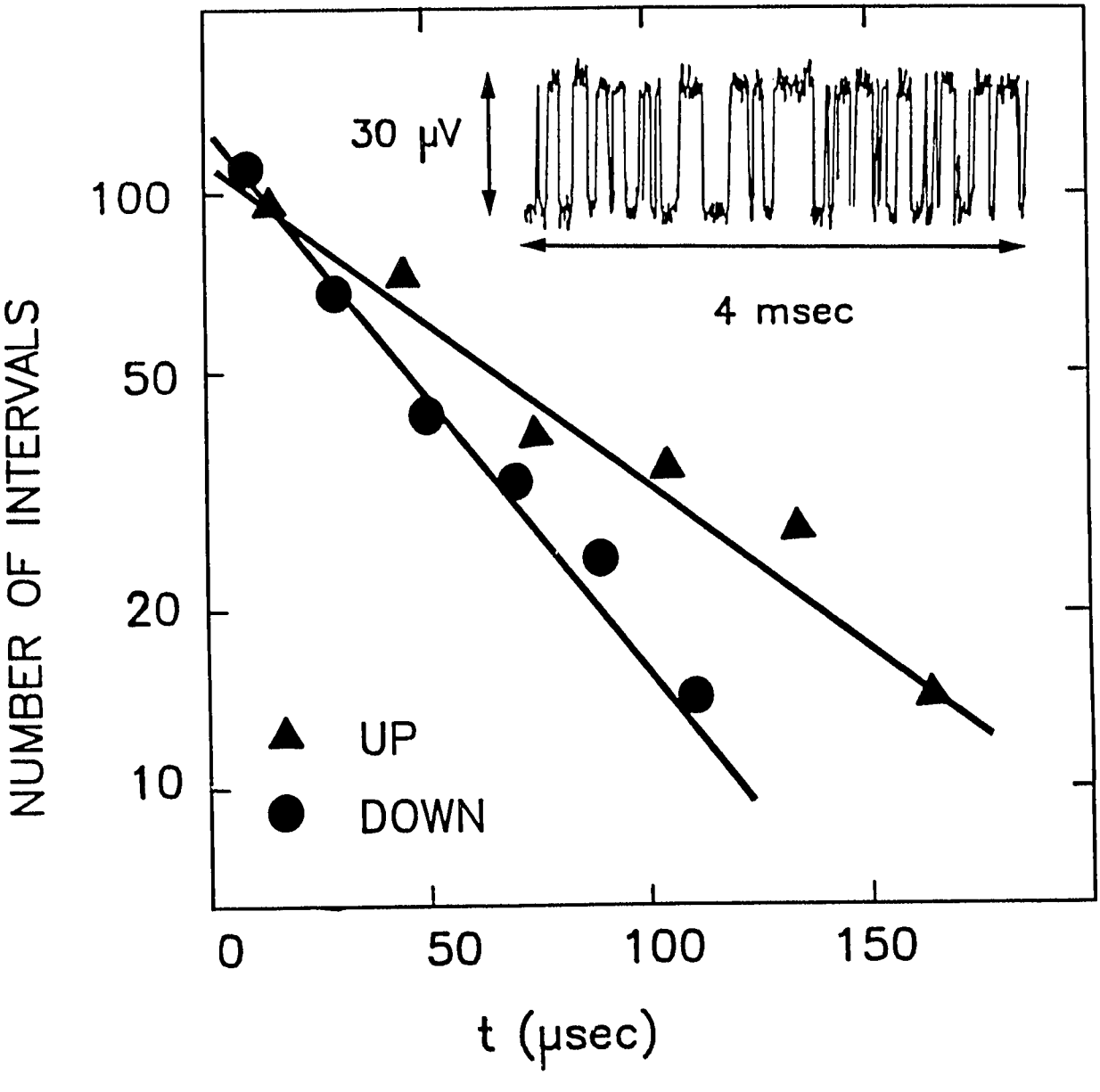

Fig. 8-8 Distribution of times in the high and low-resistance states, showing exponential dependence.

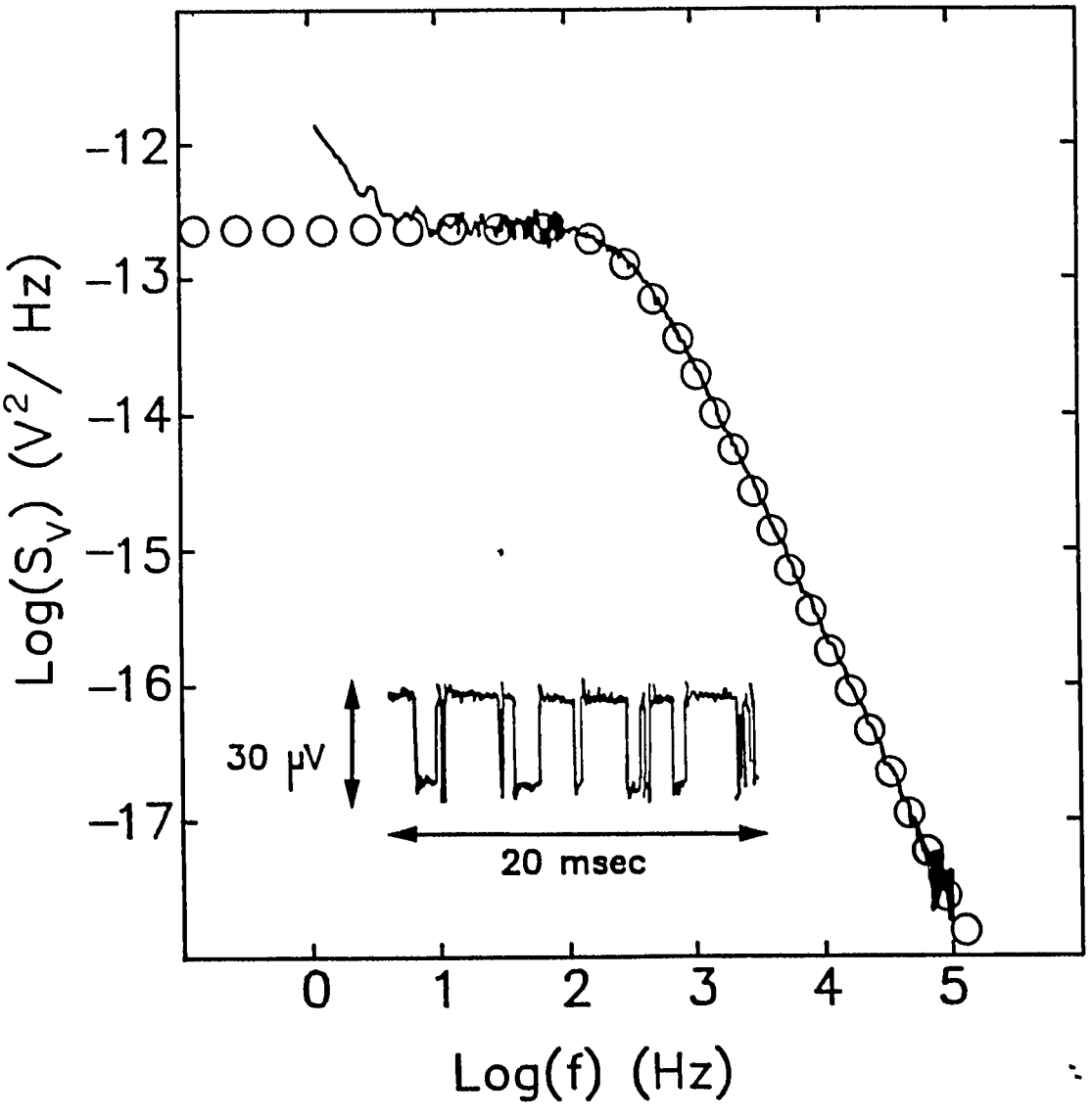

Fig. 8-9 Power Spectral Density dominated by the two-level switching of a single trap shown in the inset. O is a fit using Eqs. 8.3, δV = 28 μV, τ_{up} = 1.7 msec, τ_{down} = 0.54 msec, all measured from the time trace. T = 4.2 K, R = 250 Ω, V_{dc} = 25 mV, A = 0.2 μm^2.

Generalizing to the case of a large area tunnel junctions where a large number of such "switchers" may exist with a range of relaxation times, it is plausible to assume that the superposition of the resulting power spectra yields the observed 1/f noise. In fact the above argument attributing 1/f noise to a superposition of random fluctuations each with a characteristic time is well known [Dutta and Horn (1981)]. The importance of our own observations lies in the isolation and identification of the elementary fluctuation leading to that result. The natural question to follow is: What causes the switching? To gain further insight into the dynamics of these fluctuations we look at the dependence of the effective switching rate on 1) bias voltage 2) temperature 3) magnetic field.

VIII.C.2. Effect of Voltage, Temperature, and Magnetic Field. Microscopic Model.

The dependence of the rate (τ^{-1}) on bias voltage is approximately exponential. This is illustrated nicely in Fig. 8-10 which shows a series of power spectral densities for the same junction where only the bias voltage is varied. The knee in the Lorentzian occurs at a frequency proportional to the effective rate. It is important to note - as shown in the inset of Fig. 8-10, that both τ_{up}^{-1} and τ_{down}^{-1} vary exponentially with the bias voltage. These results agree with those of Rogers (1987) on Nb - based junctions and those of Wakai and Van Harlingen (1987) on Pb alloy junctions. The temperature dependence is illustrated in Fig. 8-11. From about 10 K to 77 K the rates vary exponentially with 1/T, and below 10 K the rates are approximately temperature independent.

Rogers and Buhrman (1985) have proposed a model explaining the microscopic origin of the switching events by the trapping and untrapping of single electrons

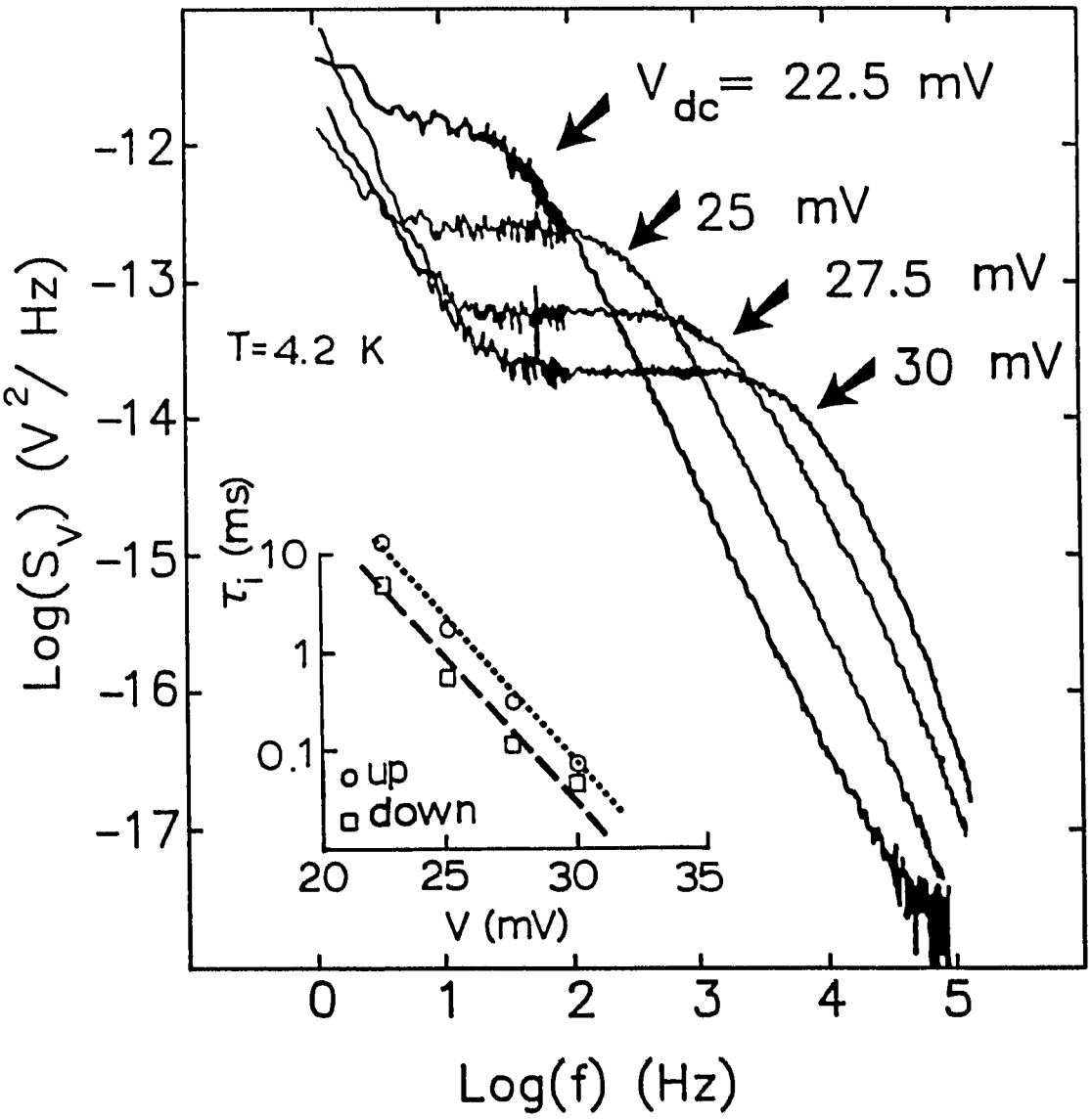

Fig. 8-10 Power Spectral Density at different bias levels. The switching rates ($1/\tau_i$) increase exponentially with voltage, as shown in the inset.

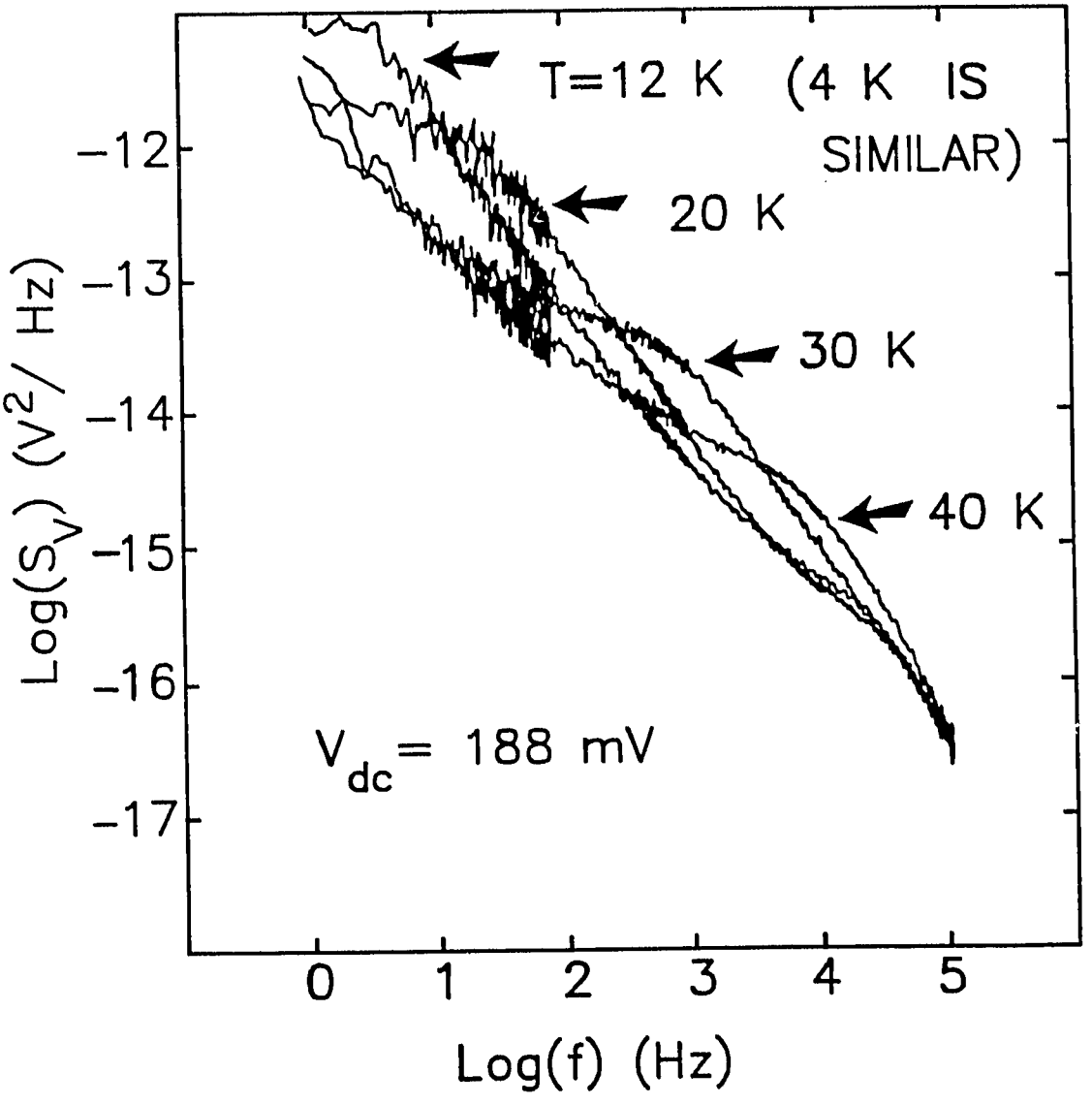

Fig. 8-11 Power Spectral Density at different temperatures. The effective rate ($1/\tau$) decreases exponentially with 1/T from ~ 40 K to ~ 10 K. Below ~ 10 K, the effective rate is approximately constant.

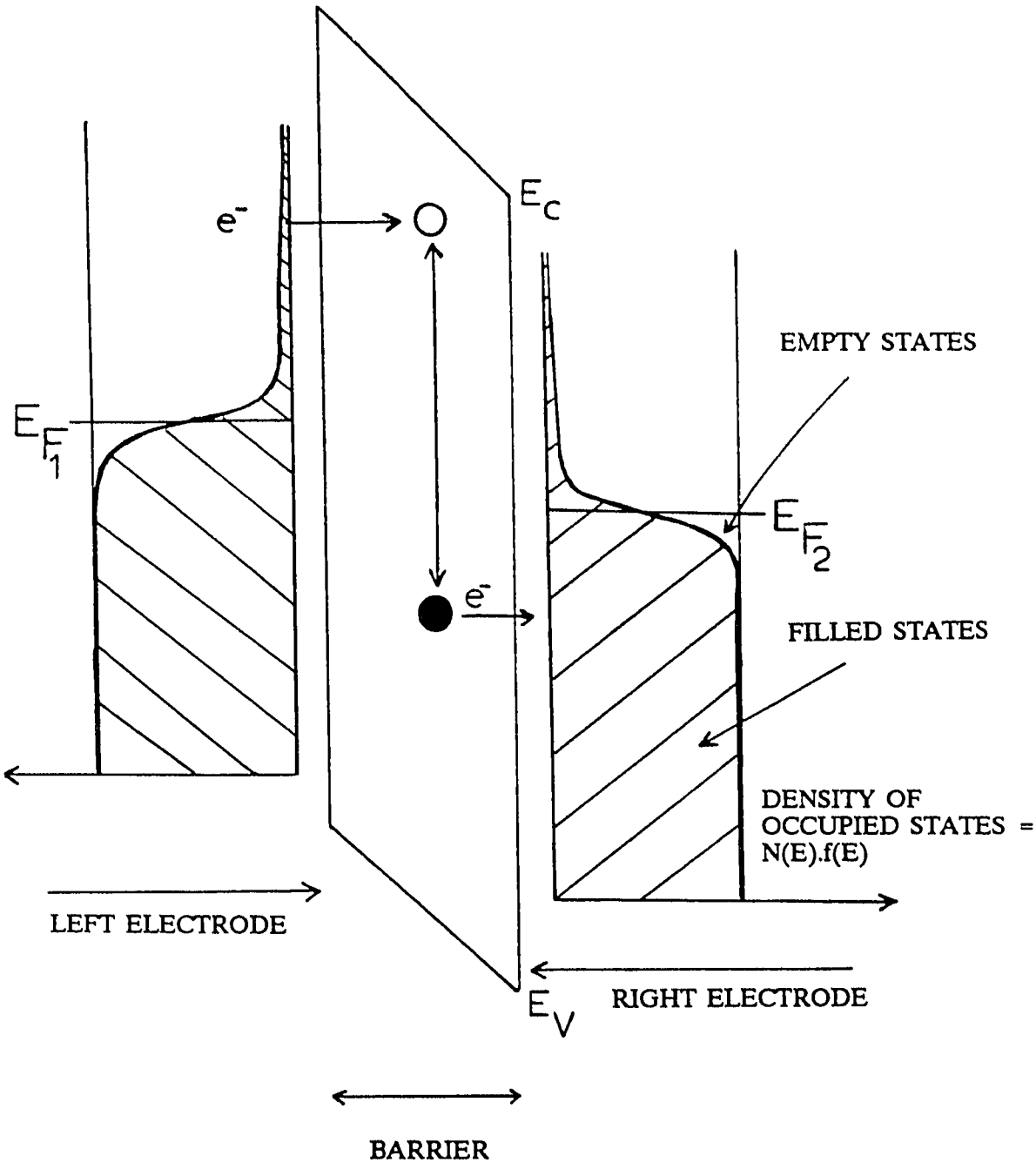

Fig. 8-12 Illustration of the Rogers and Buhrman model accounting for the bi-level switching; see text for description.

into localized defect states within the tunneling barrier. This model is illustrated in Fig. 8-12: A localized state exists in the tunnel barrier at an energy position above the Fermi level of the left electrode. The exact nature of the localized state depends on the particulars of the given tunnel barrier. In Nb-Oxide or Ta-Oxide, it could be for example an oxygen vacancy [Halbritter (1985)]. An electron from the left electrode can tunnel and be trapped into this localized state. The trapped electron causes an ionic rearrangement with the effect of 1) distorting the local properties of the insulating barrier and producing a different effective barrier thereby changing the junction resistance to a different, higher value and 2) changing the energy level of the trapped electron to below the Fermi level of the right electrode. The trapped electron can subsequently tunnel out of the localized states into an empty state in the right electrode. When the electron is thus re-emitted, the local lattice relaxes to its initial configuration restoring the initial barrier shape, and the initial value of the resistance. This model accounts for the exponential dependence of the rates on voltage and on the inverse temperature through the Fermi occupancy factor for the electron being captured into or emitted from the localized state. At the risk of being voluble let me expound on this point to avoid the reader the agony of deciphering what is a simple concept! The electron tunneling into the trap-state must have enough energy to make this transition possible. Given the energy-position of this trap state, this electron must therefore come from a state above the Fermi level of the left electrode. Those states are sparsely populated however, and the only electrons available are those within the tail of the Fermi occupancy factor $1/[1 + \exp(E/k_BT)]$. A similar argument applies to the emission of the electron into available empty states into the right electrode. Hence the exponential dependence on 1/T of both the capture and emission rates at high temperatures. Likewise, the exponential dependence of those rates on the bias

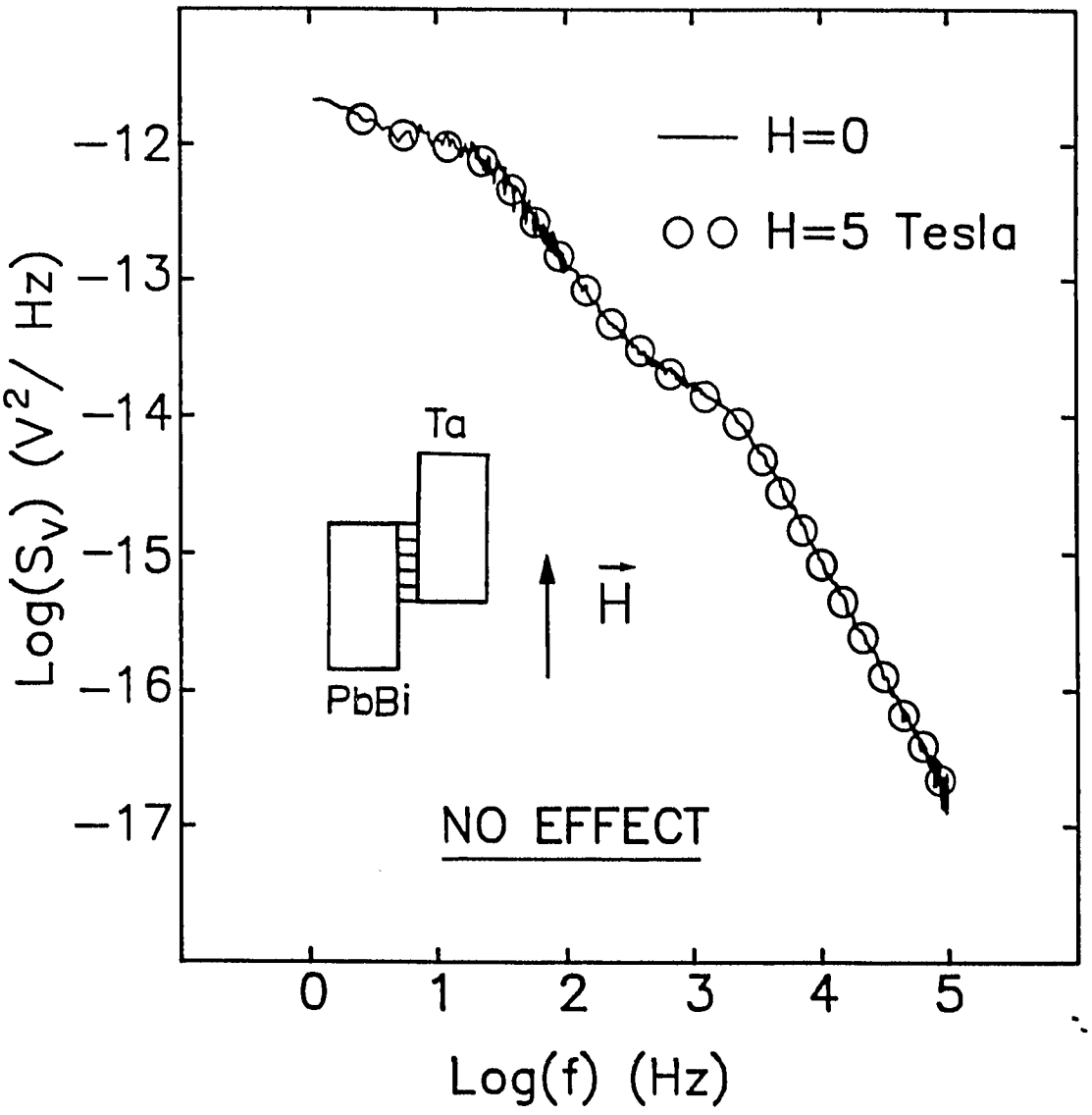

Fig. 8-13 Power Spectral Density showing two Lorentzian peaks associatd with observed two simultaneous and independent two-level switching sequences. No difference is observed in either the magnitude or the rate of the switching when a magnetif field of up to 5 Tesla is applied. T = 4.2 K, V_{dc} = 130 mV.

voltage originates from the same Fermi occupancy factor where the energy is shifted by the bias voltage applied becoming for example $1/[1 + \exp\{(E - V/2)/k_BT\}]$ for a trap in the middle of the barrier. The attempt frequency for the transitions is set by the vibrational frequency of the trap state or by the tunneling rate, whichever is lower. The deviation of the rates from thermal activation below about 10 K is attributed to transitions between the two ionic configurations via ionic tunneling.

In order to gain further insight into the microscopic mechanisms involved we have studied the effect on the switching of an external magnetic field applied parallel to the plane of the junction. As illustrated in Fig. 8-13, we find that, up to 50 kGauss, no measurable effect is observed in either the magnitude or the rates of the switching.

VIII.C.3. Correlation with Barrier Spectroscopy

Chapter 7 detailed how the differential conductance dI/dV and the logarithmic derivative $\hat{g} = d[\ell n(I/V)]/dV$ are a probe of the localized states in a tunnel barrier. As in the larger area junctions of chapter 7, we observe in the small Ta/PbBi junctions excess conductance in the bias voltage range 40-100 mV (see Fig. 8-14). This excess conductance manifests itself more clearly as a broad peak in the logarithmic derivative $\hat{g}$. Each peak indicates the onset of new conductance channels associated with localized states in the barrier. The ac modulation voltage typically used in measuring dI/dV is much larger than the magnitude δV of the telegraph noise. However, when we decrease this ac modulation to a level smaller than δV, we observe telegraph noise in the same voltage range where the excess conductance is observed. This is shown in Fig. 8-14 This correspondence is an

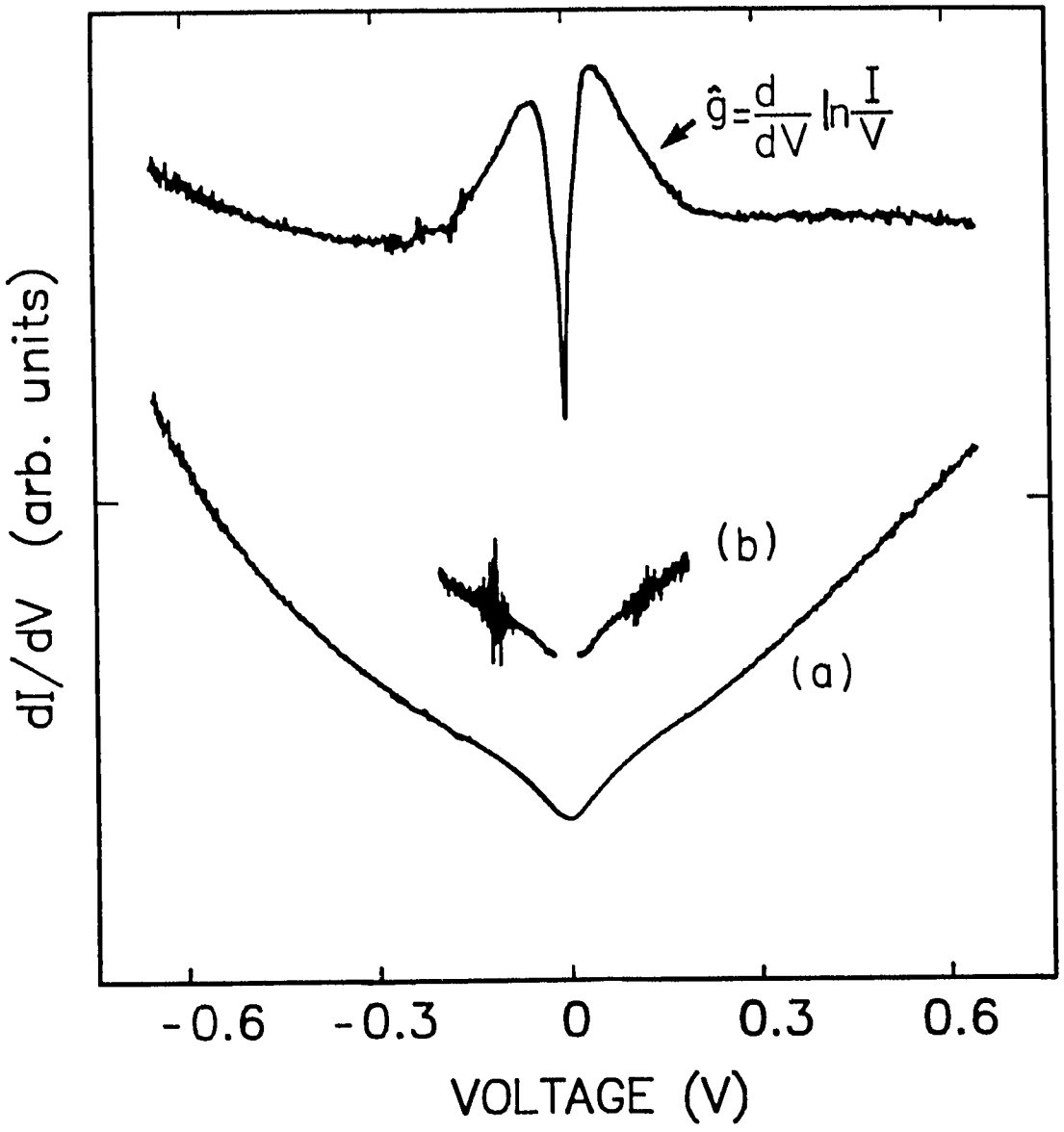

Fig. 8-14 (a) dI/dV at 10 K with an ac modulation of 500 μV; the excess conductance in the range 30-100 mV is reflected in the corresponding g shown above. (b) dI/dV at 2 K for the same junctin with an ac modulation of 8 μV (offset for clarity); telegraph noise is seen in the same bias range as the excess conductance.

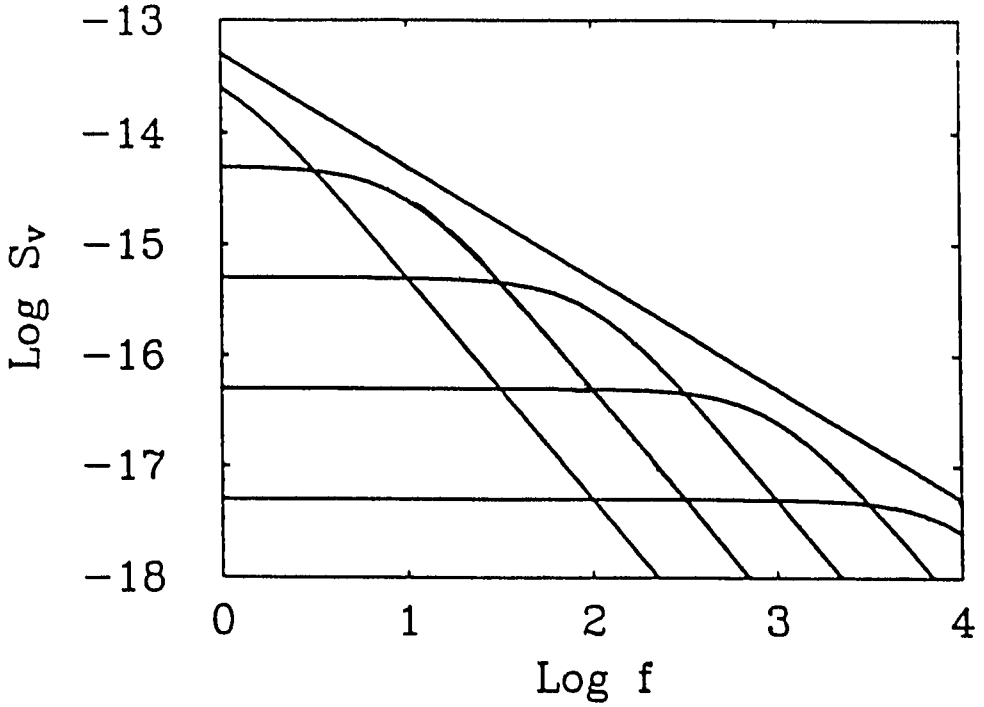

Fig. 8-15 Illustration of a 1/f spectrum arising from a sum of Lorentzian contributions.

indication that the same localized states giving rise to the excess conductance may be undergoing bi-level transitions which cause the telegraph noise.

VIII.D. Conclusions

This chapter discussed the observation and analysis of telegraph noise in the conductance of Ta/Ta Oxide/PbBi tunnel junctions. Discrete voltage switching events allow the identification of the effect of single localized states in the oxide barrier. The voltage and temperature dependence of the switching rates are consistent with a microscopic model based on the emission and capture of individual electrons at the localized sites within the barrier. This mechanism appears to be the major source of low-frequency noise in these Ta/PbBi junctions for the bias range (10 - 250 mV) where switching is observed. In larger area junctions, the superposition of fluctuations from a large number of such localized states may be at the origin of the observed 1/f noise (Fig. 8-15).

IX. SUMMARY AND CONCLUSIONS

This research has resulted in a number of contributions to the fabrication, characterization, and understanding of transport properties in tunnel junctions. The use of thin Ta surface layers on Nb has been shown to reliably produce tunnel junctions with nearly ideal characteristics. The detailed shape of the I-V curve of a Nb/Ta junction, including a sharp bound-state peak, has, for the first time, been accurately reproduced by the proximity-effect tunneling theory. Both the critical current and bound-state energy position of the junctions have been studied as a function of Ta surface-layer thickness. Calculations were performed of the critical current were including strong-coupling corrections from both base-electrode and counterelectrode metals. Self-consistent fits to the bound-state energy E_0 and product I_cR versus D_{Ta} are in accord with the proximity-effect theory and give a value for the electron reflection probability at the Nb/Ta interface of $r^2 = 0.01$. This value is consistent with the simple model which assumes that a major fraction of this interfacial scattering is due to the potential step created by the Fermi-level difference between Nb and Ta. The behavior of the phonon structure of Ta surface layers on Nb as a function of Ta thickness has been studied. It is seen that the Ta phonon structure dominates the observed spectra until $D_{Ta} \leq 50$ Å and that, by all indications, there is no mixing but a simple superposition of these spectra.

Studies of both native-oxide and surface-layer junctions reveal a general trend in barrier shape and width. A model is presented, based on the Cabrera-Mott theory of oxidation of metals, that can account for the systematic decrease of barrier height with increasing barrier width. This model, however, cannot account for the similar trends observed in deposited barriers. The complex nature of the

tunnel barrier, with parallel conductance channels, along with basic limitations imposed by data acquisition requiring a restricted range of junction resistances may in this case account for the above trend. Excess conductance which may be due to resonant tunneling through localized states in the tunnel barrier is observed to varying degrees in all junctions. An analysis based on the use of the logarithmic derivative of the conductance is applied to separate this resonant tunneling from direct barrier tunneling.

A new fabrication technique – dual ion-beam sputter deposition – is explored for the synthesis of the refractory superconductor NbN. It is shown that this method is capable of producing good quality films with superconducting transition temperatures up to 13 K on room-temperature substrates. The properties of the NbN films fabricated in this fashion are investigated through measurements of resistivity, residual resistivity ratio, superconducting energy gap by tunneling, transmission electron microscopy and Auger electron spectroscopy. The characteristics of artificial tunnel barriers on NbN are also investigated.

The fabrication of micron- and submicron-area junctions is shown to be possible by use of a "window" geometry. The intrinsic resolution limits of projection photolithography are nearly attained in this process. Ta/PbBi junctions of outstanding quality and current density in the range 10^3–10^4 A/cm^2 are produced and tested as SIS mixers in the 90-110 GHz range. Submicron Ta/PbBi junctions with current density up to 10^5 A/cm^2 reveal the existence of "telegraph noise" where the resistance of the junction switches between discrete levels. The switching rates are analyzed and their dependence on bias voltage, temperature and magnetic field is investigated. The Rogers-Buhrman model based on the trapping and untrapping of

single electrons in localized states within the tunnel barrier accounts successfully for these observations. The small area of these junctions allows the resolution of such telegraph noise by reducing the number of trap states giving rise to each sequence of switching events. In larger area junctions, the superposition of a large number of such fluctuators gives rise to the observed 1/f behavior of the noise spectral density.

APPENDIX A

Fabrication Sequence For Small-Area Ta/PbBi Junctions

A - Preparation of Substrate (Si or Fused Quartz):

1. Visually inspect the fused quartz wafer. If it has any fine cracks, discard.
2. Ultrasonic cleaning (US) in TCE (Trichloroethylene) for 1 minute.
3. US in Acetone for 1 minute.
4. US in Isopropanol for 1 minute, then blow dry (with dry N_2).
5. Bake the wafer on a hot plate at 180°C for 10 minutes.

B - Evaporation of Ge film (only for fused quartz wafers):

1. Oxygen dc glow-discharge cleaning to promote adhesion of the Ge. P_{O_2} = 120 mTorr, I = 1 mA, V = 900 V (with the 520 kΩ series resistance), for 10 - 20 seconds.
2. Evaporate 3000 Å Ge from 20-mil Ta boat with W rods in the middle, at P~10^{-6} Torr, and a rate of 20-30 Å/sec.

C - Deposition and patterning of Ta base electrode:

1. Spin photoresist AZ 1470 at 3000 RPM for one minute.
2. Bake on a hot plate at 85°C for 10 minutes. Wait 30 minutes.
3. Project the base-electrode pattern with the Zeiss microscope (40X lens, exposure time used was 40-50 seconds; source is Hg lamp). Step and repeat.
4. Soak in chlorobenzene for 5 minutes.
5. Rinse in Freon TF (Trifluorotrichlorethane). Blow dry.
6. Develop in 1:1 diluted Microposit developer for 60 seconds. Rinse with deionized (DI) water for 60 seconds. Blow dry.

7. In the ion-beam sputter deposition system, deposit 100 Å Nb followed in-situ by 3000 Å Ta.
8. Unload and lift-off in acetone.

D - Definition of the window area:

1. Spin AZ 1470 photoresist at 3000 RPM for one minute. Bake at 85°C for 15 minutes.
2. Project the window mask using the Zeiss microscope. (40X lens, exposure time is 40-60 sec). Step and Repeat. Soak in chlorobenzene for 5 minutes. Rinse in Freon TF. Blow dry.
3. Develop in 1:1 diluted Microposit developer. Rinse in DI water for 60 seconds. Blow dry.
4. Evaporate 3000 Å SiO at the rate of 25-40 Å/sec and a base pressure of ~ 10^{-6} Torr.
5. Unload and lift-off by US in acetone for ~ 2 minutes.

E - Trilayer resist for counterelectrode lift-off:

1. Spin AZ 1450J at 4000 RPM for one minute. Bake at 85°C for 15 minutes.
2. Wait 30 minutes, then blanket-expose in mask aligner for 3 minutes in the mask aligner.
3. Evaporate 500 Å of Al at ~ 10 Å/sec.
4. Spin AZ 1470 photoresist at 5000 RPM for one minute. Wait 30 minutes.
5. Bake at 85°C for 10 minutes.
6. Scribe the wafer into 6 equal parts, each containing four junctions.
7. Expose the counterelectrode mask by contact printing in the mask aligner for 70-80 seconds.
8. Develop the top photoresist layer in 1:1 diluted Microposit developer for 25-30 seconds.

9. Rinse in DI water for 60 seconds. Blow dry.
10. Project the fine features of the counterelectrode using the Zeiss microscope. (40X lens, exposure time is 50 seconds). Develop as in 8. above.
11. Etch the Aluminum with undiluted commercial Al etch. Continue etching for 5 seconds after the Aluminum disappears. Rinse with DI water for 1 minute. Blow dry.
12. Develop the bottom photoresist layer in 1:1 diluted Microposit developer. Keep developing for 5 seconds after the photoresist is gone. Rinse in DI water for one minute. Blow dry.

F - Barrier Formation and Counterelectrode deposition:

1. Load sample in the evaporator. Use silver paint to ground the Ge to the sample holder (only for fused quartz substrates). Orient the sample to be perpendicular to the ion beam. Pump down to ~ $4x10^{-7}$ Torr.
2. Ion-beam clean in three steps: a) 50% O_2, 50% Xe with P_{total} ~ $1.8x10^{-4}$ Torr at 200 V, 2 mA for 10 minutes. b) Xe alone at 200 V, 2 mA for 10 minutes. c) Xe at 160 V, 2 mA for 3 minutes.
3. Rotate the sample to be parallel to the glow discharge plate. dc glow discharge with 120 mTorr O_2, I = 2 mA, V = 1450 V with the 520 kΩ series resistance, for 8 - 15 seconds.
4. Evaporate 3000 Å PbBi at the rate of 40-60 Å/sec followed in-situ by 120 Å of Indium at the rate of 40-60 Å/sec.
5. Unload from evaporator and lift-off the counterelectrode in acetone. Sample is ready to be tested electrically.

APPENDIX B

Microwave Measurements of Ta/PbBi Junctions

The principles and techniques of detecting microwaves and millimeter-waves using superconducting junctions as SIS mixers have been comprehensively reviewed by Tucker and Feldman (1985). Previous studies of Ta/PbBi SIS mixers were conducted at 36 GHz [Face (1986a, 1987)] and used Si substrates. Two tuning elements were available in the mixer block to obtain rf matching which also implied a narrow instantaneous bandwidth. Those junctions were used to observe and accurately measure strong quantum mixing effects, conversion gain $G>1$, and a noise level within a factor of two of the quantum limit at 36 GHz. The small-area Ta/PbBi fabricated in this work were designed with the intention to 1) extend the operation of such mixers to the 90-110 GHz range and 2) allow easy and broadband tuning by use of a single tuning element in the mixer block and a filter structure on the junction electrodes. Fused quartz substrates were used to minimize dielectric loading of the waveguide [Goldsmith (1982)].

In order to obtain optimum RF coupling to the mixer over a broad tunable bandwidth, an RF matching structure on the substrate - shown in Fig. B-1 - was designed based on scaled model measurements [Raisanen et al. (1985)]. In this design, the RF filter reactance on the substrate is used as a fixed RF matching element while a noncontacting backshort provides a single adjustable tuning element. This design should allow junctions with capacitances of 30-300 fF and RF resistances of 10-100 Ω to be matched. The junction substrate with the RF filter structure is placed across the waveguide in a small channel so that the portions of the substrate

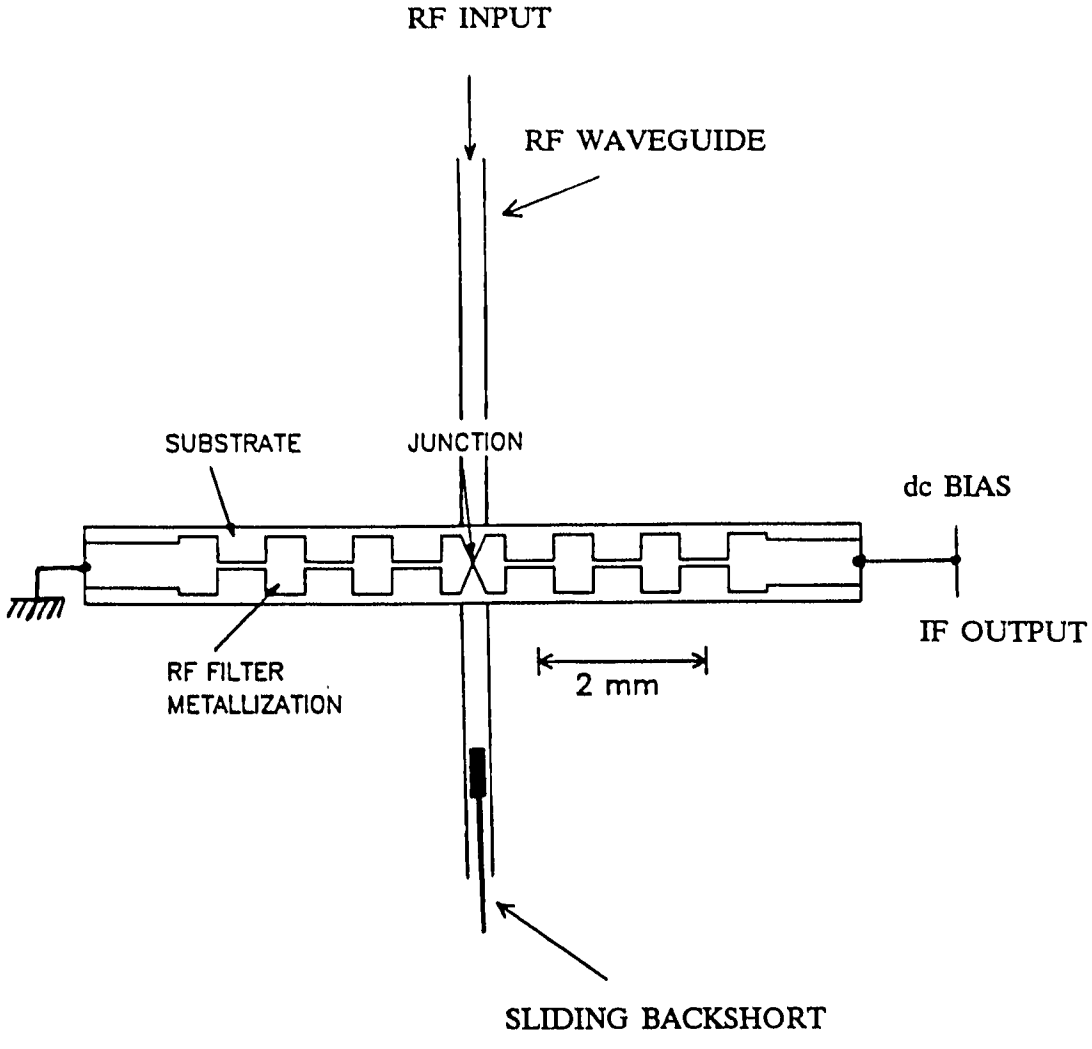

Fig. B-1 Filter structure design for junction electrodes to prevent leakage of RF from the mixer and to provide a broad-band RF match to the mixer.

outside of the waveguide form a suspended stripline circuit and provide an output for the IF signal. A choice of two transformers between the mixer block and the IF amplifier was available to allow efficient coupling to mixer output impedances of either 50 or 700 Ω. The rest of the receiver used for these measurements is a 100 GHz version of the successful 36 GHz test apparatus that has been described previously [McGrath et al. (1985, 1986)]. It makes use of cryogenic hot-cold loads at both the IF and RF to make accurate measurements of mixer gain and noise. A coaxial switch is used to compare the output of the IF matching circuit with the output of a 50 Ω IF hot-cold load. The IF mismatch is evaluated using a bidirectional coupler. A cryogenic isolator between the IF transformer and the cooled 1.5 GHz GaAs IF amplifier is used to make the amplifier insensitive to impedance variations in the mixer output.

Before accurate gain and noise measurements were made, each mixer was optimized for the maximum coupled gain at the upper sideband using a coherent signal injected in the LO-waveguide and cross-guide coupler. The double sideband (DSB) receiver noise temperature, mixer gain and noise temperature were then measured using the hot-cold loads [McGrath et al. (1985, 1986)]. the main results are summarized in table B-1. The DSB noise temperatures in Table B-1 should be multiplied by a factor of ~2 to compare with single sideband (SSB) measurements. Gain was always largest for the lowest frequencies (~ 85 GHz).

The mixing performance listed in Table B-1 is not outstanding even though the dc I-V characteristics (shown in chapter 5) are excellent. Recent measurements in the same apparatus with Pb-alloy junctions from NBS, Boulder showed excellent RF coupling, with large gain and low noise [Raisanen et al. (1987)]. This demonstrates

Table B-1. Summary of mixer results for single junctions and series arrays of six junctions. R_N is the normal state resistance, R_D the dynamic resistance at the dc bias voltage, G_A is the available gain, T_M is the mixer noise temperature and N is the number of junctions (N=6 for the array).

Junction $R_N(\Omega)$	Dynamic $R_D(\Omega)$	G_A(DSB) (dB)	T_M(DSB) (K)	Sideband Ratio (dB)	N
50	170	-13.8	117	2.5	1
350	1000	-16.7	196	...	1
77	150	-13.6	69	-0.23	1
31	50	-7.6	72	-1.82	6
19	170	-6.9	21-28	2.85	6

that the measurement apparatus is not the cause of the poor performance we observe. The most probable cause is a significant discrepancy between the actual dimensions of the RF choke structure and the intended design shown in Fig. B-1. Two less likely explanations are: 1) losses or impedance mismatches caused by the evaporated Ge film discussed in chapter 4, or 2) an excess capacitance which exceeds the usual value of 150 $fF/\mu m^2$ calculated for these junctions. Computer calculations used to fit the pumped I-V curves indicate the presence of an excess parallel inductance [Face (1986)] . This excess inductance is consistent with a separate set of calculations [Raisanen (1986b)] using an equivalent circuit model of the RF choke structure and the actual (non-ideal) choke dimensions. Future work at Yale will involve similar junctions with the correct choke dimensions. Such junctions are expected to produce excellent mixer performance.

REFERENCES

1) Ion Tech Inc., Box 1388, Ft. Collins, Co.

2) Commonwealth Scientific Corporation, Alexandria, Va.

3) IBM Research, Yorktown Heights, NY.

4) Advanced Energy, Ft. Collins, Co.

Adler, J.G. and J.E. Jackson, Rev. Sci. Inst. 37, 1049 (1966).

Andreev, A.F., Sov. Phys. JETP 19, 1228 (1984).

Anderson, P.W. and J.M. Rowell, Phys. Rev. Lett. 10, 230 (1963).

Ambegaokar,V., and A. Baratoff, Phys. Rev. Lett. 10,486 (1963);
Errata, Phys. Rev. Lett. 10, 104 (1963).

Arnold, G.B., Phys. Rev. B 18,1076 (1978); 23, 1171 (1981).

Arnold, G.B., J. Low Temp. Phys. 59, 143 (1985).

Ascherman, G., E. Friedrich, E. Justi, and J. Kramer, Physikalishe Zeitschrift 42, No. 21/22, 349 (1941).

Ashkin, M., J.R. Gavaler, J. Greggi, and M. Decroux, J. Appl. Phys. 55, 1044 (1984).

Atkinson, A., Rev. Mod. Phys. 57, 449 (1985).

Bacon, D.D., A.T. English, S. Nakahara, F.G. Peters, H. Schreiber, W.R. Sinclair, and R.B. Van Dover, J. Appl. Phys. 54, 6509 (1983).

Barner, J.B. and S.T. Ruggiero, IEEE Trans. Magn. MAG-23, 854 (1987).

Brinkman, W.F., R.C. Dynes, and J.M. Rowell, J. Appl. Phys. 41, 1915 (1970).

Cabrera, N. and N.F. Mott, Rep. Prog. Phys. 12, 163 (1949).

Celashi, S., T.H. Geballe, and W.P. Lowe, Appl. Phys. Lett. 43, 794 (1983).

Chaikin, P.M., Solid St. Commun. 17, 1471 (1975);

Chaikin, P.M. and P.K. Hansma, Phys. Rev. Lett. 36, 1552 (1976).

Chakraborty, B., W.E. Pickett, and P.B. Allen, Phys. Rev. B 14, 3227 (1976)

Chow, C.K., J. Appl. Phys. 36, 559 (1965).

Clarke, J. and R.F. Voss, Phys. Rev. Lett. 33, 24 (1974).

Coburn, J.W., Plasma Etching and Reactive Ion Etching, (American Vacuum Society Monograph Series, New York, 1982)

Cooper, L.N., Phys. Rev. 104, 1189 (1956).

Cui, G.-J., D.W. Face, E.K. Track, and D.E. Prober, IEEE Trans. Magn. MAG-23, 688 (1987).

Cukauskas, E.J., W.L. Carter, S.B. Qadri, and E.F. Skelton, IEEE Trans. Magn. MAG-21, 505 (1985a).

Cukauskas, E.J., W.L. Carter, and S.B. Qadri, J. Appl. Phys. 57, 2538 (1985b).

Cuomo, J.J., J.M.E. Harper, C.R. Guamieri, D.S. Lee, L.J. Attanasio, Angilelo, C.T. Wu, and R.H. Hammond, J. Vac. Sci. Tech. 20, 349 (1982).

Dalrymple, B.J., Ph.D. Thesis, Yale University (1983).

Danchi, W.C., J.B. Hansen, M. Octavio, F. Habbal, and M. Tinkham, Phys. Rev. B 30, 2503 (1984).

De Gennes, P.G. and D. Saint-James, Phys. Lett. 4, 151 (1963).

Deutscher, G. and P.G. De Gennes, in Superconductivity, edited by R.D. Parks, Marcel Dekker, New York (1969).

Dingham, M.J., W.R. Fawcett, and H. Bohni, J. Electrochem. Soc. 113, 656 (1982).

Dunkelberger, L.N., J. Vac. Sci. Tech. 15, 88 (1978).

Dutta, P. and P.M. Horn, Rev. Mod. Phys. 53, 497 (1981).

Dynes, R.C. and J.M. Rowell, Phys. Rev. B 11, 1884 (1975).

Eliashberg, G.M., Sov. Phys. JETP 11, 696 (1960).

Face, D.W., D.E. Prober, W.R. McGrath, and P.L. Richards, Appl. Phys. Lett. 48, 1098 (1986a).

Face, D.W. unpublished (1986b).

Face, D.W., Ph.D. Thesis, Yale University (1987); available from University Microfilms, Ann Arbor, MI 48106).

Faris, S.M., S.I. Raider, W.J. Gallagher, and R.E. Drake, IEEE Trans. Magn. MAG-19, 1293 (1983).

Feigin, L.A. and A.I. Shal'nikov, Sov. Phys. Doladv 1, 377 (1957).

Feuer, M.D., Ph.D. Thesis, Yale University (1980).

Fisher, J.C. and I. Giaever, J. Appl. Phys. 32, 172 (1961).

Frankavilla, T.L., S.A. Wolf, and E.F. Skelton, IEEE Trans. Magn. MAG-17, 569 (1981).

Fromhold, A.T. Jr., Theory of Metal Oxidation (North-Holland, New York, 1976)

Fromhold, A.T. Jr., and E.L. Cook, Phys. Rev. 158, 600 (1967).

Gadzuk, J.W., J. Appl. Phys. 41, 286 (1970).

Gallagher, W.J., Physica 108B, 825 (1981).

Gavaler, J.R., J. Talvacchio, and A.I. Braginski, Adv. Cryo. Eng. 32, 627 (1986).

Gilabert, A., Ann. Phys., 1977, t.2, 203.

Ginzburg, V.L. and L. Landau, Zh. Eksperim. i Teor. Fiz. 20, 1064 (1950).

Glang, R., in Handbook of Thin Film Technology, edited by L.I. Maissel and R. Glang (McGraw-Hill, NY 1970).

Gloersen, P.G., J. Vac. Sci. Tech. 12, 28 (1975).

Goldsmith, P.F., in Infrared and Millimeter Waves, Vol. 6, Ed. K.J. Button: Academic Press, 335, 1982.

Gor'kov, L.P., Soviet Phys. JETP 9, 1934 (1959).

Greiner, J.H., C.J. Kircher, S.P. Klepner, S.K. Lahiri, A.J. Warnecke, S. Basavaiah, E.T. Yen, J.M. Baker, P.R. Brosious, H.-C. W. Huang, M. Murakami, and I. Ames, IBM J. RES. DEV. 24, No. 2, 195 (1980).

Grundner, M. and J. Halbritter, Surf. sci. 136, 144 (1984).

Guard, R.W., J.W. Savage, and D.G. Swarthout, Trans. Am. Met. Soc. AIME 239, 643 (1967).

Gundlach, K.H., G. Faraci, G. Giaquinta, and N.A. Mancini, Phys. Lett. 43A, 27 (1973).

Gurvitch, M., M.A. Washington, and H.A. Huggins, Appl. Phys. Lett. 42, 472 (1983).

Gurvitch, M. and J. Kwo, Adv. Cryo. Eng. 30, 509 (1984).

Gurvitch, M., J.P. Remeika, J.M. Rowell, J. Geerk, and W.P. Lowe, IEEE Trans. Magn. MAG-21, 509 (1985).

Hahn, A., M. Brunner, and H. Ekrut, Thin Solid Films 102, 221 (1983).

Halbritter, J., Appl. Phys. A. 43, 1 (1987).

Halbritter, J., Surface Science 122, 80 (1982).

Halbritter, J., IEEE Trans. Magn., MAG-19,799 (1983).

Halbritter, J., J. Appl. Phys. 58, 1320 (1985), and references therein.

Harper, J.M.E., J.J. Cuomo, and H.R. Kaufman, Ann. Rev. Mater. Sci. 13, 413 (1983).

Harper, J.M.E., J.J. Cuomo, and H.T.G. Hentzell, Appl. Phys. Lett. 43, 547 (1983).

Harper, J.M.E., J.J. Cuomo, and H.T.G. Hentzell, J. Appl. Phys. 58, 550 (1985).

Hatzakis, M., B.J. Canavello, and J.M. Shaw, IBM J. RES. DEV. 24, No. 4, 452 (1980).

Hauser, J.J., H.C. Theuerer, and N.R. Westhamer, Phys. Rev. 136, A 637 (1964).

Harris, R.E., Phys. Rev. B 10, 84 (1974).

Hertel, G., D.B. McWhan, and J.M. Rowell, in Superconductivity in d- and f-Band Metals (Kernforschumgszentrum Karlsruhe, Karlsruhe, 1982) p.299.

Hikita, M., K. Takei, and M. Igarashi, J. Appl. Phys. 54, 7066 (1983).

Holm, R. and W. Meissner, Z. Phys. 74, 715 (1932).

Hooge, F.N., Physica 83 B + C, 14 (1976).

Howard, R.E., W.J. Skocpol, L.D. Jackel, P.M. Mankiewich, L.A. Fetter, D.M. Tennant, R. Epsworth, and K.S. Ralls, IEEE Trans. Elec. Dev. ED-32, 1669 (1985).

Igarashi, M., M. Hikita, and K. Takei, Adv. Cryo. Eng. 30, 535 (1984).

Jain, A.K., J.E. Lukens, and J.-S. Tsai, IEEE Trans. Magn. MAG-23, 450 (1987).

Johnson, J.B., Phys. Rev. 26, 71 (1925).

Josephson, B.D., Phys. Lett. 1, 251 (1962).

Josephson, B.D., Adv. Phys. 14, 419 (1965).

Kampwirth, R.T., D.W. Capone II, K.E. Gray, and A. Vicens, IEEE Trans. Magn. MAG-21, 498 (1985).

Kirton, M.J. and M.J. Uren, Appl. Phys. Lett. 48, 1270 (1986), and references therein.

Kleinsasser, A.W., J.M.E. Harper, J.J. Cuomo, and M. Heibulm, Thin Solid Films, 333 (1982).

Kwo, J., G.K. Wertheim, M. Gurvitch, and D.N.E. Buchanam, IEEE Trans. Magn. MAG-19, 795 (1983).

Lahiri, S.K., S. Basavaiah, and C.J. Kircher, Appl. Phys. Lett. 36, 334 (1980).

Likharev, K.K., Dynamics of Josephson Junctions and Circuits, Gordon and Breach Science Publishers, 1986.

Lin, L.-J., and D.E. Prober, Appl. Phys. Lett. 49, (1986).

McGrath, W.R., A.V. Raisanen, and P.L. Richards, IEEE Trans. Magn. MAG-21, 212, 1985; and Int. J. Infrared and Millimeter Waves 7, 543, 1986.

McMillan, W.L. and J.M. Rowell, in Superconductivity, ed. by R.D. Parks, Vol. 1, p. 561, Dekker, New York (1969).

MacDonald, D.K.C., Noise and Fluctuations (Wiley, New York 1962).

Machlup, S., J. Appl. Phys. 25, 341 (1954).

Meissner, W. and R. Ochsenfeld, Naturwiss 21, 787 (1933).

Meissner, H., Phys. Rev. 109, 686 (1958); Phys. Rev. Lett. 2, 458 (1959); Phys. Rev. 117, 672 (1960).

Meservey, R., P.M. Tedrow, and J.S. Brooks, J. Appl. Phys. 53, 1563 (1982).

Misener, A.D., H.G. Smith, and J.O. Wilhelm, Trans. Roy. Soc. Can. 29, 1 (1935); A.D. Misener, Can. J. of Research 14, 25 (1936).

Moodera, S.J.S., R. Meservey, and P.M. Tedrow, Appl. Phys. Lett. 41, 488 (982).

Mukarami, M., H.-C.W. Huang, J. Angilello, and B.L. Gilbert, J. Appl. Phys. 54, 738 (1983).

Munk, W.H., The rotation of the Earth (Cambridge Univ. Press, New York 1960), p. 162.

Musha, T. and H. Higuchi, Jap. J. Appl. Phys. 15, 1271 (1976).

Nambu, Y., Phys. Rev. 117, 648 (1960).

Ocampo, M.A., J.L. Heiras, and T.A. Will, J. Appl. Phys. 53, 3698 (1982).

Onnes, H.K., Leiden Commun. 120b, 120c, 124c (1911).

Raider, S.I., IEEE Trans. Magn. MAG-21, 110 (1985).

Raider, S.I., private communication (1986).

Parker, W.H., D.N. Langenberg, A. Deinstein, and B.N. Taylor Phys. Rev. 177, 639 (1969).

Raisanen, A.V., W.R. McGrath, D.G. Crete, and P.L. Richards, Int. J. Infrared and Millimeter Waves 6, 1169 (1985).

Raisanen, A.V., D.G. Crete, P.L. Richards, and F.L. Lloyd, to appear (1987).

Raisanen, A.V., private communication (1986).
Read, M.H. and C. Altman, Appl. Phys. Lett. 7, 51 (1965).

Rochlin, G.I., Phys. Rev. 153, 513 (1967).

Rogers, C.T., Ph.D. thesis, Cornell University (1987).

Rogers, C.T. and R.A. Buhrman, Phys. Rev. Lett. 53, 1272 (1984).

Rogers, C.T. and R.A. Buhrman, Phys. Rev. Lett. 55, 859 (1985).

Rogers, J.S., J.G. Adler, and S.B. Woods, Rev. Sci. Instr. 35, 208 (1964).

Rowell, J.M., in Tunneling Phenomena in Solids, edited by E. Burstein and S. Lundquist (Plenum, New York, 1969).

Rowell, J.M., Phys. Rev. Lett. 30, 167 (1973).

Rowell, J.M., M. Gurvitch, and J. Geerk, Phys. Rev. B 24, 2278 (1981).

Ruggiero, S.T., D.W. Face, and D.E. Prober, IEEE Trans. Magn. MAG-19, 960 (1983).

Ruggiero, S.T., E.K. Track, G.B. Arnold, and M.J. DeWeert, Phys. Rev. B 34, 217 (1986).

Ruggiero, S.T., G.B. Arnold, E.K. Track, and D.E. Prober, IEEE Trans. Magn., MAG-21, 850 (1985); and in Proceedings of the 17th International Conference on Low-Temperature Physics, North-Holland, New York, 1984, p. 847.

Schottky, W., Phys. Rev. 28, 74 (1926).

Schrieffer, , J.R., in Tunneling Phenomena in Solids, ed. by E. Burstein and S. Lundqvist, Plenum Press, New York (1969).

Simmons, J.G., J. Appl. Phys. 34, 1793 and 2581 (1963).

Shal'nikov, A., Nature 142, 74 (1938).

Shinoki, A., A. Shoji, S. Kosaka, S. Takada, and H. Hayakawa, Appl. Phys. Lett. 38, 285 (1981).

Shoenberg, D., Superconductivity, Cambridge University Press, 1952, p. 166.

Smith, L.N., J.B. Thaxter, D.W. Jillie, and H. Kroger, IEEE Trans. Magn., MAG-18, 1571 (1982).

Smith, P., S. Shapiro, J.L. Miles, and J. Nicol, Phys. Rev. Lett. 6, 686 (1961).

Spencer, E.G., and J.M. Rowell, IEEE Trans. Magn. MAG-17, 322 (1981).

Stratton, R., J. Phys. Chem. Solids 23, 1177 (1962).

Thakoor, S., H.G. LeDuc, A.P. Thakoor, J. Lambe, and S.K. Khanna, J. Vac. Sci. Tech. A4(3), 528 (1986).

Thompson, L.F., C.G. Willson, and M.J. Bowden, Eds., Introduction to Microlithography (ACS Symposium Series 219, Washington D.C., 1983).

Tinkham, M., Introduction to Superconductivity, Robert E. Krieger Publishing Co., Huntington, New York (1975).

Track, E.K., L.-J. Lin, G.-J. Cui, and D.E. Prober, Adv. Cryo. Eng. 32, 635 (1986).

Tucker, J.R. and M.J. Feldman, Rev. Mod. Phys. 57, 1055 (1985).

Umbach, C.P., A.M. Goldman, and L.E. Toth, Appl. Phys. Lett. 40, 81 (1982).

Umbach, C.P., Ph.D. thesis, University of Minnesota (1982b).

Van Der Pauw, L.G., Phillips Res. Rep. 13, 1 (1958).

Van Duzer, T. and C.W. Turner, Principles of Superconducting Devices and Circuits, Elsevier North Holland, New York (1981).

Van Kampen, N.G., in Fluctuation Phenomena in Solids, edited by R.E. Burgess (Academic, New York 1964), p. 139.

Verveen, A.A. and H.E. Derksen, Proc. IEEE 56, 906 (1968).

Villegier, J.C., L. Vieux-Rochaz, M. Goniche, P. Renard, M. Vabre, IEEE Trans. Magn. MAG-21, 498 (1985).

Voss, R.F. and J. Clarke, Nature 258, 317 (1975a).

Voss, R.F. and J. Clarke, Phys. Rev. B 13, 556 (1975b).

Wakai, R.T. and D.J. Van Harlingen, Appl. Phys. Lett. 49, 593 (1986).

Wakai, R.T. and D.J. Van Harlingen, Phys. Rev. Lett. 58, 1687 (1987).

Walmsley, D.G., E.L. Wolf, and J.W. Osmun, Thin Solid Films 62, 61 (1979).

Weber, H.W., Ed., Anisotropy Effects in Superconductors, Plenum Press, New York (1977).

Weissmantel, C. Thin Solid Films 32, 11 (1976). See also H.-J. Herler, G. Reisse, and C. Weissmantel, ibid., 65, 233 (1980).

White, G.K., Experimental Techniques in Low-Temperature Physics, Oxford University Press, Oxford, 1979.

Wisnieff, R.L., Ph.D. Thesis, Yale University (1986).

Witt, T.J. and D. Reymann, IEEE Trans. Instrum. Meas. 32, 260 (1983).

Wolf, E.L., Principles of Electron Tunneling Spectroscopy, Oxford Press, New York, 1985.

Wolf, E.L. and G.B. Arnold, Phys. Repts, 91, 31 (1982).